THE DISTORTION OF TURBULENCE
BY IRROTATIONAL STRAIN

Experiments on the irrotational homogeneous distortion of grid turbulence were conducted. Three types of strain were studied: plane strain, symmetrical contraction, and symmetrical diffusion (or expansion).

The results for plane strain (strain ratio 6 : 1) differ from those of Townsend (strain ratio 4 : 1) in that: (i) a higher degree of anisotropy was achieved, (ii) there was no evidence of an equilibrium structure, and (iii) there was a strong tendency for the turbulence to become less isotropic after straining. These results consequently fail to support Townsend's contention of the establishment of an equilibrium structure in ordinary shear flows with flow patterns that are comparatively stable.

For all types of strain, the rapid distortion theory predicted quite accurately the development of the total turbulent energy when a simple correction was applied for decay. The Reynolds stress structure agreed well with the theory in the initial stages of distortion. As streaming progressed, agreement was less satisfactory; there was an apparent transfer of energy between components. No support was found for Rotta's hypothesis concerning this transfer.

THE DISTORTION OF TURBULENCE

BY IRROTATIONAL STRAIN

THE DISTORTION OF TURBULENCE
BY IRROTATIONAL STRAIN

By

Henry J. Tucker

A thesis
Submitted to the Faculty of Graduate Studies
and Research in Partial Fulfilment of the
Requirements for the Degree of
Doctor of Philosophy

Department of Mechanical Engineering
McGill University
Montreal, P.Q.   July 1970

SUMMARY

This thesis represents a continuation of the work of
Townsend[65] on the irrotational distortion of homogeneous
turbulence. The results of his experiments form the basis
of his theory (outlined in his monograph[66]) on free turbulent
shear flow.

Here irrotational strains are classified. In their
effect on turbulence, it is postulated that three parameters
are important: F, the type of strain; ℓ_1, the strain ratio;
and I, the rate of strain parameter.

Experiments were performed in ducts which produced
three different types of strain: plane strain ($F = 0$),
symmetrical contraction ($F = -1/2$), and symmetrical diffusion
($F = 1$). Strain ratios ℓ_1 up to 6 were achieved with para-
meters $.25 \leq I_A \leq .97$.

Plane strain was produced in a duct similar to the
distorting duct used by Townsend.[65] However, here strain
ratios up to 6:1 were obtained compared with 4:1 obtained
by Townsend. The results differ from those of Townsend in
that: (1) a considerably higher degree of anisotropy was
achieved, the structural measure K attained values of 0.62
rather than the maximum of 0.42 which he found; (II) there
was no evidence that an equilibrium structure was obtained;
and (III) there was a strong tendency for the strained

turbulence to approach isotropy when the straining ceased. The failure of the present experiments to support the contention of an equilibrium Reynolds stress structure has been taken into consideration in Townsend's finite distortion model[67] of free turbulent shear flows.

Good agreement between theoretical and experimental values of $\overline{q^2}$ (twice the total energy of turbulence) was obtained throughout all ducts; the theoretical values were obtained assuming rapid distortion of isotropic turbulence with a simple correction for decay. Comparison of the measured Reynolds stress structure with the theoretical structure (based on rapid distortion of the anisotropic grid turbulence) showed good agreement in the initial stages of distortion; as the straining progressed there appeared to be a tendency for the turbulent eddies to become oriented more in a plane normal to the minimum rate of strain than that predicted by the theory. The distribution of turbulent energy between components did not agree with Rotta's[55] hypothesis (that the rate at which energy is transferred to a component depends on the energy deficit in that component below the mean energy level).

The range of the values of I_A in the present experiments was not sufficient to show a definite dependence of the turbulent structure on this parameter; however, comparison of the present results in the symmetrical contraction with the corresponding results of Uberoi[70] indicates that

the turbulent structure is influenced by the rate of strain parameter. This implies that strained turbulence acts as a viscoelastic media as suggested by Lumley[34] and an equilibrium structure is not possible unless I remains constant.

ACKNOWLEDGEMENTS

research. Financial support for the project was provided
by the Defence Research Board of Canada under Grant Number
9551-12.

CONTENTS

ix

x

FIGURES

xi

xiii

xiv

TABLES

NOMENCLATURE
(Main Text)

$A_i(\underline{k})$ — Fourier coefficient of $u_i(\underline{x})$; $\tilde{A}_i(\underline{k})$ is the Fourier coefficient of $\tilde{u}_i(\underline{x})$.

B — coefficient in equation for decay of $\overline{u^2}$ component of grid turbulence in uniform flow.

b, c — quantities appearing in spectra equations for symmetrical contraction, defined in text.

C — coefficient in equation for decay of $\overline{v^2}$ and $\overline{w^2}$ components of grid turbulence in uniform flow.

D — substantiative or Lagrangian differential operator.

d — length of a cube of fluid before deformation.

e_{ij} — deformation tensor; $e_{ij} = \frac{1}{2}\left(\frac{\partial U_i}{\partial x_j} + \frac{\partial U_j}{\partial x_i}\right)$.

E_{ij} — spectrum tensor of turbulent kinetic energy.

F — strain type parameters

I — strain rate parameter

K — structural measure of turbulence; $K = (\overline{u^2}_{max} - \overline{u^2}_{min})/(\overline{u^2}_{max} + \overline{u^2}_{min})$; K_t, value from the rapid distortion theory of anisotropic turbulence.

k — wave number $2\pi n/\overline{U}$; $\underline{k}$, wave number vector; subscripts 1, 2, 3, i, j, k refer to Cartesian coordinates.

k — constant which measures cooling effect of velocity component along the hot-wire.

L — length scale; L_u, length scale associated with energy containing-eddies.

ℓ_i — strain ratios; coordinates are chosen so that $\ell_1 \geq \ell_2 \geq \ell_3$; $(\ell_i)_h$, hypothetical strain ratio to generate turbulent structure by rapid distortion;

$(\ell_i)_e$, equivalent strain ratio; $(\ell_i)_e = \ell_i(\ell_i)_h$ (no summation).

M	mesh length
m	exponent in $\overline{v^2}$ and $\overline{w^2}$ component of turbulence decay law.
N	constant in empirical spectrum equation.
n	exponent in $\overline{u^2}$ component of turbulence decay law.
P	reference point in space
Q_{ij}	second order velocity correlation tensor
q^2	$u_i u_i =$ twice kinetic energy of turbulence; $\overline{q^2}$, time-mean value.
Re_M	Reynolds number based on M the mesh length
r	distance between two points; $\underline{r}$, vector.
S_{ij}	$\partial x_i/(\partial x_j)_A$, Lagrangian deformation tensor.
t	time; t_s, characteristic time of rate of strain; t_e, characteristic time of turbulent energy decay.
U,V,W	Eulerian velocities; $\overline{U},\overline{V},\overline{W}$, time-mean values; u,v,w, fluctuating components; u',v',w', root-mean-square values.
U_i	Eulerian velocity; u, fluctuating component; u', root-mean-square value; subscripts 1, 2, 3, i, j, k, refer to Cartesian coordinates.
x,y,z	Eulerian Cartesian coordinates
x_i	Eulerian Cartesian coordinates; subscripts 1, 2, 3, i, j, k refer to coordinates; x_g, coordinate distance to grid; x_0, coordinate distance to virtual origin of turbulence; x_0', virtual origin of v and w components of turbulence.
X,Y	elliptic integrals appearing in equations; available in tables.

Subscripts

A   reference point on the center-line at the entrance of the distorting ducts.

B   reference point on the center-line at the exit of the distorting ducts.

c   reference point on the center-line 18 inches upstream from the entrance of the distorting ducts.

d   value resulting from decay without distortion.

$i,j,k,$ refer to Cartesian coordinates, repeated sub-
$1,2,3,$ scripts indicate summation.

s   value resulting from rapid distortion without decay.

o   reference point, also used to indicate virtual origin of turbulence.

Greek Letters

α $\partial \bar{U}_1 / \partial x_1$, maximum rate of strain.

β, λ, ψ quantities appearing in equations, defined in text.

∂ partial differential operator.

∇^2 Laplacian operator, $\partial^2 / \partial x_i \partial x_i$.

γ constant in the energy equation.

δ difference

ϵ_{ijk} cyclic coefficient; zero unless $i,j,k,$ are all different; 1 if in order 123123; -1 if in order 132132.

η rotation tensor; $\eta_{ij} = \frac{1}{2} \left(\frac{\partial \bar{U}_i}{\partial x_j} - \frac{\partial \bar{U}_j}{\partial x_i} \right)$.

μ_1, μ_2, μ_3 turbulent component ratios $\overline{u_1^2}/\overline{(u_1)_A^2}$, $\overline{u_2^2}/\overline{(u_2)_A^2}$ and $\overline{u_3^2}/\overline{(u_3)_A^2}$ respectively.

ν kinematic viscosity.

Ω vorticity; $\Omega_i = \epsilon_{ijk} \frac{\partial \bar{U}_k}{\partial x_j}$; $\bar{\Omega}$, time mean value.

Ω_s strain type parameter proposed by Townsend.

ω turbulent vorticity component;

$$\omega_i = \epsilon_{ijk} \frac{\partial u_i}{\partial x_j}$$

CHAPTER 1

INTRODUCTION

The present study of the effects of irrotational
strain on turbulence is important for three reasons.
The first is related to Townsend's theory of free turbulent
shear flow which is outlined in his (1956) monograph.[66]
Townsend's model of turbulence is based on a single set of
measurements obtained when grid turbulence was subjected to
irrotational plane strain. It appeared that the turbulence
developed an equilibrium structure which was assumed to
exist in other shear flows. Because of the practical impor-
tance of Townsend's theory, it was considered worthwhile to
repeat the experiments of Townsend [65] and extend them to
higher strain ratios, also to classify irrotational strains
and extend the experimental study to three-dimensional
strains.

The second reason for studying the effects of irrota-
tional strain on turbulence is related to the first but is
more fundamental, in that attention is directed to under-
standing the process by which energy is transferred within
the turbulent motion. Much of our present understanding of
this process has been obtained from experimental and theore-
tical studies of decaying grid turbulence in uniform flow.

1

The study of grid turbulence in a uniform strain field offers the opportunity of studying the energy transfer process in the presence of energy production, which is closer to the situation in ordinary shear flows, but still avoids the complicating factors of diffusion and mean rotation which make analysis of general shear flows extremely difficult.

The third reason for studying the irrotational distortion of turbulence is because of its practical importance in subsonic wind-tunnels, and the historical significance of this application in the development of the theory.

1.1. Developments Leading to Townsend's Model of Free Turbulence

Intensive study into turbulent motion began about the turn of the present century when Reynolds[52] introduced into the theory the fundamental notion of statistical mean values and recognized the analogies between momentum transfer, transfer of heat and transfer of mass in turbulent motion.

In the years following Reynolds' discoveries, measurements were made only of mean values of velocity and pressure and not the actual turbulent velocity or pressure fluctuations. Theories at this time had to make postulates about the nature of turbulent motion which were based partly on intuition. Among the theories that were developed, those based on the concept of a "mixing length" proved to be the most fruitful. The idea arose that the turbulent motion

consists of eddies which locally are of nearly uniform size.
This concept combined with the already existing ideas of the
kinetic theory of gases, led Prandtl[48] to introduce a
mixing length into his formulation for momentum transport,
and led Taylor [58,60] independently, to introduce a similar
length in his theory on vorticity transfer. The mixing
lengths could only be defined in relation to the erroneous
conception that lumps of fluid behave like molecules of a
gas, preserving their identity until some definite point in
their path, when they mix with their surroundings. The
mixing length concepts were regarded, even by their origina-
tors, as a simplification of the true state of affairs in
the highly complicated turbulent motion, and the resulting
theories were always admittedly incomplete. A good account
of the mixing length theory of Prandtl and its defects are
given by Batchelor.[3]

In all applications of the mixing length theories it
is necessary to make more or less arbitrary assumptions
concerning the effect of turbulence on the mean motion or
of the mean motion on the turbulence. The value of the
mixing length theories has been that fairly simple assump-
tions regarding the mixing length in particular flows have
led to practical semi-empirical relation, which have been
useful from an engineering point of view. These theories
have also served a purpose in providing a framework for
further theoretical and experimental studies, and in

focusing attention on the processes which take place in the turbulent motion.

In more recent years, considerable advances have been made in our understanding of the mechanisms of turbulent motion. This has been brought about, in part, by the improvement in hot-wire instrumentation, which has allowed detailed experimental studies in many different shear flows, and also because of the extensive theoretical and experimental study in one very simple flow, that of homogeneous decaying turbulence. The latter study was the result of Taylor's idea of simplifying the problem by considering a uniform and isotropic field of turbulent fluctuations; such a field can be realized, approximately, in uniform convective flow of grid turbulence; this provides the possibility of experimentally checking statistical ideas. The introduction into the theory of space correlations by Taylor [61] and later of the spectrum function [63] was accompanied by the corresponding measurements, so that theory and experiment proceeded closely together and much insight into the mechanism of turbulence was obtained.

The conditions for the study of the ordinary anisotropic shear flows were not so fortunate. Mathematical analysis is extremely complex for anisotropic turbulence, so that there is no developed theory similar to the existing theories of istoropic turbulence. Our treatment of ordinary shear flow depends on phenomenological theories, such as

the mixing length theories, and empirical relations obtained
from experimental studies.

Experimental analysis, however, has benefited greatly
from the study of isotropic turbulence, since space correla-
tions and spectrum measurements, originally introduced for
isotropic turbulence, have been extended to many ordinary
shear flows; also many of the theoretical relations for
isotropic turbulence have been assumed to apply to the
anisotropic flows.

With the increased information available on ordinary
shear flows, there have been attempts to develop theories
which are based on a more accurate model of turbulence than
the mixing length model. One of the most promising has been
a theory proposed by Townsend,[66] which is based on a model
structure of turbulence, obtained from experimental obser-
vations in a field of homogeneous turbulence subjected to a
prolonged uniform plane strain.

Townsend [65] passed grid turbulence, which was approxi-
mately isotropic, through a duct whose cross-section varied
in shape (but not effective area) with distance along it.
The mean velocity gradients, produced by the changes in the
cross-section, acted on the turbulence passing through the
duct, distorting it in a similar way to the distortion of
ordinary two-dimensional shear flows. In ordinary shear
flows, of course, neither the turbulence nor the distortion
is homogeneous and the mean flow is rotational.

From this experimental study, Townsend reached the following conclusions: (1) the structure of turbulence, produced by uniform plane distortion, is substantially independent of eddy interaction and transport, and in the early stages of distortion, the structure is essentially the same as that produced by instantaneous distortion, for which a theory is available; (2) the mean strain establishes an equilibrium structure in the turbulent flow, which is independent of rate of strain; (3) the energy-containing eddies of turbulence are relatively stable in structure, and in the absence of strain, the time scale for development is relatively large.

The apparently rapid establishment of an equilibrium structure, substantially independent of eddy action and transport in the simple shear flow, suggested to Townsend[66] that a similar structure would be established in many ordinary shear flows. Therefore, he suggested the correct approach might be to consider the behaviour of small volumes or packets of fluid that interact to a minor extent with the surrounding turbulence, the turbulent energy produced by the mean flow being dissipated locally. The idea of following the development of a volume of fluid, large enough to contain a representative sample of the turbulence and small enough to establish mean values for a point, is useful only in situations where the intensity gradients within the shear flow are sufficiently small to make the diffusion of

turbulent energy negligible.

From examination of scales, Townsend found that
gradient type diffusion in free turbulent shear flows (jet,
wakes and mixing layers) is usually negligible. From a
survey of many experimental results, he found that time
associated with energy transfer is longer than the time
associated with the mean rate of strain; this implies that
in an interval of time sufficient for elements of fluid to
become highly distorted, the energy transfer to the elements
by intensity gradients is negligible.

In ordinary shear flows neither the turbulent motion
nor the mean rate of strain is uniform in space. However,
in free turbulent shear flows Townsend found that the scales,
associated with turbulent velocities, were considerably
smaller than the scales of the mean flow velocity variations,
which suggested that the effect of mean velocity gradients
on turbulence is locally much as it would be if the mean
flow gradients were homogeneous.

In ordinary shear flows the local mean motion is
rotational. For example, in the common two-dimensional
boundary-layer flows, strains with approximate principal
rates of strain $\frac{1}{2}(\partial \overline{U}/\partial y)$, $-\frac{1}{2}(\partial \overline{U}/\partial y)$, 0, are combined
with approximate rotation $\frac{1}{2}(\partial \overline{U}/\partial y)$ about the z axis
(here x is in direction of the main flow and y is normal
to the surface). Since no direct information was available,
Townsend assumed that in ordinary shear flows the effects

of mean rotation on the development of turbulence are negligible.

Assuming that in ordinary free turbulent shear flows: gradient type diffusion of energy is negligible, mean flow gradients may be considered homogeneous, and mean rotation effects are negligible; then conditions in these flows are similar to conditions in flows subjected to uniform plane distortion. Townsend, therefore, suggested that an equilibrium structure, of the type he observed to exist after prolonged uniform plane distortion of isotropic turbulence, would also exist in the ordinary two-dimensional free shear flows.

Townsend then proposed a simple model for the structure of free turbulent shear flow; he divided the flow into "large eddies" and the remaining fully turbulent fluid having a structure similar to that produced by uniform plane distortion. A full account of Townsend's theory is contained in his (1956) monograph.[66]

Townsend's double structure of free turbulent shear flow is, admittedly, a simplification of the true state of affairs. Also, the assumptions relating the turbulent structure of free turbulent shear flows to that developed during uniform irrotational distortion of grid turbulence are controversial. However, the assumption of constant eddy viscosity normal to the main flow direction has been a successful way of predicting free turbulence and

observations in jets and wakes have shown that the structure
of turbulence is approximately uniform over regions of
uniform strain type, which agrees with Townsend's simple
model, if the main structure of the turbulence is assumed
to be produced by the mean strain and convected throughout
the flow by the large eddies. Also, the mixing motion of
the large eddies could account for transfer of turbulence
produced by different strain types, as for example, across
the central region of jets and wakes. Townsend's model, in
a manner similar to the mixing length model, has already
provided a framework for a number of experimental and
theoretical studies, which have added to the considerable
existing information on shear flows.

Interest in the present study of the effects of
irrotational strain on turbulence arose directly from
Townsend's [65] experiments on the uniform plane distortion
of homogeneous turbulence. The main conclusions from these
experiments have already been given.

These conclusions are of such far-reaching importance
that it was considered worthwhile to repeat Townsend's
measurements, especially since there were disagreements
between the results of Townsend and those of earlier experi-
ments by MacPhail,[35] who used a similar type of distorting
duct capable of producing strain ratios up to 2, compared
with 4 attainable in Townsend's duct. In MacPhail's experi-
ments the turbulence became anisotropic near the beginning

of distortion, but returned towards the isotropic condition
near the end of distortion, instead of approaching an equili-
brium structure as reported by Townsend. It was, therefore,
decided to repeat Townsend's experiments in a similar type
of distorting duct capable of producing strain ratios up to
6; this would provide a region of uniform distortion longer
than those in the other ducts, and extend the measurements
from strain ratios of 4 to 6, to determine if, in fact, the
structure of the turbulence remains constant after strain
ratios of 4, as assumed by Townsend. It was also decided
to extend the experimental study to three-dimensional
distortions.

1.2. Production of Turbulent Energy by Distortion

Experimental study of irrotational distortion of
turbulence also offers the opportunity to check the
generally held notions of the mechanism by which energy is
transferred from the mean to the turbulent motion. In all
turbulent fluids, the kinetic energy associated with the
turbulence is continually being dissipated; unless there is
a continual supply of energy to the turbulent motion it
will gradually decay. An example of decaying turbulence is
that of grid turbulence in uniform mean flow. Where mean
velocity gradients are present, energy is transferred from
the mean to the turbulent motion, and since the transfer of
energy to the three fluctuating velocity components is

selective the resulting turbulence becomes anisotropic.

In ordinary shear flows, as for example in boundary-layers, turbulent energy is generated by interaction of the mean and the turbulent motion. However, in such flows it is extremely difficult to study the process of energy production, since both the mean gradients and turbulence are non-homogeneous, and energy is transferred from one part of the flow to another by diffusion. The study is further complicated by the mean rotation of the flow, which is again non-homogeneous. Since it is extremely difficult to study the production of turbulence in ordinary shear flow, there is considerable incentive to study the production process in a simple homogeneous irrotational shear flow. This may provide insight into the production process and offer a means of checking existing ideas on the mechanism by which turbulent energy is produced. Because the simple flow is far removed from problems of practical interest, the results are not directly applicable from an engineering point of view, but may eventually lead to practical theories, as knowledge of the influence of diffusion and mean rotation becomes available.

The basic assumption of the rapid distortion theory, that of conservation of circulation as introduced by Taylor,[62] offers an explanation of the mechanism by which energy is transferred from the mean to the turbulent motion. For distortion which is sufficiently rapid, the viscous effects

within the fluid may be neglected, and Kelvin's theorem applies, which states that the circulation in any circuit moving with the fluid is invariable. A result of this theorem is, that during distortion, the vorticity associated with an element of a vortex line remains proportional to the length of the element. Vortex elements which are stretched by the mean motion will increase in vorticity, while elements which are contracted will decrease in vorticity. Isotropic turbulence may be considered to consist of vortex elements having no favoured direction, or as being uniformly oriented in space. When isotropic turbulence is subjected to an arbitrary mean strain, the effect is to orient the vortex elements towards the direction of the maximum rate of strain, and in agreement with Kelvin's theorem to increase their vorticity. The result is an increase of the kinetic energy of the turbulent motion, this energy of course comes from the mean motion which strains and orients the vortex elements. Although straining of isotropic turbulence always leads to an increase of the turbulent energy, this is not necessarily the case with turbulence which is initially anisotropic. If anisotropic turbulence is distorted in a way which tends to change the turbulence towards isotropy, then, at least in theory, energy is transferred from the turbulent to the mean motion.

Although it is a central problem in turbulence, it is still not known in what way energy is transferred within the

turbulent motion itself. At high Reynolds numbers, it appears that energy is transferred from one eddy size to another or from one wave number to another by inertia forces and by pressure forces, with the viscous forces important only for the very high wave numbers. One hypothesis has been proposed by Obukoff,[44] who assumed that the energy transfer across the wave number k is analogous to the energy transfer from the main motion to the turbulent motion already discussed. The energy transfer would be in the direction of the higher wave numbers since the large eddies would strain and transfer energy to the smaller eddies which they contain.

The mechanism of energy transfer between different wave numbers is not fully understood for the simple case of decaying isotropic turbulence. Decaying anisotropic turbulence is even more complicated. It is well known that, at high Reynolds numbers, turbulence is more isotropic at high wave numbers (local isotropy); it appears there is a transfer of energy from one component to another, due to a tendency for eddies to become oriented more uniformly in space. It is generally agreed that pressure fluctuations within the turbulence are important in this process. Energy transfer will be discussed later in the thesis in the light of the experimental results.

1.3. Turbulence in Wind-Tunnel Contractions, Historical Development of the Distortion Theory and Related Work

Irrotational distortion of turbulence has a direct application in the design of subsonic wind-tunnels, and it was initial interest in this application which led to the development of the rapid distortion theory.

In wind-tunnels which are used to simulate free flight conditions, it is necessary to reduce the intensity of turbulence to its lowest practicable level, since turbulence effects the measurements in the tunnel, particularly those sensitive to the behaviour of the boundary-layer. The reduction in turbulence level is accomplished by passing the flow through honeycombs and damping screens in a low-speed section called a settling chamber, and then through a contraction to a higher speed working-section. The relative level of the turbulence in the working-section is greatly reduced because of the mean velocity increase, however the turbulence level in the tunnel is also influenced by the geometry of the screens and honeycombs, and by the mean stream distortion within the contraction.

It is known that the wind-tunnel contraction has a selective effect on the turbulence coming from the honey-combs and screens. The absolute value of the longitudinal component of turbulence is greatly reduced, while the absolute value of the lateral components may undergo a considerable increase. Prandtl[49] obtained a simple estimate of the reduction in the longitudinal component by assuming

the kinetic energy increase, which comes from the pressure drop in the contraction, is the same for all elements of fluid passing through the contraction. For the longitudinal components, Prandtl assumed conservation of momentum for a small rotating cylinder of fluid with its axis in the direction of the main flow. Although Prandtl's results agreed approximately with those obtained experimentally in wind-tunnel contractions, his method of analysis was inconsistent, in that different concepts were used in treating the longitudinal and lateral components of the turbulence.

Taylor [62] put Prandtl's line of reasoning, that of rotation of elements of fluid, into a concrete form and laid the foundation of what is usually referred to as the "rapid distortion theory". He assumed irrotational mean flow and considered the turbulence as being due to vorticity with components ω_i along the reference axes. Taylor showed that for rapid distortion, where the relative motion between two neighbouring particles of fluid due to the mean motion is large compared with that due to the turbulence, the vorticity in any direction remains proportional to the length of the element in that direction. The vorticity equation obtained by Taylor is the basis of the rapid distortion theory which is outlined later in this thesis.

Taylor assumed a mathematical model of the initial turbulence which amounted to vortices in rectangular cells arranged in a regular three-dimensional array. The effect

of distortion on the initial turbulence was determined
using the vorticity and element length relation already
mentioned. The final results of the analysis consisted of
expressions for the root-mean-square values of the longi-
tudinal and lateral velocity components downstream of the
distortion, expressed as ratios of the corresponding up-
stream initial values. Initial isotropic turbulence was
approximated by assuming the vortex partitions to be cubical.

There are two objections to Taylor's theory: first,
the decay process which results in reduction of root-mean-
square values of the turbulence as it passes through the
distortion is neglected; second, he treated a rather arti-
ficial model of turbulence which is not as random in space
and time as an actual turbulent field, and no choice of
parameters in Taylor's model corresponds to isotropy. The
second objection to the theory was removed by Taylor's
co-workers Batchelor and Proudman,[5] and also independently
by Ribner and Tucker;[53] both groups used Taylor's vorticity
equations to treat a Fourier integral representation of a
random turbulent field. The introduction of the spectrum
tensor makes it possible to calculate the changes in the
mean-square velocity components; also detailed information
concerning the changes in any of the statistical properties
of the turbulence may be obtained, for example, changes in
the spectrum tensor or correlation tensor.

Ribner and Tucker[53] directed their attention to

finding the development of turbulence in symmetrical wind-tunnel contractions. For initially isotropic turbulence, equations for changes in the three mean-square velocity components were obtained, and also equations for the one-dimensional longitudinal and lateral spectra. They also suggested a method of taking into account the effects of turbulent decay. Batchelor and Proudman [5] treated an arbitrary distortion and obtained equations for changes in the three mean-square velocity components. Decay effects were neglected and no explicit results were obtained for the development of the spectra.

In the rapid distortion theory of Batchelor and Proudman, and also of Ribner and Tucker, explicit results were obtained for the particular case of initially isotropic turbulence. Reynolds [51] has recently extended the theory to include initially anisotropic turbulence by considering the initial turbulence as the product of a hypothetical rapid distortion. This greatly increases the applicability of the theory and makes it valuable in predicting the development of anisotropic turbulence, especially in the initial stages of distortion.

A theoretical study of the behaviour of weak homogeneous turbulence subjected to uniform distortion was conducted by Pearson.[41] He used a linearized form of the Navier-Stokes equations which included the viscous terms. Besides uniform irrotational distortion two other cases of

distortion, uniform rotation and uniform shear, were
studied.

A similar theoretical study of homogeneous turbulence
in flow through symmetrical contractions and expansions was
carried out by Deissler[15] who started from the two-point
correlation equations and retained the viscous terms.
Deissler also studied the effects of inhomogeneity and of
shear flow in weak turbulent fields.

In the equations used by both Pearson and Deissler
the non-linear turbulent inertia terms were neglected. In
most problems of engineering interest the Reynolds number of
turbulence is not sufficiently small to allow this; at
moderately large Reynolds numbers it is the inertia of the
turbulence and not the viscosity which determines the rate
of decay.

Experimental studies of grid turbulence in uniform
irrotational plane strain (already referred to) were carried
out by MacPhail[35] (for strain ratios up to 2) and by Townsend[65]
(for strain ratios up to 4). Results of similar experi-
mental studies have more recently been reported by Maréchal[37]
for strain ratios up to 13.3. The results of Townsend and
Marechal are later compared with results of the author which
were obtained in a similar duct producing strain ratios up
to 6.

Measurements of grid turbulence subjected to strain
in symmetrical contractions were made by Uberoi.[70] Three

contractions were used which produced strain ratios up to
4, 9 and 16. Uberoi's results are later compared with
corresponding results of the author which were obtained in
a symmetrical contraction which produced strain ratios up
to 6. Considerably higher rates of strain were achieved in
Uberoi's contractions.

Turbulent wakes in a mean flow of irrotational plane
strain were studied by Reynolds.[50] Attention was directed
to the existence of theoretically predicted self-preser-
vation and to production of turbulence by the wake shear
and by the distortion. A similar investigation was also
carried out by Keffer.[28]

Attempts to generate homogeneous turbulent shear flows
have been made by Rose[54] and more recently by Champagne,
Harris and Corrsin.[9] In both of these investigations it was
found that, at sufficiently large distances from the grid
and the wall boundary layers, the component energies and
shear stress attained essentially constant values. Complete
homogeneity was not achieved because the scales continued
to grow with downstream distance. These homogeneous rota-
tional flows are closer to ordinary shear flows than the
irrotational flows studied here.

Observations and a revised theory on free shear flows
are contained in a recent publication by Townsend.[67] In his
latest theory the equilibrium structure hypothesis, origi-
nally used to account for the observed Reynolds stress

structure of free shear flows, is abandoned and the structure is now accounted for by mean finite strain or effective strain. The effective strain is shown to vary from flow to flow.

Lumley[34] has recently suggested that (at sufficiently high Reynolds numbers) the structure of turbulence subjected to irrotational strain depends on the (strain rate)(time scale) product. This product is the rate of strain parameter I which appears in the present thesis (I was introduced independently by the author and commented on by Dr. Reynolds in correspondence of Sept. 1969). Lumley points out, in effect, that equilibrium structure can only be obtained if I is constant.

CHAPTER 2

THEORY

A complete theory for the development of homogeneous turbulence subjected to uniform irrotational strain is not available. For turbulence which is distorted instantaneously the problem becomes linear and a solution exists.

The theory presented here starts with tensor representation and the classification of irrotational strains. The single parameter representation of the type of strain as proposed by Townsend[66] was not found convenient and a different strain type parameter F is introduced here. A parameter I to represent the intensity of the strain is also introduced and it is suggested that for high Reynolds numbers the parameters F and I together with the strain ratio ℓ_1, are the important variables which determine the structure of turbulence produced by irrotational strain. Equations are developed from which the shape of a duct can be found to produce an arbitrary type of strain.

Starting with the general vorticity equations, the conditions for neglect of the inertia and viscous terms are considered; the neglect of these terms leads to the rapid distortion theory. An outline of the theory as developed by Batchelor and Froudman[5] and Ribner and Tucker[53] is given

21

and the results are presented and discussed. An extension
to the theory to include initially anisotropic turbulence
as obtained by Reynolds[51] is outlined, and finally a simple
method of correcting for decay is given.

2.1. Representation and Classification of Strains

2.1.1. Mathematical Representation of Strain Rate

The velocity of a particle of fluid at a point
$P(x_i)$, in the neighbourhood of a reference particle at
$P_0(x_i)_0$, see Fig. 1, is found from Taylor's theorem,

$$U_i(x_k,t) = (U_i)_0 + \delta x_j \frac{(\partial U_i)_0}{\partial x_j} + \frac{(\delta x_j)^2}{2!} \frac{(\partial^2 U_i)_0}{\partial x_j^2} + .. \quad (1)$$

Neglecting quadratic and higher order terms in δx_j,
Eq. (1) becomes

$$U_i = (U_i)_0 + e_{ij} x_j + \eta_{ij} x_j \quad (2)$$

where

$$e_{ij} = \tfrac{1}{2}\left[\partial U_i/\partial x_j + \partial U_j/\partial x_i\right]_0 \quad (3)$$

$$\eta_{ij} = \tfrac{1}{2}\left[\partial U_i/\partial x_j - \partial U_j/\partial x_i\right]_0 \quad (4)$$

Here e_{ij} represent the components of the symmetrical rate
of strain tensor and η_{ij} the components of the anti-
symmetrical rotation tensor.

Eq. (2) shows that the velocity of an element near a reference particle P_0 may be considered as: (1) a translation with velocity components $(U_i)_0$ equal to the velocity at P_0, (2) a rigid body rotation about an axis through P_0, and (3) a deformation of the element represented by $(\partial U_i / \partial x_j)_0 \delta x_j$, the products of the rate of strain and the coordinate distances between P and P_0. When the mean flow field is irrotational then the velocity of the element may be considered as a translation and a deformation only.

The experimental work in this thesis is limited to irrotational mean flow fields (pure strain fields) which are approximately homogeneous in space and time.

A homogeneous irrotational mean flow field may be represented by a single rate of strain tensor which for an indiscriminate choice of the reference axes system will have nine components represented by $\bar{e}_{ij}$. However, if the principal axes of the symmetrical tensor $\bar{e}_{ij}$ are chosen as the reference axes, the rate of strain is represented by the tensor

$$\bar{e}_{ij} = \begin{vmatrix} \partial \bar{U}_1 / \partial x_1 & 0 & 0 \\ 0 & \partial \bar{U}_2 / \partial x_2 & 0 \\ 0 & 0 & \partial \bar{U}_3 / \partial x_3 \end{vmatrix}$$

With the off-diagonal components zero. Irrotational mean strains may therefore be represented by a triple of numbers

$$\bar{e}_{ij} = (\partial \bar{U}_1/\partial x_1, \quad \partial \bar{U}_2/\partial x_2, \quad \partial \bar{U}_3/\partial x_3)$$

Since the x_1, x_2 and x_3 axes may be interchanged freely, the order in which the numbers appear in the triple is unimportant from the point of view of representation of the rate of strain. We may therefore choose the axes so that the numbers appearing in the triples are in decreasing order, that is $\partial \bar{U}_1/\partial x_1 \geq \partial \bar{U}_2/\partial x_2 \geq \partial \bar{U}_3/\partial x_3$; it follows that the strain ratios are also in decreasing order, ie., $\ell_1 \geq \ell_2 \geq \ell_3$. When considering rates of strain this convention is used throughout the thesis, and is convenient in treating the rapid distortion theory and in comparing the structures of turbulence produced by the same type of strain.

2.1.2. Classification of Irrotational Strains

Irrotational strains may be classified as follows:

(1) diffusion (expansion), having two positive rates of strain,

(2) contraction, having two negative rates of strain, and

(3) plane strain, having one positive, one zero and one negative rate of strain.

This classification is summerized in Table 1 below. For incompressible fluids, continuity requires that $\partial \bar{U}_i/\partial x_i = 0$, and therefore an irrotational strain is completely specified if any two of the principal rates of strain are given. As shown in Table 1, the sign of

$\partial \bar{u}_2 / \partial x_2$ is sufficient to classify the type of strain.

TABLE 1

Classification of Irrotational Strains

Strain Class	Sign		
	$\partial \bar{u}_1 / \partial x_1$	$\partial \bar{u}_2 / \partial x_2$	$\partial \bar{u}_3 / \partial x_3$
diffusion	positive	positive	negative
contraction	positive	negative	negative
plane strain	positive	zero	negative

2.1.3. Parameters which Determine the Effects of Irrotational Distortion on Turbulence

In considering the effects of irrotational strain on turbulence it is necessary to use parameters which characterize both the strain and the turbulence. The following parameters are used here:

(1) F, the strain type parameter;

(2) $\ell_{\prime}$, the strain ratio which is a measure of the extent of the strain;

(3) I, the strain rate parameter, which is a measure of the strain rate relative to the rate of decay of the turbulence.

The parameters F and $\ell_{\prime}$ depend only on the strain, the parameter I depends on the strain and also on the

turbulence. We will now consider these parameters in more detail.

An irrotational rate of strain is completely specified by $\partial \bar{U}_1/\partial x_1$ and $\partial \bar{U}_2/\partial x_2$, two principal components of the rate of strain tensor. If $\partial \bar{U}_1/\partial x_1$ is chosen arbitrarily as a scale then the dimensionless quantity

$$F = (\partial \bar{U}_2/\partial x_2)/(\partial \bar{U}_1/\partial x_1), \quad -\tfrac{1}{2} \leq F \leq 1 \tag{5}$$

is a measure of the type of strain. F is always of the same sign as $\partial \bar{U}_2/\partial x_2$ and therefore the sign of F is sufficient to classify the strain; positive F indicates diffusion, negative F indicates contraction, zero F indicates plane strain.

The type of strain parameter F defined here, is simpler than the parameter Ω_s proposed by Townsend which is defined as

$$\Omega_s = \frac{(\partial \bar{U}_1/\partial x_1)(\partial \bar{U}_2/\partial x_2)(\partial \bar{U}_3/\partial x_3)}{(\partial \bar{U}_1/\partial x_1)^2 + (\partial \bar{U}_2/\partial x_2)^2 + (\partial \bar{U}_3/\partial x_3)^2}$$

No special arrangement of the components $\partial \bar{U}_1/\partial x_1$ $\partial \bar{U}_2/\partial x_2$ and $\partial \bar{U}_3/\partial x_3$ is required.

With reference axes chosen so that $\partial \bar{U}_1/\partial x_1 \geq \partial \bar{U}_2/\partial x_2 \geq \partial \bar{U}_3/\partial x_3$ and strain ratios $\ell_1 \geq \ell_2 \geq \ell_3$ the relative magnitudes of the three strain ratios are related to the type of strain. If the type of strain is specified, the strain ratio ℓ_1 alone is sufficient to measure the extent of the strain.

As a measure of the rate of strain it is desirable to use a dimensionless parameter which includes a measure of the turbulence within the strain field. A suitable parameter I is the ratio of the time scale of the turbulence and the time scale of the rate of strain.

A time scale which characterizes the rate of strain is simply

$$t_s = 1/(\partial \overline{U}_1/\partial x_1) \tag{6}$$

As a time scale for the turbulence, a logical choice is the time scale t_e associated with the energy-containing eddies. However, for turbulence of high Reynolds numbers, the time scale of the energy-containing eddies is the time scale of the decay, we can use

$$t_e = -\overline{q^2}/\left[(d\overline{q^2})_d/dt\right] = \frac{\overline{q^2}}{2\epsilon} \tag{7}$$

The time scale t_e for grid turbulence varies with distance from the virtual origin and with the mean velocity as shown in Appendix A.

The rate of strain parameter is defined as

$$I = t_e/t_s = -\overline{q^2}(\partial \overline{U}_1/\partial x_1)/\left[(d\overline{q^2})_d/dt\right] \tag{8}$$

For distorted grid turbulence t_e and hence I vary throughout the distortion; however, for comparison of ducts producing the same type of strain I_A, the value at the beginning of the distortion, may arbitrarily be chosen to

characterize the rate of strain. The parameter I_A behaves similar to $\partial \bar{U}_1/\partial x_1$ and varies from zero in uniform mean flow to infinity for instantaneous distortion.

The time scale of turbulence t_e defined above is convenient for treating uniform distortion of grid turbulence reported here, because the quantities $\overline{q^2}$ and $\overline{dq^2}/dt$ at the beginning of the distortion are available from the experiments. However, if the parameter I is used in more general shear flows, any time scale associated with the energy-containing eddies can be used, for example the time scale $L_u /(\overline{q^2})^{\frac{1}{2}}$, where L_u is a length scale associated with the energy-containing eddies.

In summary, a uniform irrotational strain may be represented by two parameters F and I. The sign of the form parameter determines the type of strain, and the rate of strain parameter I includes a measure of the turbulence within the field. The strain ratio ℓ_1 provides a measure of the extent of the strain.

2.2. Duct Geometry to Produce an Arbitrary Irrotational Strain

2.2.1. Design Considerations

If the coordinate systems $(x_i)_A$ and x_i are referred to the same origin moving with the mean velocity of a fluid particle as shown in Fig. 2, the position of the fluid element at time $t = 0$ is at $(x_i)_A$ and its position at time t is at x_i, then the position of a fluid particle

within the element is given by

$$x_i(t) = (x_j)_A \left[\partial x_i / (\partial x_j)_A \right] = (x_j)_A S_{ij}(t) \qquad (9)$$

If the tensor $S_{ij}(t)$ is uniform then the vector $x_i(t)$ is
obtained from $(x_i)_A$ by a linear transformation of the axes
of reference. As pointed out by Batchelor,[5] $S_{ij}(t)$ is
uniform is exactly true for a box type distortion where the
fluid is contained within boundaries and the distortion is
caused by a linear motion of the boundaries, since the fluid
will then undergo a similar linear transformation. However,
in most engineering problems distortion of the fluid is
caused by flow past fixed boundaries; as for example in wind-
tunnel contractions. In these problems the distortion
tensor $S_{ij}(t)$ is not exactly uniform since particles of
fluid which lie on a lateral plane upstream of the distor-
tion will not lie on a plane after being distorted, as in
the case of a box type distortion, but will lie on a curved
surface with the particles near the center of the tunnel
farther downstream than those near the walls. The radius
of curvature of the curved surface will be of the order of
the tunnel width, so that for situations where the scale of
the turbulence is small compared with the tunnel width the
distortion tensor is approximately uniform.

A tunnel may be designed with a distorting section
whose geometry is capable of providing any type of strain
F which is uniform within the approximation stated above.

In designing a tunnel to produce a given type of strain, we choose Cartesian coordinates for the tunnel along the principal axes of the rate of strain tensor so that

$$
\begin{vmatrix} \partial \bar{U}_1/\partial x_1 & 0 & 0 \\ 0 & \partial \bar{U}_2/\partial x_2 & 0 \\ 0 & 0 & \partial \bar{U}_3/\partial x_3 \end{vmatrix} \equiv \partial \bar{U}_1/\partial x_1 \begin{vmatrix} 1 & 0 & 0 \\ 0 & F & 0 \\ 0 & 0 & -(F+1) \end{vmatrix}
$$

As already stated in Sec. 2.1.1. $\partial \bar{U}_1/\partial x_1 \geq \partial \bar{U}_2/\partial x_2 \geq \partial \bar{U}_3/\partial x_3$; this choice of the axes is necessary in order to specify the type of strain by a single parameter F. It is convenient to locate the origin on the center-line of the tunnel at the entrance to the distorting section. The longitudinal axis of the tunnel which is the direction of the main flow may be chosen as any one of the x_1, x_2 and x_3 directions and in general three different duct geometries will result, depending on the choice. In practice it is not desirable to choose the main flow direction in the direction of the negative rates of strain because this would result in adverse positive pressure gradients which might cause instability in the flow and separation. Referring to Table 1, there are two duct geometries which produce a given diffusion or a given plane strain, and a single duct geometry for contraction. We will find the design equations for the curved surfaces of the distorting duct for the two general cases: the first where the main flow is in the direction of x_1; the second where the main flow is in the

direction of x_2.

2.2.2. Streamline Equations, Main Flow in the x_1-Direction

These design equations will apply to all possible
strain types: diffusion, contraction and plane strain. Let
the maximum rate of strain $\partial \bar{U}_1/\partial x_1 = \alpha$, then

$$\partial \bar{U}_1/\partial x_1 = \alpha, \quad \partial \bar{U}_2/\partial x_2 = \alpha F, \quad \partial \bar{U}_3/\partial x_3 = -\alpha(F+1) \quad (10)$$

If we assume that the mean flow in the tunnel produces a
box type distortion, an approximation discussed previously,
then fluid particles on a plane $x_1 = 0$ will remain on a plane
throughout the distortion and $\bar{U}_1 = \bar{U}_1(x_1)$, similarly
$\bar{U}_2 = \bar{U}_2(x_2)$ and $\bar{U}_3 = \bar{U}_3(x_3)$. The partial derivatives may
then be replaced by total derivatives and Eq. (10) becomes

$$d\bar{U}_1/dx_1 = \alpha, \quad d\bar{U}_2/dx_2 = \alpha F, \quad d\bar{U}_3/dx_3 = -\alpha(F+1) \quad (11)$$

with boundary conditions

$$\left.\begin{array}{ll} x_1 = 0, & \bar{U}_1 = (\bar{U}_1)_A \\ x_2 = 0, & \bar{U}_2 = 0 \\ x_3 = 0, & \bar{U}_3 = 0 \end{array}\right\} \quad (12)$$

Integrating Eq. (11) and applying the boundary conditions
(12) gives:

$$\left.\begin{array}{l} \bar{U}_1 = \alpha x_1 + (\bar{U}_1)_A \\ \bar{U}_2 = \alpha F x_2 \\ \bar{U}_3 = -\alpha(F+1)x_3 \end{array}\right\} \quad (13)$$

The differential equation of the streamlines are:

$$dx_1/\overline{U}_1 = dx_2/\overline{U}_2 = dx_3/\overline{U}_3 \tag{14}$$

$$dx_1/\left[\alpha x_1 + (\overline{U}_1)_A\right] = dx_2/\alpha F x_2 \tag{15}$$

$$dx_1/\left[\alpha x_1 + (\overline{U}_1)_A\right] = dx_2/-\alpha(F-1)x_3 \tag{16}$$

If the distorting duct is rectangular in cross-section with sides of length $2(x_2)_A$ and $2(x_3)_A$ at the beginning of distortion $(x_1 = 0)$, then the walls of the distorting duct are defined by streamlines passing through $(0, \pm(x_2)_A, x_3)$ and $(0, x_2, \pm(x_3)_A)$. Integration of Eq. (15) gives

$$(1/\alpha)\,\ln(\alpha x_1 + (\overline{U}_1)_A)\Big|_0^{x_1} = (1/\alpha F)\,\ln x_2 \Big|_{(x_2)_A}^{x_2} \tag{17}$$

$$x_2 = (x_2)_A \left(1 + \left[\alpha/(\overline{U}_1)_A\right]x_1\right)^F$$

Similarly,

$$x_3 = (x_3)_A \left(1 + \left[\alpha/\overline{U}_1)_A\right]x_1\right)^{-(F+1)} \tag{18}$$

2.2.3. Streamline Equations, Main Flow in the x_2-Direction

In the case of diffusion and plane strain, the main flow velocity may be chosen along the x_2-direction without adverse pressure gradients. Assuming box type distortion in the tunnel, $\overline{U}_1 = \overline{U}_1(x_1)$, $\overline{U}_2 = \overline{U}_2(x_2)$ and $\overline{U}_3 = \overline{U}_3(x_3)$, and

$$d\overline{U}_1/dx_1 = \alpha, \quad d\overline{U}_2/dx_2 = \alpha F, \quad d\overline{U}_3/dx_3 = -\alpha(F+1) \tag{19}$$

For main flow in the x_2-direction, the boundary conditions are:

$$\left.\begin{array}{ll} x_2 = 0, & \bar{U}_2 = (\bar{U}_2)_A \\ x_1 = 0, & \bar{U}_1 = 0 \\ x_3 = 0, & \bar{U}_3 = 0 \end{array}\right\} \tag{20}$$

After integration, Eq. (19) with the boundary conditions given by Eq. (20), we obtain:

$$\left.\begin{array}{l} \bar{U}_1 = \alpha x_1 \\ \bar{U}_2 = \alpha F x_2 + (\bar{U}_2)_A \\ \bar{U}_3 = -\alpha(F+1)x_3 \end{array}\right\} \tag{21}$$

Introducing these values into the general Eq. (14) which defines the streamlines, we obtain:

$$dx_2/(\alpha F x_2 - (\bar{U}_2)_A) = dx_1/\alpha x_1 \tag{22}$$

$$-dx_3/\left[\alpha(F+1)x_3\right] = dx_1/\alpha x_1 \tag{23}$$

Assuming the distorting duct is rectangular in cross-section with sides of length $2(x_1)_A$ and $2(x_3)_A$ at the beginning of the distortion $(x_2 = 0)$, then the walls of the distorting duct are defined by the streamlines passing through $((x_1)_A, 0, x_3)$ and $(x_1, 0, (x_3)_A)$. Integration of Eq. (22) for $0 \le F \le 1$ gives

$$(1/F)\, \ln(\alpha F x_2 + (\bar{U}_2)_A)\Big|_0^{x_2} = \ln x_1 \Big|_{(x_1)_A}^{x_1}$$

$$x_1 = (x_1)_A (1 + \left[\alpha F/(\bar{U}_2)_A\right] x_2)^{1/F} \tag{24}$$

Similarly, integration of Eq. (23) for $0 < F \leq 1$ gives

$$x_3 = x_3^A (1 + \left[\alpha F/(\bar{U}_2)_A\right] x_2)^{-(F+1)/F} \tag{25}$$

When $F \to 0$, integration of Eqs. (22) and (23) with the boundary conditions, we obtain:

$$x_1 = (x_1)_A \; e^{(\alpha x_2)/(\bar{U}_2)_A} \tag{26}$$

$$x_3 = (x_3)_A \; e^{(-\alpha x_2)/(\bar{U}_2)_A} \tag{27}$$

Equations (26) and (27) may also be obtained from Eqs. (24) and (25) by expanding the terms in brackets by the Binomial theorem and then letting $F \to 0$. Equations (17), (18) and (24), (25) give the duct geometry for any type of irrotational strain F; the equations are approximate because a box type distortion was assumed.

2.3. Rapid Distortion of Isotropic Turbulence

A complete mathematical solution to the problem of turbulence within a homogeneous pure strain field appears at present to be impossibly difficult. However, Taylor has shown that if the mean strain is sufficiently rapid, so that the relative motion between two neighbouring particles due to the mean motion is large compared with that due to turbulence, then the Navier-Stokes equations are reduced to simple linear equations and a complete solution can be obtained.

2.3.1. Simplification of the Vorticity Equation for Rapid Distortion

The implications contained in the assumption of rapid distortion can be seen by examining the vorticity equations which are obtained by taking the curl of the Navier-Stokes equations to eliminate the pressure terms. The general vorticity equation using Eulerian variables is

$$\frac{\partial(\bar\Omega_i+\omega_i)}{\partial t} + (\bar U_j+u_j)\frac{\partial(\bar\Omega_i+\omega_i)}{\partial x_j} = (\bar\Omega_j+\omega_j)\frac{\partial(\bar U_i+u_i)}{\partial x_j} + \nu\frac{\partial^2(\bar\Omega_i+\omega_i)}{\partial x_j} \quad (28)$$

For irrotational mean flows $\bar\Omega_i = 0$, Eq. (28) becomes

$$\frac{D\omega_i}{Dt} = \omega_j\frac{\partial\bar U_i}{\partial x_j} + \omega_j\frac{\partial u_i}{\partial x_j} + \nu\frac{\partial^2\omega_i}{\partial x_j^2} \quad (29)$$

$$\begin{array}{cccc} \text{I} & \text{II} & \text{III} & \text{IV} \end{array}$$

where

$$\frac{D\omega_i}{Dt} = \omega_j\frac{\partial\omega_i}{\partial t} + (\bar U_j+u_j)\frac{\partial\omega_i}{\partial x_j}$$

signifies differentiation following a single fluid particle, often referred to as the substantiative derivative or the Lagrangian derivative. Equation (29) states that the change (1) in vorticity of the turbulent motion following a particle of fluid is equal to (II) the production of vorticity by the mean motion straining the turbulent eddies, plus (III) the transfer of vorticity amongst the turbulent eddies by one

eddy straining another and through inertial interaction, plus (IV) the diffusion of vorticity by the influence of viscosity. For very rapid mean strains, (II) which contains the mean rate of strain $\partial \bar{U}_i/\partial x_j$ becomes dominant and the decay terms (III) and (IV) may be neglected in Eq. (29), which then becomes

$$D\omega_i/Dt = \omega_j \, \partial \bar{U}_i/\partial x_j \tag{30}$$

According to Lamb[32] (p.206) a line segment δx_i following the mean fluid motion will have a Lagrangian derivative

$$D\delta x_i/Dt = \delta x_j \, \partial \bar{U}_i/\partial x_j \tag{31}$$

From a comparison of Eqs. (30) and (31) it follows that for all time t,

$$\omega_i \sim \delta x_i \tag{32}$$

This result is well known, the change in vorticity components of an element of fluid is proportional to the change in length along the respective axes. When the term containing the viscosity is neglected in Eq. (29) the fluid becomes ideal, and Kelvin's theorem for the conservation of circulation also leads directly to Eq. (32), which embodies the entire dynamics of rapid distortion.

The rapid distortion theory presented later gives a complete solution to Eq. (32). It will be shown that when the vorticity which comprises the turbulence is strained by the mean motion, the vorticity strength

increases in such a way as to maintain the constancy of circulation of the fluid elements, and in this way energy is transferred from the mean to the turbulent motion. This is, in effect, a statement of Eq. (30); the left hand side representing the increase in vorticity following a fluid element and the right hand side $\omega_j \, \partial \bar{U}_i/\partial x_j$ representing the production of turbulent energy by the mean rate of strain $\partial \bar{U}_i/\partial x_j$ acting on the vorticity ω_j within the fluid element.

It is interesting to compare the mean production terms $\omega_j \, \partial \bar{U}_i/\partial x_j$ and the inertial decay terms $\omega_j \, \partial u_i/\partial x_j$ appearing in Eq. (29). The inertial decay term may be considered as representing the transfer of turbulent energy by the straining motion of the turbulence itself, the motion of the larger eddies strains the smaller turbulent eddies thus transferring energy from the larger to the smaller eddies.

2.3.2. Conditions for Neglect of Inertial Decay

In Eq. (29) the inertial decay term $\omega_j \, \partial u_i/\partial x_j$ may be neglected when it is small in comparison with the production term $\omega_j \, \partial \bar{U}_i/\partial x_j$; that is, when

$$\left| \omega_j \, \partial \bar{U}_i/\partial x_j \right| \gg \left| \omega_j \, \partial u_i/\partial x_j \right| \tag{33}$$

With the principal axes chosen so that $\partial \bar{U}_1/\partial x_1 \geq \partial \bar{U}_2/\partial x_2 \geq \partial \bar{U}_3/\partial x_3$ then a sufficient condition to replace Eq. (33) is that

$$\partial \bar{U}_1/\partial x_1 \gg |\partial u_i/\partial x_j|; \qquad (34)$$

ie., the turbulent velocity gradients must be small in comparison with the maximum mean velocity gradient. This is essentially the condition for rapid distortion stated in the original paper of Taylor[62] that during the process of distortion the displacement between any two fluid particles should be determined uniquely by the mean strain, which implies that the influence of the turbulent motion on the displacement is negligible for all stages of the distortion. It is in this sense that the distortion is required to be sufficiently rapid.

As introduced earlier, $1/(\partial \bar{U}_1/\partial x_1)$ may be considered as a time scale t_s representing the mean rate of strain. Similarly, $1/(\partial u_1/\partial x_j)$ may be taken as representing a time scale associated with the turbulent motion, or more exactly as a time scale associated with the energy-containing eddies since $\omega_j \partial u_i/\partial x_j$ determines the rate of energy transfer through the energy-containing eddies. The time scale $1/(\partial u_i/\partial x_j)$ may therefore be replaced by the time scale $t_e = -\overline{q^2}/\left[(d\overline{q^2})_d/dt\right]$. From Eq. (34) the condition for rapid distortion then becomes

$$1/(\partial \bar{U}_1/\partial x_1) \ll -\overline{q^2}/\left[(d\overline{q^2})_d/dt\right] \quad \text{or} \quad I \gg 1 \qquad (35)$$

2.3.3. Conditions for Neglect of Viscous Decay

The viscous decay term (IV) in Eq. (29) is linear.

If the random turbulent motion is considered to be composed
of individual plane waves, or Fourier components, then the
viscous effects will act on individual waves separately,
without mutual interference. The effect of viscosity on a
single wave, in the absence of distortion, may be obtained
by considering decay in a fluid having no mean motion. The
component of a wave may be written as

$$\omega_i = \Omega_i \, e^{i\underline{k}\cdot\underline{x}} \tag{36}$$

The viscous decay corresponding to term (IV) in Eq. (29)
becomes

$$\nu(\partial^2\omega_i/\partial x_j{}^2) = \nu k^2\omega_i \tag{37}$$

Clearly, the viscous decay effects become larger for the
higher wave numbers, that is, the smaller eddies.

From the many experiments on the decay of grid
turbulence, for example those reported by Batchelor,[6] it is
found that even at moderately high Reynolds numbers the
rate of decay is independent of the viscosity in the initial
period of decay. Apparently the time scale of viscous
decay is large compared with the time scale of the energy-
containing eddies. If we take $1/\nu k^2$ to represent a time
scale for viscous decay of eddies having wave number k,

$$-\overline{q}^2/\left[(d\overline{q}^2)_d/dt\right] \ll 1/\nu k^2 \tag{38}$$

Therefore, for grid turbulence having moderately high

Reynolds numbers a sufficient condition for instantaneous distortion is given by Eq. (35) only, since in the energy-containing range the viscous decay is a relatively slow process.

The time scale of viscous dissipation $1/\nu k^2$ decreases for the higher wave numbers and there will always be a high range of wave numbers for which Eq. (38) is not satisfied. These eddies of higher wave numbers may be regarded as an energy sink with the rate of decay determined by the eddies in the energy-containing range.

For low Reynolds number turbulence, for example in the final period of decay, the inertial decay term (III) of Eq. (29) becomes small in comparison with the viscous decay term (IV). There is then very little energy transferred from one eddy size to another and viscous effects are important for all eddy sizes. Neglecting the inertial decay terms in Eq. (29), it becomes

$$D\omega_i/Dt = \omega_j \, \partial \bar{U}_i/\partial x_j + \nu(\partial^2 \omega_i/\partial x_j) \qquad (39)$$

For uniform mean strains this equation is linear and a solution may be obtained for a finite rate of strain. As already mentioned solutions to this problem have been obtained by Pearson,[41] Deissler[15] and Fox.[17] However for ordinary turbulent flows at moderately high Reynolds numbers inertial decay terms cannot be neglected.

2.4. Rapid Distortion Theory.

The instantaneous distortion of isotropic turbulence is now treated. The method first introduced by Taylor[62] is followed up to the point where the field of turbulence is represented mathematically, and then the Fourier representation of the turbulent field, following the method of Ribner and Tucker[53] is used. This method treats the distortion of a single Fourier component and then the effect of distortion on the turbulent field is found by summation; this is permissible since the problem becomes linear when instantaneous distortion is assumed. The method of Ribner and Tucker[53] provides a good physical insight into the influence of distortion on the turbulent fluid but their solution is limited to symmetrical plane contraction. Batchelor and Proudman[5] treated an arbitrary distortion; their results are introduced near the end of the discussion.

2.4.1. Effect of Rapid Distortion of Isotropic Turbulence on the Mean-Square Velocity Components

Consider an arbitrary distortion caused by a pure strain in a fluid flow where the mean stream velocity $\bar{U}_1$ is changed to $\ell_1 \bar{U}_1$ in a small interval of time compared with the time required for appreciable turbulent motion. A cube of fluid of finite dimensions d will be changed by the strain to a parallelipiped of sides $\ell_1 d$, $\ell_2 d$ and $\ell_3 d$ as shown in Fig. 2. If we assume a coordinate system moving with the element of fluid, then a particle of fluid

originally located by the vector $(x_i)_A$ within the element
will be located by vector x_i after the distortion, where

$$
\left.
\begin{aligned}
x_1 &= \ell_1 (x_1)_A \\
x_2 &= \ell_2 (x_2)_A \\
x_3 &= \ell_3 (x_3)_A
\end{aligned}
\right\}
\tag{40}
$$

Assuming incompressible fluid, the continuity condition
requires that $\ell_1 \, \ell_2 \, \ell_3 = 1$.

The vorticity of the turbulent motion inside the
volume shown in Fig. 2 is carried along by the flow. If
the time interval for distortion by the mean flow is small
compared with the time for appreciable decay, then circu-
lation of the fluid element is conserved, and the change in
vorticity during distortion can be found using Cauchy's
equation given by Lamb[32]

$$
\omega_i = (\omega_j)_A \left[\partial x_i / (\partial x_j)_A \right]
\tag{41}
$$

If the distortion throughout the volume is uniform, then
from Eq. (41),

$$
\partial x_1 / (\partial x_1)_A = \ell_1, \quad \partial x_2 / (\partial x_2)_A = \ell_2, \quad \partial x_3 / (\partial x_3)_A = \ell_3
$$

$$
\partial x_i / (\partial x_j)_A = 0, \quad i \neq j
\tag{42}
$$

and combining Eqs. (41) and (42) we obtain:

$$
\left.
\begin{aligned}
\omega_1 &= \ell_1 (\omega_1)_A \\
\omega_2 &= \ell_2 (\omega_2)_A \\
\omega_3 &= \ell_3 (\omega_3)_A
\end{aligned}
\right\}
\tag{43}
$$

The method used in the derivation of Eq. (43) is essentially the same as that of Taylor.[62] This equation is also the equivalent to Eq. (32) obtained earlier in this thesis by neglecting the decay terms in the general vorticity equation. Equation (43) relates the vorticity at $t > 0$ to the initial vorticity at $t = 0$, and contains the entire dynamics of the distortion effect. In order to apply Eq. (43) to determine the changes in intensities, we will follow the method of Ribner and Tucker[53] and consider the effect of distortion on a Fourier model of the turbulent field.

For a coordinate system moving with the fluid particle shown in Fig. 2, the mean components of velocity are suppressed and only the components of the turbulent velocity remain, which at any given instant can be represented by a set of three-dimensional Fourier integrals,

$$u_i(x_1,x_2,x_3) = \iiint_{-\infty}^{\infty} A_i(k_1,k_2,k_3) \; e^{i(k_1 x_1 + k_2 x_2 + k_3 x_3)} dk_1 dk_2 dk_3 \tag{44}$$

or in the abbreviated form

$$u_i(\underline{x}) = \int_{-\infty}^{\infty} A_i(\underline{k}) \; e^{i\underline{k}\cdot\underline{x}} \; d\underline{k} \tag{45}$$

where the coefficients are given by the companion equation

$$A_i(\underline{k}) = \frac{1}{(2\pi)^3} \int_{-\infty}^{\infty} u_i(\underline{x}) \; e^{-i\underline{k}\cdot\underline{x}} \; d\underline{k} \tag{46}$$

These equations are given and discussed by Batchelor.[4] Mathematically, $u_i(\underline{x})$ and $A_i(\underline{k})$ are termed three-dimensional Fourier components of each other. For incompressible flow,

the velocity components u_i satisfy continuity or $\partial u_i/\partial x_i = 0$; this together with Eq. (45) gives the continuity equation $A_i k_i = 0$.

The physical interpretation of the Fourier model of a turbulent field is given by Ribner and Tucker.[53] Equation (45) represents a superposition of plane sinusoidal waves or Fourier components of all wave lengths and all directions. The normal to the waves are in the direction of the wave number vector $\underline{k}$ and the length of the waves are $2\pi/k$, where k is the wave number. These waves are all transverse because from the continuity condition $A_i k_i = 0$; the magnitude vector A is perpendicular to the wave normal vector $\underline{k}$.

We now consider the effect of distortion, as shown in Fig. 2, on a typical Fourier component represented at station A by

$$(\tilde{u}_i)_A = (\tilde{A}_i)_A \, e^{i\underline{k}_A \cdot \underline{x}_A} \tag{47}$$

The vorticity $(\tilde{\omega}_i)_A$ is obtained by taking the curl of Eq. (47), that is

$$(\tilde{\omega}_i)_A = \epsilon_{ijk} \, (\partial \tilde{u}_k/\partial x_j)_A$$

whence

$$(\tilde{\omega}_i)_A = i \, \epsilon_{ijk} \, k_j (\tilde{A}_k)_A \, e^{i\underline{k}_A \cdot \underline{x}_A} \tag{48}$$

The vorticity at any station downstream from A is obtained from Eq. (43); the equations are

$$\omega_l = i \, \epsilon_{ijk} \, \ell_l \, k_j (\tilde{A}_k)_A \, e^{i\underline{k}_A \cdot \underline{x}_A} \tag{49}$$

and two similar equations for the $\tilde{\omega}_2$ and $\tilde{\omega}_3$ components, where $(\underline{x})_A$ is the radius vector to the fluid particle at time $t = 0$ when the fluid element is at station A. The corresponding vector to the fluid particle at time t is $\underline{x}$. Using values of $(x_i)_A$ from Eq. (40), $(\underline{k} \cdot \underline{x})_A$ becomes

$$(\underline{k} \cdot \underline{x})_A = \frac{(k_1)_A x_1}{\ell_1} + \frac{(k_2)_A x_2}{\ell_2} + \frac{(k_3)_A x_3}{\ell_3} = \underline{k} \cdot \underline{x} \qquad (50)$$

where $\underline{k}$ with components $(k_1)_A/\ell_1$, $(k_2)_A/\ell_2$, $(k_3)_A/\ell_3$ defines a new wave number vector. The velocity at time t (whose curl is given by Eq. (49) and which satisfies continuity) is

$$\tilde{u}_i = \tilde{A}_i \, e^{i\underline{x} \cdot \underline{k}} \qquad (51)$$

where

$$\tilde{A}_1 = \frac{1}{\ell_1} \left((\tilde{A}_1)_A - \sum \frac{(\tilde{A}_j k_j k_i)_A}{\ell_j^2 k^2} \right) \qquad (52)$$

It can be seen from Eqs. (51) and (52) that the distortion alters the initial plane wave given by Eq. (47) so that the wave number $(\underline{k})_A$ is transformed into $\underline{k}$ having components $(k_1)_A/\ell_1$, $(k_2)_A/\ell_2$, $(k_3)_A/\ell_3$. The amplitude vector $(\tilde{A}_i)_A$ is transformed into the projection of $((\tilde{A}_1)_A/\ell_1$, $(\tilde{A}_2)_A/\ell_2$, $(\tilde{A}_3)_A/\ell_3)$ on a plane normal to the wave number vector $\underline{k}$.

Equations (51) and (52) were obtained by considering a single Fourier component. For the complete Fourier integral representation of the turbulent field, $(\tilde{u}_i)_A$ may

be interpreted as $d(u_i)_A$, $\tilde{u}_i$ as du_i, $(\tilde{A}_i)_A$ as $(A_i \, d\underline{k})_A$ and $\tilde{A}_i$ as $A_i \, dk$. If we define

$$d \, Z(\underline{k}) = \underline{A}(\underline{k}) \, d\underline{k} \tag{53}$$

then Eq. (52) becomes

$$dZ_1 = \frac{1}{\ell_1}(dZ_1)_A - \frac{(k_1)_A}{\ell_1 k^2}\left[\frac{(k_1)}{\ell_1^2}dZ_1 + \frac{k_2}{\ell_2^2}dZ_2 + \frac{k_3}{\ell_3^2}dZ_3\right]_A \tag{54}$$

and two similar equations for dZ_2 and dZ_3.

From the relation between the Fourier coefficients of the turbulent velocity distribution before and during the distortion, it is possible to deduce the effect of the distortion on any of the statistical parameters describing the turbulence. Of special interest is the change in the energy-spectrum tensor from which changes in turbulent intensities may be found.

In the analysis a number of well known relations from the statistical theory of turbulence will be assumed, these relations are given and discussed in detail by Batchelor[4]. The three-dimensional energy-spectrum $E_{ij}(\underline{k})$ is related to $dZ_i(\underline{k})$ by

$$E_{ij}(\underline{k}) = \lim_{dk \to 0} \overline{dZ_i^*(\underline{k}) \, dZ_j(\underline{k})} \tag{55}$$

where dZ^* is the complex conjugate of dZ. The correlation tensor is defined by

$$R_{ij}(\underline{r}) = \overline{u_i(\underline{x}) \, u_j(\underline{x} + \underline{r})} \tag{56}$$

and is related to the three-dimensional energy-spectrum tensor by the Fourier equations:

$$R_{ij}(\underline{r}) = \int E_{ij}(\underline{k}) \, e^{i\underline{k}\cdot\underline{r}} \, d\underline{k} \qquad (57)$$

$$E_{ij}(\underline{k}) = \frac{1}{(2\pi)^3}\int R_{ij}(\underline{r}) \, e^{-i\underline{k}\cdot\underline{r}} \, d\underline{r} \qquad (58)$$

Also, continuity requires that

$$k_i \, E_{ij}(\underline{k}) = 0 \qquad (59)$$

If the value of dZ_1 and its conjugate from Eq. (45) are substituted in Eq. (55) then

$$E_{11} = \frac{1}{\ell_1^2}(E_{11})_A + \frac{(k_1)_A^2}{\ell_1^2 k^4}\left[\left(\frac{k_2^2}{\ell_2^2}+\frac{k_3^2}{\ell_3^2}\right)\left(\frac{1}{\ell_2^2}+\frac{1}{\ell_3^2}-\frac{2}{\ell_1^2}\right)+k_1^2\left(\ell_1^2-\frac{1}{\ell_1^4}\right)\right]_A$$

$$(E_{11})_A + \frac{(k_2)_A^2}{\ell_2^2 k^4}(\ell_3^2-\ell_2^2)(k_1^2+k_2^2+\frac{\ell_2^2}{\ell_3^2}k_3^2)_A (E_{22})_A$$

$$+ \frac{(k_3)_A^2}{\ell_3^2 k^4}(\ell_2^2-\ell_3^2)(k_1^2+\frac{\ell_3^2}{\ell_2^2}k_2^2+k_3^2)_A(E_{33})_A \qquad (60)$$

Similarly equations for E_{22} and E_{33} are obtained and only the diagonal components E_{11}, E_{22}, E_{33} have values other than zero. We see from Eq. (60), that if the initial spectrum $(E_{ij})_A$ and the distortion ℓ_i are specified, the spectrum after distortion E_{ij} may be determined.

The results are most useful if the spectrum tensor

is integrated over all values of the wave number to obtain the effect of distortion on the energies associated with the different velocity components. The complexity of Eq. (60) makes the integration extremely difficult unless $[E_{ij}(k)]_A$ has a simple form, for example in isotropic turbulence, where

$$[E_{ij}(k)]_A = \left[\frac{E(k)}{4\pi k^4}(k^2 \delta_{ij} - k_i k_j)\right]_A \tag{61}$$

$$[E(k)]_A = [2\pi k^2 E_{ii}(k)]_A \tag{62}$$

For this case of initially isotropic turbulence Eq. (60) becomes, after some simplification,

$$E_{11}(k) = \frac{[E(k)]_A}{4\pi \ell_1^2(k)_A^2 k^4}\left[k_1^2\left(\frac{k_2^2}{\ell_2^4}+\frac{k_3^2}{\ell_3^4}\right)+\left(\frac{k_2^2}{\ell_2^4}+\frac{k_3^2}{\ell_3^2}\right)^2\right]_A \tag{63}$$

and two similar equations for $E_{22}(k)$ and $E_{33}(k)$. As can be seen from comparison of Eqs. (61) and (62), the turbulence is made anisotropic by the distortion.

The effect of the distortion on the energies associated with the different velocity components may be obtained by considering $R_{ij}(\underline{r})$ at a single point in space. At position A, Eqs. (56) and (57) give for $i=1$, $j=1$,

$$R_{11}(0) = (\overline{u_1^2})_A = \int [E_{11}(k)\,dk]_A \tag{64}$$

Using surface area S and the radius vector $\mathcal{k}$ to define the $\mathcal{k}$ space, we obtain from Eqs. (61) and (64),

$$\overline{(u_1^2)}_A = \int_0^\infty \frac{E(k)_A}{4\pi(k)_A^2} \, dk \int_0^S \sin^2 \theta \, d \, S \, (k) \tag{65}$$

Similarly, from Eq. (63)

$$\overline{u_1^2} = \int_0^\infty \frac{E(k)_A}{4\pi(k)_A^2} \, dk \, \frac{1}{\ell_1^2} \int_0^S \left[k_1^2 \left(\frac{k_2^2}{\ell_2^4} + \frac{k_3^2}{\ell_3^4} \right) + \left(\frac{k_2^2}{\ell_2^2} + \frac{k_3^2}{\ell_3^2} \right) \right.$$

$$\left. + \left(\frac{k_1^2}{\ell_1^2} + \frac{k_2^2}{\ell_2^2} + \frac{k_3^2}{\ell_3^2} \right)^{-2} \right] dS \tag{66}$$

For isotropic turbulence in taking the ratio $\overline{(u_1^2)}_A / \overline{u_1^2}$ the integrals containing $E(k)_A$ cancel and, as shown by Batchelor and Proudman[5] the remaining integration can be carried out over a surface of radius k to give

$$\mu_1 = \frac{\overline{u_1^2}}{\overline{(u_1^2)}_A} = \frac{3}{4} \left[\frac{1}{\ell_1^2} - \frac{\ell_1^{-2} - \ell_2^{-2} - \ell_3^{-2}}{(\ell_1^2 - \ell_2^2)(\ell_1^2 - \ell_3^2)^{\frac{1}{2}}} (X-Y) \right] \tag{67}$$

where

$$X = \int_0^\beta \frac{d\lambda}{(1+\lambda^2)^{\frac{1}{2}}(1-\psi^2\lambda)^{\frac{1}{2}}}, \qquad Y = \int_0^\infty \left(\frac{1-\lambda^2\psi^2}{1-\lambda^2} \right)^{\frac{1}{2}} d\lambda,$$

$$\lambda = \beta \frac{k_1}{k}, \qquad \beta = 1 - \frac{\ell_3^2}{\ell_1^2}, \qquad \psi^2 = \frac{\ell_1^2 - \ell_2^2}{\ell_1^2 - \ell_3^2}$$

Numerical tables of X and Y, for example those of Jahnke and Emde[26] are available. Using a similar procedure μ_2 and μ_3 are obtained:

$$\mu_2 = \frac{\overline{u_2^2}}{(\overline{u_2^2})_A} = \frac{3}{4}\left[-\frac{\ell_3^2}{\ell_1^2(\ell_2^2-\ell_3^2)} + \frac{\ell_2^{-2}-\ell_3^{-2}-\ell_1^{-2}}{(\ell_1^2-\ell_2^2)(\ell_1^2-\ell_3^2)^{\frac{1}{2}}}\left(X-\frac{\ell_1^2-\ell_3^2}{\ell_2^2-\ell_3^2}Y\right)\right]$$

$$(68)$$

$$\mu_3 = \frac{\overline{u_3^2}}{(\overline{u_3^2})_A} = \frac{3}{4}\left[\frac{\ell_2^2}{\ell_1^2(\ell_2^2-\ell_3^2)} + \frac{\ell_3^{-2}-\ell_1^{-2}-\ell_2^{-2}}{(\ell_2^2-\ell_3^2)(\ell_1^2-\ell_3^2)^{\frac{1}{2}}}Y\right] \quad (69)$$

Equations (67), (68) and (69) give the effects of rapid distortion on the three components of the turbulent energy; the effect on the total turbulent energy may be found by addition.

Using the above equations, the curves in Figs. 3, 4, 5 and 6 have been plotted using the type of strain as a parameter and the strain ratio as the independent variable. As shown in Fig. 3 the effect of plane strain, $F = 0$, on the turbulent components is similar to that of symmetrical fluid contraction, $F = -\frac{1}{2}$. In both cases the distortion tends to align the vortex elements in the direction of the maximum rate of strain and to increase the energy in the $\overline{u_2^2}$ and $\overline{u_3^2}$ components of the turbulence and decrease the energy in the $\overline{u_1^2}$ component which is in the direction of the maximum rate of strain. Symmetrical diffusion $F = 1.0$, tends to orient the vortex elements in a plane normal to the two positive rates of strain and to increase the intensities of all three turbulent components.

The effect of strain is to transfer energy from the mean to the turbulent motion; as shown in Fig. 4 the total

turbulent energy of initially isotropic turbulence is always increased by strain.

The local structure of the turbulence produced by rapid distortion is shown in Fig. 5. It is interesting that all types of strain tend to produce turbulence in which half of the total turbulent energy is contained in one of the components.

The structural measure K, which is given in Fig. 6, shows that the structure of the turbulence produced by plane strain and symmetrical contraction is farthest removed from the structure produced by a symmetrical diffusion. The K curves for all types of strain become asymptotic for high strain ratios.

2.4.2. Effect of Rapid Distortion of Isotropic Turbulence on the One-Dimensional Spectra

The elements of the three-dimensional energy-spectrum tensor E_{ij} cannot be obtained from direct measurements but may be obtained by taking the Fourier transforms of the measured correlation tensor as shown in Eq. (58). The components of the correlation tensor are defined by Eq. (56) and are measured by correlating the signals from two hot-wire probes separated by a distance r.

If a single hot-wire probe is placed in a moving stream it will develop a fluctuating output voltage whose one-dimensional frequency spectrum is related to a diagonal element of the three-dimensional spectrum tensor. The mean-

square velocity component $\overline{u_1}^2$ may be considered as a diagonal component of the correlation tensor for vector distance $\underline{r} = 0$, since from Eq. (56),

$$R_{11}(0) = \overline{u_1}^2 \tag{70}$$

The contribution to the mean-square velocity component is from all waves with wave number components in the direction of the x_1-axis. From Eq. (57),

$$R_{11}(0) = \overline{u_1}^2 \iiint\limits_{-\infty}^{\infty} E_{11}(k) \, dk_1 \, dk_2 \, dk_3 \tag{71}$$

If following Taylor[63] we define $\overline{u_1}^2 = \int_0^{\infty} E_1(k_1) dk_1$ where $E_1(k)$ is the one-dimensional spectrum tensor, then

$$\int_0^{\infty} E_1(k_1) dk_1 = \overline{u_1}^2 = 2 \int_0^{\infty} \left[\iint\limits_{-\infty}^{\infty} E_{11}(k) dk_2 dk_3 \right] dk_1 \tag{72}$$

$$E_1(k_1) = 2 \iint\limits_{-\infty}^{\infty} E_{11}(k) \, dk_2 \, dk_3 \tag{73}$$

The one-dimensional spectrum may be considered as a slice of the three-dimensional spectrum between wave numbers $|k_1|$ and $|k_1| + |dk_1|$. Similarly, defining $\overline{u_2}^2 = \int_0^{\infty} E_2(k_1) dk_1$ and $\overline{u_3}^2 = \int_0^{\infty} E_3(k_1) dk_1$, then

$$E_2(k_1) = 2 \iint\limits_{-\infty}^{\infty} E_{22}(k) \, dk_2 \, dk_3 \tag{74}$$

$$E_3(k_1) = 2 \iint\limits_{-\infty}^{\infty} E_{33}(k) \, dk_2 \, dk_3 \tag{75}$$

$E_2(k_1)$ and $E_3(k_1)$ are conveniently measured using an X-wire arrangement of two hot-wire elements.

For isotropic turbulence $\left[E_{ij}(k)\right]_A$ is given by Eq. (63). If following Taylor and Batchelor we let

$$\left[\frac{E\ (k)}{4\pi k^4}\right]_A = \frac{N}{(k_1{}^2 - \gamma^2)^3}$$

where N and γ are constants, then Eq. (63) becomes, for $i = j = 1$,

$$\left[E_{11}(k)\right]_A = \frac{N(k_2{}^2 + k_3{}^2)}{(k_1{}^2 + k_2{}^2 + k_3{}^2 + \gamma^2)_A{}^3} \tag{76}$$

Using this value of $\left[E_{11}(k)\right]_A$ in Eq. (73), it can be integrated to give

$$\left[E_1(k_1)\right]_A = \frac{\pi N}{(k_1{}^2 + \gamma^2)} \tag{77}$$

Similarly the one-dimensional lateral spectrum functions are obtained, they are

$$\left[E_2(k_1)\right]_A = \left[E_3(k_1)\right]_A = \frac{\pi N(3k_1{}^2 + \gamma)_A}{2(k_1{}^2 + \gamma^2)_A{}^2} \tag{78}$$

$\left[E_2(k_1)\right]_A$ and $\left[E_3(k_1{}^2)\right]_A$ are equal because of the isotropy of the turbulence.

The effect of mean distortion on these one-dimensional spectra is found from determination of the spectra at time t. Equation (73) is

$$E_1(k_1) = 2 \iint\limits_{-\infty}^{\infty} E_{11}(k)\ dk_2\ dk_3$$

If $\underline{k}$ is expressed in terms of $\underline{k}^A$ by

$$k_1 = \left(k_1\right)_A / \ell_1, \quad k_2 = \left(k_2\right)_A / \ell_2, \quad k_3 = \left(k_3\right)_A / \ell_3$$

and $E_i(k_1)$ is defined by

$$E_i(k_1) = \ell_1 E_i \left(k_1\right)_A$$

so that

$$\int_0^\infty \left[E_i \left(k_1\right) dk\right]_A = \int_0^\infty E_i \left(k_1\right) dk_1 \tag{79}$$

then

$$E_1(k_1)_A = \frac{2}{\ell_1 \ell_2 \ell_3} \int\int_{-\infty}^\infty E_{11}\left[\left(\frac{k_1}{\ell_1}, \frac{k_2}{\ell_2}, \frac{k_3}{\ell_3}\right) dk_2\, dk_3\right]_A \tag{80}$$

Two similar equations are obtained for $E_2(k_1)_A$ and $E_3(k_1)_A$. The spectrum tensor elements E_{11}, E_{22} and E_{33} for an arbitrary distortion have been evaluated in Eq. (63). Integration of Eq. (80) is best effected in polar coordinates. For the case of symmetrical plane contraction where $\ell_2 = \ell_3$, the integration has been carried out by Ribner and Tucker.[53] The results are expressed in terms of a normalized wave number $(k_1)_A / \gamma$, defining

$$b = \frac{(k_1)_A^2}{\gamma^2} + 1 \tag{81}$$

$$c = \frac{\left[(\ell_2^2/\ell_1^2) - 1\right](k_1)_A^2}{\gamma^2} \tag{82}$$

then the final result for the longitudinal spectrum in a symmetrical contraction is

$$E_1(k_1) = \frac{2\pi N}{\ell_1^2 \gamma^2 c^3}\left[3 + 4c + c^2 + \frac{c}{2b} + (2 + 4b + 2c + bc + \frac{3b}{c})\ln(\frac{b}{b+c})\right]$$

(83)

The corresponding equation for the lateral spectra in a symmetrical contraction is

$$E_2(k_1) = E_3(k_1) = \frac{\pi N}{2\gamma^2 \ell_2^2 c^2}\left[\frac{(3b-2)c^2}{b^2} - 4(1-\frac{\ell_2^2}{\ell_1^2})(b-1)\left(\frac{2b+c}{2b}\right.\right.$$
$$\left.\left. + \frac{b+c}{b}\ln(\frac{b}{b+c}) + \frac{1-\ell_2^2/\ell_1^2}{2c}\left\{\frac{6b+5c}{2} + \frac{(b+c)(3b+c)}{c}\ln(\frac{b}{b+c})\right\}\right)\right]$$

(84)

2.5. Approximate Method of Treating Rapid Distortion of Anisotropic Turbulence

The method outlined for determining the effects of an arbitrary rapid distortion on initially isotropic turbulence could, in theory, be used for any turbulence where the components of the initial energy-spectrum tensor are known. However, the details of the turbulence, which are completely specified by the spectrum tensor, are in general not known and cannot be measured directly. The initial spectrum tensor may be obtained by measuring and integrating the correlation tensor; however, this method is not accurate because of inherent errors in the hot-wire measurements.

On the mathematical side, difficulty of integrating the initially anisotropic spectrum function over the wave number space to obtain the turbulent intensity ratios depends on the mathematical model of the initial energy-spectrum, but appears in most cases to be extremely difficult, except

perhaps if numerical methods are employed. The assumption of an initially isotropic turbulence greatly simplifies the problem, since the spectrum tensor is then specified and also the isotropic spectrum tensor, given by Eq. (61), contains $E_A(k)_A$ an arbitrary function which in the expressions for intensity ratio Eqs. (67), (68) and (69) cancel making the integration relatively simple.

The exact method of treating the distortion of anisotropic turbulence which takes into account the spectral details of the initial turbulence is extremely difficult. However, an approximate method has recently been proposed by Reynolds[51] which was found to be valuable in the present work. The experimental grid turbulence at the beginning of distortion was anisotropic and correlation between the turbulent intensities and those predicted by the original instantaneous distortion theory were unsatisfactory during the initial stages of distortion; however, the correlation became satisfactory when the initial anisotropy of the turbulence was taken into account.

The anisotropic turbulence at the beginning of distortion in the present experiments may be considered as having been produced by the application of an axisymmetric hypothetical instantaneous distortion (or more specific a symmetrical diffusion) of strain ratio $(\ell_i)_h$ to turbulence which was initially isotropic. This anisotropic turbulence is distorted by the actual strain ratio ℓ_i in passing through

the tunnel. In the rapid distortion theory it is the cumulative strain which determines the character of the distorted turbulence, independent of the manner in which it is applied. Therefore, the hypothetical and actual stresses need not be considered separately and the equations for rapid distortion of isotropic turbulence may be applied assuming an equivalent strain ratio of $(\ell_1)_e$ where

$$(\ell_i)_e = (\ell_i)_h \, \ell_i \quad \text{(no summation)} \tag{85}$$

$(\ell_i)_h$ represents the anisotropy at the initiation of the actual straining process.

In general the hypothetical type of strain $(F)_h$ and the actual type of strain F will be different so that the strain represented by $(\ell_i)_e$ will not be uniform throughout the Eulerian space. However, the instantaneous theory of Batchelor and Proudman[5] will still apply if the requirement in Eq. (41) concerning uniformity (namely that $\partial \overline{U}_i / (\partial x_j)_A$ must be uniform) is met. The distortion need be uniform only in the Lagrangian sense, ie., when the reference axis is moving with a fluid element the distortion must be uniform throughout the element. The size of the fluid element referred to is of course finite and sufficiently large to contain a sample of the turbulence.

If the mean-square intensities of the turbulence at the beginning of distortion are measured, then the values of $(\ell_i)_h$ may be obtained from Eqs. (67), (68) and (69) or

from the plotted values of these equations given in Fig. 5.
For the actual distortion, ℓ_i is known; determination of
$(\ell_i)_e$ from Eq. (85) gives values for use in Eqs. (67), (68)
and (69), from which the intensities at any stage of the
distortion may be determined.

The equivalent type of strain F_e may be determined
from the calculated values of $(\ell_i)_e$. For uniform rates of
strain

$$\ell_1 = x_1/(x_1)_A = \bar{U}_1/(\bar{U}_1)_A$$

and

$$\ell_2 = x_2/(x_2)_A = \bar{U}_2/(\bar{U}_2)_A$$

Using these relations and Eqs. (13) and (17) for flow in the
x_1-direction or Eqs. (21) and (24) for flow in the x_2-
direction we obtain

$$F = \ln \ell_2/\ln \ell_1$$

We now define

$$F_e = \ln(\ell_2)_e/\ln(\ell_1)_e$$

The equivalent type of strain F_e is simply the hypothetical
uniform strain required to produce the equivalent strain
ratios $(\ell_i)_e$. It should be noted that for uniform distor-
tion of anisotropic turbulence F_e, will vary throughout the
distortion.

When the initial turbulence is anisotropic comparison

of the experimental structure with the theoretical structure, from the rapid distortion theory, is more meaningful when F_e is used instead of the actual type of strain F. This is especially true when comparing the structures produced in the different ducts as shown later in the thesis.

2.6. Approximate Method for Including Decay Effects in the Distortion Theory

In practical turbulent fields, the decay effects are generally not small compared with the distortion effects, and there is considerable incentive to attempt to apply the theory outside the valid range by assumptions concerning the simultaneous effects of decay and distortion. This is especially necessary if development of quantities, such as the turbulent components $\overline{u_1^2}$, $\overline{u_2^2}$ and $\overline{u_3^2}$ are considered.

A simple method of combining the effects of decay and of instantaneous distortion is given below. The method is essentially the same as that proposed by Ribner and Tucker.[53] We rewrite Eq. (29) for vorticity, which is

$$\frac{D\omega_i}{Dt} = \omega_j \frac{\partial \overline{U}_i}{\partial x_j} + \omega_j \frac{\partial u_i}{\partial x_j} + \gamma \frac{\partial^2 \omega_i}{\partial x^2_j} \qquad (29)$$

$$\underset{\text{Production}}{\underbrace{\quad I \qquad\qquad II \quad}} \qquad \underset{\text{Decay}}{\underbrace{III \qquad\quad IV}}$$

We have seen that, neglecting the decay terms III and IV, the equation can be solved to give the effect of instantaneous distortion. If the production term II in the

vorticity equation is neglected, then the equation becomes

$$\frac{D\omega_i}{Dt} = \omega_j \frac{\partial u_i}{\partial x_j} + \gamma \frac{\partial^2 \omega_i}{\partial x_j^2} \qquad (86)$$

$$\underbrace{\text{I} \qquad \underbrace{\text{III} \qquad \text{IV}}_{\text{Decay}}}$$

This is the equation for decay of turbulence in uniform flow. A complete solution of Eq. (86) is possible if the non-linear inertia terms III are neglected. This would correspond to turbulence in uniform flow at very low Reynolds numbers, for example grid turbulence in the final period of decay where inertia effects are negligible. A solution of the complete Eq. (86) has not yet been achieved. However there have been many experimental studies of the decay of turbulence in uniform flow behind grids from which empirical relations are available.

In the approximate method of treating Eq. (29) the decay and distortion are considered to occur alternately in small steps starting from the initial turbulence. Each stream tube is considered to be distorted instantaneously and then allowed to decay without distortion, this process being repeated continually in time. In effect, the decay and distortion are assumed to act independently without interaction.

This approximate method may be applied to the total turbulent energy $\overline{q^2}$. Let the change in $\overline{q^2}$ due to decay be

$(d\overline{q^2})_d$ and the change in $\overline{q^2}$ due to distortion be $(d\overline{q^2})_s$.

The effect of decay is a function of the decay time

$$(\overline{q^2}/\overline{q_A^2})_d = f_1(t) \tag{87}$$

The effect of distortion in the absence of decay is obtained from the instantaneous distortion theory as a function of the strain ratios, which for a given duct geometry and mean velocity may also be expressed as a function of time, that is

$$(\overline{q^2}/\overline{q_A^2})_s = f_2(t) \tag{88}$$

The corresponding differential forms are

$$(d\overline{q^2})_d = \overline{q_A}^2\, f_1'(t)\, dt$$

or

$$(d\overline{q^2})_d/\overline{q^2} = \left[f_1'(t)/f_1(t)\right] dt \tag{89}$$

Similarly,

$$(d\overline{q^2})_s/\overline{q^2} = \left[f_2'(t)/f_2(t)\right] dt \tag{90}$$

It is assumed that Eq. (89) applies to the decay effect per step, and Eq. (90) to the contraction effect per step, with the value of $\overline{q^2}$ between the steps being common to both equations. The total effect per step is then

$$d\overline{q^2}/\overline{q^2} = \left[(d\overline{q^2})_d + (d\overline{q^2})_s\right]/\overline{q^2}$$

whence

$$d\overline{q^2}/\overline{q^2} = \left[f_1'(t)/f_1(t)\right] dt + \left[f_2'(t)/f_2(t)\right] dt \tag{91}$$

Integration of Eq. (91) between time $t = 0$ and $t = t$, gives

$$\overline{q^2}/\overline{q_A^2} = f_1(t)\ f_2(t) \tag{92}$$

That is, if the effect of contraction alone is expressed by $f_1(t)$, and the effect of decay alone by $f_2(t)$, then the joint effect is expressed by the product $f_1(t)\ f_2(t)$.

In this method of combining the effects of decay and distortion, it is assumed that anisotropic turbulence of intensity $\overline{q^2}$ will decay at the same rate as isotropic turbulence having the same value of $\overline{q^2}$. There is no data available on the decay of anisotropic turbulence, but from agreement of the actual turbulence with Eq. (91), which will be shown later, it appears that this assumption is valid.

From the structure of turbulence determined from the rapid distortion theory and the calculated values of $\overline{q^2}$ as outlined above the values of the individual components can be calculated.

CHAPTER 3

EXPERIMENTAL EQUIPMENT AND INSTRUMENTATION
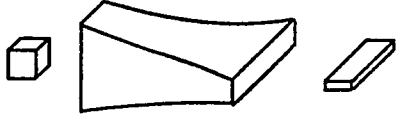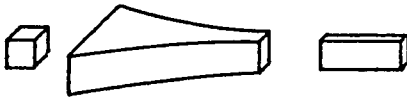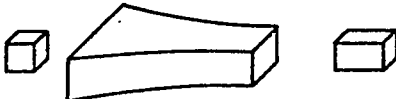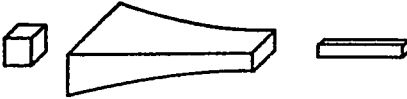
3.1. Experimental Ducts

Experiments on uniform strain of grid turbulence were carried out in five different ducts which are shown in Table 2. Three of the ducts (the distortion duct no. 1 and the two-dimensional contractions, ducts no. 2 and no. 3) were designed to produce plane strain, strain type parameter $F = 0$. The equivalent symmetrical contraction (duct no. 4) was designed to produce strain of type parameter $F = -1/2$, and the equivalent symmetrical diffuser (duct no. 5) to produce strain of type parameter $F = 1$. These nominal types of strain were not achieved in the experiments because of the effect of initial anisotropy of the grid turbulence.

In the distorting duct the values of the strain rate parameter were 0.24, 0.31, and 0.32; this was the result of changing the grid which changed the location of the virtual origin of the turbulence. In the two-dimensional contractions, more widely differing values of the strain rate parameter ($I_A = 0.32$ and $I_A = 0.97$) were obtained by changing the duct geometry. The lower value of I_A was achieved in duct no. 3; this duct was formed by modifying duct no. 2 making the contraction more gentle, thus reducing the strain ratio in the same length of duct.

63

TABLE 2

Ducts used for the uniform distortion of grid turbulence

Strain type	Duct	Duct no.		Grids	Strain ratio l (max.)	Strain rate parameter $(I)_A$	Strain type parameter F	Rate of strain tensor
Plane strain (lateral)	Distorting duct	1		A	6.0	0.32		
				B	6.0	0.24		
				C	6.0	0.31		
Plane strain (longitudinal)	Two-dimensional contraction	2		A	5.4	0.97	0	$\dfrac{\partial U_1}{\partial x_1} \begin{vmatrix} 1 & 0 & 0 \\ 0 & 0 & 0 \\ 0 & 0 & -1 \end{vmatrix}$
		3		A	2.8	0.32		
Symmetrical fluid contraction	Equivalent symmetrical contraction	4		A	5.8	0.95	-1/2	$\dfrac{\partial U_1}{\partial x_1} \begin{vmatrix} 1 & 0 & 0 \\ 0 & -1/2 & 0 \\ 0 & 0 & -1/2 \end{vmatrix}$
Symmetrical fluid diffusion	Equivalent symmetrical diffuser	5		A	2.3	0.25	1	$\dfrac{\partial U_1}{\partial x_1} \begin{vmatrix} 1 & 0 & 0 \\ 0 & 1 & 0 \\ 0 & 0 & -2 \end{vmatrix}$

The maximum value of the strain ratio for each duct is shown in Table 2. The distorting duct produced a strain ratio of 6 (determined from the duct design equations) which was higher than the strain ratio of 4 achieved in Townsend's duct, but less than the value 13.3 achieved in the duct used by Maréchal. Strain ratios in the remaining ducts were obtained from measured mean velocities, $\ell_1 = \overline{U}/(\overline{U})_c$, $\overline{U}$ was the mean-velocity near the end of the duct where the final turbulence measurements were taken.

The design shapes of the ducts were obtained by choosing values of F, ℓ_1 and the duct length, and applying Eqs. (17), (18) or (24), (25), or (26), (27), which were derived in Secs. 2.2.2. and 2.2.3. The dimensions were adjusted to allow for the growth of the boundary layer.

Accurate prediction of boundary layer thickness is difficult since the flows in the distorting ducts are three-dimensional with varying pressure gradients. As an approximation, the displacement thickness was calculated for two-dimensional turbulent flow over a smooth flat plate in zero pressure gradient:

$$\delta_1(x) = 0.0462 \; x \; (\overline{U}_\infty x/\nu)^{-1/5}$$

This formula and its notation are given in Schlichting.[56] As an approximation x was taken as the distance downstream from the grid and $\overline{U}_\infty$ the mean velocity at the grid, which in the design was taken as 20 fps.

3.2. Grids

The grids which were used in the experiments are described and shown diagramatically in Table 3. Grids A, B and C were used in the distorting duct and grid A was used in the remaining ducts.

The small square grid A was made of perforated steel which was commercially available from stock. Measurements of the bar and opening dimensions taken at ten random locations on the grid, showed that the grid was dimensionally close to homogeneous. The dimensions varied not more than ±0.001 in. as shown in the diagram of Table 3.

The large square grid B was approximately geometrically similar to grid A. It was constructed from 1/2 in. by 1/8 in. engravers brass bars. Uniform mesh size and a uni-plane grid were achieved by milling slots in the bars which interlocked on assembly. The joints were fastened with countersunk machine screws. A dimensional check similar to that on the small square grid showed that the dimensions varied less than ±0.002 in. The mesh length ratio of the large and small square grids was 2.67. Both grids were geometrically similar except in thickness, the thickness of the large grid was 0.125 in. rather than the required 0.080 in. This deviation from similarity was not considered significant.

Grid C, the diamond grid, was made of expanded and flattened aluminum, which was commercially available from stock. Measurements of the bar and hole dimensions, taken

TABLE 3

Grids used in the experiments

Grid	Name & Description	Mesh length M(in.)	Solid-ity σ	Diagram
A	<u>Small square grid</u> Perforated steel from commercial stock	0.687	0.47	
B	<u>Large square grid</u> Fabricated from engravers brass bars	1.836	0.47	
C	<u>Diamond grid</u> Expanded and flattened aluminum from commercial stock	0.593*	0.32	

*Equivalent mesh length assumed as the square-root of the mesh area.

at ten random locations, showed that this grid was dimen-
sionally less homogeneous than grid A. The dimensions
varied by ±0.002 in., as shown in the diagram of Table 3.

3.3. Distorting Wind-Tunnel

Two different wind-tunnels were used in the experi-
ments. A special wind-tunnel was built incorporating the
distorting duct no. 1; this tunnel is referred to in the
thesis as the distorting wind-tunnel. A brief description
of the tunnel construction and calibration is given here;
more complete details of the tunnel are given in a separate
report by the author.[68]

3.3.1. Description, Distorting Wind-Tunnel

The arrangement of the distorting wind-tunnel is
shown in Fig. 10. Air entered the tunnel through a bell-
mouth and then passed through a curved bronze screen and
curved aluminum honeycomb, located at the entrance of an
8:1 two-dimensional contraction. Immediately downstream of
the contraction a sealed slot was provided for inserting
the different grids. The working-section consisted of a
2 ft. long parallel flow section adjacent to the grid,
followed by the distorting section, and finally a 4 ft. long
parallel flow section. The length of this latter section
was increased to 12 ft. in order to study the decay of
anisotropic turbulence for longer decay times. After

passing through the working-section, the air entered a 3 ft. long metal transition section connected to a 39 in. diameter, 7 bladed, axial flow fan driven by a $7\frac{1}{2}$ hp electric motor which exhausted the air to the room atmosphere. Vibrations from the fan to the working-section of the tunnel were reduced by a neoprene flexible connection located between the main tunnel and the transition section of the fan. The air velocity in the tunnel could be controlled by adjusting damper blades at the fan outlet; this gave steady mean-velocities up to 70 fps.

The distorting section of duct shown in Fig. 11 was designed to produce a strain ratio $\ell_1 = 6$. In the design, the cross-sectional area, before allowing for the growth of the boundary-layers, was kept constant with the dimensions 7.5 in. wide by 45 in. high at the inlet, changing to 45 in. wide by 7.5 in. high at the outlet, in a length of 8 ft. The actual dimensions of the distorting duct after allowing for boundary layers are shown in Fig. 10.

The reasons for choosing this design were as follows: The strain ratio of 6 allowed measurements to be extended beyond the strain ratio of 4 possible in Townsend's duct, without the tunnel becoming too large. The 7.5 in. inlet width of the duct was chosen sufficiently small to keep the tunnel size within practical limits and at the same time the width was considered to be reasonably large compared with the turbulent scales, estimated by the mesh length of the

grids; a possible exception was when using grid B. The aspect ratio of the distorting section at inlet, of necessity, was the same as the strain ratio and this fixed the height at 45 inches. The length of the distorting section was chosen as a compromise between desirable rapid distortion and acceptable transition angles between the parallel and distorting sections. A shorter duct would produce a higher rate of strain and larger transition angles which would increase the possibility of flow separation near the corners because of adverse pressure gradients. A length of 8 ft. was chosen for the distorting section which gave a maximum transition angle of $22\frac{1}{2}^{\circ}$ approximately the same as the transition angle which had worked satisfactorily in Townsend's tunnel.

The right walls (looking downstream) of sections 3 and 4, as shown in Fig. 10, were constructed of 1/8 in. plexiglas which allowed good visibility for locating probes within the tunnel. The left walls of sections 3 and 4 were provided with large access doors with tight neoprene seals. The remaining curved surfaces of the distorting duct were constructed of 1/8 in. plywood supported on 5/8 in. plywood ribs as were the curved surfaces of the throat of section 1. The remaining walls and flanges of the tunnel were constructed of 5/8 in. plywood. The bell-mouth of section 1 was made of 6 in. diameter cardboard tubes.

3.3.2. Traversing Equipment, Distorting Wind-Tunnel

Two sets of traversing equipment were provided for the tunnel; the first to traverse the tunnel cross-section at the entrance of the distorting section and the second to traverse along the longitudinal center-line of the tunnel. The first traversing gear was mounted on an aluminum support outside the tunnel and the arm of the probe holder entered the tunnel through a slot, which after each location of the probe was sealed with cloth adhesive tape. Vernier scales allowed the probe to be positioned to within ±0.002 in. in the vertical direction and to within ±0.01 in. in the horizontal direction.

The second traversing gear allowed probes to be positioned at any point on the longitudinal center-line of the distorting section and adjoining parallel flow sections. The probes were supported at the end of a 1/2 in. square brass bar, approximately 3 ft. long, which in turn was supported so that its center-line was aligned with the longitudinal center-line of the tunnel. The supports for the brass bar were brass slider bearings which were fastened with screws to 3/8 in. diameter rods passing vertically through the tunnel. Holes for the vertical rods were spaced approximately 15 in. apart, and when particular rods and bearings were not required they were removed and the holes were sealed with cloth adhesive tape from inside. A small braided metal cable, attached to the downstream end of the

brass bar and extending over pulleys to outside the tunnel, allowed the probe to be positioned by downstream movement from outside the tunnel. Accurate scales were marked along the center-lines of the plexiglas and the opposite side walls; this allowed the location of the probe to be determined by sighting across the tunnel.

3.3.3. Center-Line Mean Velocities, Distorting Wind-Tunnel

Mean velocities along the center-line of the tunnel were measured using the separate total and static pressure probes. The velocities were made dimensionless using the mean velocity at a point C located 18 in. before the entrance of the distorting section (6 in. behind the grid). The resulting dimensionless velocity distributions for grid A and mean velocity of approximately 20 fps is shown in Fig. 12. Velocity distributions for grid C at mean velocities of 20, 40 and 60 fps are shown in Fig. 13, together with the velocity distribution in the wind-tunnel at a mean velocity of 40 fps without the grid.

The dimensionless velocity distributions are all approximately identical. The presence of the grid did not appreciably change the velocity distribution in the tunnel as can be seen by comparing the dimensionless velocities, at a mean velocity of 40 fps, with and without the grid. The mean velocity in the tunnel appears to influence the velocity distributions slightly; this can be seen by

comparing the values in Fig. 13 for grid C at mean velocities
of 20, 40 and 60 fps. At 20 fps the dimensionless velocity
appears to be slightly higher in the downstream part of the
tunnel; this was probably caused by the increased thickness
of the boundary-layer at the lower velocity.

In designing the working-section of the distorting
tunnel, equations were used which assumed that the longi-
tudinal mean velocity would remain constant. The actual
longitudinal velocity peaked at the entrance and exit of
the distorting duct. The streamlines, instead of having
sharp transition angles in these regions as assumed in the
design, were, of course, curved; this decreased the cross-
sectional area of the flow and caused local high velocities.
The high velocities in the transition zones are natural to
the flow and cannot be avoided but could be decreased by
having a longer distorting duct; this of course would de-
crease the rate of strain and make it more difficult to
compare the actual turbulence with that predicted by the
rapid distortion theory.

The longitudinal velocity in the central region of
the distorting duct was about 5 percent lower than the
velocity directly behind the grid; the reason, most likely,
was that the displacement thickness was over-estimated when
the approximate formula was used. The velocity in the
central region of the distorting duct varied about one
percent in a length of 50 inches. This was considerably

better than the 20 in. of approximately constant velocity
achieved by Townsend in his distorting tunnel, and may
partly account for the different results which will be
discussed later. Overall, the mean longitudinal velocity
throughout the working-section of the tunnel varied less
than 10 percent; this was considered acceptable.

3.3.4. Background Turbulence, Distorting Wind-Tunnel

The background turbulent intensities along the
center-line of the empty tunnel (ie., without the grid) are
shown in Fig. 14 for mean velocity $\bar{U}_c$ of 20 fps. The back-
ground turbulence is lowest in the distorting section; the
three components of the turbulence are approximately equal
and less than 0.3%, that is,

$$u'/\bar{U} < 0.3 \times 10^{-2}, \quad v'/\bar{U} < 0.3 \times 10^{-2}, \quad w'/\bar{U} < 0.3 \times 10^{-2}.$$

These values were obtained after correcting for instrument
noise using the method described later in Sec. 3.6. The
turbulent intensities increased downstream in the parallel
flow section, and the u' and v' components attained values
of approsimately 0.45% and the w' component approximately
0.40%. This increase in the background turbulence may
have been due to acoustic noise and vibrations from the fan,
or to boundary-layer growth which allowed turbulent fluid
to reach the center of the duct.

The effect of mean velocity on the background

turbulence in the tunnel is shown in Fig. 15, where values
of the relative turbulent intensities versus mean velocity
at 36 in. from the entrance to the distorting section are
shown. The values of u', v' and w' decreased slightly with
increase in the mean velocity, the large decrease in $u'/\bar{U}$,
$v'/\bar{U}$ and $w'/\bar{U}$ was mainly due to an increase in $\bar{U}$.

When measurements of distorted grid turbulence were
corrected for combined background turbulence and instrument
noise, the corrections did not significantly change the
results; therefore, the level of background turbulence in
the tunnel was considered to be satisfactory.

3.4. The Blower Wind-Tunnel

The McGill blower wind-tunnel was used to generate
flow through the remaining three distorting ducts: the two-
dimensional contractions, ducts nos. 2 and 3; the equivalent
symmetrical contraction, duct no. 4; and the equivalent
symmetrical diffuser, duct no. 5. A general description of
this tunnel is contained in a report by Wyganski and
Gartshore.[76] A brief description of the tunnel is given
here before discussing its characteristics.

3.4.1. Description, Blower Wind-Tunnel

The general arrangement of the blower wind-tunnel
is shown in Fig. 34. The tunnel was an open return type
having an exit 30 in. wide by 17 in. high to which the

distorting ducts were attached. The tunnel had a single-stage centrifugal fan (Buffalo 980 BL) driven at 700 rpm. The velocity in the tunnel was controlled by variable inlet vanes on the fan. The air was filtered by a 2 in. thick fiberglas filter which formed the walls of a large box at the fan inlet. After leaving the fan, the air passed through a diffuser to a large settling chamber which contained an aluminum honeycomb and had provisions for three bronze screens. The upstream and center screens, which were used in the experiments reported, here were 14 by 15 mesh, of 0.020 in. and 0.022 in. diameter wires; the screen used downstream was 21 by 23 mesh, of 0.015 in. and 0.017 in. diameter wires. The contracting section which led to the working-section was a two-dimensional type having a contraction ratio of 6:1.

3.4.2. Calibration and Background Turbulence, Blower Wind-Tunnel

A survey of the total and static pressure at the exit of the tunnel was made by Wyganski and Gartshore[16] At approximately 35 fps the mean velocity varied less than 1.2% over the cross-section at the exit of the contraction and at approximately 130 fps the variation was less than 0.4%.

The longitudinal component of the background turbulence in the tunnel was measured at the center point of the exit of the wind-tunnel contraction. The value of $u'/\overline{U}$

decreased from about 1.3% at a mean velocity of 20 fps to about 0.4% at a mean velocity of 130 fps and appeared to approach this value asymptotically.

The background turbulent intensities which were measured along the center-lines of ducts nos. 2, 4 and 5 (inlet velocities 20 fps) are shown in Figs. 37, 47 and 55 respectively. The turbulence was approximately the same at the entrance to the distorting sections of duct no. 2 and duct no. 4 with values

$$u'/\bar{U} \simeq v'/\bar{U} \simeq w'/\bar{U} \simeq 0.5 \times 10^{-2}$$

The longitudinal component of the background turbulence remained approximately constant but the lateral components decreased in the downstream direction to less than 0.2%, ie., $v'/\bar{U} \simeq w'/\bar{U} < 0.2 \times 10^{-2}$. The corresponding turbulence was slightly higher in duct no. 5. This duct had a low pressure drop and hence required the control damper at the fan to be more closed to maintain the duct inlet velocity at 20 fps. The high turbulence was probably due to turbulence generated by the dampers.

At the beginning of the experimental program it was thought that the background turbulence in the tunnel was not objectionable. It was felt that the character of the original background turbulence would be lost in passing through the grid and that the characteristics of the turbulence downstream of the grid would be approximately the

same as for low background turbulence. However, it was found that during distortion the structure of the turbulence did not develop as expected, and it was suspected that the results were influenced by the background turbulence of the tunnel.

An attempt was made to decrease the background turbulence by placing a perforated metal grid ($\frac{1}{4}$ in. diameter holes with $\frac{1}{2}$ in. square spacing between centers) in the diffuser behind the fan. However, measurements of the root-mean-square values of the longitudinal component of turbulence at the center-point of the tunnel contraction at the exit, showed that the additional grid did not reduce the background turbulence.

In order to investigate further the effect of a grid in reducing the background turbulence in the tunnel, a wire screen having a 14 by 15 mesh of 0.020 in. and 0.022 in. diameter wires was placed at the exit of the tunnel contraction. With the two-dimensional contraction no. 3 in position, measurements of the root-mean-square values of the three turbulent components were measured on the center-line, 24 in. downstream from the screen. When these values were compared with those taken at the same location and the same mean velocity with the screen absent, it was found that the screen had no influence on the background turbulence. Apparently the screen turbulence decayed to a negligible value in the 24 in. parallel flow (representing approximately

250 mesh lengths), leaving the background turbulence the same as before the screen was installed.

A part of the background turbulence in the tunnel could be sound waves generated by the fan. Dryden and Schubauer[16] have shown that when the level of the free-stream turbulence in a wind-tunnel is reduced by screens and a contraction, the remaining fluctuations may be partly due to sound waves coming from the fan. These sound waves form a more or less continuous spectrum, which is probably dominated by the frequency of the fan blades. The pulsations of long wave lengths are not reflected from the tunnel walls and are therefore plane sound waves.

In order to determine further the nature of the background turbulence on the tunnel, a spectrum analysis was made of the turbulence measured at a point on the center-line of the parallel duct, 7 in. downstream of the tunnel contraction, with distorting duct no. 2 in position and mean velocity 20 fps. The results of the spectrum analysis are shown in Fig. 38. The spectrum of the background turbulence was fairly continuous for $k < 400$, i.e., frequencies up to 1280 cps; at higher frequencies the measured values were probably due to instrument noise. Because of the limitations of the spectrometer, the spectrum below 20 cps could not be analyzed. However, assuming that the mean-square value of the thermocouple type rms meter on the Disa anemometer represented the total turbulent energy, it was

found that 80% of the turbulent energy associated with the longitudinal component was contained in frequencies below 20 cps.

3.4.3. Two-Dimensional Contractions

The two-dimensional contractions, ducts nos. 2 and 3, were made by adjusting the flexible side walls of a single duct, which is shown schematically in Fig. 35. The duct had an inlet 30 in. wide by 17 in. high to match the outlet of the blower tunnel to which it was connected by flanges, with the turbulence generating grid located at the junction. A 2 ft. long parallel section was followed by an 8 ft. long distorting section. In the experimental arrangement, air was blown through the duct and exhausted directly to the room atmosphere.

The duct was built using a base of 4 ft. by 10 ft. by 1 in. plywood, supported on a Dexion stand. The parallel flow section was made of 3/4 in. plywood. The sides and top of the contracting section were made of 1/4 in. plexiglas; the sides, which were strips of plexiglas approximately 17 in. wide, were clamped between the base and the top by 1/4 in. diameter threaded bolts. When the bolts clamping the sides were loosened the 1/4 in. plexiglas sides, which were quite flexible, could be shaped accurately by means of a number of adjusting screws. The shape of the contracting section was obtained using the method outlined in Sec. 3.1.

of the thesis.

The probe support and traversing gear allowed probes to be positioned at any point on the longitudinal center-line of the parallel and distorting sections of the duct. The arrangement was similar to that used for traversing along the longitudinal center-line of the distorting tunnel. The probes were held at the end of a 3 ft. long by 1/2 in. square bar which was supported along the center-line of the duct on 3/8 in. vertical rods spaced about 15 in. apart, and extending through the duct. In this duct the probe holding bar was lengthened to extend beyond the exit; this allowed the probes to be positioned from outside the tunnel.

3.4.4. Equivalent Symmetrical Contraction

The duct for the experiments on symmetrical con-traction is shown schematically in Fig. 45. It was made by modifying the existing duct used for the two-dimensional contractions, described above. The parallel section of the duct remained unchanged and the distorting section was converted by placing liners of the correct shape inside to form the top and the bottom of the contraction. The sides of the existing duct, which were·flexible, were adjusted to form the sides of the contraction. The liners were made of 1/4 in. plywood fastened to 3/4 in. plywood ribs.

The probe support and traversing gear were the same as used in the duct for longitudinal plane strain.

Measurements could be taken at any point on the center-line of the duct in the parallel and distorting sections.

3.4.5. Equivalent Symmetrical Diffuser

The equivalent symmetrical diffuser, duct no. 5 is shown schematically in Fig. 53. The duct had an inlet 17 in. high by 30 in. wide to match the outlet of the blower tunnel. The 2 ft. long parallel section was followed by the distorting section. The duct was attached to the blower tunnel and the framed grid was located between the flanges. Air passed through the duct and was exhausted to the room atmosphere.

The parallel section of the duct, including flanges, was made from 3/4 in. plywood except for the left wall looking downstream which was made of 1/4 in. plexiglas. The distorting section of the duct was made of 1/4 in. plywood held in position by a number of flanges. The duct was supported by clamping 2 in. by 2 in. wooden legs to the flanges.

The distorting section was designed to produce a uniform mean rate of strain with the mean flow in the direction of x_1. The design was based on a strain ratio of 2.5 in a length of 8 ft. The traversing gear was the same as that described in Sec. 3.4.3. for the two-dimensional contractions.

3.5. Turbulence Measurements

All turbulent intensities were measured using Disa, type 55A01, constant temperature hot-wire anemometers. Three anemometers of the same type were available in the laboratory, and during the runs the readings were checked using two units. Disa hot-wire probes were also used; these had platinum plated tungsten wires, 0.005 mm diameter, approximately 1.0 mm long (the length to diameter ratio of the wires was approximately 200). The tungsten wires were connected to nickel supports by a combined method of welding and electroplating.

Measurements of the axial turbulent velocity component u' were made with a wire normal to the probe axis and to the mean flow. The static sensitivity to the u' fluctuations was determined, in effect, by obtaining the local tangent to the experimental curve of mean d-c voltage versus mean velocity. During calibration the air temperature was constant within $\pm 0.5^\circ F$.

Values of the lateral fluctuating components v' and w' and the Reynolds stresses $\overline{uv}$ and $\overline{uw}$ were measured using a normal wire and a single slanting wire; the latter was located at approximately 45° to the probe axis and to the direction of the mean flow. To measure v' and $\overline{uv}$ the slanting wire was located in the uv-plane, with the axis of the probe in the direction of the mean flow. Two readings with the slanting wire were obtained, one at angle

ϕ and one at $-\phi$, obtained by rotating the probe 180° about its axis. The single normal and the two slanting wire readings gave three equations from which the three unknowns u', v' and $\overline{uv}$ were determined. The derivation of the hot-wire equations are given in Appendix B.

The constants n_I and n_{II} in the normal hot-wire equations (see Appendix B, Eqs. (B.26), (B.27) and (B.28)) were obtained from an $\bar{E}^2$ versus $\bar{U}^c$ calibration as outlined in Sec. B.5. of Appendix B. The constant s_1/s_2 was determined by calibration of the hot-wires in a developed pipe flow which is outlined in Appendix C. As a check the constants s_1 and s_2 were also obtained using Equations (B.22) and (B.23) of Appendix B: ϕ, the angle of the slanting wire, was measured directly; c, the exponent in the hot-wire equation, was obtained by calibration; k, the constant which measures the cooling effect of the velocity component along the hot-wire, was assumed to be 0.20 as suggested by the separate results of Webster,[76] Champagne[8] and Patel.[45]

Turbulence measurements based on the pipe calibration value of s_1/s_2 were considered to be the more reliable and, unless specified otherwise, these measurements are reported in the thesis. Turbulence measurements based on the separate values of ϕ, c and k were slightly different than those based on the pipe calibration. In the blower wind-tunnel these differences were relatively unimportant because of the possible larger errors due to background turbulence.

In the distorting wind-tunnel the different methods of determining the constants did not (for $\mathcal{l}_1 > 2$) effect the structural measure K but changed the values of $\overline{u_i^2}/(\overline{U}_c)^2$ and $\overline{u_i^2}/\overline{q^2}$ slightly. This is discussed later in the thesis.

The one-dimensional spectra were measured using two Disa type 55A01 constant temperature hot-wire anemometers, a Disa type 55A06 correlator, a Bruel and Kjaer spectrometer type 2112, and Disa X-wires. As a check on the X-wire measurements, the one-dimensional longitudinal spectra were also measured using a single normal hot-wire. Errors due to close spacing of Disa X-wires have been studied by Jerome and Burling[27] and by Guitton and Patel.[22]

3.6. Use of Filters, Background Turbulence and Noise Corrections

The instrument noise of the Disa hot-wire anemometer was measured by obtaining the rms voltage reading with the wire enclosed in a small container, in which the turbulence motion was assumed to be negligible. It was found that a large proportion of the instrument noise was in the high frequency range; this suggested the use of low-pass filters to eliminate the high frequencies.

For all the turbulence measurements the 20 kc/s low-pass filter of the Disa anemometer was used. Observations of measured spectra showed that frequencies associated with grid turbulence were well below this value and hence not affected. The use of the 20 kc/s low-pass filter eliminated about 60% of the (no filter) instrument noise.

To obtain the background turbulence in the different ducts, readings along the center-lines of the ducts were taken without the grid and corrected for instrument noise by subtracting from each mean-square voltage, the mean-square voltage of the instrument noise obtained at the same wire operating conditions. This method of correcting for instrument noise is permissible, since the turbulence and the instrument noise are uncorrelated.

The turbulence intensity measurements which were taken in the ducts when the grids were present were corrected for background turbulence by two methods.

Method I: The 20 kc/s low-pass filter of the hot-wire anemometer was used in taking the measurements. Readings of the grid turbulence in the different ducts were corrected for combined instrument noise and background turbulence by subtracting from each mean-square voltage, the mean-square voltage obtained at the same location in the empty tunnel, under the same hot-wire operating conditions and using the same filter. This method assumed that the grid turbulence and the background turbulence behaved independently.

Method II: The 20 kc/s low-pass filter and the 20 cps high-pass filter of the hot-wire anemometer were used in taking the measurements. The readings were corrected for instrument noise by subtracting from the measured mean-square voltages, the mean-square voltages of the instrument noise obtained using the same filters and at the same wire

operating conditions. In the blower tunnel over 80% of the background turbulent energy was contained in frequencies below 20 cps. Only about 10% of the energy associated with the grid turbulence was contained in these frequencies.

Method I was used to correct for background turbulence and instrument noise in duct no. 1 used with the distorting wind-tunnel. Method I and method II were used to correct for background turbulence and instrument noise in the remaining duct used with the blower wind-tunnel.

CHAPTER 4

EXPERIMENTAL RESULTS AND DISCUSSION

4.1. Decay of Grid Turbulence in Uniform Flow

There have been many experimental studies of the
decay of grid turbulence in steady uniform flow. In most
experiments especially constructed bi-plane grids were
used, having square mesh and either round or square bars.
Even when using similar bi-plane grids there have been
discrepancies between the findings of different investi-
gators regarding the detailed structure of the turbulence
produced by the grids, and the experimental laws of decay.
This is illustrated by the results of different researchers
which are compared in the report by Comte-Bellot and
Corrsin[11]

The grids used in the present experiments were of the
single plane type, two were commercially available from
stock; these grids were chosen because they were cheap and
each grid was approximately homogeneous in geometry.
Unfortunately no information was available on the structure
of the turbulence generated by the grids or on the behaviour
of the turbulence during decay, and so experiments were
undertaken to obtain this information.

4.1.1. Experimental Arrangement and Measurements

The experiments on decaying grid turbulence in uniform flow were performed in the distorting wind-tunnel which had a long parallel flow section and the lowest background turbulence of the available wind-tunnels. The arrangement of the distorting wind-tunnel is shown in Fig. 10. Wind-tunnel details and the arrangement of the traversing gear which allowed measurements to be taken along the center-line of the working-section have already been given. For these experiments the grid was removed from its regular location in the slot at the entrance to the wind-tunnel and was temporarily located at the downstream end of the distorting duct at the entrance of the 12 ft. long parallel flow section.

Using the small square grid A, measurements were made with mean velocity $\bar{U}_C$ steady at approximately 20 fps. For the diamond grid C, the mean velocity $\bar{U}_C$ was steady at approximately 20, 40 and 60 fps. These velocities were approximately the same as those used in the experiments on distortion, which are treated later. For both grids, measurement of the turbulent intensities u', v' and w' and the mean velocity $\bar{U}$ were made at points along the center-line of the parallel duct, extending a distance of 10 ft. downstream from the grid. The turbulence readings were corrected for combined instrument noise and tunnel background noise by method I given in Sec. 3.6. In all cases

the corrections were small and changed the turbulence intensities $\overline{u_i^2}/\bar{U}^2$ by less than 3% for both grids.

4.1.2. Turbulent Structure during Decay

It was found that the turbulence produced by both grids was anisotropic. The component u' in the main flow direction was higher than the turbulence components v' and w' in the transverse directions. The values of v' and w' were equal within the accuracy of measurement.

A convenient measure of anisotropy of the turbulence is u'/v' which for isotropic turbulence has a value of unity. Values of u'/v' versus $(x-x_0)/M$ are shown in Fig. 7. The turbulence was anisotropic for both grids, but there was a definite tendency towards isotropy at increasing distances from the grids. The values of u'/v' were approximately the same for both grid A and grid C and were approximately independent of the mesh Reynolds number of grid C.

It is interesting to compare the results obtained here for perforated type grids with those obtained by various investigators using the more conventional square mesh bi-plane grids of round rods; results of Corrsin, Wyatt, Kestler and Vrebalovich and Uberoi have been reported by Comte-Bellot and Corrsin[11] together with their own results. The figures used in their report to compare results is shown as an insert in Fig. 7. The present results fall well within the range of the results of the other investigators;

they all obtained values of u'/v' which were greater than unity. The tendency observed here towards isotropy agrees with the results of Corrsin and Comte-Bellot and Corrsin, the results of Uberoi show a slightly opposite tendency.

In the present results, if the constants s_1 and s_2 were obtained from the measured values of ϕ and c and the assumed value of $k = 0.2$, then the values of u'/v' would be 0.92 of the values shown in Fig. 7. At 40 mesh lengths from the grid instead of 1.2 the value of u'/v' would be 1.1 and at 140 mesh lengths the turbulence would be close to isotropic with values of u'/v' near 1.0.

4.1.3. Rates of Decay

It has been customary to represent grid turbulence decay by power laws over various periods during the lifetime of the turbulence. Here it was assumed that the equations for the u' and v' components of the turbulence were of the form:

$$\bar{U}^2/\overline{u^2} = B(x-x_0)^n \tag{93}$$

$$\bar{U}^2/\overline{v^2} = C(x-x_0')^m \tag{94}$$

These equations allowed the virtual origins and the rates of decay of the u' and v' components of the turbulence to be different.

The values of n, B and x_0 were obtained using the experimental data in Eq. (95) which was obtained from

Eq. (93)

$$(\bar{U}^2/\bar{u^2})^{1/n} = B^{1/n} x - B^{1/n} x_o \qquad (95)$$

An initial value of $n = 1$ was assumed and the rms error was found for a straight line through the points $(\bar{U}^2/\bar{u^2})^{1/n}$, x. The value of n was then increased by increments until the smallest rms error was obtained. This gave the value of n. The value of x_o was obtained by dividing the intercept $B^{1/n} x_o$ by the slope $B^{1/n}$. The values of m, C and x_o' were obtained from the experimental data in the same way using Eq. (94). It was found that for any one grid x_o and x_o' were nearly equal. In order to simplify the results a single value of x_o was chosen and n and m were changed to the values obtained for the lines having this value of x_o.

For grid A the experimental values of the relative turbulent intensities, $\bar{u^2}/\bar{U}^2$, $\bar{v^2}/\bar{U}^2$, $\bar{w^2}/\bar{U}^2$ and $\bar{q^2}/\bar{U}^2$ were plotted against the distance from the virtual origin, $x - x_o$, on log-log paper as shown in Fig. 8. The points lie close to straight lines which indicate that the decay of the individual components of the turbulence and the total turbulent energy may each be represented by power laws. As the turbulence decayed it became more isotropic as indicated by the tendency for the $\bar{u^2}/\bar{U}^2$ and the $\bar{v^2}/\bar{U}^2$ (or $\bar{w^2}/\bar{U}^2$) lines to converge at increasing distances from the virtual origin. The values of n and m are the negative slopes of the

TABLE 4

Comparison of the decay of turbulence for perforated and bi-plane grids

Reference	Re_M x 10^{-3}	$\overline{U}$ (fps.)	M (in.)	σ solidity	Type of grid	$\overline{u^2}$ - decay		$\overline{v^2}, \overline{w^2}$ - decay	
						n	$\dfrac{x_q - x_o}{M}$	m	$\dfrac{x_q - x_o}{M}$
Corrsin (1942)	8.5	33	0.50	0.44	Bi-plane,round rods	1.30	1	1.22	1.5
	17	33	1.00	0.44	" "	1.28	3	1.14	2.5
	26	49	1.00	0.44	" "	1.35	1	1.16	1
Batchelor and Townsend (1947-1948)	5.5	21	0.50	0.34	" "	1.13	5	–	–
	11	42	0.50	0.34	" "	1.25	8	–	–
Uberoi (1963)	29	56	1.00	0.44	" "	1.20	4	1.20	4
Baines and Paterson (1951)	24	26	1.75	0.44	Bi-plane,square rods	1.37	3	–	–
Comte-Bellot and Corrsin (1965)	17	33	1.00	0.34	" "	1.33	1.5	1.27	1.5
	34	66	1.00	0.34	" "	1.27	2.5	1.24	2
Tucker (present values)	6.8	20	0.69	0.47	Perforated sq. grid	1.35	4.7	1.17	4.7
	5.8 11.6 17.4	20 40 60	0.59	0.32	Perforated diamond grid	1.35	5.0	1.23	5.0

corresponding straight lines.

Results for the three different mesh Reynolds numbers Re_M of the diamond grid C are shown in Fig. 9. The lateral components of the turbulence v' and w' were equal within the accuracy of measurement, average values of $(\overline{v^2} + \overline{w^2})/2\overline{U}^2$ are plotted together with $\overline{u^2}/\overline{U}^2$ and $\overline{q^2}/\overline{U}^2$. The turbulence for grid C was similar to that of grid A. As usually found (for grid turbulence at high mesh Reynolds numbers) the Reynolds number effect was not significant.

The constants in the decay laws which were found for the two grids used here are shown in Table 4, together with the corresponding constants for square mesh bi-plane grids of round rods and square rods reported in the paper by Comte-Bellot and Corrsin." The values of n, m and x_0/M found for the square perforated grid A and the diamond grid C are not greatly different from those reported by Comte-Bellot and Corrsin for the bi-plane grids.

Because of the initial anisotropy of the grid turbulence, it was necessary to account for this in the rapid distortion theory in order to obtain agreement between the theoretical and experimental results in the initial stages of distortion.

4.2. Plane Strain (lateral), Strain Type Parameter F = 0

Plane strain having type parameter $F = 0$ was produced in the distorting wind-tunnel, the duct which produced the

strain is shown schematically in Fig. 11 with reference axes x_1, x_2, x_3 as indicated. The distorting duct was of the same general shape as the ducts used by MacPhail[35] Townsend[65] and Marechal[36] in their separate experiments.

4.2.1. Experimental Results Using Grid A

The small square mesh grid A was placed in the grid slot of the distorting wind-tunnel. The tunnel had a 12 ft. long parallel flow section located behind the distorting section. Measurements of the turbulent components u_1', u_2', u_3' and the longitudinal mean-velocity $\bar{U}_2$ were made at points along the center-line of the tunnel. During measurement the mean velocity $(\bar{U}_2)_c$ was steady at approximately 20 fps. Periodic checks of the mean velocity and temperature at fixed reference points behind the grid showed that during the run the mean velocity varied less than 0.7% and the temperature remained within the range $76^\circ F$. to $81^\circ F$. The temperature at which the hot-wires were calibrated was $80 \pm 0.5^\circ F$.

Values of the turbulent intensities $\overline{u_i^2}/(\bar{U}_2)_c^2$ and $\overline{q^2}/(\bar{U}_2)_c^2$ versus $(x_2 - (x_2)_0)$, the distance from the virtual origin of the turbulence (obtained for decay in uniform flow), are shown in Fig. 16. In the absence of distortion, the total turbulent energy and the separate components of the turbulent energy decayed along the straight lines which are shown (reproduced from Fig. 8).

For plane lateral distortion, neglecting decay, the behaviour of grid turbulence can be obtained, approximately, from the instantaneous distortion theory applied to isotropic turbulence. Turbulent energy is produced by distortion, as can be seen from the increase in $\overline{q^2}/(\overline{q^2})_A$ shown in Fig. 4. Distortion acts selectively on the individual components of the turbulence, increasing the values of the u_2' and u_3' components and decreasing the value of the u_1' component, as shown for the parameter $F = 0$ in Fig. 3.

In considering the behaviour of the total turbulent energy $\overline{q^2}/2$ during distortion, two opposing processes were present: the first was viscous decay which tended to decrease the value of $\overline{q^2}$; the second was the production of turbulent energy by the distortion, which tended to increase its value. From Fig. 16, we see that in the initial stages of distortion the decay effects were dominant; as the turbulence became distorted to higher strain ratios the production effects became more significant until, for a strain ratio near 3, the values of $\overline{q^2}$ reached a minimum. Here the production apparently balanced the decay and the turbulence was in a state of energy equilibrium. At higher strain ratios the production was dominant and the turbulence energy increased until distortion ceased at a strain ratio of 6.

In the parallel flow section after the distortion

there was no production of turbulent energy and the viscous decay caused $\overline{q^2}$ to decrease. Values of $\overline{q^2}/(\overline{U}_2)_c^2$ fall approximately on a straight line of the same negative slope as that of grid turbulence in uniform flow. Apparently the rate of decay of the highly anisotropic turbulence was not too different than the rate of decay of the more nearly isotropic grid turbulence. This was the assumption made in order to correct the instantaneous distortion theory for decay.

The theoretical curve $\overline{q^2}/(\overline{U}_2)_c^2$ shown in Fig. 16 was obtained starting from the measured value at the beginning of distortion and assuming isotropic turbulence. The rapid distortion theory was used and corrected for decay by the method outlined in Sec. 2.6.. Agreement between the experimental and theoretical values of $\overline{q^2}/(\overline{U}_2)_c^2$ was remarkably good throughout the distorting section. Agreement was not as good when the rapid distortion theory was applied to the actual anisotropic turbulence using the equivalent strain ratios $(\ell_i)_e$; this applied to all the ducts tested.

The theoretical curves for the components of the turbulence, which are shown in Fig. 16, were obtained using the rapid distortion theory applied to the actual anisotropic turbulence to determine the fraction of turbulent energy in each of the three components (this gave the theoretical curves in Fig. 17 which will be discussed later).

The fractions were applied to the theoretical values of $\overline{q^2}/(\overline{U}_2)_c^2$ to give the theoretical curves of the components shown in Fig. 16. There was good agreement between the experimental and theoretical values of $\overline{u_3^2}/(\overline{U}_2)_c^2$ throughout the distorting section, however, the experimental values of $\overline{u_1^2}/(\overline{U}_2)_c^2$ became higher than the theoretical values as the strain ratio increased while the experimental values of $\overline{u_2^2}/(\overline{U}_2)_c^2$ became lower than the theoretical values. Apparently there was a transfer of turbulent energy to the lowest component.

The energy transfer between the components of turbulence which determine the rate of decay of each component of turbulence appeared to depend on the degree of anisotropy of the turbulence. This is illustrated by considering the experimental values of $\overline{u_1^2}/(\overline{U}_2)_c^2$ in Fig. 16. In parallel flow before distortion where the turbulence was slightly anisotropic, the values of $\overline{u_1^2}/(\overline{U}_2)_c^2$ decreased during decay while in the parallel flow after the distortion, where the turbulence was highly anisotropic and the value of turbulent intensity $\overline{u_1^2}$ was small compared to the intensity of the other components, there was an increase in the value of $\overline{u_1^2}/(\overline{U}_2)_c^2$ during the overall turbulence decay.

The local structural measures $\overline{u_i^2}/\overline{q^2}$, versus strain ratio are shown in Fig. 17. At the entrance of the distorting section the turbulence was anisotropic with $\overline{u_3^2}/\overline{q^2} \simeq 0.41$ and $\overline{u_1^2}/\overline{q^2} \simeq \overline{u_2^2}/\overline{q^2} \simeq 0.29$; turbulence of this type is

produced by a rapid strain of type parameter $F = 1$ and strain ratios $(\ell_1)_h = (\ell_2)_h = 1.20$, $(\ell_3)_h = 0.70$. The theoretical curves shown in Fig. 17 were obtained assuming that an instantaneous strain was then applied to this turbulence as outlined in Sec. 2.5.

For strain ratios up to 1.5, the experimental values of $\overline{u_1^2}/\overline{q^2}$, $\overline{u_2^2}/\overline{q^2}$ and $\overline{u_3^2}/\overline{q^2}$ were close to the theoretical values. At higher values of the strain ratio the measured values of $\overline{u_3^2}/\overline{q^2}$ continued to agree closely with the theory; however, at values of $\ell_1 > 1.5$, the measured values of $\overline{u_1^2}/\overline{q^2}$ became higher and the measured values of $\overline{u_2^2}/\overline{q^2}$ became lower than the corresponding theoretical values. The structure of the turbulence during distortion may be considered as the product of two opposing effects: the first effect is produced by the distortion which tends to orient the eddies in the direction of the maximum rate of strain; the second and opposing effect is a tendency of the turbulence to return towards isotropy which is an integral part of the decay process.

The local intensity ratios $\overline{u_i^2}/\overline{q^2}$, although useful as a measure, give little insight into the structure of the turbulence. This deficiency may be removed by using the hypothetical strain ratios $(\ell_1)_h$, $(\ell_2)_h$ and $(\ell_3)_h$ to measure the turbulent structure. These ratios may also be considered as a measure of the direction of the eddies which comprise the turbulence as explained below.

If we imagine the actual turbulence as if it were produced by a hypothetical instantaneous distortion of $(\ell_1)_h$, $(\ell_2)_h$ and $(\ell_3)_h$ applied to isotropic turbulence, the eddies of the isotropic turbulence which are uniformly distributed in space would tend to become oriented in the direction of the higher strain ratios, and hence the values of $(\ell_1)_h$, $(\ell_2)_h$ and $(\ell_3)_h$ could be considered to measure the space orientation of the eddies. For example, if the value of the structural triple $((\ell_1)_h, (\ell_2)_h, (\ell_3)_h)$ were (6, 1, 1/6), the eddies could be considered as oriented mostly in the x_1-direction, less in the x_2-direction, and least in the x_3-direction, since this would be the result if a volume 1 x 1 x 1 units, containing vortex elements uniformly distributed in space, were distorted to a volume of 6 x 1 x 1/6 units. The triple $((\ell_1)_h, (\ell_2)_h, (\ell_3)_h)$ might therefore be considered as a measure of the orientation of the eddies in space. The triple could also be considered as a measure of the turbulent structure since it is obtained from the local intensity ratios $\overline{u_1^2}/\overline{q^2}$, $\overline{u_2^2}/\overline{q^2}$ and $\overline{u_3^2}/\overline{q^2}$ using the rapid distortion theory, Eqs. (67), (68) and (69) or more simply using Fig. 5.

We will discuss the turbulent structure shown in Fig. 16 in terms of the structural triple. The structure of the grid turbulence at the beginning of the distortion was (1.20, 1.20, 0.70). The eddies of the grid turbulence compared with isotropic turbulence, which has a structure

(1, 1, 1), were oriented more in a plane parallel to the grid. When turbulence is distorted, the rapid distortion theory for anisotropic turbulence, predicts a structure of (7.20, 1.20, 0.11) at the end of the distorting section. The actual turbulence at the end of the distorting section had an approximate structure (4.50, 2.46, 0.09). Apparently during distortion there was a tendency for the eddies of the actual turbulence to become oriented more in the plane normal to the minimum rate of strain than that predicted by the theory.

In the parallel section located after the distorting section there was a tendency for the turbulence to become more isotropic; this is shown by the approach of the local intensity ratios $\overline{u_1^2}/\overline{q^2}$, $\overline{u_2^2}/\overline{q^2}$ and $\overline{u_3^2}/\overline{q^2}$ towards equality. This tendency was greatest near the beginning of the parallel flow where the turbulence was highly anisotropic.

In order to compare the results obtained here with those of Townsend[65] and Maréchal[37] the structural measure $K = (\overline{u^2}_{max} - \overline{u^2}_{min})/(\overline{u^2}_{max} + \overline{u^2}_{min})$ was calculated for different strain ratios. The ducts used by Townsend, Maréchal and the present author were all of the same general shape and were designed to produce uniform plane strain of type $F = 0$; the rates of strain as measured by the parameter I_A were nearly the same in all ducts, .54, .66 and .32 respectively; the maximum strain ratios achieved in the three ducts were different, 4, 13.3 and 6 respectively.

Experimental values of the structural measure K, obtained by the present author, by Townsend[65] and by Maréchal[37] are plotted against strain ratio in Fig. 18. In obtaining the theoretical curve which is shown, the turbulence was assumed anisotropic at the beginning of the distortion to agree with the grid turbulence in the present experiments and the values of K were based on $(\ell_i)_e$.

As shown in Fig. 18 the experimental values of K, for strain ratios greater than 1.5, are less than the theoretical values and appear to fall on a curve which belongs to the same family as the theoretical curve. An empirical curve, $K = 0.63 \, K_t$ is shown. The subscript t indicates the theoretical value obtained from the rapid distortion theory. It appears that the experimental values agree closely with this curve up to the maximum strain ratio of 6 where an experimental value of $K \simeq 0.62$ was obtained.

It is interesting to compare the present results with the results of Maréchal[37] whose distorting section produced strain ratios up to 13.3. Two geometrically similar grids were used in his experiments. The turbulent structure as measured by K was approximately the same for both grids. Points from Maréchal's curve are shown in the main Figure and his Figure is also shown as an insert in Fig. 18. The results of Maréchal agree closely with those of the present author up to the strain ratios of 6, the highest value in

the author's tunnel. A maximum K value of 0.62 was achieved by Maréchal for a strain ratio near 8.7, beyond this strain ratio his K decreased slightly and at the end of his distorting section was approximately 0.60. The falling off of Maréchal's K values beyond the strain ratio of 8.7 may have been caused by flow conditions in the transition region near the end of the distorting duct. The falling off of Townsend's values of K may be attributed to the same cause, this is discussed below.

Agreement of the present results with those of Townsend is not as satisfactory, especially for strain ratios above 2.5. Townsend's curve appears to reach an asymptotic value near 0.42 after a strain ratio of 4, the maximum obtainable in his tunnel. This is considerably less than $K \simeq 0.55$ at strain ratio of 4 achieved by Maréchal and by the present author. This cannot be explained as the result of differences in the strain rate parameter; the value of I_A in Townsend's duct was 0.54 compared with the present value of 0.32, and might therefore be expected to give higher values of K which would be closer to those of the instantaneous distortion theory.

The falling off of Townsend's values for strain ratios near 4 may possibly be the result of the failure of the experimental duct to establish the hypothetical uniform straining throughout its length. Fig. 12 of the mean velocity in the present duct and the corresponding measure-

ments of Townsend and Maréchal show that near the entrance and the exit of the distorting section the longitudinal distortion differed considerably from the hypothetical uniform value achieved in the central region. In Townsend's duct uniformity was achieved for a range of strain ratios 1.5 to 3, in the present duct for strain ratios 1.5 to 4 and in Maréchal's duct for a range of strain ratios 1.5 to 8.7. Hence, Townsend's results, in particular, may have been influenced by the non-uniformity of the strain near the end of the distortion.

Figure 12 and the corresponding curves of Townsend and Maréchal also show that the strain was not instantaneously reduced to the hypothetical zero on entrance to the parallel duct. The present results show that the return towards isotropy took place only after the fluid had moved a short distance along the parallel duct corresponding approximately to the start of zero longitudinal strain.

In the parallel flow following the distortion, the turbulence studied here showed a marked tendency towards isotropy as shown in the approach of the structural measure K towards zero. The return to isotropy was most rapid for the highly anisotropic turbulence and slower as the trubulence approached the isotropic condition.

The failure in the present experiments for the turbulent structure to reach an equilibrium value and the rapid return to isotropy after distortion is important in

relation to Townsend's theory of free turbulence and will
be discussed more thoroughly later in the thesis.

The results of the experiments in the distorting
wind-tunnel, which are shown in Figs. 16, 17 and 18 and which
have just been discussed, were obtained using hot-wire
constants from pipe calibration. In order to show the
effects of determining the hot-wire constants from the
separate values of ϕ and c and k results using these
constants are shown in Figs. 19 and 20.

The variations in the local turbulent intensity
ratios are shown in Fig. 20. When compared with the cor-
responding values in Fig. 17, it can be seen that the cal-
culations based on ϕ , c and k decreased the isotropy of
the grid turbulence before distortion. When the turbulence
was distorted to strain ratios near 6, values of $\overline{u_3^2}/\overline{q^2}$
close to 0.55 were obtained, compared with values close to
0.52 shown in Fig. 17.

As already discussed in Sec. 2.4.1., the rapid
distortion theory shows that no one component of the tur-
bulence can contain more than 0.5 of the total turbulent
energy. Neglect of decay terms in the theory should not
effect this limiting energy ratio, because the rapid
distortion theory includes all types of eddy orientations.
Assuming this, the pipe calibration method of determining
the constants gave the more accurate turbulence measurements.
It should be noted that the method of determining the hot-

wire constants had no influence on the structural measure K for strain ratios greater than 2.

Spectra of the longitudinal component of the turbulence at different locations along the distorting duct were measured using a single normal hot-wire; these spectra are shown in Fig. 21. Spectra measurements at the same locations using X-wires are shown in Fig. 22. The spectra at corresponding locations obtained by the two methods are almost identical. To show this more clearly some of the spectra from Fig. 21 are replotted as solid points in Fig.22. In the present experiments it appears that errors introduced in the measurement of the one-dimensional spectra by the use of Disa X-wires are not sufficient to influence the discussion.

The low Reynolds number grid turbulence studied here cannot be expected to have an equilibrium range charac- terized by a spectrum curve of slope (-5/3). Comparison of the spectrum curve at the beginning of distortion with the line of slope (-5/3) in Fig. 21, shows that at high wave numbers there is no agreement.

Comparison of the measured spectra with spectra obtained for grid turbulence in uniform parallel flow (such as that obtained by Sato and reported by Hinze[24] and shown as an insert in Fig. 21) shows that the spectra of the distorted and undistorted turbulence behave in a similar manner. At increasing distances from the grid there is a tendency for

the spectrum curves in the high wave number range to be shifted in the direction of lower wave numbers. The reason for this is that the turbulence corresponding to high wave numbers decays at a faster rate than the turbulence of lower wave numbers.

The one-dimensional spectra of $\overline{u_1^2}$ and $\overline{u_3^2}$, the lateral components of turbulence, are shown in Figs. 23 and 24. The lateral spectra are similar to the longitudinal spectra shown in Fig. 21.

In order to detect small differences in the $\overline{u_1^2}$, $\overline{u_2^2}$ and $\overline{u_3^2}$ spectra at the end of the distorting section, these spectra were plotted in Fig. 25. The spectra of $\overline{u_2^2}$ and $\overline{u_3^2}$ the high energy components are approximately identical. The spectra of $\overline{u_1^2}$ the low energy component contains a relatively larger proportion of energy in the higher wave number range. It appears that the transfer of energy to the low energy component takes place mostly at the higher wave numbers. This is consistent with obser- vations in isotropic turbulence that energy transfer takes place from low to higher wave numbers.

4.2.2. Experimental Results using Grid B

For this experiment the mesh Reynolds number of the turbulence was increased by using the large mesh grid B in place of the geometrically similar small mesh grid A. It should be noted that changing the grid to one of a

different mesh size without changing its location with respect to the distorting section does not significantly change I_A the intensity parameter; also the other parameters ℓ_1 and F are not changed.

Grid B was located in the grid slot and, as before, measurements of u_1', u_2', u_3' and the longitudinal mean velocity $\bar{U}_2$ were taken along the center-line of the tunnel with the mean velocity near the grid steady at approximately 20 fps. During the time the measurements were being taken, periodic checks of the mean velocity and temperature at fixed reference points behind the grid showed that the mean velocity varied less than 0.5% and that the temperature remained within the range 80°F. to 82°F. The temperature at which the hot-wires were calibrated was $81.5 \pm 0.5^\circ$F.

Values of $\overline{u_i^2}/(\bar{U}_2)_c^2$ and $\overline{q^2}/(\bar{U}_2)_c^2$ are plotted versus dimensionless distance from the virtual origin in Fig. 26. When compared with Fig. 16 which contains the corresponding values for the small mesh grid A, it can be seen that the results for both grids are in approximate agreement, however, when using grid B the agreement between theoretical and experimental values of $\overline{q^2}/(\bar{U}_2)_c^2$ and $\overline{u_3^2}/(\bar{U}_2)_c^2$ is less satisfactory.

The local structural measures $\overline{u_i^2}/\overline{q^2}$ are plotted versus distance from the beginning of the distortion and strain ratio in Fig. 27. When compared with Fig. 17, which shows corresponding values for grid A, the results are

approximately identical. As before when compared with the
theoretical curves obtained for the initially anisotropic
grid turbulence, the values of $\overline{u_3^2}/\overline{q^2}$ agree closely with the
theoretical, while at the higher strain ratios the values of
$\overline{u_1^2}/\overline{q^2}$ are higher and the values of $\overline{u_3^2}/\overline{q^2}$ are lower than
the theoretical. In the parallel duct downstream from the
distortion the tendency for the turbulence to approach
isotropy is again apparent.

For comparison, values of the structural measure K
for grids A and B are shown in Fig. 28. Both grids gave
approximately the same values of K in both the distorting
and parallel sections of the duct except near the end of the
distorting section where lower values of K were obtained for
grid B. This may have been due to the length scales of the
turbulence becoming large in comparison with the width of
the tunnel in this region. The same reason may in part
explain the falling off of Townsend's K values and also
those of Maréchal near the end of their distorting sections.

It appears that the structure of turbulence developed
by lateral plane strain was not greatly affected by changing
the mesh Reynolds number. This is as expected because there
was no appreciable change in the important parameters F, I_A
and ℓ_1.

4.2.3. Experimental Results using Grid C

In order to determine the effect of grid geometry,
measurements were made in the distorting tunnel using the

diamond grid C. Two sets of measurements were made at two
steady mean velocities, and from the results the effect of
changing the grid Reynolds number by changing the mean
velocity was determined.

These experiments were actually the first performed
in the tunnel. The diamond shaped grid had a low solidity,
$\sigma = 0.37$, which could be expected to generate homogeneous
turbulence, however, the turbulence was of low relative
intensity and was difficult to measure accurately.

Grid C was placed in position in the grid slot of
the distorting tunnel, which had at this time a 4 ft.
parallel section behind the distorting section and not the
12 ft. length as shown in Fig. 10. Measurements of the
turbulence intensities u_1', u_2', u_3' and the mean velocity
$\bar{U}_2$ were taken along the center-line of the tunnel. Two
sets of readings were taken: one with mean velocity steady
at approximately 20 fps and the other at 40 fps. During
the time the measurements were being taken, periodic checks
of the mean velocity and temperature at fixed reference
points behind the grid showed that for each run the mean
velocity varied less than 0.5% and the temperature remained
within a 3°F. range.

For the mean velocity of 20 fps, the relative
intensities $\overline{u_1^2}/(\bar{U}_2)_c^2$ and $\overline{q^2}/(\bar{U}_2)_c^2$ are plotted versus
distance from the virtual origin as shown in Fig. 29. The
straight lines which were obtained experimentally for the

grid C turbulence in uniform flow are also shown for
comparison. The relative turbulent intensities behaved
similarly to those of the square grids A and B as shown in
Fig. 16 and Fig. 26 respectively, but the actual values are
lower because of the lower solidity of the daimond grid.
As in the case of the square grids the two opposing processes
of production and decay determine the behaviour of the
turbulence.

For comparison, curves of the component and total
turbulent intensities obtained from the rapid distortion
theory of the anisotropic grid turbulence with corrections
for decay are shown in Fig. 29. As before, the measured
values of $\overline{q^2}/(\overline{U}_2)_c{}^2$ and $\overline{u_3{}^2}/(\overline{U}_2)_c{}^2$ agree well with the
theoretical values throughout the distorting section. In
the case of $\overline{u_1{}^2}/(\overline{U}_2)_c{}^2$ and $\overline{u_2{}^2}/(\overline{U}_2)_c{}^2$ agreement is less
satisfactory at the higher strain ratios.

Comparing the relative turbulent intensities for the
diamond grid of 20 fps shown in Fig. 29, with the corres-
ponding intensities for the same grid at 40 fps shown in
Fig. 31, it can be seen that the plots are approximately
identical. In both cases there is a noticeable tendency
toward isotropy in the parallel flow after the distortion.
Small differences which are noticeable near the end of the
distorting section and in the adjoining parallel flow section
are probably due to difficulty in measuring accurately the
low turbulent intensities. During these readings the rms

meter values fluctuated about 5%; this accounts for the scatter in the plotted values.

The local turbulent intensity ratios for velocities 20 fps and 40 fps are shown in Fig. 30 and Fig. 32. The local turbulent intensities behaved similarly at both velocities.

The structural measure K for velocities 20 fps and 40 fps is shown in Fig. 33, together with the empirical curve $K = 0.63\ K_t$. The measured values of K again agree approximately with this curve which shows that the structure of turbulence was approximately independent of the grid geometry. It is also evident that changing Re_M by changing the mean-velocity did not change the turbulent structure.

4.3. Plane Strain (Longitudinal), Type Parameter $F = 0$

Longitudinal plane strains having type parameter $F = 0$ were produced in the two-dimensional contractions, duct no.2 and duct no. 3, with strain ratios ℓ_1 of 5.4 and 2.8 and strain rate parameters I_A of 0.97 and 0.32 respectively. Experiments were performed in these ducts to determine the effects of changing the strain rate parameter. Also, by comparing the results in the two-dimensional contractions with those in the distorting duct, the effects, if any, of changing direction of the mean flow relative to the strain could be determined.

4.3.1. Characteristics of the Two-Dimensional Contractions

Mean velocities along the center-line of the two-dimensional contractions (duct no. 2 and duct no. 3) were measured using separate total and static pressure probes. The resulting velocity distributions with the small square grid in position and mean velocities at the inlet of the contraction, steady at approximately 20 fps, are shown in Fig. 36. Except in the transition region near the entrance of the contraction, the experimental points fall approximately on straight lines which shows that the rates of strain were nearly uniform throughout both contractions.

With the grid removed from the tunnel the three components of the turbulence were measured at points on the center-line of the ducts. Corrections were made for instrument noise as described in Sec. 3.6. and the relative intensities $u'/\bar{U}$, $v'/\bar{U}$ and $w'/\bar{U}$ were calculated using $\bar{U}$ the local mean velocity at each point on the center-line. The background turbulence in duct no. 2 is shown in Fig. 37. At the entrance of the contraction the relative intensities were

$$u'/\bar{U} \simeq v'/\bar{U} \simeq 0.45 \times 10^{-2}, \quad w'/\bar{U} \simeq 0.30 \times 10^{-2}$$

the u' component remained approximately constant throughout the contraction. The v' and w' components decreased in the downstream direction and at the exit attained values of

$$v'/\bar{U} \simeq w'/\bar{U} \simeq 0.10 \times 10^{-2}$$

In comparison with the grid turbulence the background turbulence was high and it was necessary to correct the readings. It is interesting to note that the background turbulence during contraction behaved differently than the grid turbulence; when grid turbulence was distorted the component in the direction of the maximum rate of strain (ie., $u'/\bar{U}$) was decreased more than the lateral components as shown later in this thesis.

The spectra of the background turbulence in the blower wind-tunnel is shown in Fig. 38. However, 80% of the total energy of the background turbulence was below 20 cps which could not be analyzed by the spectrometer.

4.3.2. Experimental Results

With grid A in position, measurements of the turbulent components u'_1, u'_2, u'_3 and the longitudinal mean velocity $\bar{U}$ were made at points along the center-line of duct no. 2 and duct no. 3. During the measurement the mean velocity in the parallel section of the duct was steady at approximately 20 fps. Periodic checks of the mean velocity at fixed reference points behind the grid showed that during each run the mean velocity varied less than 0.5% and the temperature less than 6°F.

The turbulence readings were corrected for combined background turbulence and instrument noise by method I of Sec. 3.6. and values of the turbulent intensities $\overline{u_i^2}/(\bar{U}_1)_c^2$,

and $\overline{q^2}/(\overline{U}_1)_c^2$ were plotted against $(t - t_o)$ the time from the virtual origin; the plotted values for duct no. 2 and duct no. 3 are shown in Fig. 39 and Fig. 41 respectively. Straight lines are drawn in the figures which show the decay of the turbulence in uniform flow; also curves are shown which were obtained from the rapid distortion theory as outlined previously.

It can be seen from the figures that all the experimental values fall close to the theoretical curves, especially near the beginning of the contraction.

From Fig. 39 it can be seen that in duct no. 2 which had the higher contraction ratio the experimental values of $\overline{u_1^2}/(\overline{U}_1)_c^2$ were higher than the theoretical values near the end of the contraction. Apparently there was a transfer of energy to this component. Similar behaviour was not noticeable in duct no. 3 where the strain ratios were lower.

The experimental values of the local structural measures $\overline{u_i^2}/\overline{q^2}$ are plotted versus strain ratio for duct no. 2 and duct no. 3 in Fig. 40 and Fig. 42 respectively. Curves obtained for the instantaneous distortion of anisotropic grid turbulence are also shown for comparison. The measured values of $\overline{u_3^2}/\overline{q^2}$ agree closely with the theoretical values for duct no. 3, agreement is less satisfactory for duct no. 2. The experimental values of $\overline{u_2^2}/\overline{q^2}$ and $\overline{u_1^2}/\overline{q^2}$ in both ducts agree closely with the theoretical values near the beginning of the contraction, but near the end of the

contraction the experimental values of $\overline{u_1^2}/\overline{q^2}$ are higher, and the experimental values of $\overline{u_2^2}/\overline{q^2}$ are lower than the theoretical values, especially in duct no. 2 which had the higher contraction ratio.

The structural measure K versus strain ratio for the two contractions are shown in Fig. 43. A theoretical curve obtained by applying the instantaneous distortion theory to the anisotropic grid turbulence, is also shown. The experimental values of K agree remarkably well with the theoretical curve except in duct no. 2 for strain ratios $\ell_1 > 4$.

Comparing the values of K for duct no.2, $I_A = 0.97$, with those of duct no. 3, $I_A = 0.32$, it appears that slightly lower values were obtained in duct no. 3 which had the lower strain rate parameter, however, the possible error in the experimental values is such that no definite conclusions can be made regarding the effect of the strain rate parameter.

In order to check the results obtained in duct no.2, careful measurements were taken near the exit of the duct using the filter system and correcting for background turbulence by method II in Sec. 3.6. The values obtained are shown as solid points in Figs. 40, 41, and 43 and are in good agreement with the values obtained using method I to correct for background turbulence.

The one-dimensional spectra of the longitudinal

component of turbulence at different distances along duct no. 2 are shown in Fig. 44. The spectra appear to be closer to self-preserving than the equivalent $\overline{u_2^2}$ spectra in distorting duct no. 1 which is shown in Fig. 23.

4.4. Symmetrical Fluid Contraction, Strain Type Parameter F = -1/2

Symmetrical fluid contraction has a strain type parameter (F = -1/2); this is the minimum value of F. From the results of the instantaneous distortion theory applied to isotropic turbulence shown in Figs. 3, 4 and 5 it appears that the structure of turbulence produced by this type of strain is approximately the same as the structure produced by plane strain F = 0.

4.4.1. Characteristics, Equivalent Symmetrical Contraction

Mean velocities along the center-line of duct no. 4 (the equivalent symmetrical contraction) were measured using the separate total and static pressure probes. The resulting velocity distribution with grid A in position and mean velocity at the inlet of the contraction steady at approximately 20 fps is shown in Fig. 46. The experimental values fall close to a straight line which indicates that the rate of strain $\partial \overline{U}_1 / \partial x_1$ was uniform throughout the contraction.

With the grid removed from the tunnel, the three components of the turbulence were measured at points on the center-line of the duct. The values obtained after correcting

for instrument noise are shown in Fig. 47. The background turbulence was similar to that observed in the two-dimensional contraction. The longitudinal component remained fairly constant along the duct at values

$$u'/\bar{U} \simeq 4.5 \times 10^{-2}$$

The lateral components decreased from values

$$v'/\bar{U} \simeq w'/\bar{U} \simeq 4.5 \times 10^{-2}$$

at the entrance to values near 2.0×10^{-2} at the exit.

4.4.2. Experimental Results

With grid A in position the turbulence components u', v', w' and the longitudinal mean velocity $\bar{U}_1$ were measured at points along the center-line of the duct. During the measurements the mean velocity in the parallel section of duct was steady at approximately 20 fps. Periodic checks of the mean velocity and temperature at fixed points behind the grid showed that during the run the mean velocity varied less than 1.0% and the temperature less than $3^{\circ}F$.

After correcting the turbulence readings for combined background turbulence and instrument noise by method I of Sec. 3.6. the values of the intensities $\overline{u_i^2}/(\bar{U}_1)_c^2$ and $\overline{q^2}/(\bar{U}_1)_c^2$ were plotted versus the time from the virtual origin $(t - t_0)$ as shown in Fig. 48. Straight lines are shown in the figure to represent the decay of the grid

turbulence in the absence of strain and also curves are shown which were obtained from the rapid distortion theory by the method outlined previously.

The experimental values of $\overline{q^2}/(\overline{U}_1)_c^2$, $\overline{u_2^2}/(\overline{U}_1)_c^2$ and $\overline{u_3^2}/(\overline{U}_1)_c^2$ lie fairly close to the theoretical curves, especially for values of the strain ratio ℓ_1 from 1 to 2. For higher strain ratios the experimental values are slightly lower. The experimental values of $\overline{u_1^2}/(\overline{U}_1)_c^2$ also agree with the theoretical for strain ratios less than 2; for higher strain ratios the experimental values are considerably higher than the theoretical values. Again the disagreement between the experimental and theoretical values can be attributed to transfer of energy between the components of turbulence which is neglected in the theory.

From the minimum shown in the values of $\overline{q^2}/(\overline{U}_1)_c^2$, it appears that turbulence reached an energy equilibrium near a strain ratio of 2.5; here the energy produced by the mean strain acting on the turbulence was balanced by the loss of energy due to turbulent decay.

Experimental values of $\overline{u_i^2}/\overline{q^2}$ are plotted against strain ratio in Fig. 49. Theoretical curves assuming instantaneous distortion of the anisotropic grid turbulence are shown for comparison. At the beginning of distortion, up to strain ratio 2, agreement is good but there is less agreement at higher strain ratios. As already mentioned this was caused by the transfer of energy between components

which resulted in the turbulence becoming more isotropic.

Fig. 50 shows the experimental values of the structural parameter K and also a theoretical curve assuming rapid distortion of anisotropic grid turbulence. Again, agreement between experimental and theoretical values is good for low strain ratios, but the experimental values are lower than the theoretical for strain ratios above 2.

A value of $K = 0.76$ which was obtained from the experimental results of Uberoi[70] in a 4:1 symmetrical contraction (strain ratio $\ell_1 = 4$) is shown in Fig. 50. This value falls approximately on the theoretical curve. The value of the strain rate parameter I_A in Uberoi's duct was 5.0 compared with $I_A = 0.95$ in the duct used by the author. This may be the reason why Uberoi's value of K is closer to the theoretical. Other values of Uberoi ($K = 0.80$ for $\ell_1 = 9$ and $K = 0.75$ for $\ell_1 = 16$) would fall below the theoretical if Fig. 50 were extended to show higher strain ratios.

Accurate measurements were made using a filter system and correcting for background turbulence by method II of Sec. 3.6. These values are shown as solid points in Figs. 48, 49 and 50. As shown in Fig. 48 the values of the longitudinal component of turbulence $\overline{u_1^2}/(\overline{U}_1)_c^2$ are lower than the values obtained using method I. Differences due to the low u_1' component also appear in Fig. 49 and Fig. 50.

There are obvious inherent errors in both methods

of correcting for background turbulence which influence

mostly the low readings near the end of the duct and in

particular the measurements of the lowest component of the

turbulence. Measurements in duct no. 5, which are discussed

later, show that correction by method II in particular are

suspect.

The one-dimensional spectra of $\overline{u_1}^2$, $\overline{u_2}^2$ and $\overline{u_3}^2$

were measured at locations on the center-line of duct no. 4

at 0 in., 36 in. and 72 in. from the entrance to the con-

traction. The spectra of $\overline{u_1}^2$, the longitudinal component

of the turbulence, is shown in Fig. 51. The three spectra

are approximately identical.

The $\overline{u_2}^2$ spectra are shown in Fig. 52. The spectro-

meter readings for the $\overline{u_2}^2$ spectra were identical to those

for the $\overline{u_3}^2$ spectra which are not shown.

4.5. Symmetrical Fluid Diffusion, Strain Type Parameter F = 1.0

A section of duct in which the cross-sectional area

increases in the direction of the flow is referred to as a

diffuser. In a symmetrical diffuser the strain form para-

meter F is 1.0. Duct no. 5, which is shown schematically

in Fig. 53, is not a diffuser but a contraction, however,

the strain type parameter produced in this duct is identical

to that of a symmetrical diffuser and in this thesis is

referred to as an "equivalent symmetrical diffuser". This

type of duct was used to avoid the adverse pressure gradients

which exist in a real diffuser.

4.5.1. <u>Characteristics, Equivalent Symmetrical Diffuser</u>

The mean velocities along the center-line of the duct were measured by total and static pressure probes. The resulting velocity distribution with grid A located in the tunnel and mean velocity in the parallel section steady at approximately 20 fps is shown in Fig. 54. The experimental values fall close to a straight line showing that the rate of strain $\partial \bar{U}_1 / \partial x_1$ was close to uniform throughout the distorting section.

The grid was removed from the tunnel and the three components of the turbulence were measured at points along the center-line of the duct. The readings were corrected for instrument noise and the turbulence intensities were plotted as shown in Fig. 55. At the entrance of the distorting section the intensities were:

$$u'/\bar{U} \simeq v'/\bar{U} \simeq w'/\bar{U} \simeq 0.6 \times 10^{-2}$$

The longitudinal intensity of the turbulence $u'/\bar{U}$ remained approximately constant throughout the length of the duct, while the values of the lateral components $v'/\bar{U}$ and $w'/\bar{U}$ decreased and near the end of the duct were

$$v'/\bar{U} \simeq w'/\bar{U} \simeq 0.25 \times 10^{-2}$$

The background turbulence in duct no. 5 was higher than

that measured in ducts no. 2 and 4. The pressure loss in duct no. 5 was lower than in the other ducts and this required a closing of the control damper to keep the overall pressure drop in the wind-tunnel constant to maintain the same mean velocity. The more closed damper setting may have caused the higher turbulence.

4.5.2. Experimental Results

Grid A was positioned in the wind-tunnel and the turbulence components u_1', u_2', u_3' and the mean velocity U were measured at points along the center-line of the duct. The mean velocity in the parallel section of duct was steady at approximately 20 fps. Periodic readings of a pitot tube and thermometer at fixed locations behind the grid showed that during the run the mean velocity varied less than 1.0% and the temperature less than $3°F$.

The turbulence readings were corrected for combined background turbulence and instrument noise and the intensities $\overline{u_i^2}/(\overline{U}_1)_c^2$ and $\overline{q^2}/(\overline{U}_1)_c^2$ were plotted against time from the virtual origin $(t - t_0)$ as shown in Fig. 56. The straight lines show the experimentally determined decay of the grid turbulence in uniform flow. The theoretical curves were obtained from the instantaneous distortion theory as outlined earlier. It is seen that the experimental values of $\overline{q^2}/(\overline{U}_1)_c^2$, $\overline{u_3^2}/(\overline{U}_i)_c^2$ and $\overline{u_2^2}/(\overline{U}_1)_c^2$ agree approximately with the theory. Agreement between the $\overline{u_1^2}/(\overline{U}_1)_c^2$ component

is less satisfactory.   .

The experimental values of the local structure measure $\overline{u_i^2}/\overline{q^2}$ are plotted versus strain ratio in Fig. 57. Curves obtained for the instantaneous distortion of anisotropic grid turbulence are also shown. Agreement between the experimental and theoretical values of $\overline{u_3^2}/\overline{q^2}$ is good for all strain ratios. At the beginning of distortion there is fair agreement between the experimental and theoretical values of $\overline{u_1^2}/\overline{q^2}$ and $\overline{u_2^2}/\overline{q^2}$ up to strain ratio 1.5; at higher strain ratios agreement is less satisfactory.

The experimental values of structural measure K are shown in Fig. 58 and also the theoretical curve for the instantaneous distortion of anisotropic grid turbulence. The measured values of K are lower than the theoretical values. Approximate agreement is obtained if the experimental values are compared with the empirical curve, $K = 0.85\ K_t$.

Careful measurements were taken at three locations near the exit of the duct and corrected for background turbulence using method II outlined in Sec. 3.6. The obtained values are shown as solid points in Figs. 56, 57 and 58. In Fig. 57 the values are lower than the theoretical and in Fig. 58 the values of K are higher than the theoretical; one would not expect this and the experimental values corrected using method II are probably in error.

The spectra of the longitudinal component of the

turbulence measured on the center-line at 0 in., 36 in. and 72 in. from the entrance of the distorting section are shown in Fig. 59. The spectra appear to be close to self-preserving.

4.6. General Discussion of Results

In the thesis the experiments in the different ducts have been treated separately. In this section there is a general discussion of results and also discussion related to Townsend's models of free turbulence and to turbulent energy distribution and transfer between components.

4.6.1. Turbulent Structure Produced by Irrotational Strain

An attempt is made here to present more general results of the effect on grid turbulence of irrotational strain. In Fig. 60 the experimental values of $\overline{u_1^2}/\overline{q^2}$ are plotted against F, the solid points indicate values corrected by method II of Sec. 3.6. Values obtained by other researchers in corresponding ducts are also shown for comparison.

A higher degree of anisotropy was obtained by Uberoi[70] in both his symmetrical contractions. This can be explained as due to the high values of I_A in his contractions; $I_A = 5.0$ and $I_A = 13.35$ compared with $I_A = 0.95$ in the present contraction. It appears from this comparison that higher anisotropy is obtained for higher values of I_A or as the

time scale of the turbulence becomes larger in comparison with the time scale of distortion.

Comparison of the present results in the distorting duct with those in the two-dimensional contraction, which produces the same nominal type of strain, shows good agreement. The degree of anisotropy achieved in the distorting duct for strain ratio of 6:1 was higher than that achieved by Townsend for strain ratio of 4:1. The values of $\overline{u_i^2}/\overline{q^2}$ of Maréchal were not available for comparison.

Values in the equivalent symmetrical diffuser are shown. There are no known measurements by other workers available for comparison.

Because of the anisotropy of the initial grid turbulence, comparison with theoretical values is more meaningful when $\overline{u_i^2}/\overline{q^2}$ are plotted against the effective type of strain F_e as shown in Fig. 61. Unlike F the values of F_e vary throughout the ducts, and F_e (final value) indicates F_e at the position where the values of $\overline{u_i^2}/\overline{q^2}$ were measured. The values ℓ_1 and I_A were not the same in all the ducts; this must be kept in mind when comparing the experimental values with the theoretical values from the rapid distortion theory which for convenience is shown for strain $\ell_1 = .60$.

The theory indicates that close to 50% of the turbulent energy should be contained in the $\overline{u_3^2}$ component. Experimental values slightly higher than this were obtained,

the deviation was within the range of the errors of measurement. The energy contained in the lowest energy component was higher and the energy in the intermediate component was lower than the values obtained from the rapid distortion theory. This was explained previously as a tendency for turbulent eddies to be oriented more in a plane normal to the minimum rate of strain than that predicted by the theory.

The structural parameter K obtained in different experimental ducts is shown in Fig. 62. The broken line was drawn through the experimental points of the distorting duct and approximately through the experimental points of the remaining ducts. In the distorting duct the experimental values of the author are for $\ell_1 = 6$. Agreement with the K value of Maréchal for $\ell_1 = 13.3$ indicates that the structure of distorted turbulence is not highly sensitive to continued straining beyond strain ratios 6:1.

4.6.2. Townsend's Models of Free Turbulent Shear Flow

The conclusions reached by Townsend [65] in his experiments on homogeneous irrotational strain, namely: attainment of an equilibrium structure characterized by a structural measure of $K = 0.42$ independent of the rate of strain; and slow return to isotropy after strain, are not supported by the results of the present experiments. Here, in a distorting duct of geometry similar to that used by Townsend, K values near 0.62 were achieved (Fig. 18); there was no

evidence of the establishment of an equilibrium structure; and after distortion there was a strong tendency for the turbulence to approach isotropy. The results were independent of the mean velocity and the grid geometry (Fig. 33). The lower values of $K = 0.55$ obtained with grid B (Fig. 28) can be attributed to the fact that the mesh length and hence the turbulent scales were large in comparison with the duct size. The results in the distorting duct (excluding the return to isotropy after distortion) are supported by the results of Maréchal[37] in a similar duct and by the present measurements in the two-dimensional contraction (Fig. 43) which produced the same nominal type of strain. The failure of Townsend to obtain higher values of K (Fig. 18) can be attributed to the limitations of his apparatus, in particular to the low maximum strain ratio 4:1 available in his tunnel.

There is no evidence in the present experimental results to support the author's hypothesis that the rate of strain parameter I influences the structure of strained turbulence. This can be attributed to the fact that the values of I_A for any one type of strain did not vary sufficiently to produce detectable structural changes. In the two-dimensional contractions, ducts 2 and 3 where I_A values of 0.97 and 0.32 were obtained respectively (Fig. 43), a strain ratio of only 2.5 was achieved in duct no. 3. This prevented comparison at higher strain ratios where

structural changes would be more pronounced. When the present results in the distorting duct ($I_A = 0.32$) are compared with results in the corresponding duct of Maréchal ($I_A = 0.66$), as in Fig. 18, no difference in structure is apparent. Comparison of the present results in the symmetrical contraction ($I_A = 0.95$) with those of Uberoi[70] in the 9:1 contraction ($I_A = 13.35$) shows that Uberoi achieved a higher degree of anisotropy; his K values reached 0.80 compared with 0.62 in the present experiments. This difference in structure can be attributed to the higher value of I_A obtained by Uberoi.

The observation of Townsend[66] that the Reynolds stress structure of turbulence in plane strain resembles the structure from rapid finite distortion is supported by the results of the present experiments. This resemblence is apparent for all the different types of strain investigated, especially in the initial stages of distortion, as can be seen by comparing the experimental and theoretical values shown in Figs. 20, 27, 30, 32, 40, 42, 49 and 57. The present experiments support Townsend's contention that a process similar to that envisaged in the rapid distortion theory is present in free turbulent shear flows.

Taking into consideration the high degree of anisotropy found in the present distorting duct and the lack of evidence of an equilibrium structure (Tucker and Reynolds[69]), Townsend[67] has proposed a revised theory based on turbulent

structure produced by finite strain. On examining struc-
tures in different free turbulent shear flows, the mean
total strain or the effective strain was found by Townsend
to vary from flow to flow.

Townsend still contends that turbulent flows are
comparatively stable and that eddies lose energy and decay
without considerable change in their flow patterns. As
support for this observation Townsend [67] uses the experi-
mental results of Comte-Bellot and Corrsin [11] for decaying
grid turbulence in uniform flow. He found the index of
anisotropy $\overline{u_1^2}/\overline{u_2^2}$ - 1 decreased by a factor of two while
the energy decreased by a factor of twenty. In the present
experiments, in the parallel section following the dis-
torting duct where the turbulence was highly anisotropic,
it was found that $(\overline{u_{max}^2}/\overline{u_{min}^2})$-1 decreased by a factor of
2.64 while the energy $\overline{q^2}$ decreased by a factor of only 1.25.
These values were obtained for grid A, $\overline{U}_c$ = 20 fps, using
measured values at 12 in. and 44 in. from the entrance of
the parallel section as shown in Fig. 18. It appears that
for highly anisotropic turbulence the tendency towards
isotropy is much greater than for the less anisotropic grid
turbulence. In ordinary shear flows, where comparatively
high anisotropy exists, the structure of the turbulence may
not be as stable and permanent as suggested by Townsend.

Additional evidence of the strong tendency towards
isotropy is the fact that the high anisotropy predicted by

the rapid distortion theory was not achieved. For example, in the distorting duct, the anisotropy measure K attained a value of 0.62 rather than the value of 0.94 predicted by the theory. This can be attributed to the rapid rate at which eddies depart from the alignment produced by strain.

4.6.3. <u>Energy Distribution and Transfer between Components</u>

It is usually believed that pressure fluctuations tend to transfer turbulent energy from the more energetic to the less energetic components (see, for example, Batchelor[4] and Hinze[24]). The viscous forces both dissipate and transport energy, Comte-Bellot and Corrsin[11] speculate that dissipation destroys component energy at a rate proportional to that energy and that the transport of energy by viscosity is negligible compared with the turbulent transport.

As an hypothesis for the transfer of turbulent energy between components Rotta[55] proposed a linear dependence on the component energy deficiency below the mean energy level, in effect

$$\frac{1}{\rho \epsilon} \, p \, \overline{\frac{du_1}{dx_1}} = -C(\overline{u_1^2} - 1/3\overline{q^2})/1/3\overline{q^2}$$

and two similar equations for u_2 and u_3, C is a constant. Some support for Rotta's hypothesis is given by the results of Champagne, Harris and Corrsin[9] and by Lumley[34].

In the present experiments Rotta's hypothesis is best tested in a qualitative way using the results in the distorting wind-tunnel where the three components of the turbulence attained widely differing vlues as shown in Fig. 17. If Rotta's hypothesis were correct then one would suspect that applying a correction to the instantaneous distortion structure would lead to values in close agreement with the experimental values. Examination of Fig. 17 shows that, near the end of the distorting duct, approximately equal values of $\overline{u_2^2}/\overline{q^2}$ and $\overline{u_3^2}/\overline{q^2}$ predicted by the theory were not obtained in the experiments.

In fact, the conception of energy transfer between components from high to low energy components may be misleading. The success of the rapid distortion theory in predicting the development of the component energies in the initial stages of distortion would lead one to believe that the arrangement of the eddies which comprise the turbulence is important in determining the structure. In establishing a physical model to explain the deviation from the rapid distortion structure for high strain ratios, one may speculate that reorientation of eddies and spreading of vortex elements from elliptical towards circular forms may be responsible for the actual observed structure. The Reynolds stress structure supports the speculation that eddies tend to become oriented in a plane normal to the minimum rate of strain.

CHAPTER 5

CONCLUSIONS

The results of the present experiments on homogeneous plane strain lead to significantly different conclusions than those of Townsend[65] in his corresponding experiments. Extending the strain ratios to 6:1, from the 4:1 of Townsend, showed that the Reynolds stress structure of turbulence continued to develop throughout the distorting duct and a high degree of anisotropy was achieved; the anisotropy measure K attained values near .62 compared with .42 of Townsend. Results similar to those of the author were also obtained by Marechal.[37] The present experiments fail to support Townsend's conclusions regarding the establishment of an equilibrium structure in his experiments and consequently fail to support Townsend's contention of the establishment of an equilibrium structure in ordinary shear flows.

Townsend also claimed that the equilibrium structure was independent of the rate of strain. Significant in this connection is the high degree of anisotropy, $K = 0.82$, achieved by Uberoi[70] in a symmetrical contraction with the rate of strain parameter $I = 13.6$. In the equivalent experiments here with $I = .92$ a K value of only .62 was achieved.

It appears that the turbulent structure depends on the rate of strain or more exactly on the rate of strain parameter I, and implies that an equilibrium structure can only be obtained if I is constant:- a condition which is not satisfied (as shown by Lumley[34]) in homogeneous shear flows.

The results of the present experiments also differed significantly from those of Townsend in that here the strained turbulence rapidly became less anisotropic when the straining ceased. The index of anisotropy $\overline{u_1^2}/\overline{u_2^2} - 1$ decreased by a factor of 2.64 while the energy decreased by a factor of only 1.25. This does not support Townsend's [67] contention that turbulent flows are comparatively stable and that eddies lose energy in decay without considerable change in their flow patterns.

In relation to the rapid distortion theory, it was found that development of the total turbulent energy for all types of strain was predicted quite accurately by applying a simple correction to allow for decay. In the correction it was assumed that the initial rate of decay of $\overline{q^2}$ remained unchanged throughout the distortion and that the change in $\overline{q^2}$ due to strain was the same as for initially isotropic turbulence.

The turbulent structure in the initial stages of distortion agreed well with that predicted by the rapid distortion theory applied to anisotropic turbulence. As straining progressed in the experiments on plane strain and

symmetrical contraction half the total turbulent energy was
contained in a single component in agreement with the theory
but the distribution in the remaining components was more
even than indicated by the theory.

No support was found in the present experiments for
Rotta's[55] hypothesis that the rate at which energy is
transferred to a component depends on the energy deficit
in that component below the mean energy level.

REFERENCES

1. Batchelor, G.K. and Townsend, A.A.
    Decay of Vorticity in Isotropic Turbulence; Proceedings Royal Society, London, 190A, pp. 534-550 (1947)

2. Batchelor, G.K. and Townsend, A.A.
    Decay of Isotropic Turbulence in the Initial Period; Proceedings Royal Society, London, 193A, pp. 539-558 (1948)

3. Batchelor, G.K.
    Note on Free Turbulent Flows, with Special Reference to the Two-Dimensional Wake; Journal of the Aeronautical Science, Vol. 17, pp. 441-445 (1950)

4. Batchelor, G.K.
    The Theory of Homogeneous Turbulence; Cambridge Univ. Press (1953)

5. Batchelor, G.K. and Proudman, I.
    The Effect of Rapid Distortion of a Fluid in Turbulent Motion; Quarterly Journal of Mechanics and Applied Mathematics, Vol. 7, pp. 83-108 (1954)

6. Batchelor, G.K.
    The Theory of Homogeneous Turbulence; Cambridge University Press (1960)

7. Bradshaw, P., Ferris, D.H. and Atwell, N.P.
    Calculations of the Boundary Layer Development using the Turbulent Kinetic Energy Equation; Journal of Fluid Mechanics, Vol. 28, pp. 593-616 (1967)

8. Champagne, F.H.
    Turbulence Measurements with Inclined Hot-Wires; Boeing Scientific Research Laboratories Document D1-82-0491 (1965)

9. Champagne, F.H., Harris, V.G. and Corrsin, S.
    Experiments on Nearly Homogeneous Turbulent Shear Flow; Journal of Fluid Mechanics, Vol. 41, pp. 81-139 (1970)

10. Collis, D.C. and Williams, M.J. — Two Dimensional Convection from Heated Wires at Low Reynolds Numbers; Journal of Fluid Mechanics, Vol. 6, pp. 357-384 (1959)

11. Comte-Bellot, G.and Corrsin, S. — The Use of a Contraction to Improve the Isotropy of Grid Generated Turbulence; Journal of Fluid Mechanics, Vol. 25, pp. 657-682 (1966)

12. Corrsin, S. — Decay of Turbulence behind Three Similar Grids, Aeronautical Engineering Thesis, California Institute of Technology (1942)

13. Davies, P.O.A.L. and Fisher, M.J. — Heat Transfer from Electrically Heated Cylinders; Proceedings Royal Society, London, 280A, pp. 486-527 (1964)

14. Deissler, R.G. — Effects of Inhomogeneity and of Shear Flow in Weak Turbulent Fields; Physics of Fluids, Vol.4, pp. 1187-1198 (1961)

15. Deissler, R.G. — Weak Locally Homogeneous Turbulence in Idealized Flow through a Cone; NASA Technical Note D-3613 (1966)

16. Dryden, H.L. and Schubauer, G.B. — The Use of Damping Screens for the Reduction of Wind-Tunnel Turbulence; Journal of Aeronautical Sciences, Vol. 14, No. 4, pp. 221-228 (1947)

17. Fox, J. — Velocity Correlations in Weak Turbulent Shear Flows; Physics of Fluids, Vol. 7, pp. 562-564 (1964)

18. Frost, V.A. — Rapid Homogeneous Deformation of Turbulence in a Gas; Doklady Akademii Nauk, Vol. 133, No. 4, pp. 773-776 (1960)

19. Gartshore, I.S. — The Streamwise Development of Two-Dimensional Wall Jets and Other Two-Dimensional Shear Flows; Ph.D. Thesis, McGill University (1965)

20. Grant, H.L. and Nisbet, I.C.T. The Inhomogeneity of Grid Turbulence; Journal of Fluid Mechanics, Vol. 2, pp. 163-172 (1957)

21. Grant, H.L. The Large Eddies of Turbulent Motion; Journal of Fluid Mechanics, Vol. 4, pp. 149-191 (1958)

22. Guitton, D.E. and Patel, R.P. An Experimental Study of the Thermal Wake Interference between closely Spaced Wires of a X-Type Hot-Wire Probe; M.E. Res. Lab., McGill Univ. Report No.69-7 (1969)

23. Heisenberg, W. On the Theory of Statistical and Isotropic Turbulence; Proceedings of the Royal Society, London, Vol. A195, pp. 402-406 (1948)

24. Hinze, J.O. Turbulence: an Introduction to its Mechanism and Theory; McGraw Hill Book Co. Inc. (1959)

25. Hsu, S.T. Engineering Heat Transfer; D.Van Nostrand Company (1963)

26. Jahnke, E. and Emde, F. Tables of Functions; Fourth Ed., Dover Publications, New York (1945)

27. Jerome, F.E. and Burling, R.W. Communication to Disa (Dansk Industri Syndikat A/S, Herlev, Denmark) (May 1969)

28. Keffer, J.F. The Uniform Distortion of a Turbulent Wake; Journal of Fluid Mechanics, Vol. 22, pp. 135-159 (1965)

29. Kjellström, B. and Hedberg, S. Calibration of Disa Hot-Wire Anemometer and Measurements in a Circular Channel for Confirmation of the Calibration; Disa Information, No. 9 (1970)

30. King, L.V. On the Convection of Heat from Small Cylinders in a Stream of Fluid. Determination of Convection Constants of Small Platinum Wires with Application to Hot-Wire Anemomitry; Philosophical Transactions, Royal Society, London, A214, pp.373-432 (1914)

31. Kolmogoroff, A.N.   The Local Structure of Turbulence
                          in Incompressible Viscous Fluids
                          for Very Large Reynolds Numbers;
                          Comptes Rendus (Doklady) de
                          l'Academie des Sciences de
                          l'U.R.S.S. 30, pp. 301-305 (1941)

32. Lamb, H.   Hydrodynamics, Sixth Edition,
                          Cambridge University Press(1937)

33. Laufer, J.   The Structure of Turbulence in
                          fully Developed Pipe Flow; NACA
                          Report 1174 (1954)

34. Lumley, J.L.   Towards a Turbulent Constitutive
                          Relation; Journal of Fluid Mech-
                          anics, Vol.41, pp. 413-434 (1970)

35. MacPhail, D.C.   Turbulence Changes in Contracting
                          and Distorted Passages; Royal
                          Aircraft Establishment, Aero
                          Report 1928 (1944)

36. Maréchal, J.   Dispositif Experimental pour
                          l'Etude de la Deformation Plane
                          de la Turbulence Homogene; Comptes
                          Rendus de l'Académie des Sciences,
                          Paris, 265A, pp. 69-71 (1967)

37. Maréchal, J.   Anisotropic d'une Turbulence de
                          Grille Deformee par un Champ de
                          Vitesse Moyenne Homogene; Comptes
                          Rendus de l'Académie des Sciences,
                          Paris, 478A, pp. 478-480 (1967)

38. Maréchal, J.   Sur quelques Longueurs de Cor-
                          rolation Longitudinales dans une
                          Turbulence de Grille Soumise à
                          une Deformation Plane; Comptes
                          Rendus l'Académie des Sciences,
                          Paris, 267A, pp. 656-659 (1968)

39. McAdams, W.H.   Heat Transmission, Third Edition,
                          McGraw-Hill Book Co. Inc. (1954)

40. Moffatt, H.K.   The Interaction of Turbulence
                          with Rapid Uniform Shear; SUDAE
                          Rep. No. 242, Stanford University
                          (1965)

41. Newman, B.G. and Leary, B.G.

The Measurement of the Reynolds Stresses in a Circular Pipe as a Means of Testing a Hot-Wire Anemometer; Aeronautical Research Laboratories, Report A72, Australia (1950)

42. Newman, B.G.

Personal Communication (June, July 1969)

43. Newman, B.G.

The Growth of Self-Preserving Turbulent Jets and Wakes; M.E. Res. Lab., McGill University, Report No. 68-10 (1968)

44. Obukoff, A.M.

On the Distribution of Energy in the Spectrum of Turbulent Flow; Comptes Rendus de l'Academie des Sciences de l'U.R.S.S. 32, p. 19 (1941)

45. Patel, R.P.

Measurement of the Reynolds Stresses in a Circular Pipe as a Means of Testing a Disa Constant Temperature Hot-Wire Anemometer; M.E. Res. Lab., McGill University, Tech. Note 63-6 (1963)

46. Patel, R.P.

Reynolds Stresses in Fully Developed Turbulent Flow down a Circular Pipe; M.E. Res. Lab., McGill University, Report No. 68-7 (1968)

47. Pearson, J.R.A.

The Effect of Uniform Distortion on Weak Homogeneous Turbulence; Journal of Fluid Mechanics, Vol. 5, pp. 274-288 (1959)

48. Prandtl, L.

Bericht uber Untersuchungen zer ausgebildeten Turbulenz; Zeitshlift für Angewandte Mathematik und Mechanik, 5, pp. 136-139 (1925)

49. Prandtl, L.

Attaining a Steady Air Stream in Wind Tunnels; NACA TM 726 (1933)

50. Reynolds, A.J.

Observations on Distorted Turbulent Wakes; Journal of Fluid Mechanics, Vol. 13, pp. 333-335 (1962)

51. Reynolds, A.J.   Personal Communication
                            (February, 1967)

52. Reynolds, O.   On the Dynamical Theory of
                            Incompressible Viscous Fluids and
                            the Determination of the Criterion;
                            Proceedings Royal Society, London,
                            56, pp. 40-45 (1894)

53. Ribner, H.S. and   Spectrum of Turbulence in a
    Tucker, M.   Contracting Stream; NACA Report
                            No. 1113 (1953)

54. Rose, W.G.   Results of an Attempt to Generate
                            a Homogeneous Turbulent Shear
                            Flow; Journal of Fluid Mechanics,
                            Vol. 25, pp. 97-120 (1967)

55. Rotta, J.C.   Statistiche Theorie Nichthomogener
                            Turbulenz; Zeitschrift für Physik,
                            Bd. 129, s. 547-572 (I), Bd. 131
                            s. 51-57 (II) (1951)

56. Schlichting, H.   Boundary Layer Theory; Pergamon
                            Press Ltd. (1955)

57. Shamroth, S.J. and   The Development of the Reynolds
    Elrod, H.G. (Jr.)   Stress Tensor in a Turbulent
                            Shear Flow; ASME Paper No.
                            70-FE-2 (1970)

58. Taylor, G.I.   Eddy Motion in The Atmosphere;
                            Philosophical Transactions,
                            215A, pp. 1-26 (1915)

59. Taylor, G.I.   Diffusion by Continuous Movements;
                            Proceedings of the London Mathe-
                            matical Society, Ser. 2, Vol. 20,
                            pp. 211-212 (1921)

60. Taylor, G.I.   The Transport of Vorticity and
                            Heat through Fluids in Turbulent
                            Motion; Proceedings Royal Society,
                            London, 135A, pp. 685-702 (1932)

61. Taylor, G.I.   Statistical Theory of Turbulence,
                            Parts I-IV; Proceedings of the
                            Royal Society A151, pp. 421-478
                            (1935)

62. Taylor, G.I.　　Turbulence in a Contracting Stream; Zeitschriift für Angewandte Mathematik und Mechanik; Band 15 Heft 1, pp. 91-96 (1935)

63. Taylor, G.I.　　The Spectrum of Turbulence; Proceedings Royal Society, London, 1964A, pp. 476-490 (1938)

64. Townsend, A.A.　　On the Fine Scale Structure of Turbulence; Proceedings of the Royal Society, London, Vol. A208, pp. 534-542 (1951)

65. Townsend, A.A.　　The Uniform Distortion of Homogeneous Turbulence; Quarterly Journal of Mechanics and Applied Mathematics, Vol. 7, pp. 104-127 (1954)

66. Townsend, A.A.　　The Structure of Turbulent Shear Flow; Cambridge University Press (1956)

67. Townsend, A.A.　　Entrainment and the Structure of Turbulent Flow; Journal of Fluid Mechanics, Vol. 41, pp. 13-46 (1970)

68. Tucker, H.J.　　Description and Calibration of the McGill Distorting Tunnel; M.E. Res. Lab., McGill University, Tech. Note 66-4 (1966)

69. Tucker, H.J. and Reynolds, A.J.　　The Distortion of Turbulence by Irrotational Plane Strain; Journal of Fluid Mechanics, Vol. 32, pp. 657-673 (1968)

70. Uberoi, M.S.　　Effect of Wind Tunnel Contraction on Free Stream Turbulence; Journal of Aeronautical Sciences, Vol. 23, pp. 754-764 (1956)

71. Uberoi, M.S.　　Equipartition of Energy and Local Isotropy in Turbulent Flows; Journal of Applied Physics, Vol. 28, pp. 1165-1170 (1957)

72. Uberoi, M.S.　　Energy Transfer in Isotropic Turbulence; The Physics of Fluids, Vol. 6, pp. 1048-1056 (1963)

73. Uberoi, M.S. and Wallis, S.

Small Axisymmetric Contraction of Grid Turbulence; Journal of Fluid Mechanics, Vol. 24, pp. 539-543 (1966)

74. Uberoi, M.S. and Wallis, S.

Effect of Grid Geometry on Turbulence Decay; The Physics of Fluids, Vol. 10, p. 1216 (1967)

75. Webster, C.A.G.

A Note on the Sensitivity of Yaw of a Hot-Wire Anemometer; Journal of Fluid Mechanics, Vol. 13, pp. 307-312 (1962)

76. Wygnanski, I.and Gartshore, I.S.

General Description and Calibration of the McGill 17 in. x 30 in. Blower Cascade Wind Tunnel; M.E. Res. Lab., McGill University, Technical Note 63-7 (1963)

APPENDIX A

CALCULATION OF THE STRAIN RATE PARAMETER I

A.1. Time Scale of Grid Turbulence

The results of the present experiments on grid turbulence in uniform flow show that the decay of the total energy of turbulence can be represented by the empirical equation

$$\frac{\bar{U}^2}{\overline{q^2}} = A\left(\frac{x}{M} - \frac{x_o}{M}\right)^p \qquad (A.1)$$

For a particular grid, A and p are constants. Rewriting Eq. (A.1) we obtain

$$\overline{q^2} = \frac{\bar{U}^2 M^p}{A}(x - x_o)^{-p} \qquad (A.2)$$

The derivative with respect to time is

$$\frac{d\overline{q^2}}{dt} = \bar{U}\frac{d\overline{q^2}}{dx} = \frac{-p\bar{U}^3 M^p}{A}(x - x_o)^{-(p+1)} \qquad (A.3)$$

The characteristic time of the grid turbulence defined by $t_e = -\overline{q^2}/(d\overline{q^2}/dt)$ is, from Eqs. (A.2) and (A.3),

$$t_e = \frac{x - x_o}{p\,\bar{U}} \qquad (A.5)$$

The time scale of the grid turbulence varies directly as

distance from the virtual origin but by definition here is taken at the beginning of the distortion where x = 0; then

$$t_e = -x_o/(p\,\bar{U}) \qquad\qquad (A.6)$$

It is interesting to note that the time scale of grid turbulence does not depend on the mesh length M.

A.2. Rate of Strain Parameter I, Distorting Duct

Since $x_1/(x_1)_A = \ell_1$ and $\alpha = \partial\bar{U}_1/\partial x_1$, then Eq. (26) for the distorting duct becomes

$$\ell_1 = e^{\dfrac{x_2}{(x_2)_A}\dfrac{\partial\bar{U}_1}{\partial x_1}} \qquad\qquad (A.7)$$

$$\ln \ell_1 = \frac{x_2}{(x_2)_A}\,\frac{\partial\bar{U}_1}{\partial x_1} \qquad\qquad (A.8)$$

The characteristic time of the rate of strain is

$$t_s = \frac{1}{\partial\bar{U}_1/\partial x_1} = \frac{x_2}{(\bar{U}_2)_A \ln\ell_1} \qquad\qquad (A.9)$$

x_2 and ℓ_1 are corresponding values at any point along the distortion. Using x, y, z coordinates in Eq. (A.9) for compatability with Eq. (A.6), then the rate of strain parameter is

$$I = \frac{t_e}{t_s} = -\frac{x_o\,\ln\ell_1}{px} \qquad\qquad (A.10)$$

The rate of strain parameter depends on the duct geometry; it also depends slightly on grid geometry, mainly because of change in the location of the virtual origin; it does not depend on mean velocity.

A.3   Rate of Strain Parameter I, Remaining Ducts

The rate of strain parameter in each of the remaining ducts (two-dimensional contractions, the equivalent symmetrical contraction and the equivalent symmetrical diffuser) may be obtained from the measured longitudinal mean velocity profile which is approximately linear

$$\frac{\partial \bar{U}}{\partial x} = \frac{\bar{U} - \bar{U}_A}{x} \tag{A.11}$$

$$t_s = \frac{1}{\partial \bar{U}/\partial x} = \frac{x}{\bar{U} - \bar{U}_A} \tag{A.12}$$

Since $\bar{U}/\bar{U}_A = \ell_1$ the rate of strain parameter

$$I = \frac{t_e}{t_s} = \frac{x_0(\ell_1 - 1)}{px} \tag{A.13}$$

Again the rate of strain parameter depends on the duct geometry, only slightly on the grid geometry and is independent of the mean velocity.

APPENDIX B

TABLE OF CONTENTS

(Turbulence Measurements Using Non-Linearized Constant Temperature Hot-Wire Anemometer)

NOMENCLATURE

APPENDIX B

A   coefficient in hot-wire equation

a   cross-sectional area of hot-wire

B   coefficient in hot-wire equation

C   constant; C_1, constant in Hilperts equation; C_2, C_3, constants in hot-wire conduction equation.

c   exponent in hot-wire equation

d   diameter of hot-wire

E   voltage across the hot-wire; $\bar{E}$, time-mean value; e, turbulent fluctuation of the voltage; e_I, e_{II}, e_{III} values at orientation I, ll, III of hot-wire to the mean flow.

Gr   Grashof number

h   coefficient of heat transfer between fluid and surface

I   electric heating current; $\bar{I}$, time-mean value; i, turbulent fluctuation of current.

k   coefficient; characteristic of the cooling by the velocity component along the hot-wire.

k_w,k_f thermal conductivity; k_w, of hot-wire; k_f, at mean film temperature.

ℓ length of the hot-wire, ft.

n   sensitivity of the hot-wire; n_I, n_{II}, n_{III}, sensitivity at orientations I, II, and III of the hot-wire to the mean flow.

Pr   Prandtl number

148

q   rate of heat transfer; q_c, by forced convection; q_k, by conduction; q_r, by radiation; q_t by combined conduction, convection and radiation.

R   inside radius of pipe

r   radial distance from pipe center-line

Re   Reynolds number, dimensionless.

R_w electric resistance of hot-wire; $\bar{R}_w$, time-mean value; R_0, at reference temperature; R_a, at air temperature; r_w, turbulent fluctuation.

s_1, s_2 hot-wire orientation constants

T   absolute temperature, ^oR; T_w, of the hot-wire; T_a, of the air.

t   temperature, ^oF; t_w, of the hot-wire; t_{wm}, mean temperature of hot-wire; t_a, of the air.

U   Eulerian velocity; $\bar{U}$, time-mean value; $u' = \sqrt{\overline{u^2}}$, root-mean-square turbulent velocity component; subscripts 1, 2, 3, i, j, k refer to Cartesian coordinates; U_N, U_T, the velocity components normal and tangential to the hot-wire respectively; U_E, the effective velocity in cooling the hot-wire; $U_\tau = \frac{\tau_0}{\rho}$, friction velocity.

x_i Eulerian Cartesian coordinates

y   distance from pipe wall, $y = (R-r)$

Greek Letters

α temperature coefficient of electrical resistance

ϵ_w emissivity of hot-wire

θ $(t_w - t_a)$, ^oF.

ν kinematic viscosity; ν_f at mean film temperature.

π 3.1416

ρ local electrical resistance of the hot-wire; ρ_0, at reference temperature.

ρf fluid density

σ Stefan-Boltzman constant

ϕ angle between the hot-wire and the mean flow direction

γ shear stress; γ_0, at wall.

APPENDIX B

TURBULENCE MEASUREMENTS USING NON-LINEARIZED CONSTANT TEMPERATURE HOT-WIRE ANEMOMETER

Some of the fundamentals of hot-wire anemometry are considered here and equations are developed for use in determining the turbulence intensities and shear stresses, taking into account the cooling effect of the component of the velocity parallel to the wire, and for arbitrary exponent in the cooling law. The experimental procedures for obtaining the constants in the equations are given.

B.1. Heat Loss from Hot-Wires

The detecting element of a hot-wire anemometer is a very fine short metal wire, which is heated by an electric current. Under conditions of thermal equilibrium the heat generated by the electric current is equal to the heat transferred from the wire by the combined effects of free convection, forced convection, conduction to the supports, and radiation. The total heat loss may then be determined from the power input to the wire and is given by the equation

$$q_t = 3.413 \ I^2 R_w \qquad \text{(B.1)}$$

The constant 3.413 is a conversion factor to change $I^2 R_w$

151

watts to Btu/hr.

B.1.1. <u>Radiation</u>

For wire sizes and operating temperatures generally used, the heat loss due to radiation is negligible. In the experiments reported here a tungsten wire of nominal size 0.005 mm diameter, 1.0 mm long (1.9685 x 10^{-4} in. diameter, 3.937 x 10^{-2} in. long) was operated at a mean temperature near 400°F. in ambient air near 80°F. The heat loss by radiation is estimated using the mean wire temperature and the emissivity of tungsten, $\epsilon_w = 0.05$, in the equation

$$q_r = \sigma \epsilon_w \pi d \ell (T_w^4 - T_a^4) \tag{B.2}$$

This equation is equivalent to that given by McAdams[39]. The overall exchange factor for a small body in a large enclosure is approximately equal to ϵ_w the emissivity of the small body. The estimated radiation heat loss from the wire is 2.13 x 10^{-7} Btu/hr. This is negligible compared with the minimum total heat loss from the wire, $q_t = 0.109$ Btu/hr, which occurred at a velocity of approximately 20 fps, the lowest in the experiments. The total heat loss was obtained using experimental values of I and R_w in Eq. (B.1).

B.1.2. <u>Natural Convection</u>

Under ordinary operating conditions and at reasonably high velocities, the influence of natural convection on the

heat loss from the wire is also negligible. Natural convection heat loss depends mainly on the value of the Grashof number Gr, while the forced convection effects depend on the Reynolds' number Re. According to Collis and Williams,[10] the natural convection effects are important only at very low velocities and are negligible when

$$Re > Gr^{1/3} \qquad\qquad (B.3)$$

The property values are determined at the ambient temperature. This is in approximate agreement with the experimental conclusions of Van der Heggs Zijnen (reported by Hinze[24]) who found that natural convection effects may be neglected, when

$$Re > 0.5; \qquad Gr\ Pr < 10^{-4}$$

with the properties also evaluated at the ambient temperature. In the present experiments, with the mean velocities generally greater than 20 fps and the ambient temperature near 80°F,

$$Re \simeq 1.94, \qquad Gr \simeq 1.19 \times 10^{-6}, \qquad Pr \simeq 0.69$$

These values are well within the range recommended above, where the natural convection effects may be neglected.

B.1.3. <u>Forced Convection</u>

There have been many experimental studies of forced convection heat transfer from heated cylinders placed normal

to the flow. The early experimental results of Hilpert obtained in air are widely quoted in the literature, and are given by McAdams.[39] The experimental results are expressed in the following form,

$$Nu = C_1 Re^c \qquad\qquad (B.4)$$

The original results of Hilpert were expressed using integrated mean property values (see comments by Hsu[25] and Collis and Williams[10]). In the equation, the values of c and C_1 depend on the value of the Reynolds' number; as the Reynolds' number increases the exponent c increases and the coefficient C_1 decreases.

B.1.4. Wire Conduction and Temperature Distribution

Under operating conditions heat is conducted along the wire to the supports. This results in a non-uniform temperature distribution, with the wire being cooler near the supports. A simple equation which represents approximately the temperature distribution of the wire, may be obtained if the following assumptions are made: (1) the radial temperature gradients in the wire are negligible (2) the electrical resistance of the wire is a linear function of the wire temperature, ie.,

$$\rho(t) = \rho_0(1 + \lambda t_w) \qquad\qquad (B.5)$$

and (3) the film coefficient h is a function of the

velocity but not of the temperature difference $(t_w - t_a)$.
For steady state conditions these assumptions lead to the
following linear differential equation,

$$d^2\theta/dx^2 + C_2\theta + C_3 = 0 \tag{B.6}$$

where

$$\theta = t_w - t_a$$

$$C_2 = \frac{3.413\ I^2\ \rho_0\alpha}{k_w a^2} - \frac{\pi dh}{k_w a}$$

$$C_3 = \frac{3.413\ I^2\ \rho_0}{k_w a^2}$$

If the origin is taken at the center of the wire, and it is
assumed that the temperature distribution of the wire is
symmetrical and the temperature of the supports remains at
the ambient temperature, then the following boundary
conditions apply:

$$\frac{d\theta}{dx} = 0 \quad \text{at} \quad x = 0$$

$$\theta = 0 \quad \text{at} \quad x \pm \frac{\ell}{2}$$

The solution of Eq. (B.6) becomes, for negative values of
C_2,

$$\theta = \frac{C_3}{C_2} \left[\frac{\cosh \sqrt{|C_2|}\ x}{\cosh \sqrt{|C_2|}\ \ell/2} - 1 \right] \tag{B.7}$$

The heat conduction to the supports is

$$q_k = 2k_w \, a \, \frac{C_3}{\sqrt{|C_2|}} \, \tanh \sqrt{|C_2|} \, \frac{\ell}{2} \qquad (B.8)$$

Equations (B.7) and (B.8) are well known (King,[30] Davies and Fisher[13] and Hinze[24]).

B.1.5. Combined Effects of Conduction and Forced Convection

Assuming the heat losses by radiation and free convection are negligible, the total heat loss from the wire is the sum of the losses by conduction and forced convection and is given by

$$q_t = q_k + q_c \qquad (B.9)$$

The heat loss by forced convection is obtained from the equation

$$q_c = h \, \pi \, d \, \ell \, (t_{wm} - t_a) \qquad (B.10)$$

where h is determined by obtaining the Nusselt number in Hilpert's equation (B.4). Since the temperature of the wire varies along its length, a mean wire temperature t_{mw} is used in Eq. (B.10) such that a correct q_c is obtained. Using Eqs. (B.1), (B.4), (B.9) and (B.10), we find that for a wire placed normal to the flow direction $\bar{U}_1$.

$$I^2 = C_4 + C_5 U_1^{\,c} \qquad (B.11)$$

where

$$C_4 = \frac{q_c}{3.413 \, R_w} \; ; \qquad C_5 = \frac{\pi k_f C_1 d^c \ell}{R_w \, 3.413 \, \nu_f^{\,c}} (t_{wm} - t_a)$$

If the equation for forced convection, an equation of the form $Nu = C_6 + C_7 Re^c$, is used in place of Hilpert's equation, Eq. (B.11) has the same form but additional terms are contained in C_4.

It is not practical to determine the values of C_4 and C_5 from the equations given above because it is difficult to determine the quantities which appear in the equations with sufficient accuracy. It is preferable to consider Eq. (B.11) as a likely form of an empirical equation relating the current I and the velocity U_1 and then verify the equation and determine the values of C_4 and C_5 by calibration. In the constant temperature method of operation the calibration is carried out using Eq. (B.12) which follows. The calibration should be carried out under the same operating conditions and over the same range of velocities as those existing when the hot-wire measurements are taken.

B.2. Constant Temperature Operation

In the constant temperature method of operation an electronic feed-back system is used to keep the resistance of the wire, and hence its temperature, constant. In a hot-wire placed normal to the flow, which is in the direction of x_1, the heat loss from the wire represented by I^2 depends on the velocity U_1 as given in Eq. (B.11). In practice the bridge d-c voltage, which is proportional to the probe current, is measured so that Eq. (B.11) becomes

$$E^2 = A + B \, U_1{}^c \qquad \text{(B.12)}$$

B.2.1. Effective Cooling of Slanting Wire

The measurement of the turbulent shear stresses and lateral intensities requires that the sensitivity of the hot-wire, when placed at an angle to the mean flow, be known. For a wire positioned at an angle ϕ to the flow direction, with $20° < \phi < 90°$, the cooling of the wire is determined mainly by the velocity component perpendicular to the wire. The cooling effect of the component of velocity in the direction of the wire is very small and has generally been neglected. An empirical equation for the effective cooling velocity, which includes the velocity component along the wire, is given by Hinze,[24] it is

$$U_E{}^2 = U_N{}^2 + k^2 U_T{}^2 \qquad \text{(B.13)}$$

According to Hinze, the factor k has a value between 0.1 and 0.3, and the value of k decreases as the velocity increases. More recently Webster[15] determined k to be 0.20, with no dependence on the wire ℓ/d ratio, and only a weak dependence on velocity. The work of Champagne[8] on the directional sensitivity of hot-wires was more extensive. He found that k depended on the wire ℓ/d ratio and for platinum wires of $\ell/d = 200$, the value of k was 0.20; this is the same as the value found by Webster. In the present experiments tungsten wires of $\ell/d = 200$ were used; the value

of k was assumed to be 0.20.

B.2.2. <u>Sensitivity of Slanting Wire to Fluctuating Velocity</u>

Using Cartesian coordinates x_1, x_2, x_3, with x_1 in the main flow direction, the instantaneous velocities are: $\bar{U}_1 - u_1$, u_2, u_3. For an inclined wire at an angle ϕ to the mean flow, and located in the $x_2 x_3$ plane, the instantaneous velocity component perpendicular to the wire, is

$$U_N = \left\{ \left[(\bar{U}_1 + u_1)\sin\phi + u_2\cos\phi \right]^2 + u_3{}^2 \right\}^{\frac{1}{2}} \qquad (B.14)$$

Assuming weak turbulence, so that

$$u_1 \ll \bar{U}_1, \quad u_2 \ll \bar{U}_1, \quad u_3 \ll \bar{U}_1$$

and neglecting the terms containing quadratic and higher powers of the fluctuating velocities, the above equation becomes

$$U_N = (\bar{U}_1 + u_1)\sin\phi + u_2\cos\phi \qquad (B.15)$$

Similarly, the longitudinal component is

$$U_T = (\bar{U} + u_1)\cos\phi - u_2\sin\phi \qquad (B.16)$$

Substituting Eqs. (B.15) and (B.16) in Eq. (B.13), it becomes

$$U_E{}^2 = \left[(\bar{U}_1 + u_1)\sin\phi + u_2\cos\phi \right]^2 + k^2 \left[(\bar{U} + u_1)\cos\phi - u_2\sin\phi \right]^2 \qquad (B.17)$$

For the inclined wire, U_E is used in place of U_1 in

Eq. (B.12), which gives

$$E^2 = A + B U_E{}^c \tag{B.18}$$

If we substitute U_E from Eq. (B.17) in Eq. (B.18), expand using the binominal theorem, and take the time averages and if we neglect the terms containing quadratic and higher powers of the fluctuating velocities, then Eq. (B.18) becomes

$$\bar{E}^2 + 2\bar{E}e = A + B\bar{U}_1{}^c (\sin^2\phi + k^2\cos^2\phi)^{c/2}$$

$$+ c\ \bar{\bar{U}}^{(c-1)}(B\ \sin^c\phi\ s_1)(u_1 + \frac{s_2}{s_1} u_2) \tag{B.19}$$

If the corresponding mean-value equation is subtracted from Eq. (B.19), the following equation is obtained

$$e = n(u_1 + \frac{s_2}{s_1} u_2) \tag{B.20}$$

where

$$n = (B\ \sin^c\phi\ s_1)\ \frac{c\ \bar{\bar{U}}^{(c-1)}}{2\bar{E}} \tag{B.21}$$

$$s_1 = \left[1 + \frac{k^2 c}{2} \cot^2\phi + k^4\ \frac{c(c-2)}{8} \cot^4\phi + \ldots \right] \tag{B.22}$$

$$s_2 = \cot\phi\left\{1-k^2\left[1 - \frac{(c-2)}{2} \cot^2\phi\right] + k^4\ \frac{\cot^2\phi}{2}\right.$$

$$\left. + k^4\ \frac{\cot^2\phi}{2}\left[2 - c + \frac{(c-2)(c-4)}{4} \cot^2\phi\right] + \ldots\right\} \tag{B.23}$$

Eq. (B.20) is a general equation and may also be used for the normal wire if the angle ϕ is taken as 90°.

B.3. Measurement of Turbulent Intensities and Shear Stresses

If a wire is located normal to the flow, as shown in position I Fig. B.1, and a single slanting wire is placed alternately in positions II and III in the x_1 x_2 plane, then from Eq. (B.20)

$$e_I = n_I u_1$$
$$e_{II} = n_{II}(u_1 + \frac{s_2}{s_1} u_2) \tag{B.24}$$
$$e_{III} = n_{II}(u_1 - \frac{s_2}{s_1} u_2)$$

If position III is obtained by rotating the wire 180° about the axis of the wire support, then $n_{II} = n_{III}$. Squaring and taking time averages, Eq. (B.24) becomes

$$\overline{e_I}^2 = n_I^2 \overline{u_1}^2$$
$$\overline{e_{II}}^2 = n_{II}^2 (\overline{u_1}^2 + 2 \frac{s_2}{s_1} \overline{u_1 u_2} + \frac{s_2^2}{s_1^2} \overline{u_2}^2) \tag{B.25}$$
$$\overline{e_{III}}^2 = n_{II}^2 (\overline{u_1}^2 - 2 \frac{s_2}{s_1} \overline{u_1 u_2} + \frac{s_2^2}{s_1^2} \overline{u_2}^2)$$

From Eq. (B.25)

$$\overline{u_1}^2 = \overline{e_I}^2 / n_I^2 \tag{B.26}$$

$$\overline{u_2}^2 = (s_1^2/s_2^2) \left[(\overline{e_{II}}^2 + \overline{e_{III}}^2)/2n_{II}^2 \right] \tag{B.27}$$

$$\overline{u_1 u_2} = (s_1^2/s_2^2) \left[(\overline{e_{II}}^2 - \overline{e_{III}}^2)/4n_{II}^2 \right] \tag{B.28}$$

The values of $\overline{e_I^2}$, $\overline{e_{II}^2}$ and $\overline{e_{III}^2}$ were obtained by squaring the voltages which were read from the rms meter of the hot-wire anemometer, with the wires in positions I, II and III. $\overline{u_3^2}$ and $\overline{u_1 u_3}$ were obtained by locating the slanting wire in the $x_1 x_3$ plane; the equations were (B.27) and (B.28) with u_2 replaced by u_3.

In the present experiments the values of n_I and n_{II} were obtained by calibration as outlined later in Sec. B.5. The constant (s_1^2/s_2^2) was obtained by calibration in developed pipe flow as given in Appendix C. As a check constants s_1 and s_2 were also obtained as outlined below.

B.4. Determination of Constants s_1 and s_2

The values of s_1 and s_2 were determined using c, ϕ and k in Eqs. (B.22) and (B.23); c was obtained by cali-bration (see Sec. B.6), ϕ was measured and an empirical value of k was used.

For the wires used here ($\ell/d = 200$) a k value of 0.20 was assumed which was in agreement with the published results of Webster,[15] Champagne,[8] Patel,[46] Kjellström and Hedberg.[29] The angle ϕ (assumed the same as the angle of the wire to the probe axis) was measured by positioning the probe in a slide pro-jector and projecting the wire image on a paper screen. To minimize image distortion the wire was located near the center of the lens and the screen was positioned perpendicular to the

projector. Double the angle φ was measured by revolving the probe 180° about the probe support axis. For each slanting wire the angle 2φ was measured ten times and φ obtained by averaging. Repeatability of the measurement was good, for a typical slanting wire ten values of the angle φ fell within the range 44°-26' to 44°-38'.

B.5. Determination of the Constants n_I and n_{II} by Calibration

The hot-wires were calibrated in the distorting tunnel with the turbulence generating grid removed. The normal wire was located perpendicular to the flow direction as shown in position I of Fig. B.1; the slanting wire was located at an angle φ to the flow direction, in position II. The wires were placed beside a pair of straight static and total pressure tubes near the center-line of the tunnel, in a region of uniform velocity. The air speed in the tunnel was varied and static and velocity pressures and bridge d-c voltages were measured over a range of velocities corresponding to those in the main experiment. For any calibration the readings were obtained in a period of about 20 minutes; the temperature in the tunnel remained constant during calibration within an estimated ±0.5°F. The calibrations were carried out at approximately the same temperatures as those in the main experiments.

The equation relating the bridge d-c voltage to the velocity $\bar{U}_1$ was assumed to be of the form

$$\bar{E}^2 = A + B(\bar{U}_1^2 \sin^2\phi + k^2\bar{U}_1^2 \cos^2\phi)^{c/2} \qquad (B.29)$$

which after expansion becomes

$$\bar{E}^2 = A + (B \sin^c\phi \ s_1) \ \bar{U}_1^c \qquad (B.30)$$

The values of A, $(B \sin^c\phi \ s_1)$ and c were obtained by calibration. The procedure was to assume a value of c and then use the computer to find the equation of a straight line passing through the points of $\bar{E}^2$ and $\bar{U}^c$ and the rms error. The value of c was varied until the rms error assumed a minimum value. The intercept of the straight line with the $\bar{E}^2$ axis determined the value of A; the slope of the line the value of $(B \sin^c\phi \ s_1)$; the values of n were then determined using Eq. (B.21). For the normal wire

$$n_I = slope_I \ \frac{c_I \ \bar{U}_I^{(c_I-1)}}{2\bar{E}_I} \qquad (B.31)$$

For the slanting wire

$$n_{II} = slope_{II} \ \frac{c_{II} \ \bar{U}_{II}^{(c_{II}-1)}}{2\bar{E}_{II}} \qquad (B.32)$$

B.6. <u>Determination of the Exponent c by Calibration</u>

Measured values of the exponent c for a number of wires (0.005 mm diameter, $\ell/d = 200$) are shown in Table B1. The values of c vary between 0.39 and 0.45 with an average near 0.42. The hot-wire equation

$$\bar{E}^2 = A + slope \ \bar{U}_1^c$$

contains three empirical constants; the rms error in $\bar{E}^2$ is not very sensitive to small changes in c if the remaining two empirical constants are adjusted. In the present experiments a constant value of c = 0.45 was used for all wires, as shown in Table B1 the rms errors in $\bar{E}^2$ are not increased appreciably. The effect on the turbulence values of using c = 0.45, instead of the calibration value, is negligible.

A typical calibration curve is shown in Fig. B.2 using the calibration value c = 0.43 and also the standard value c = 0.45. Both values of c gave results which fall approximately on straight lines. Sample calibration curves for a slanting hot-wire are shown in Fig. B.3.

TABLE B1

Experimental Values of Exponent c in Hot-Wire Equation

Wire No.*	Velocity Range (fps)	Points of Calibration	Best Fit		c = 0.45
			c	rms Error	rms Error
N-6	12–82	8	0.40	0.156	0.231
N-8	22–92	11	0.43	0.093	0.096
N-8	12–68	16	0.39	0.203	0.233
S-3	18–82	14	0.45	0.130	0.130
S-6	12–82	14	0.40	0.200	0.229
S-6	12–72	11	0.40	0.075	0.124
S-6	18–75	11	0.45	0.096	0.096

* N indicates normal wire; S indicates slanting wire.

APPENDIX C

CALIBRATION OF HOT-WIRES IN DEVELOPED PIPE FLOW

The experiments described here were carried out to calibrate the hot-wires by measuring a known shear stress distribution (obtained from measured pressure drop) in developed pipe flow. From the experiments the most suitable value of the constant appearing in the hot-wire equations was determined (ie., the constant (s_1^2/s_2^2) in Eqs. (B.27) and (B.28)). The experiments were also useful as a means of gaining familarity with, and confidence in, the hot-wire measurement techniques.

C.1. Experimental Equipment

A straight brass pipe of 3.004 inches inside diameter and $\ell/d = 60$ was connected to the laboratory supply of low pressure air as shown in Fig. C.1. This apparatus had been used in the early experiments of Patel, with a bleed at the inlet to the pipe; in the present experiments the bleed was closed and the flow throttled at the blower outlet using a perforated plate. The pipe was in three sections; these were butt joined and held concentric using hose couplings. The sections were aligned accurately using two piano wires stretched along the pipe, one at the top and the other at the side.

The static pressures along the pipe were measured using the static pressure taps which are shown located in Fig. C.1. The total pressure at the outlet of the pipe was measured by traversing a 0.0625 inch diameter pitot tube across the flow. The pitot tube had sharpened lips formed by reaming the inside.

The outlet of the pipe was traversed using a traversing mechanism with a dial guage (smallest scale division 0.001 inches). To avoid backlash errors, measurement was made approaching the station from one direction. The reference location and alignment of each probe were obtained by polishing the inside of the pipe and observing the mirror image of the probe. Final alignment of the slanting hot-wire was completed when no variation of the anemometer mean voltage occurred on rotation of probe about its axis.

C.2. Results and Discussion

The mean velocity of the pipe, obtained from the pitot traverse, is shown in Fig. C.2. The logarithmic velocity distribution

$$\bar{U}/U_\tau = 2.5 \ln\left(\frac{yU_\tau}{\nu}\right) + 5.5$$

obtained by Nikaradse and reported by Schlichting[56] for flow in smooth pipes at high Reynolds numbers, is shown for comparison; disagreement is noticeable especially near the center region of the pipe. The present results lie within

The range of results of various investigators which are reported by Patel.

The outlet of the pipe was traversed, first with the normal hot-wire and then with the slanting hot-wire. The constant (s_1^2/s_2^2) was then obtained using the shear stress from measured pressure drop in Eq. (B.28), and n_{II} from mean velocity calibration. It is interesting that calculation of the shear stress from constants s_1 and s_2, determined using measured values of ϕ and c and assumed value of $k = 0.20$, was less satisfactory than when $k = 0.00$ was used as shown in Fig. C.3. This could be due to errors in measuring ϕ and c accurately.

Measured values of $u'/\bar{U}$, $v'/\bar{U}$ and $w'/\bar{U}$ are shown in Fig. C.4 together with corresponding curves of Laufer. The measured values of $u'/\bar{U}$ are slightly higher and the values of $w'/\bar{U}$ are lower than those of Laufer.[33] There is good agreement between the values for $v'/\bar{U}$.

The author's results are compared with those of Patel[46] in Fig. C.5. There is good agreement for the $u'/\bar{U}$ component. Agreement is not good for the $v'/\bar{U}$ and $w'/\bar{U}$ component.

$\overline{U}$ u_1 u_2
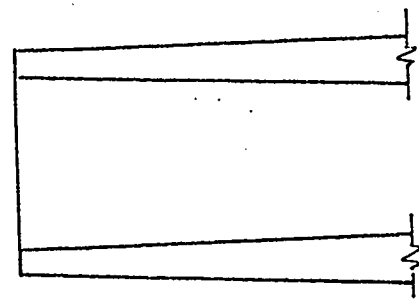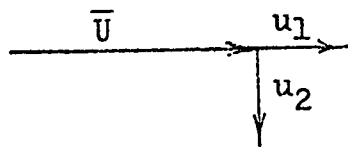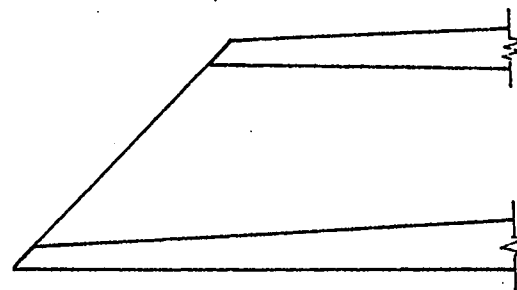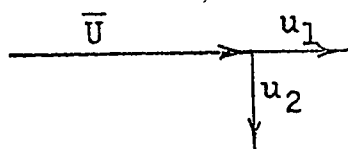
Position I

Position II
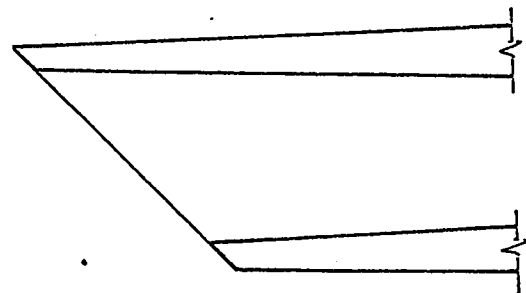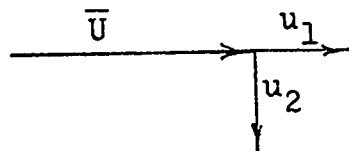
Position III

Fig. B.1. Measurement of $\overline{u_1^2}$, $\overline{u_2^2}$ and $\overline{u_1 u_2}$ with the hot-wire anemometer.
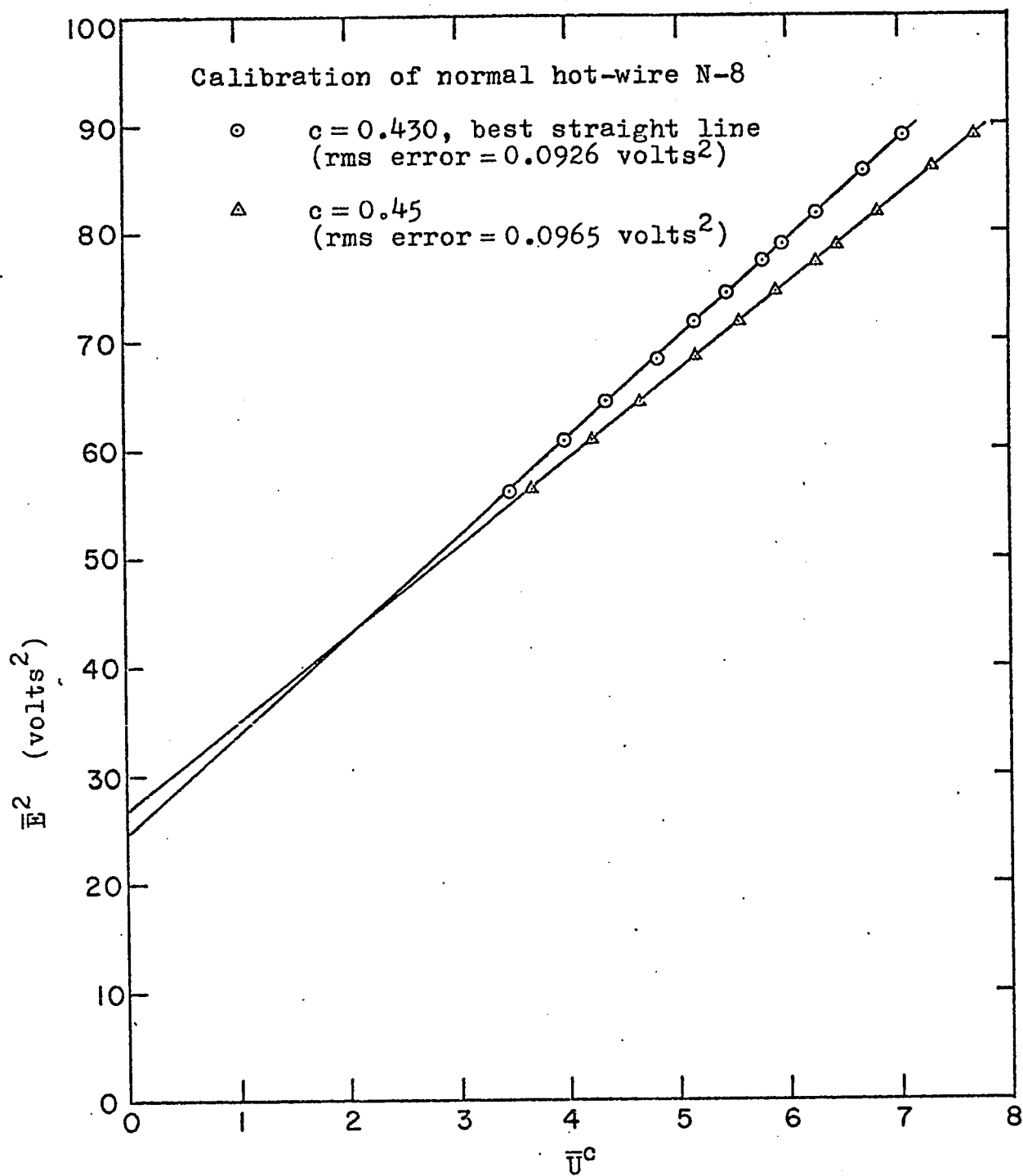
Fig. B.2. Calibration of typical normal hot-wire.
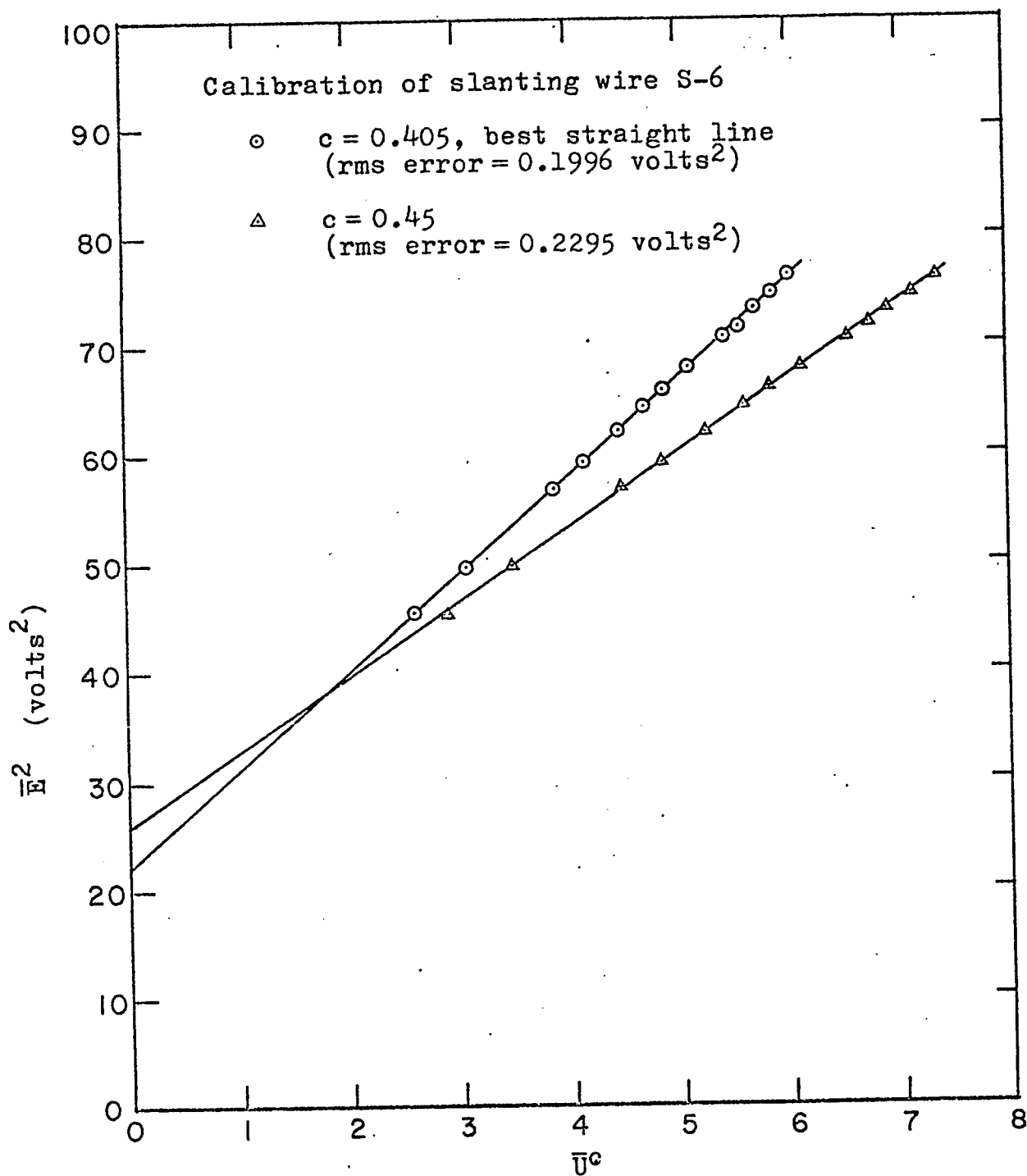
Fig. B.3.   Calibration of typical slanting hot-wire.

14 ft.(approx.)

8 ft(approx)

.907"

14.03" 38.03" 68.30" 77.20" 95.20"

Pressure taps

Bleed closed

4 ft.radius (approx.)

Clamped hose couplings

3" I.D. Brass pipe (measured I.D. 3.004")

Honeycomb

Rough support

2nd Floor

Flow throttled by perforated plate

1st Floor

172
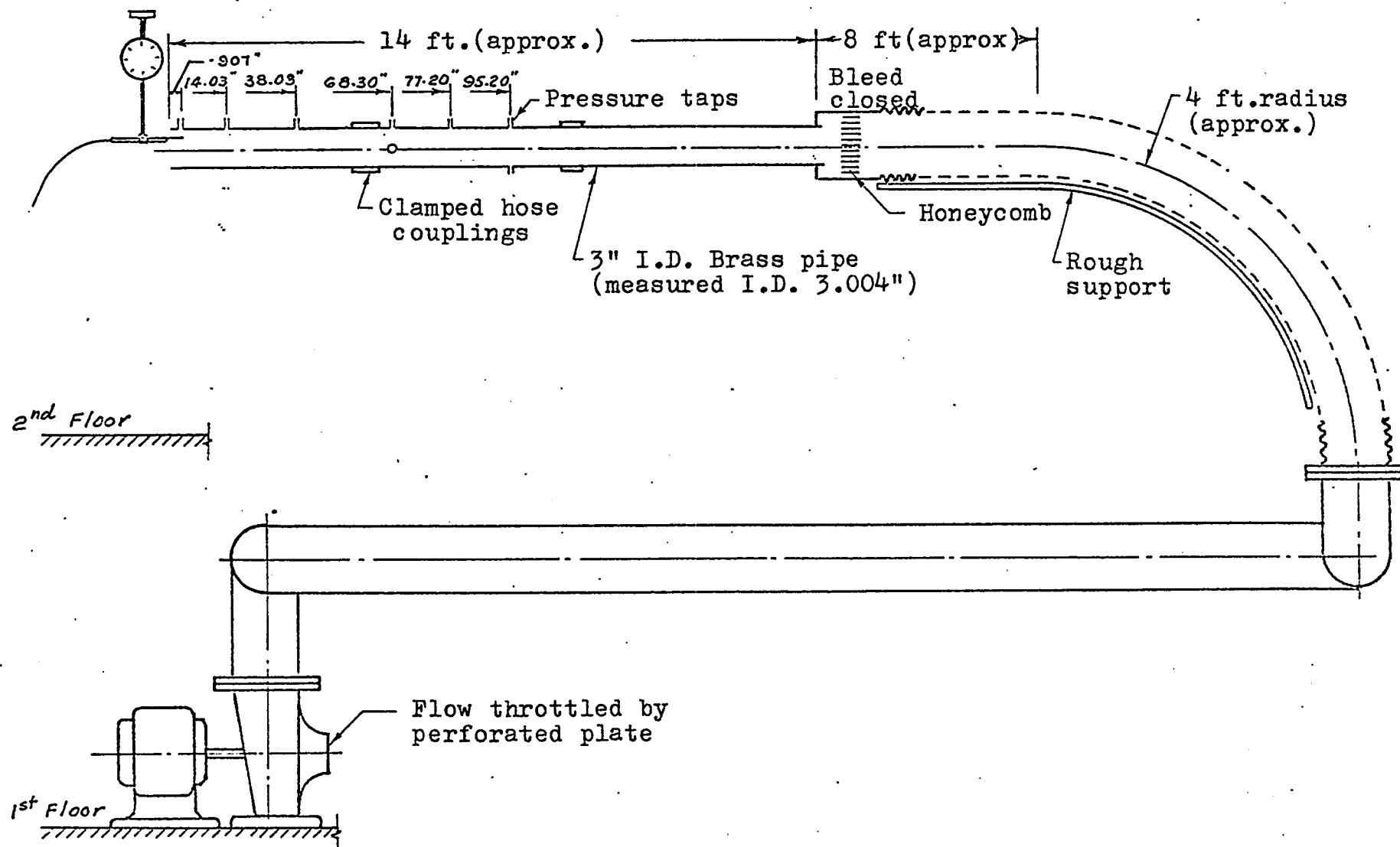
Fig. C.1. Layout of apparatus for hot-wire pipe calibration.

$$\frac{\bar{U}}{U_\tau} = 2.5 \ \ln\left(\frac{y \ U_\tau}{\nu}\right) + 5.5$$
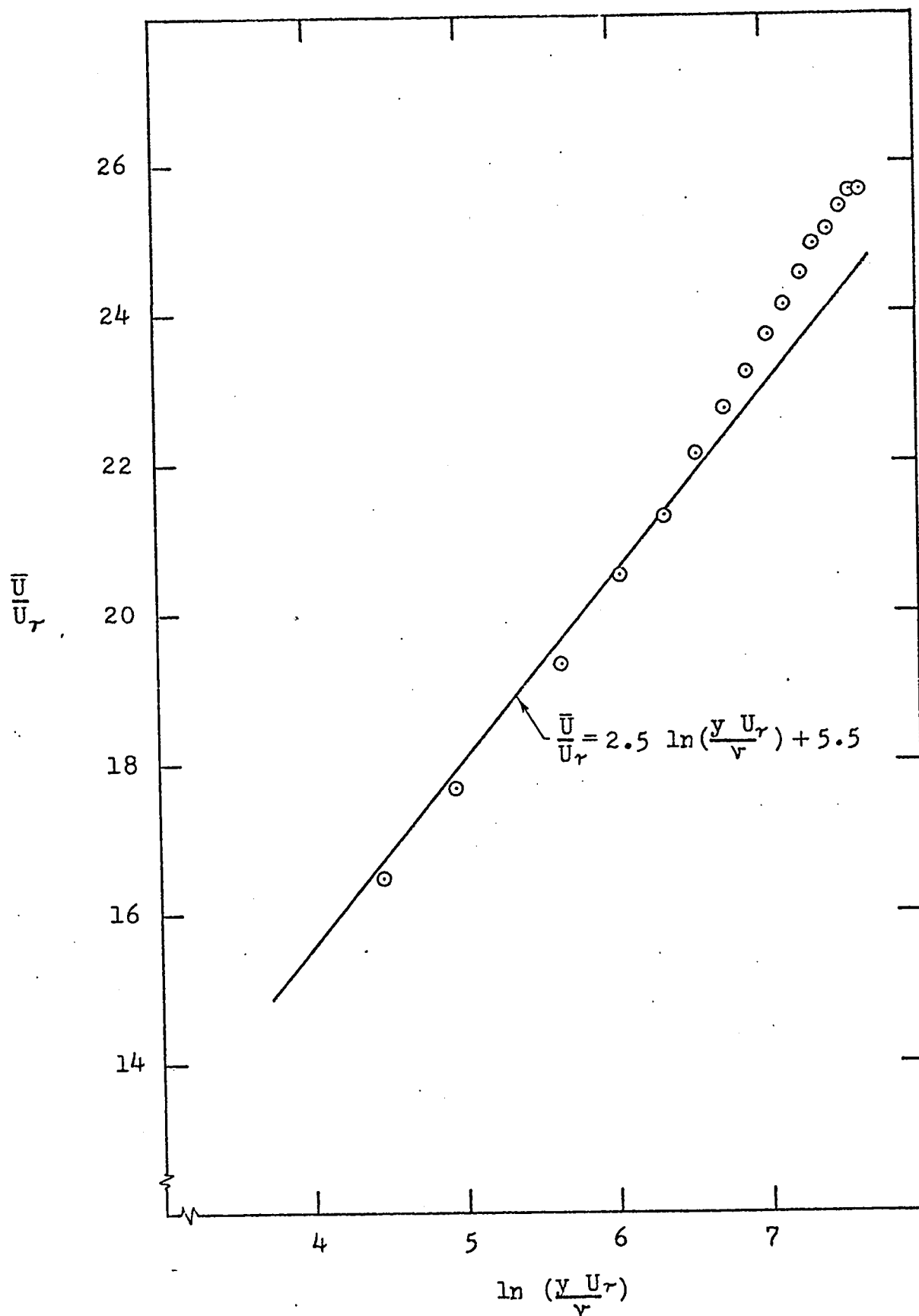
Fig. C.2. Mean velocity distribution in developed pipe flow.
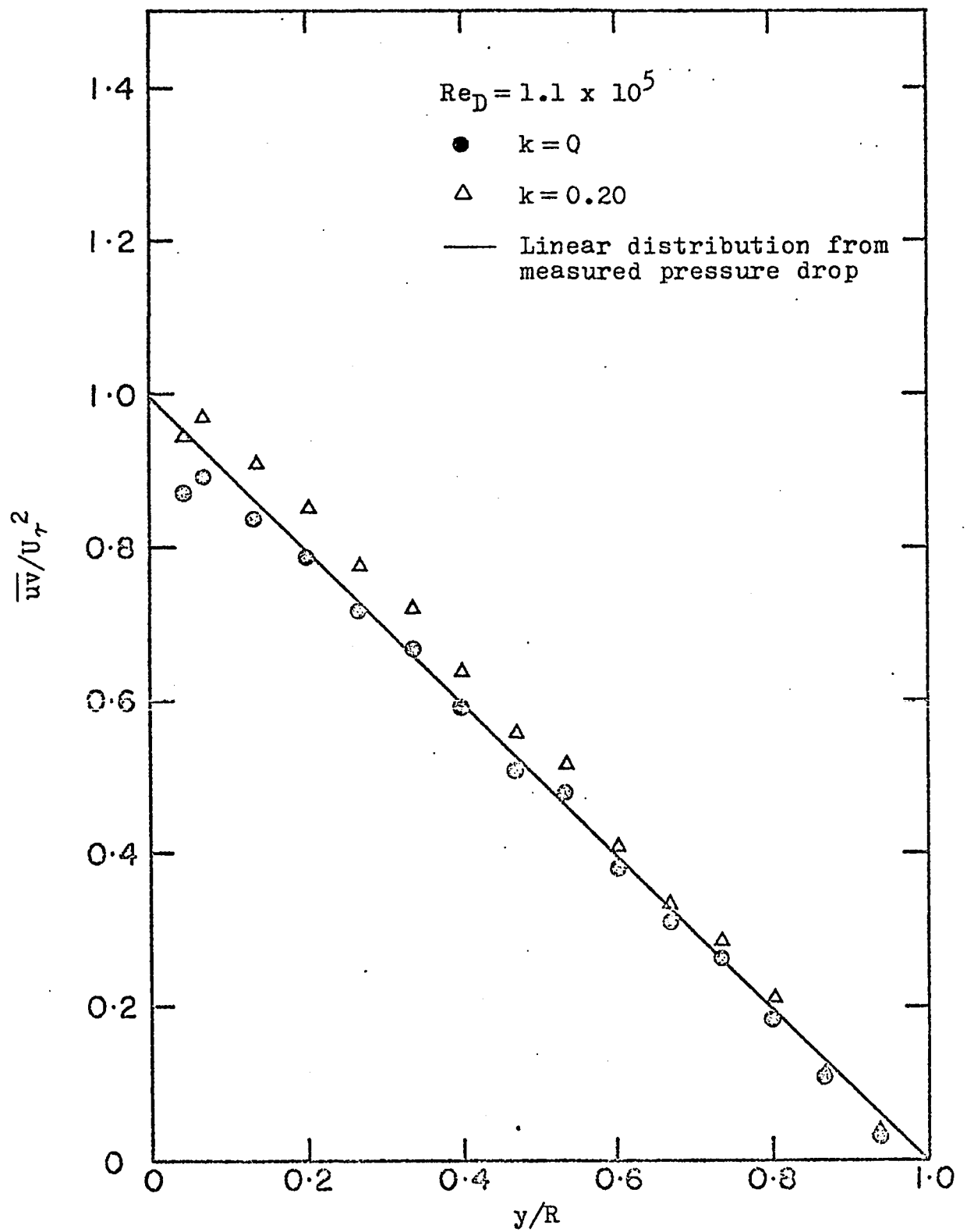
Fig. C.3. Reynolds shear stress distributions in developed pipe flow.
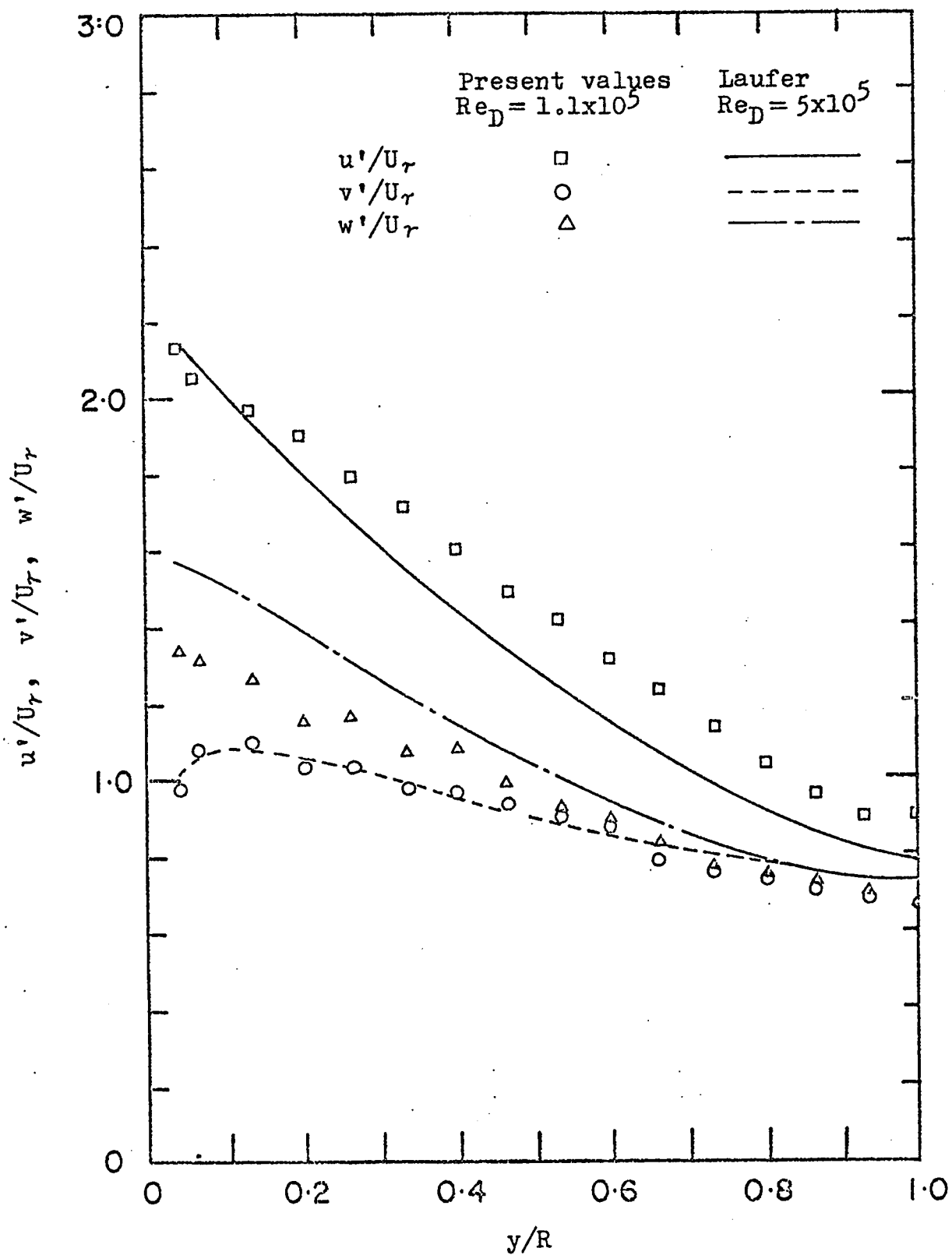
Fig. C.4. Distributions of turbulent intensities in developed pipe flow (comparison with Laufer[33])
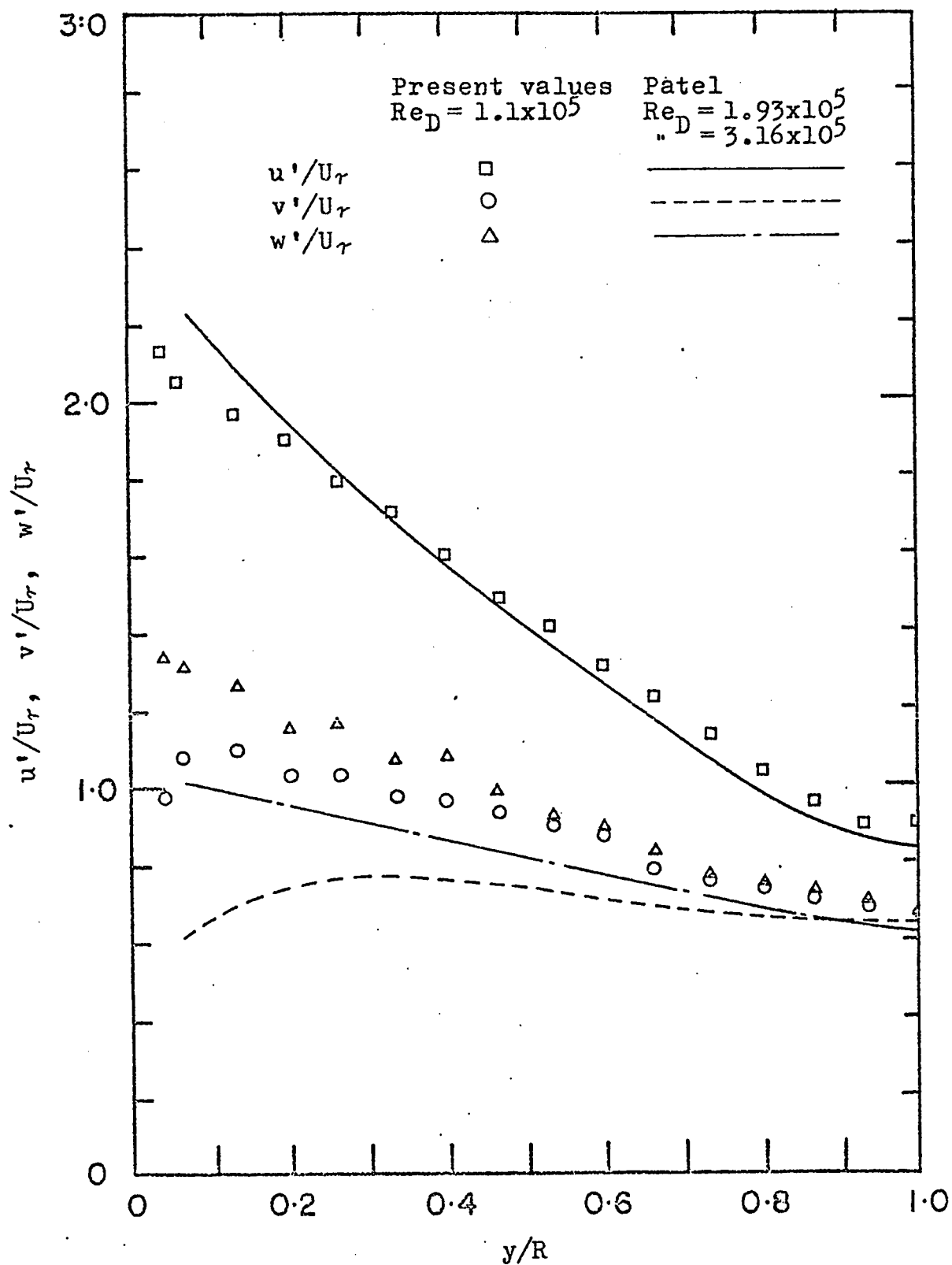
Fig. C.5. Distributions of the turbulent intensities in developed pipe flow (comparison with Patel[46])
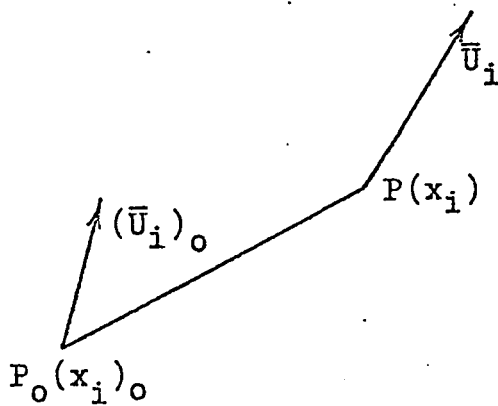
Fig. 1. Velocity vectors at neighbouring points in a fluid
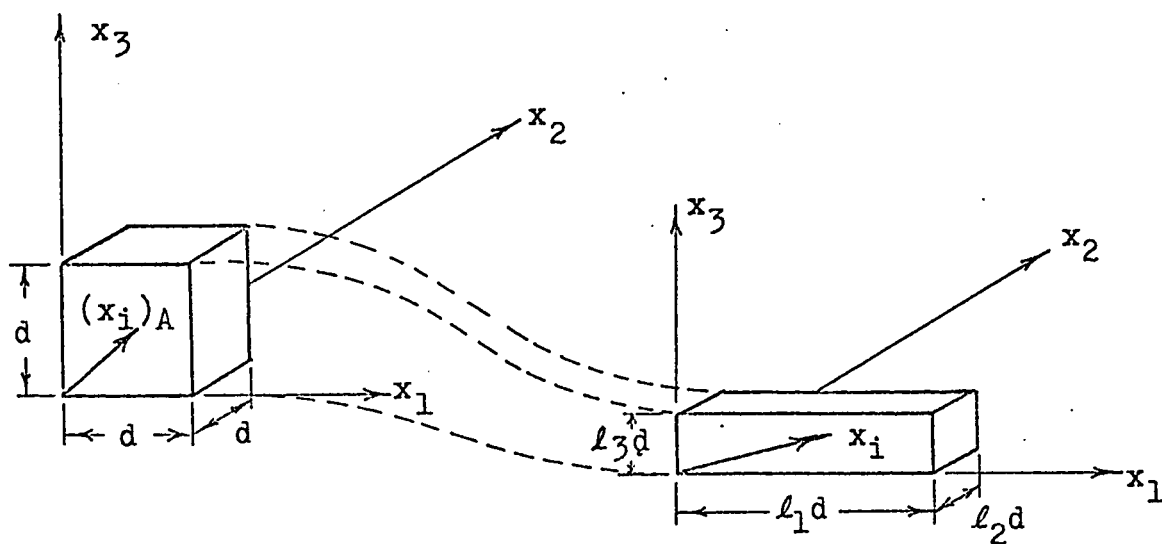
Fig. 2. Distortion of a fluid element by irrotational strain.
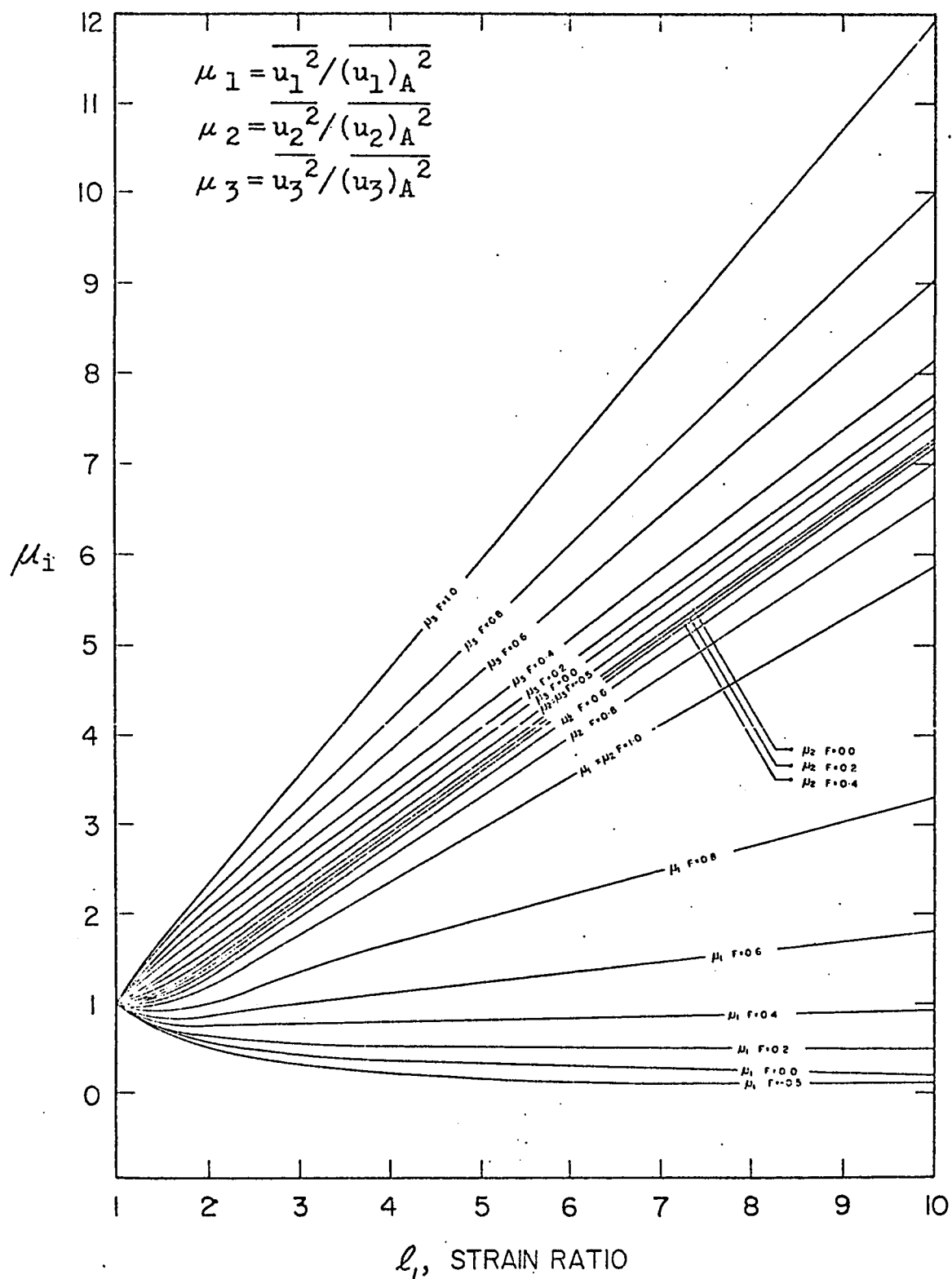
Fig. 3. Variations of the component turbulent intensities from the rapid distortion theory.
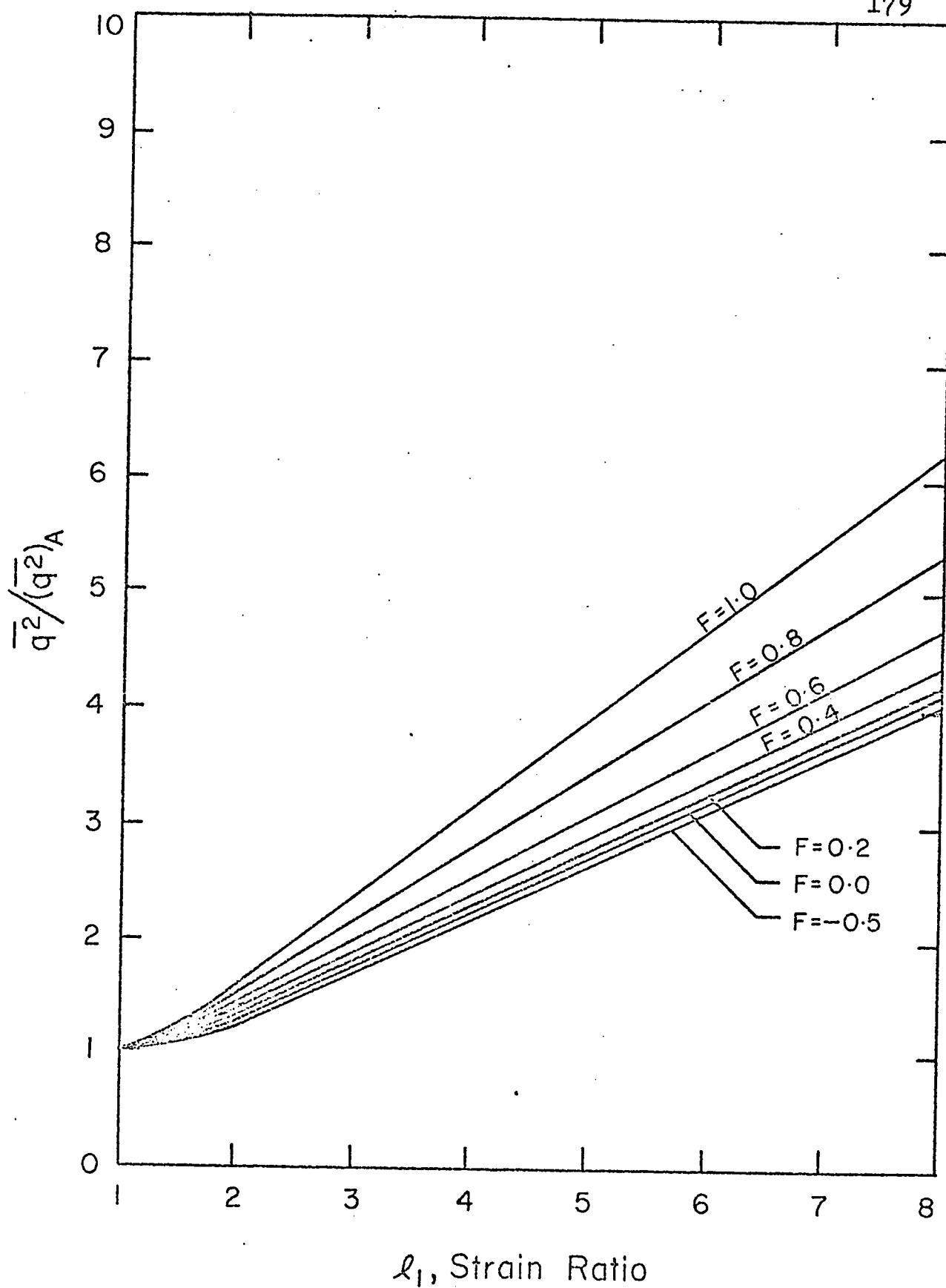
Fig. 4. Variations of the total turbulent intensity from the rapid distortion theory.
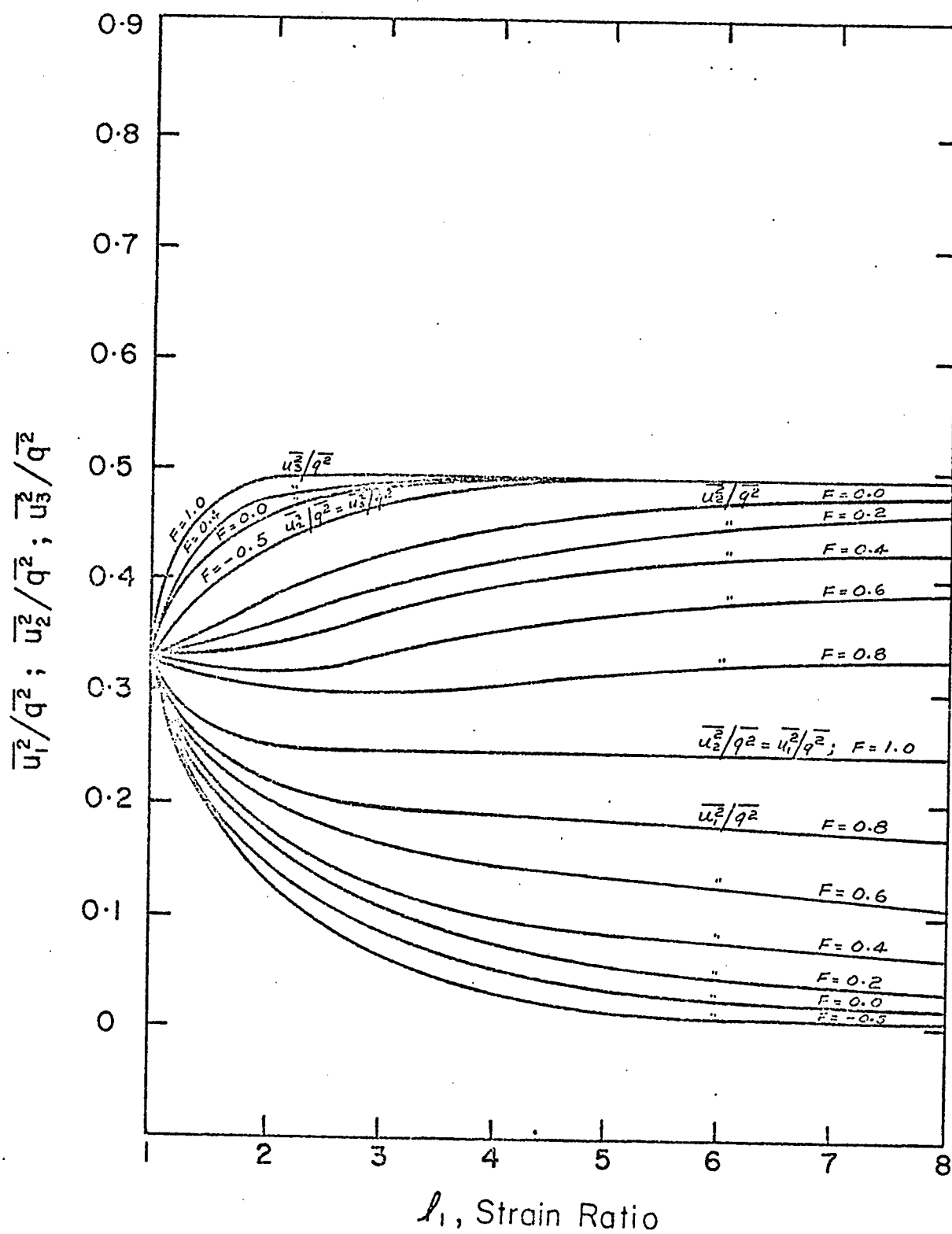
Fig. 5. Variations of the local turbulent intensity ratios from the rapid distortion theory
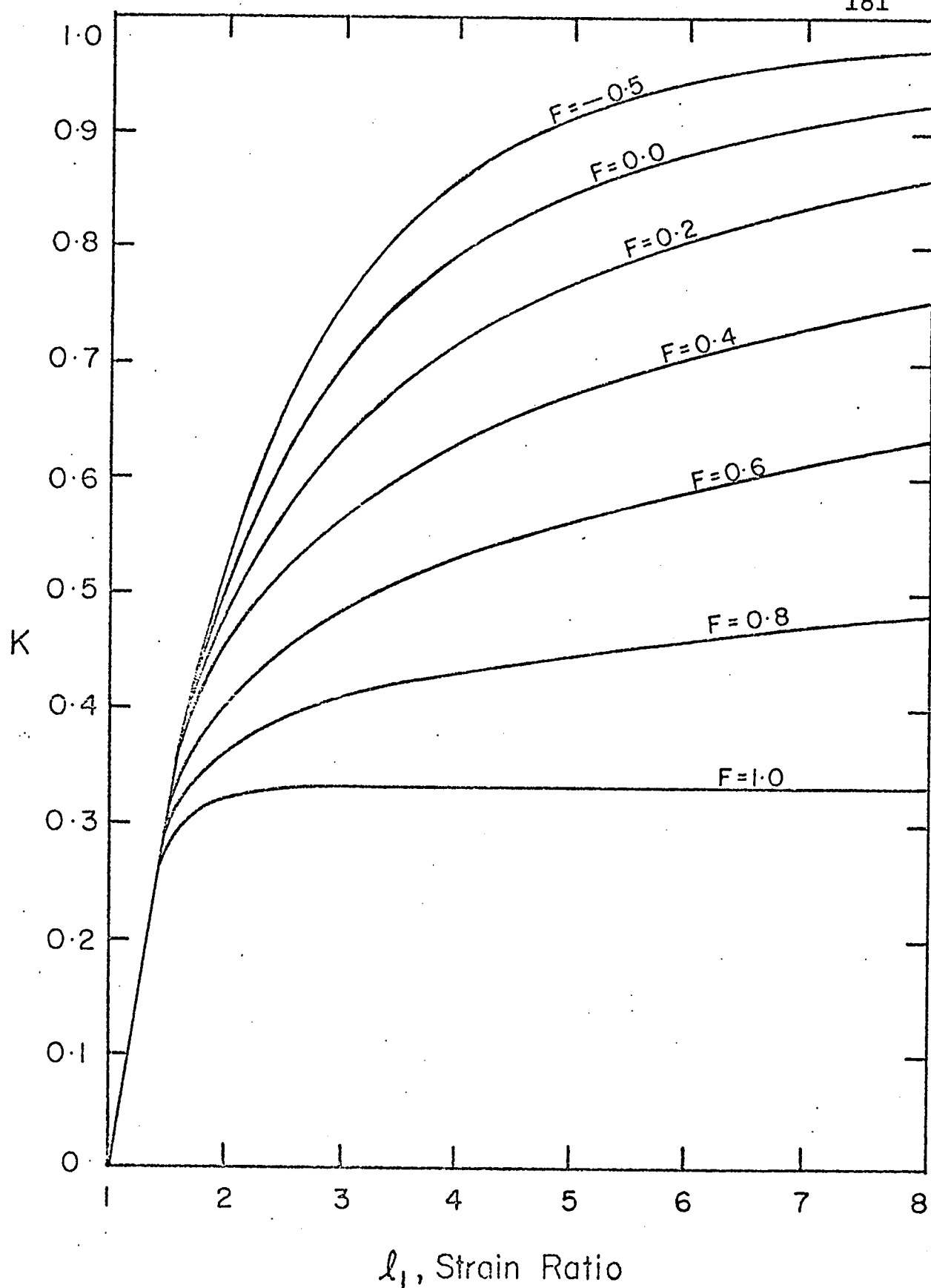
Fig. 6.   Variations of the structural measure K from
the rapid distortion theory.
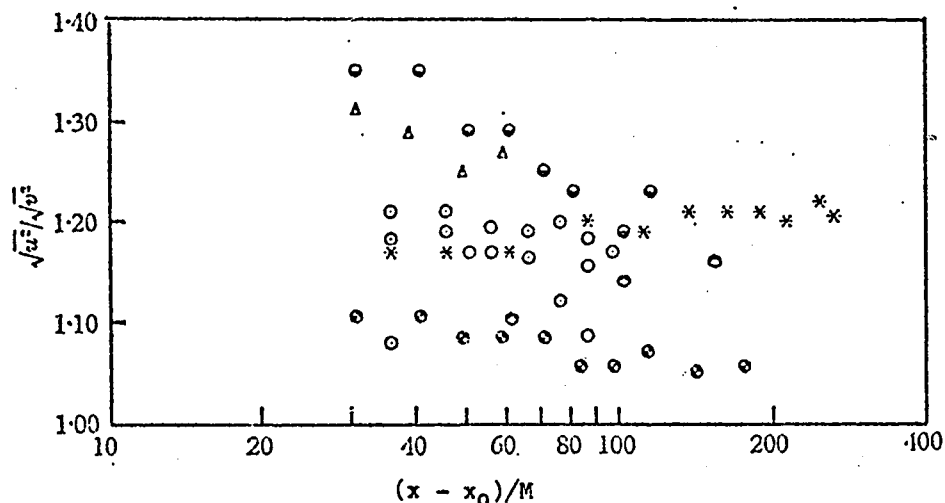
Anisotropy of grid generated turbulence (round rod bi-plane grids).
⊖,⊖, Corrsin (1942); ⊙ , Wyatt (1955); △ , Kistler & Vrebalovich
(1961); ✻ , Uberoi (1963); ⊕ , Comte-Bellot & Corrsin (1966).
(Comte-Bellot & Corrsin" reprinted from J. Fluid Mech. (1966)
Vol. 25, Part 4, p.663.)

$(x - x_0)/M$, mesh lengths from the virtual origin.
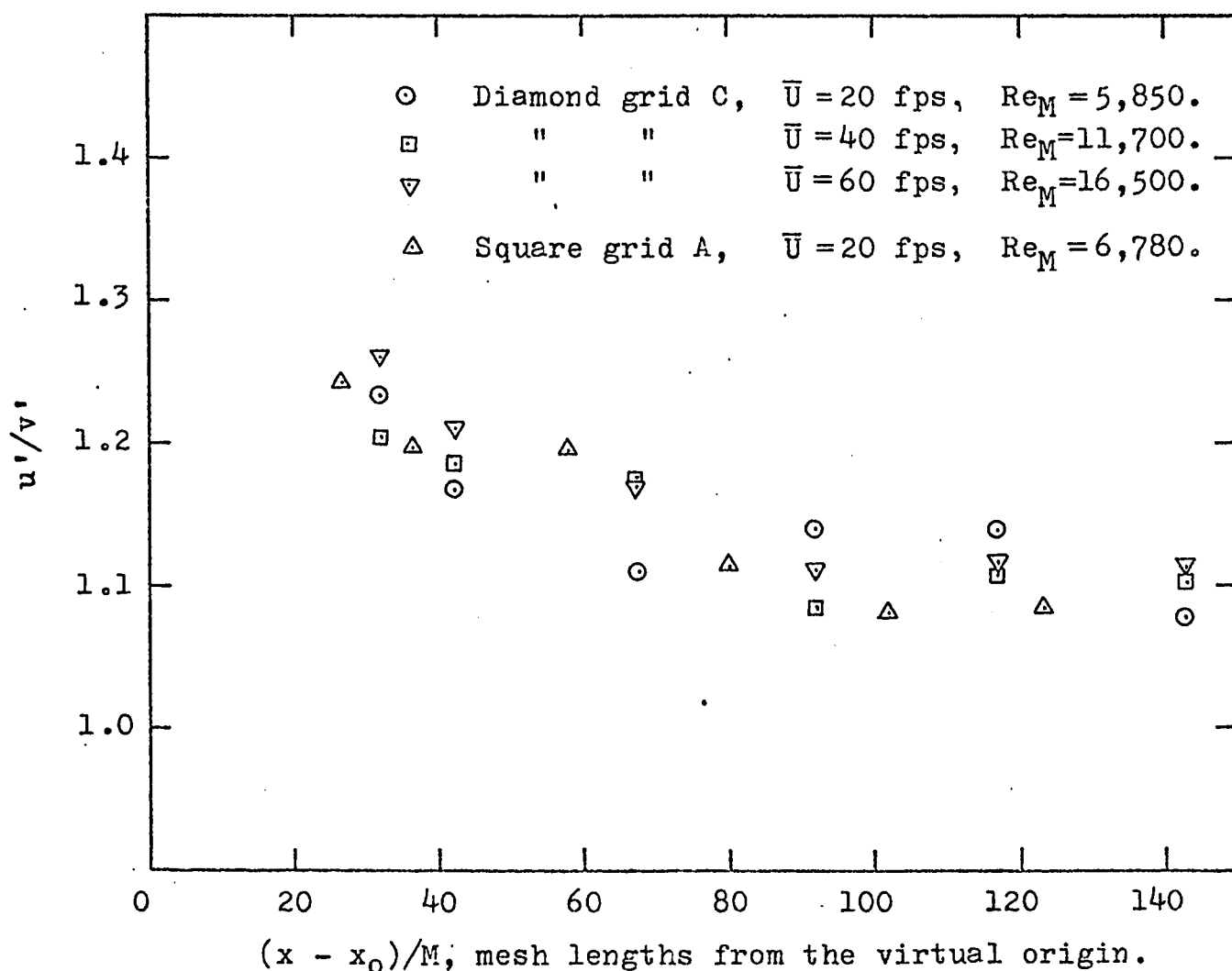
Fig. 7. Anisotropy of grid turbulence during decay in uniform
flow.
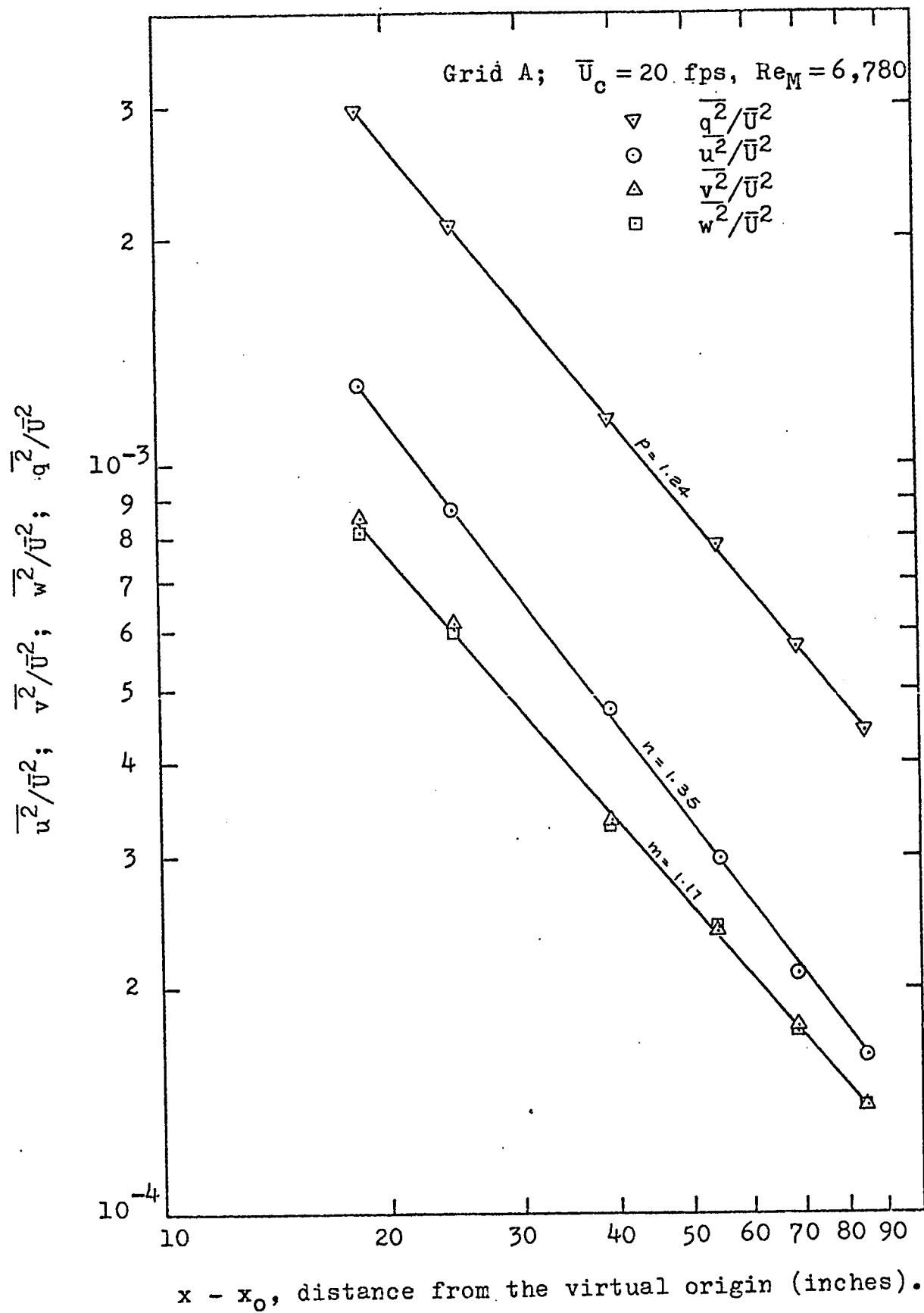
Fig. 8. Decay of turbulence in uniform flow using grid A.
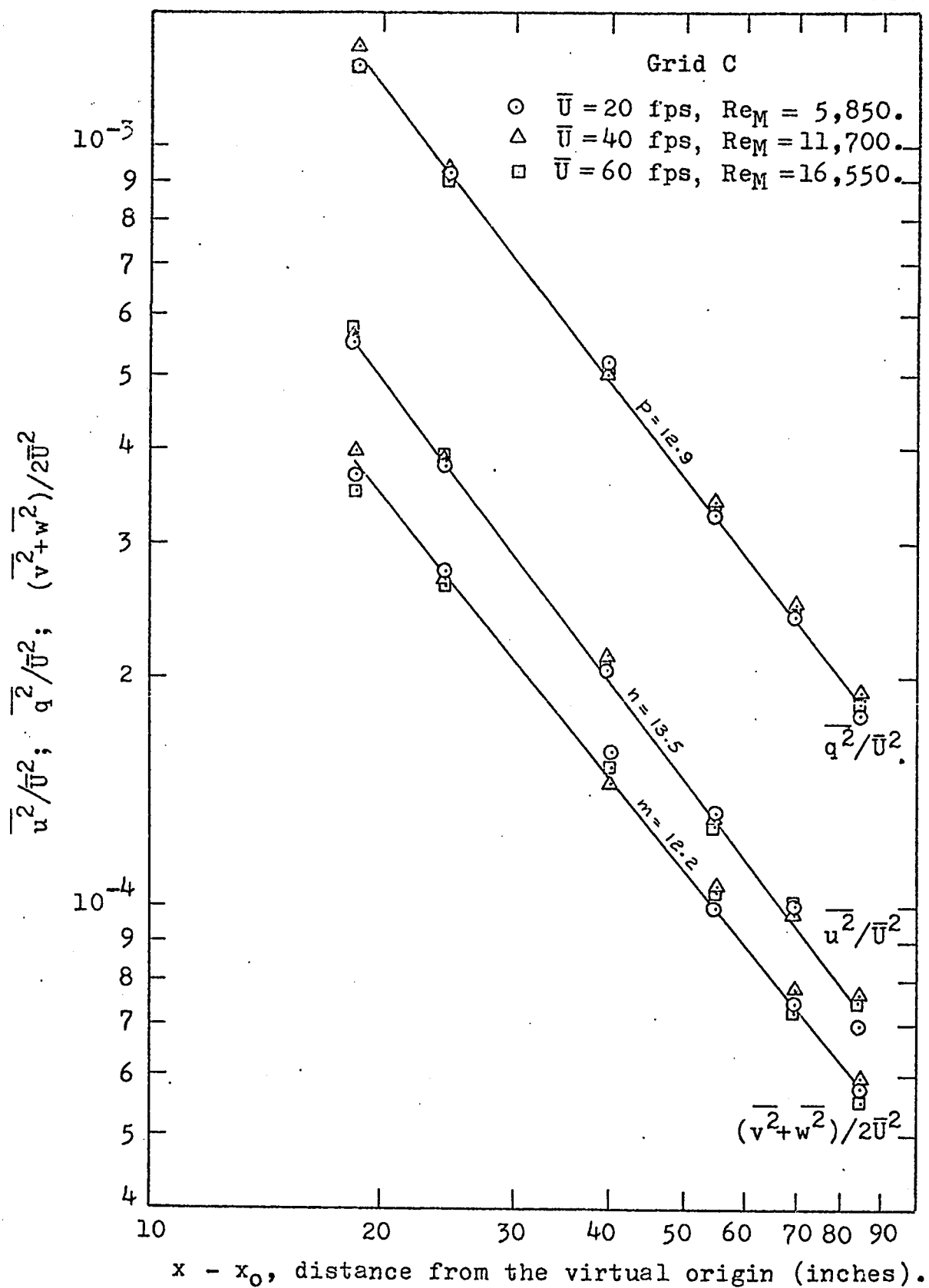
Fig. 9. Decay of turbulence in uniform flow using grid C.

Tunnel Dimensions

Section No.	Name	Dimensions in inches		
		Inlet	Outlet	Length
1	Intake	45 x 64 3/4	45 x 7 1/?	52 1/2
2	Parallel Flow Section	45 x 7 1/2	45 1/8 x 7 5/8	25
3	Distorting Section	45 1/8 x 7 5/8	8 1/8 x 45 5/8	96 1/2
4	Parallel Flow Section	8 1/8 x 45 5/8	8 3/16 x 45 11/16	48
5	Parallel Flow Section	8 3/16 x 45 11/16	8 5/16 x 45 13/16	96
6	Flexible Joint	8 3/16 x 45 11/16	8 3/16 x 45 11/16	6
7	Transition Section	8 3/16 x 45 11/16	39.3 dia.	36
8	Fan	39.3 dia.	39.3 dia.	29
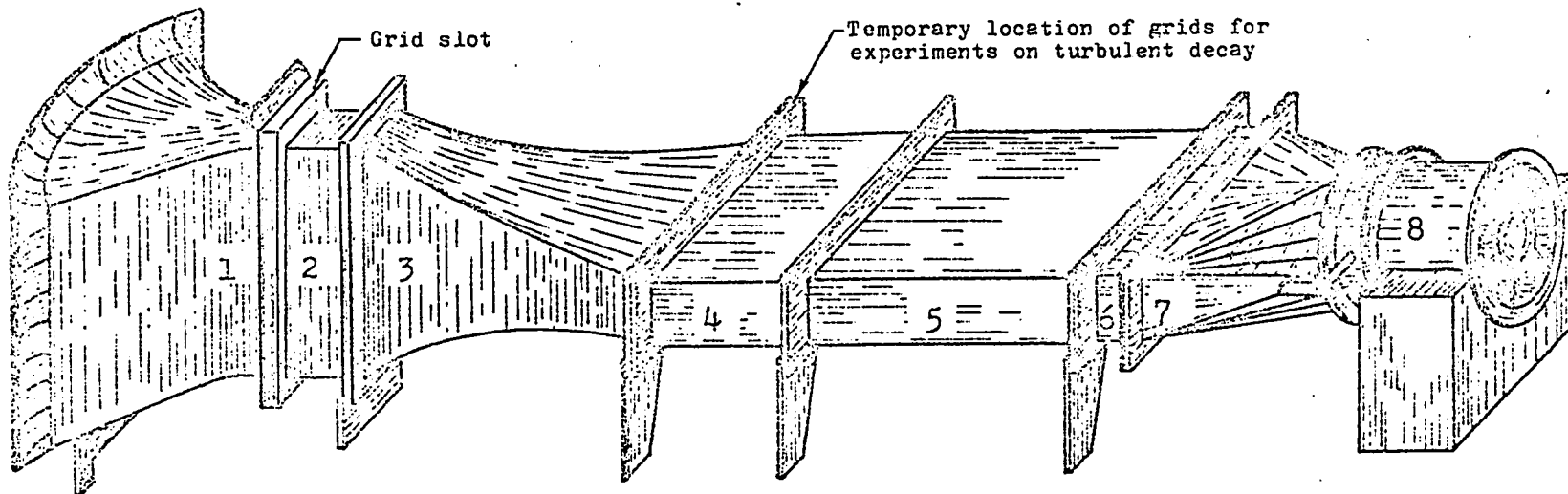
Fig. 10. General arrangement of the distorting wind-tunnel
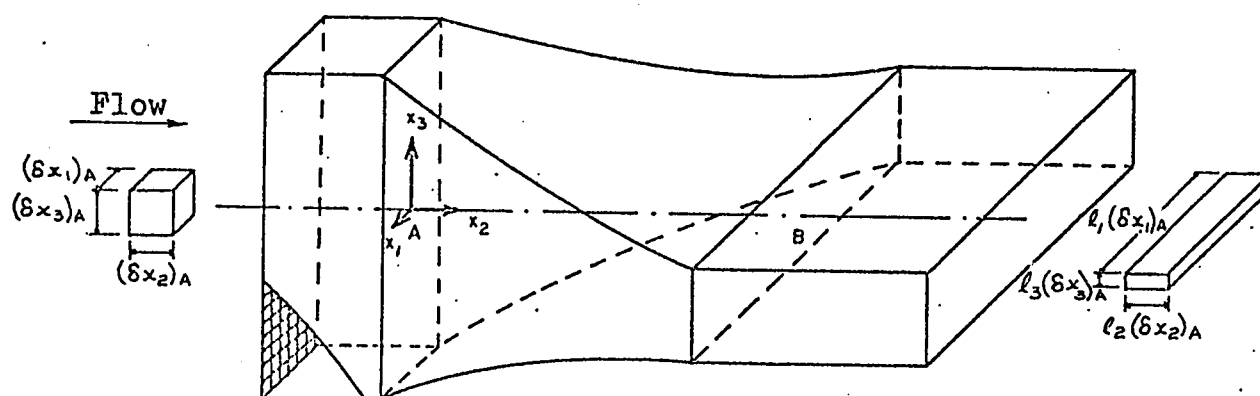
Fig. 11.   Schematic representation of the working-section
of the distorting wind-tunnel.

Distance from the entrance of the distorting section, (inches).
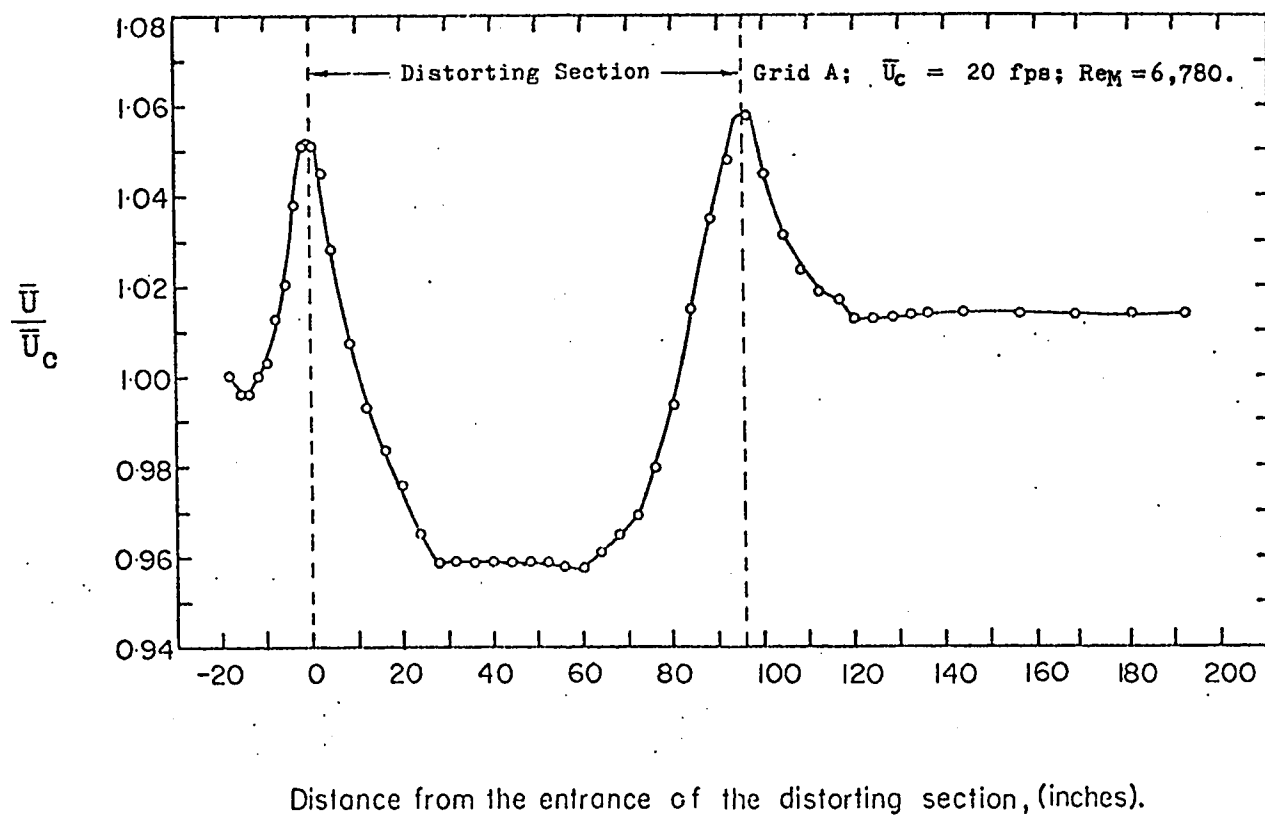
Fig. 12. Mean velocity along the center-line of the distorting wind-tunnel using grid A.
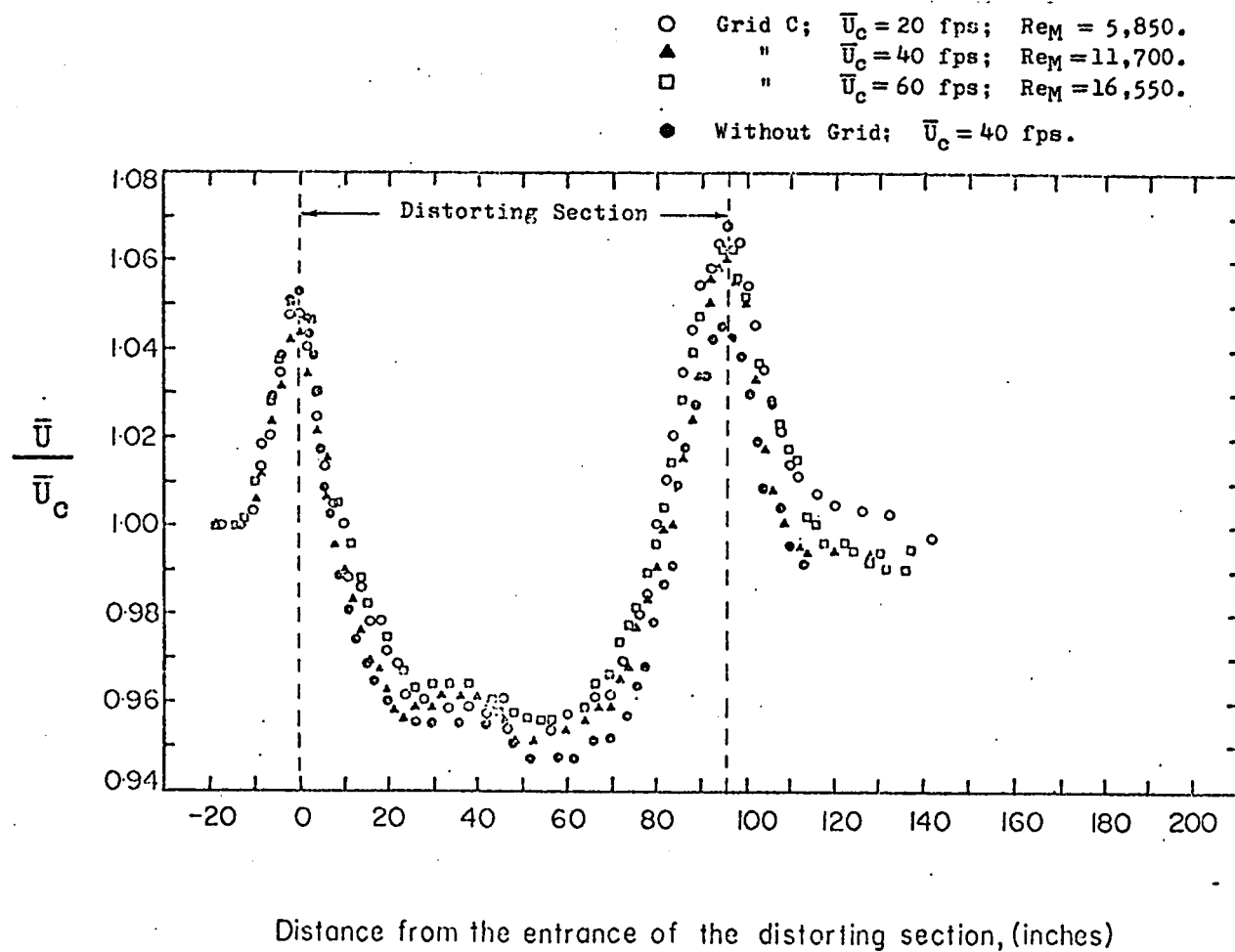
Fig. 13. Mean velocities along the center-line of the distorting wind-tunnel using grid C.
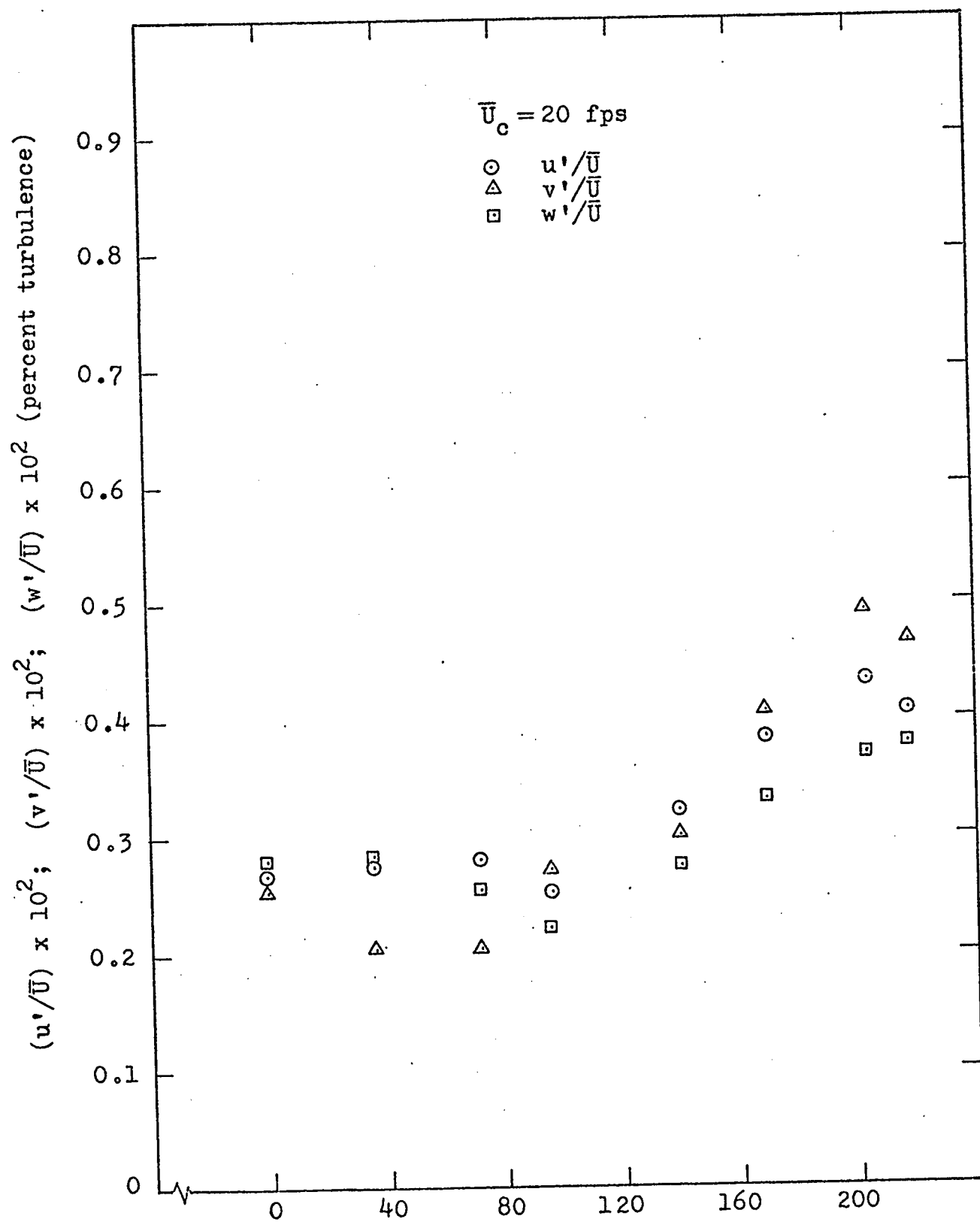
Fig. 14. Background turbulence along the center-line of the distorting wind-tunnel.
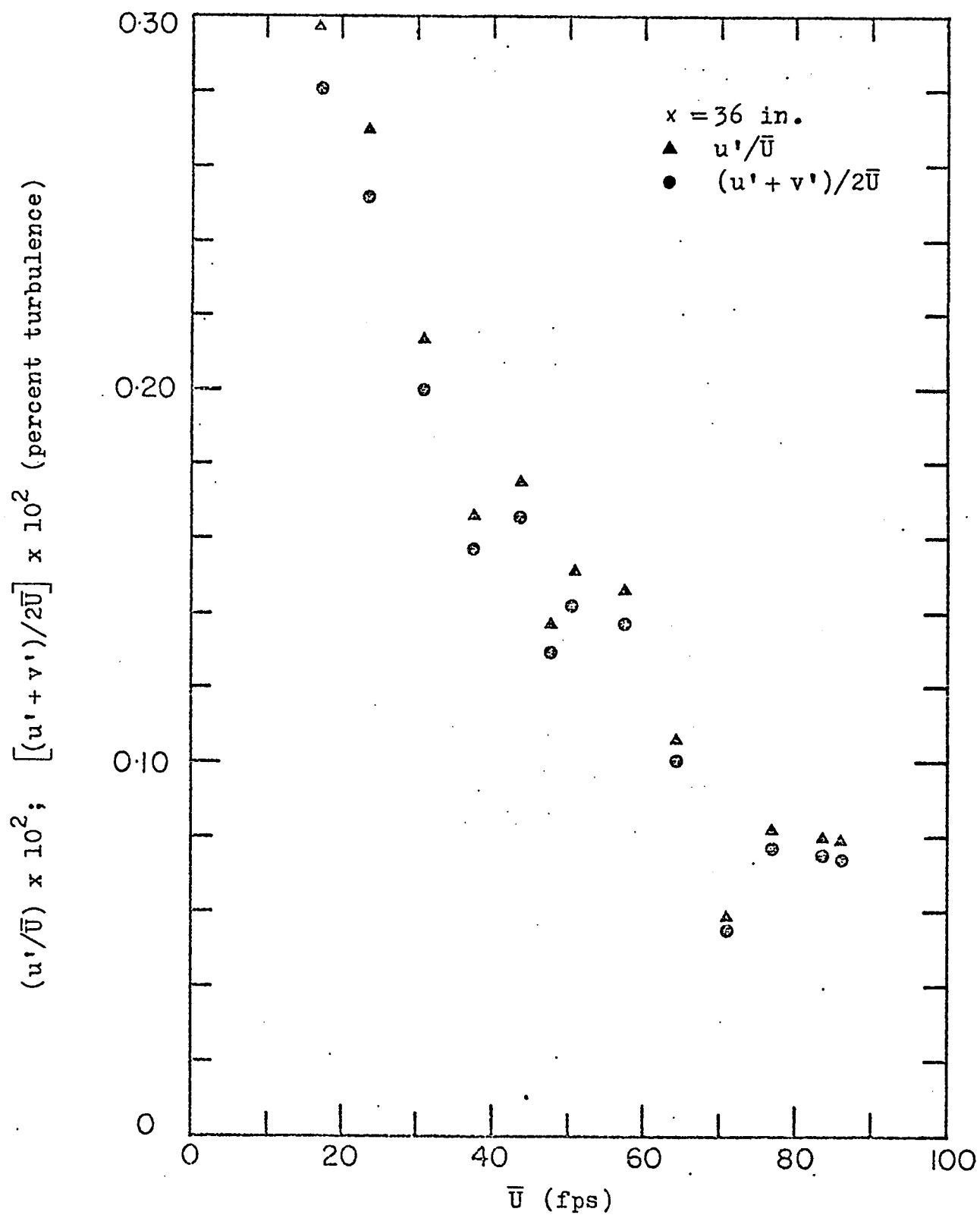
Fig. 15. Variation of the background turbulence with mean velocity in the distorting wind-tunnel
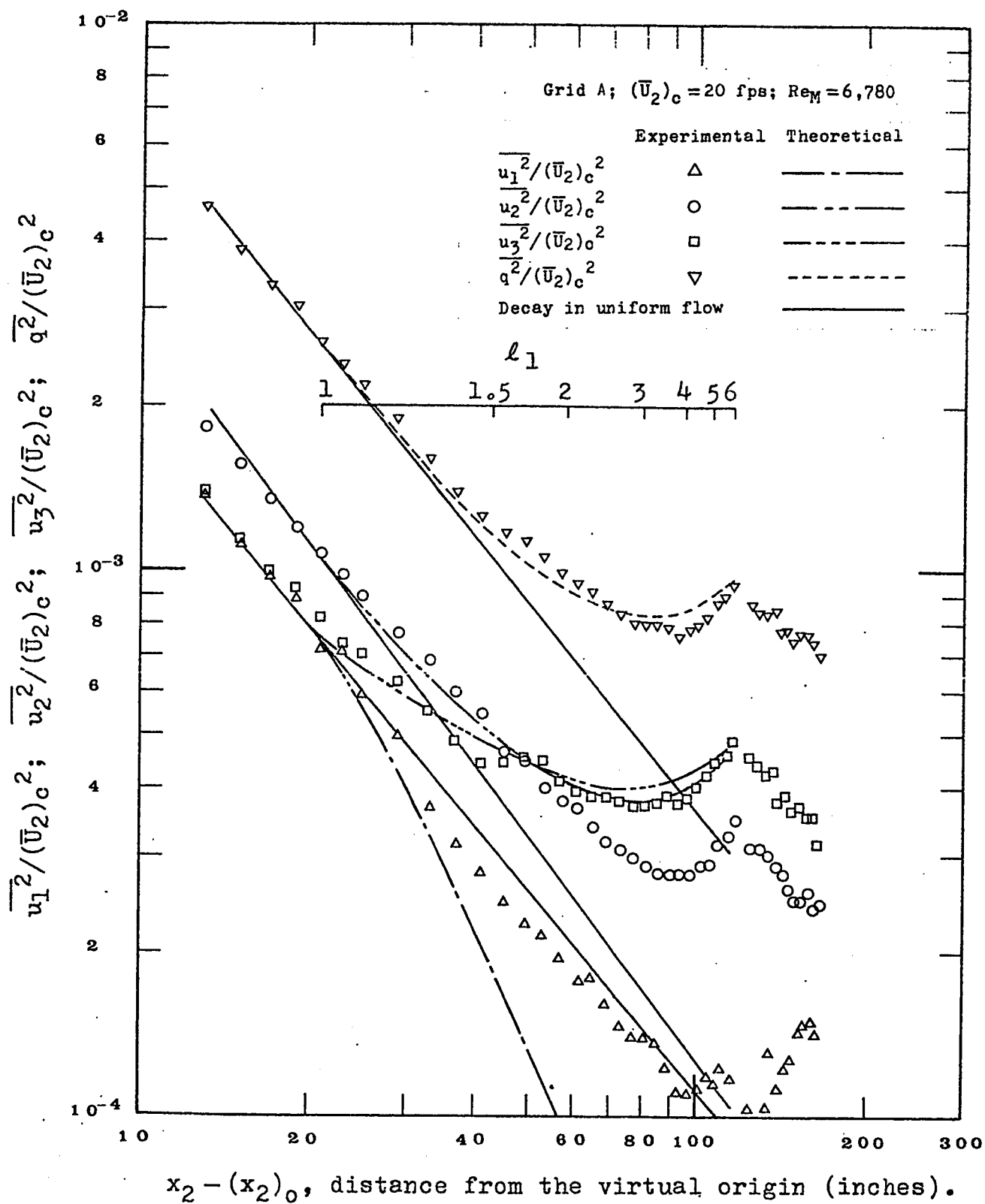
Fig. 16. Variations of turbulent intensities in the distorting wind-tunnel using grid A.
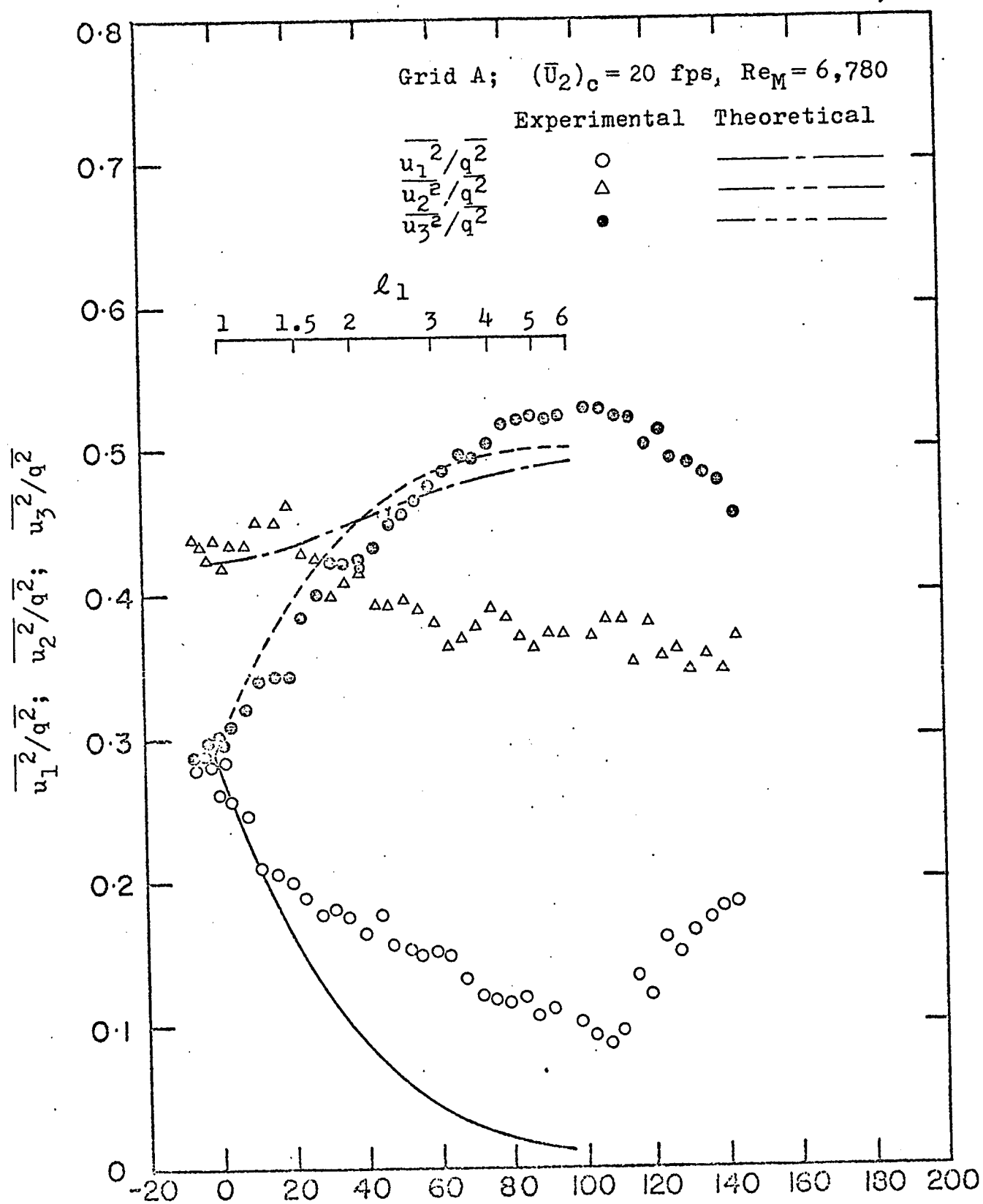
Distance from the entrance of the distorting section (inches).

Fig. 17. Variations of local turbulent intensity ratios in the distorting wind-tunnel using grid A.
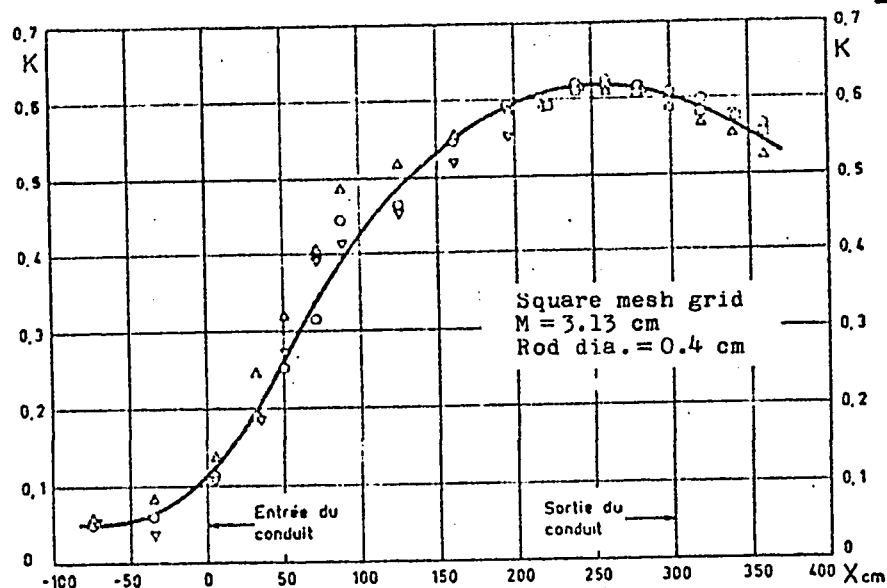
Maréchal's[37]curve (symbols not identified, reprinted from
Compte Rendus de l'Academie des Sciences, Paris, 487A, 1967)
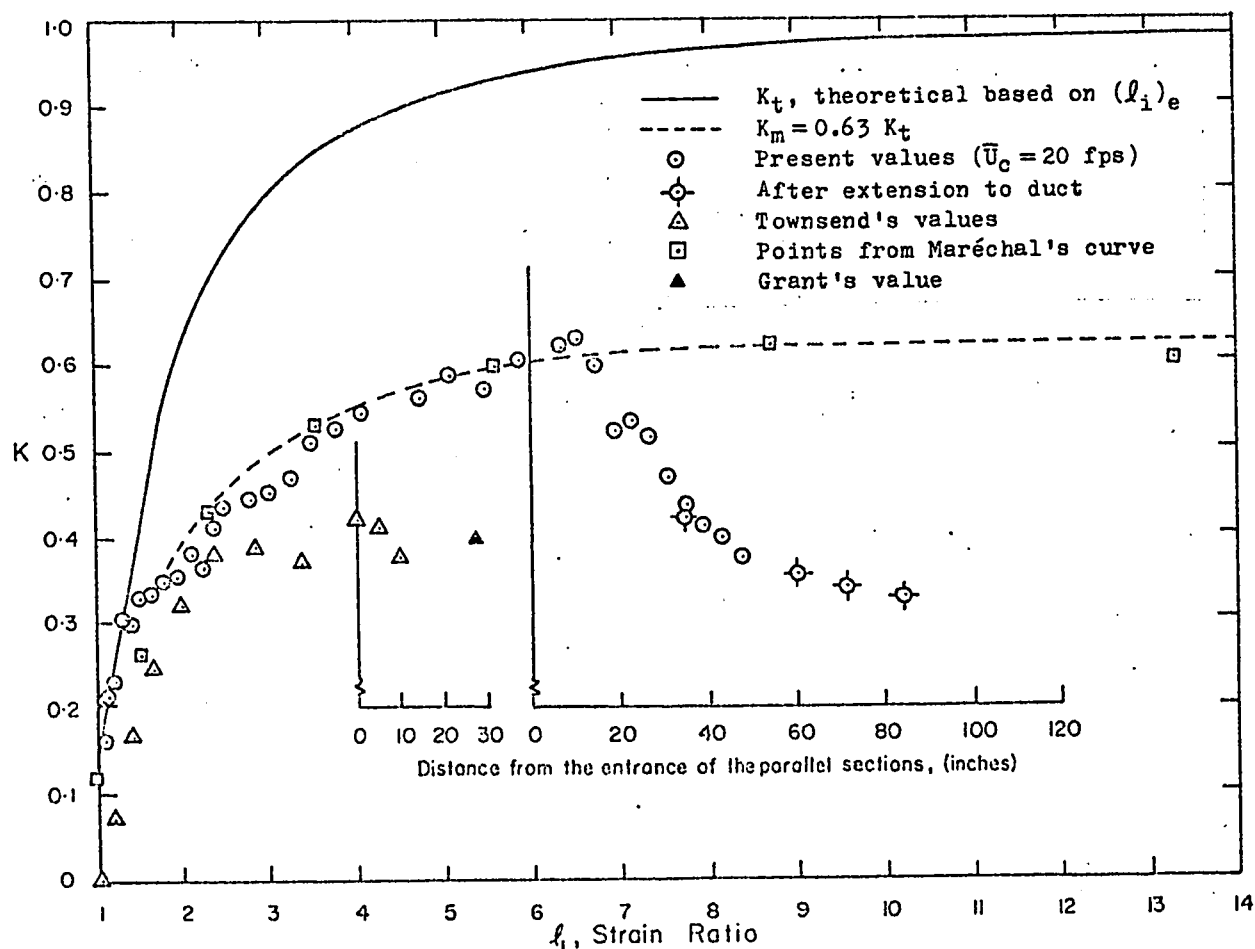
Fig. 18.   Variations of the structural measure K in the
distorting wind-tunnel using grid A.
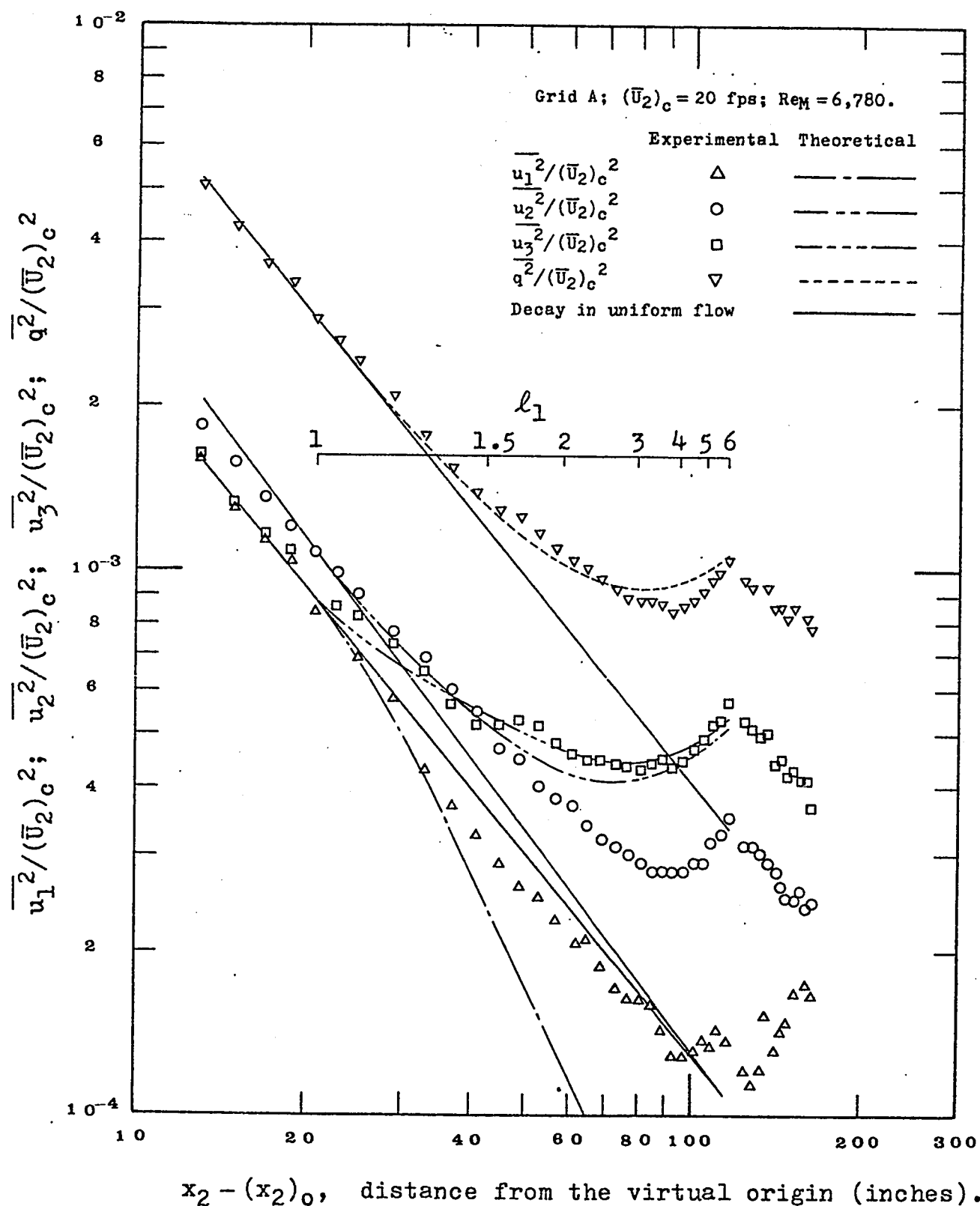
Fig. 19. Variations of turbulent intensities in the distorting wind-tunnel using grid A, k = 0.20.
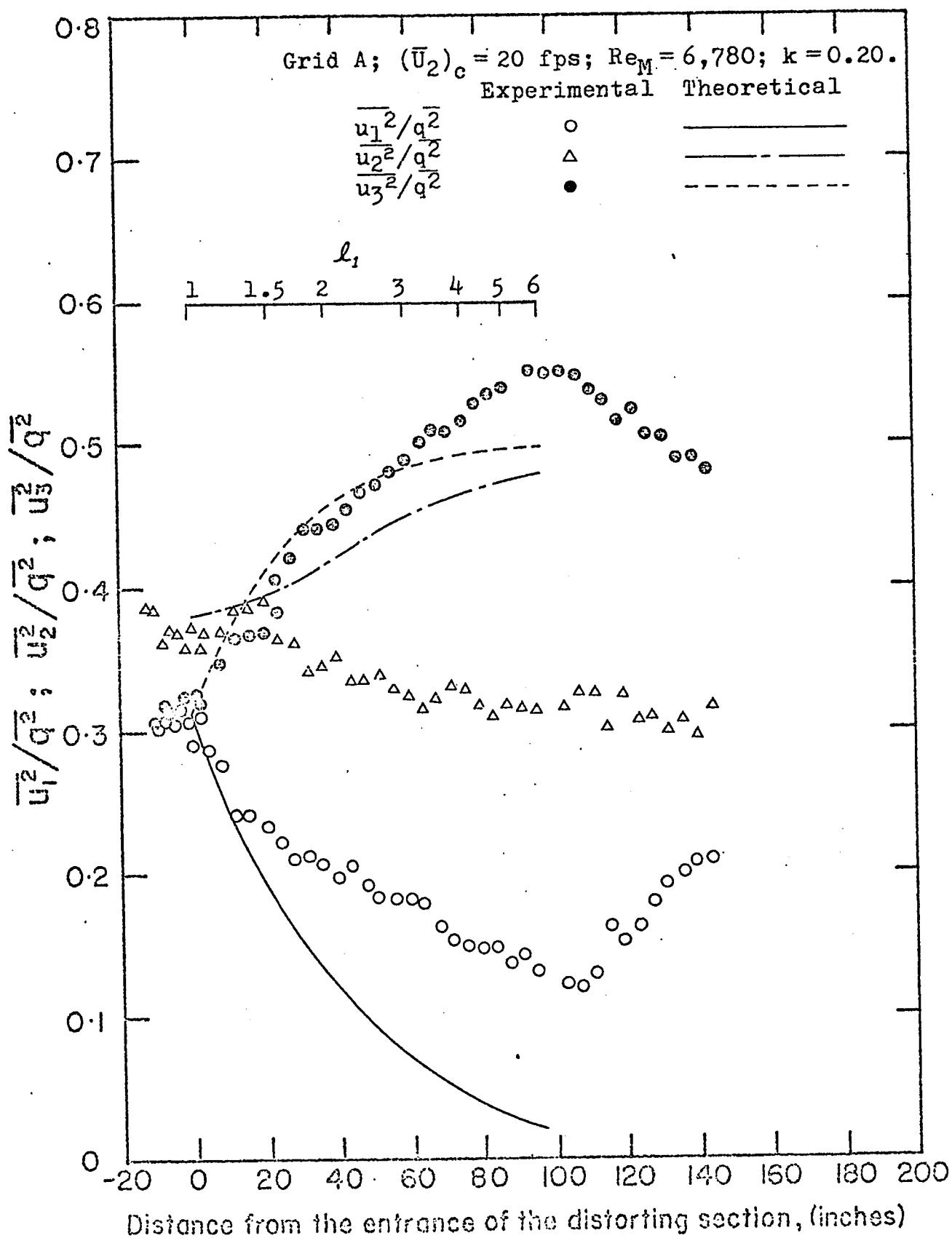
Fig. 20. Variations of local turbulent intensity ratios in the distorting wind-tunnel using grid A; k = 0.20.
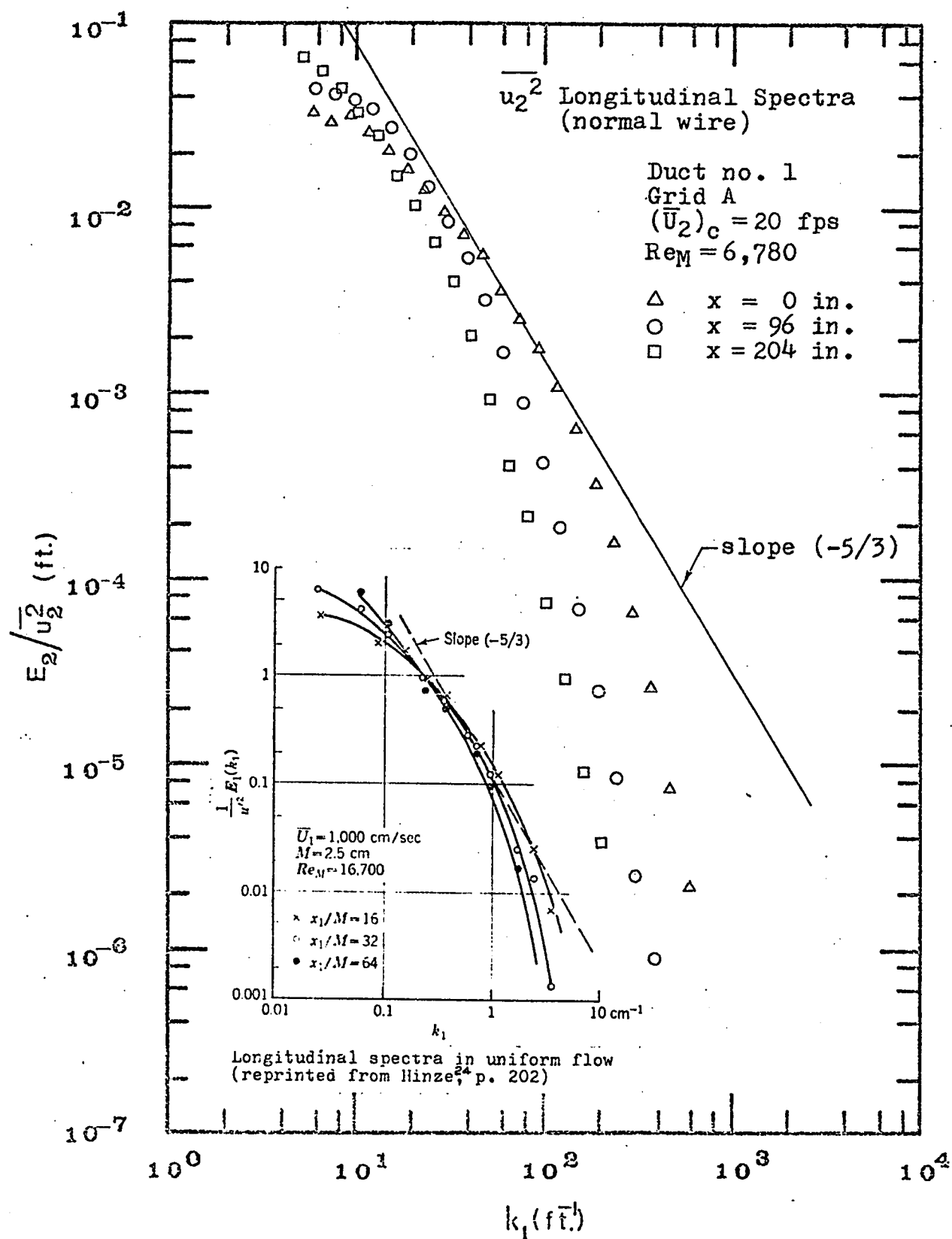
Fig. 21. Changes in the one-dimensional $\overline{u_2^2}$ spectrum in the distorting wind-tunnel (using normal wire).
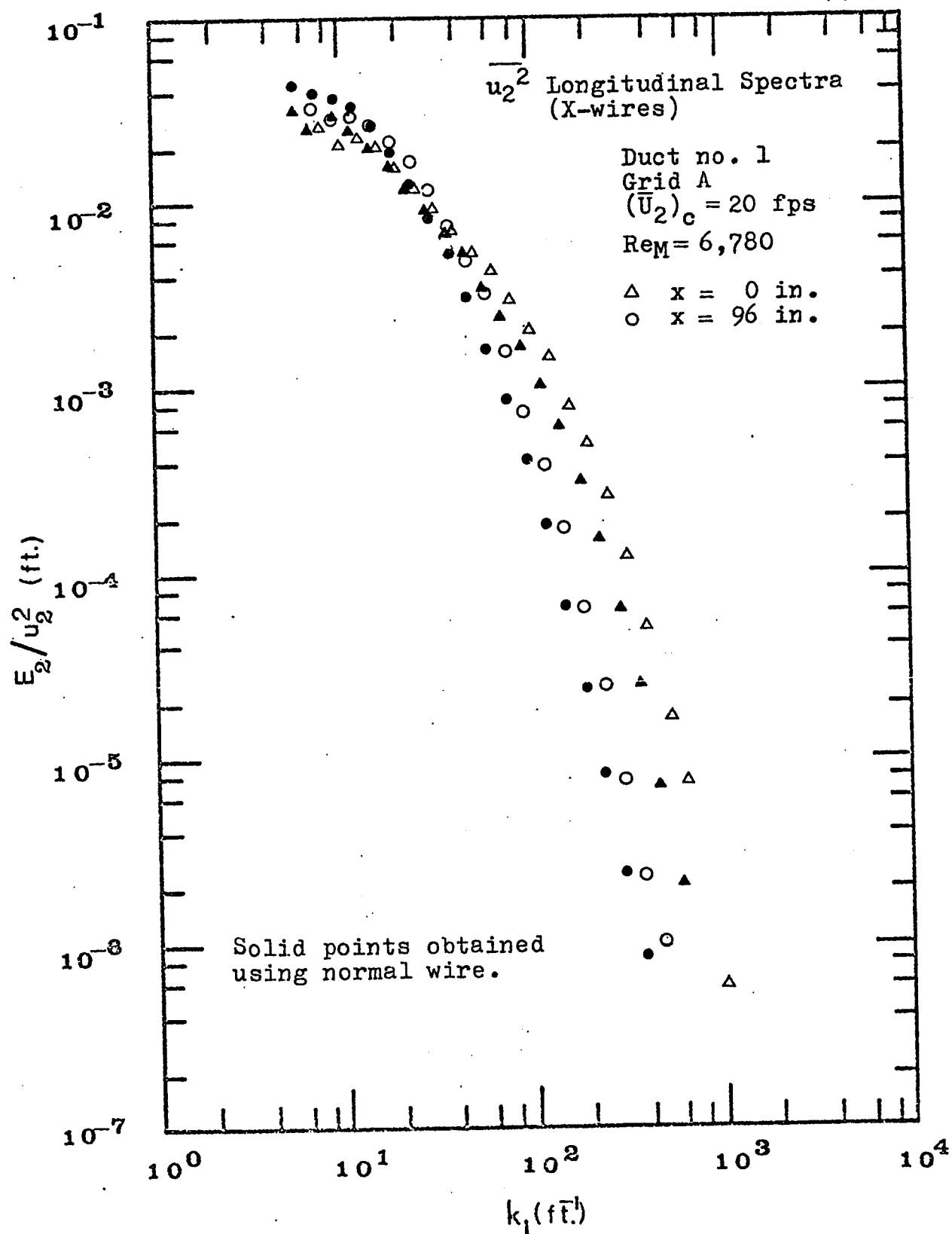
Fig. 22. Changes in the one-dimensional $\overline{u_2^2}$ spectrum in the distorting wind-tunnel (using X-wires).
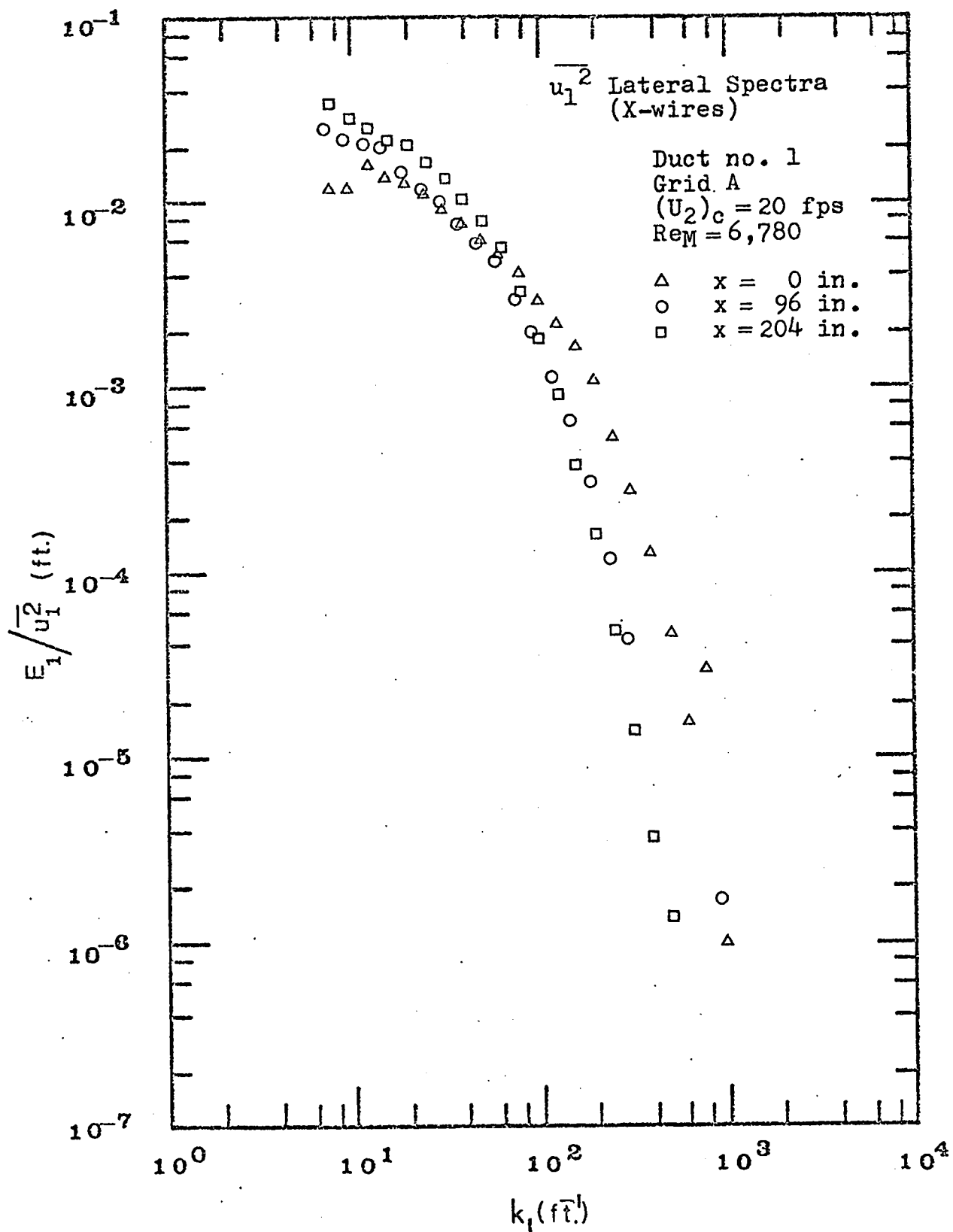
Fig. 23. Changes in the one-dimensional $\overline{u_1^2}$ spectrum in the distorting wind-tunnel.
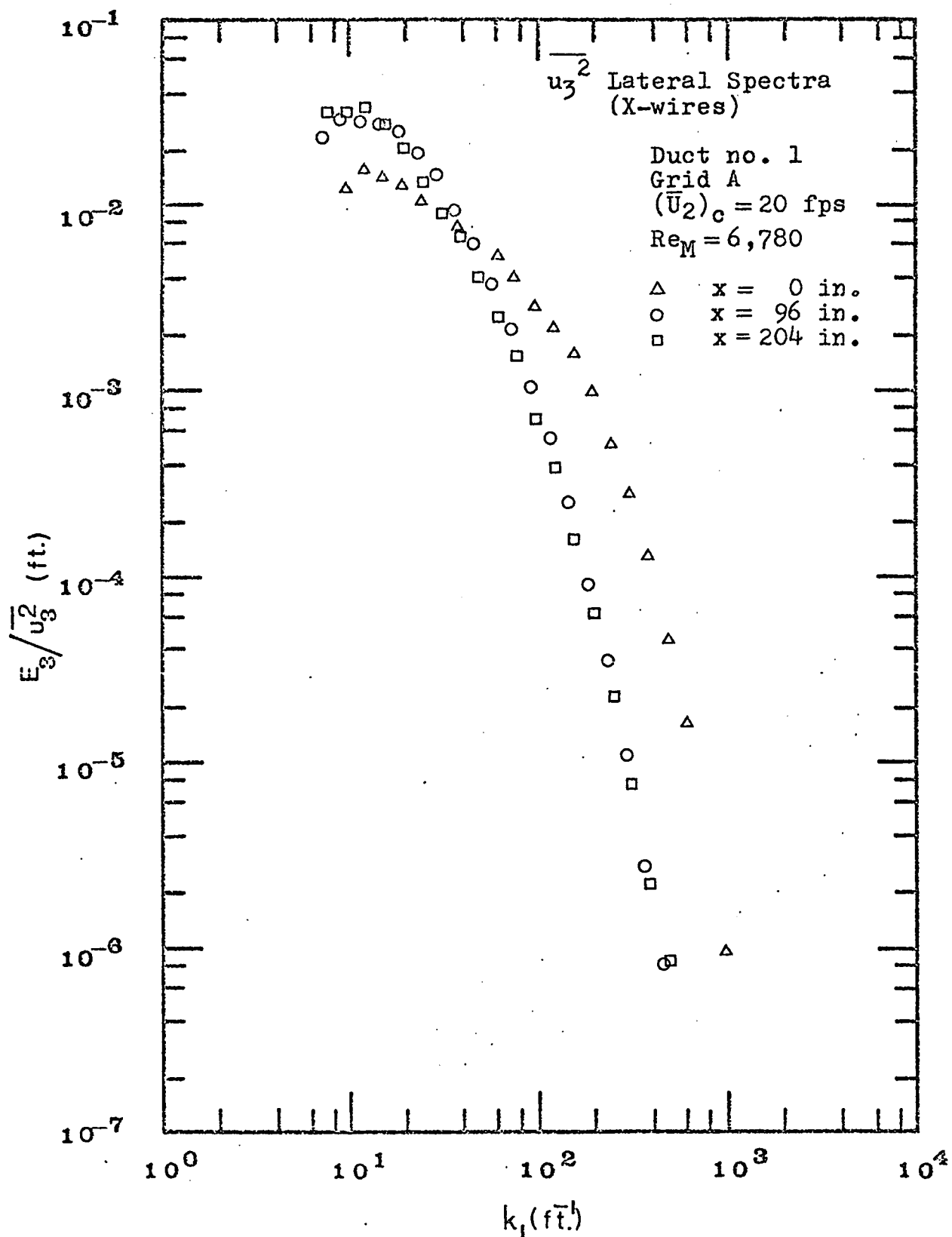
Fig. 24. Changes in the one-dimensional $\overline{u_3^2}$ spectrum in the distorting wind-tunnel.
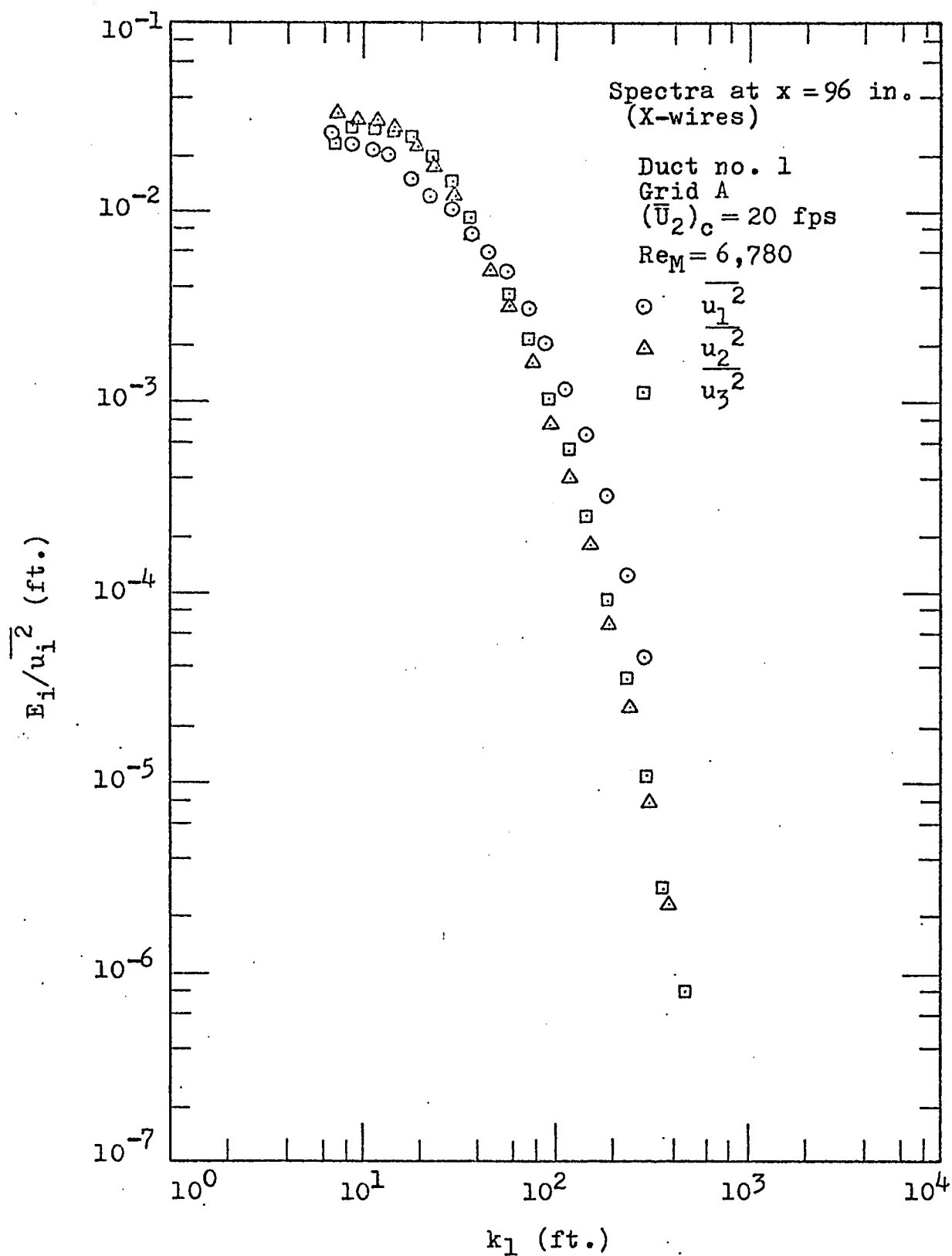
Fig. 25. Comparison of $\overline{u_1}^2$, $\overline{u_2}^2$ and $\overline{u_3}^2$ spectra in the distorting wind-tunnel after distortion.
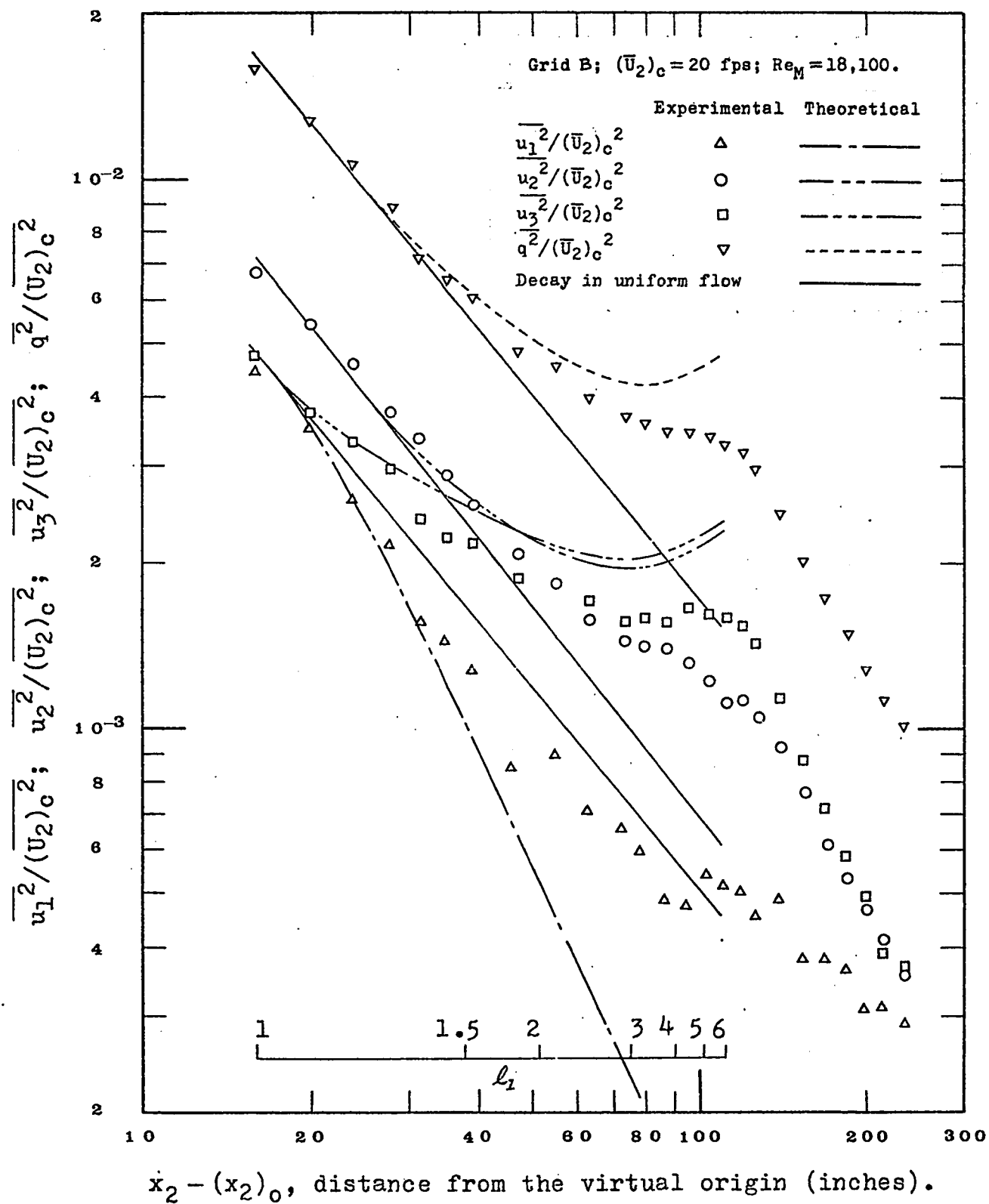
Fig. 26. Variations of turbulent intensities in the distorting wind-tunnel using grid B.
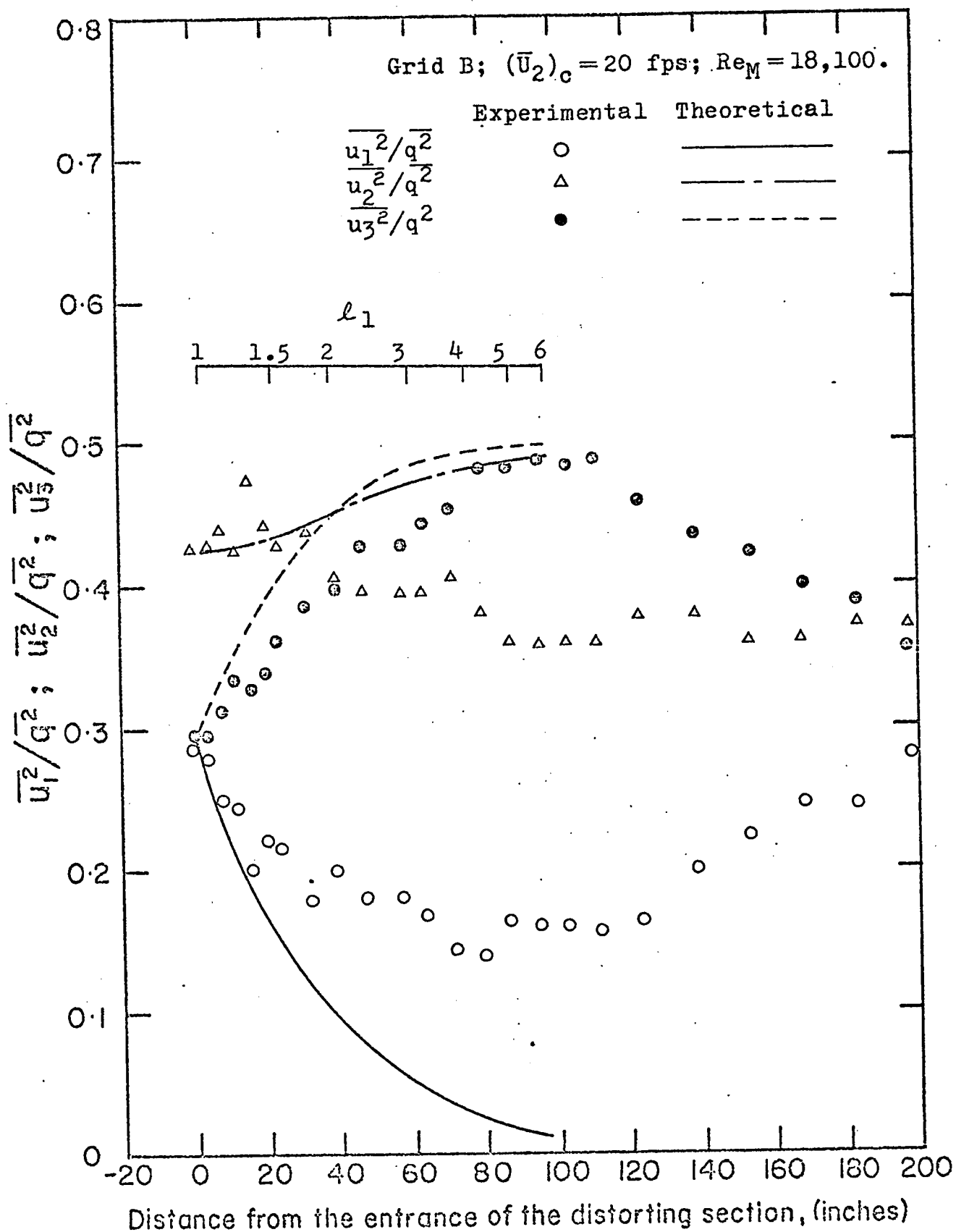
Fig. 27. Variations of the local turbulent intensity ratios in the distorting wind-tunnel using grid B.
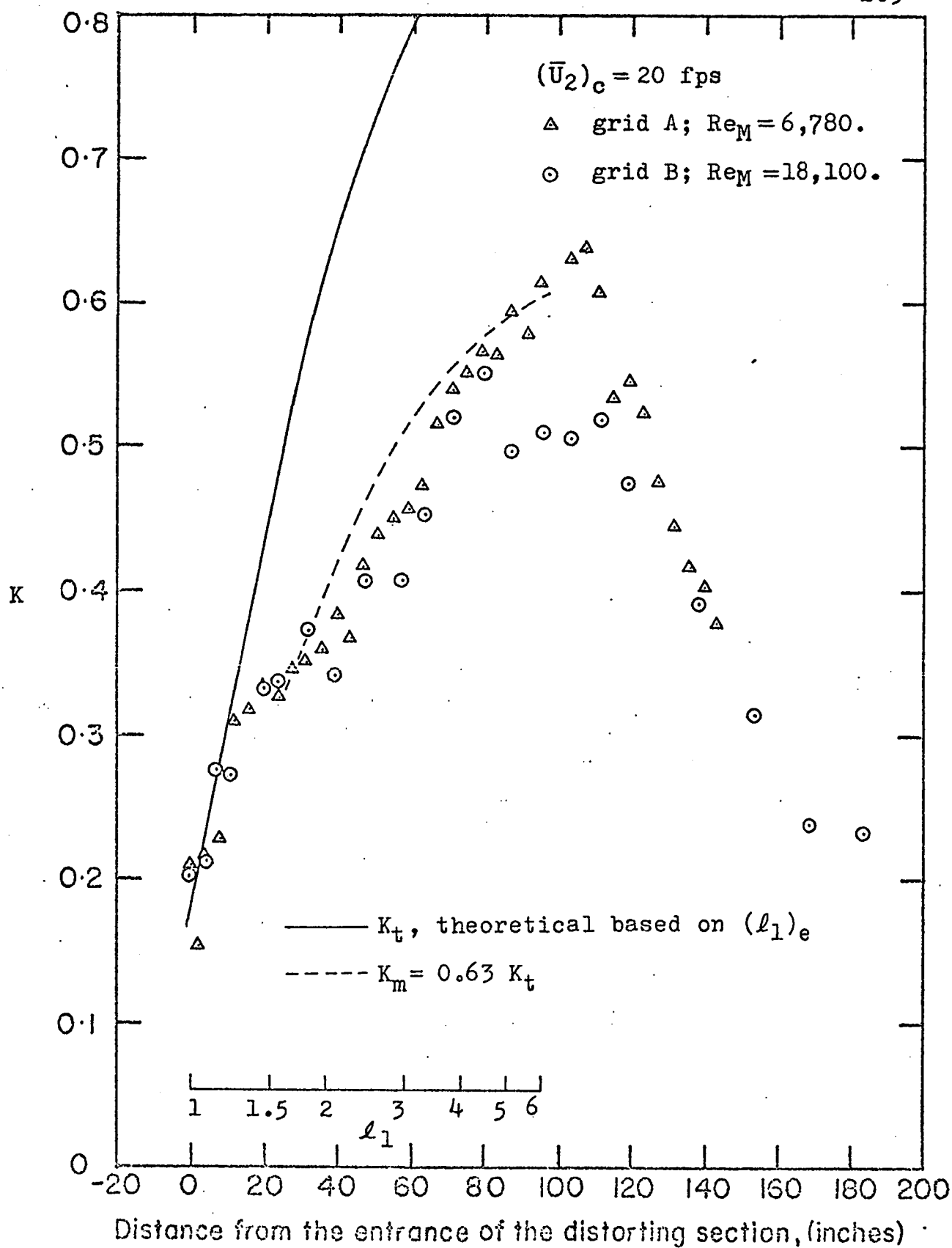
Fig. 28. Comparison of the structural measure K in the distorting wind-tunnel for geometrically similar grids A and B.
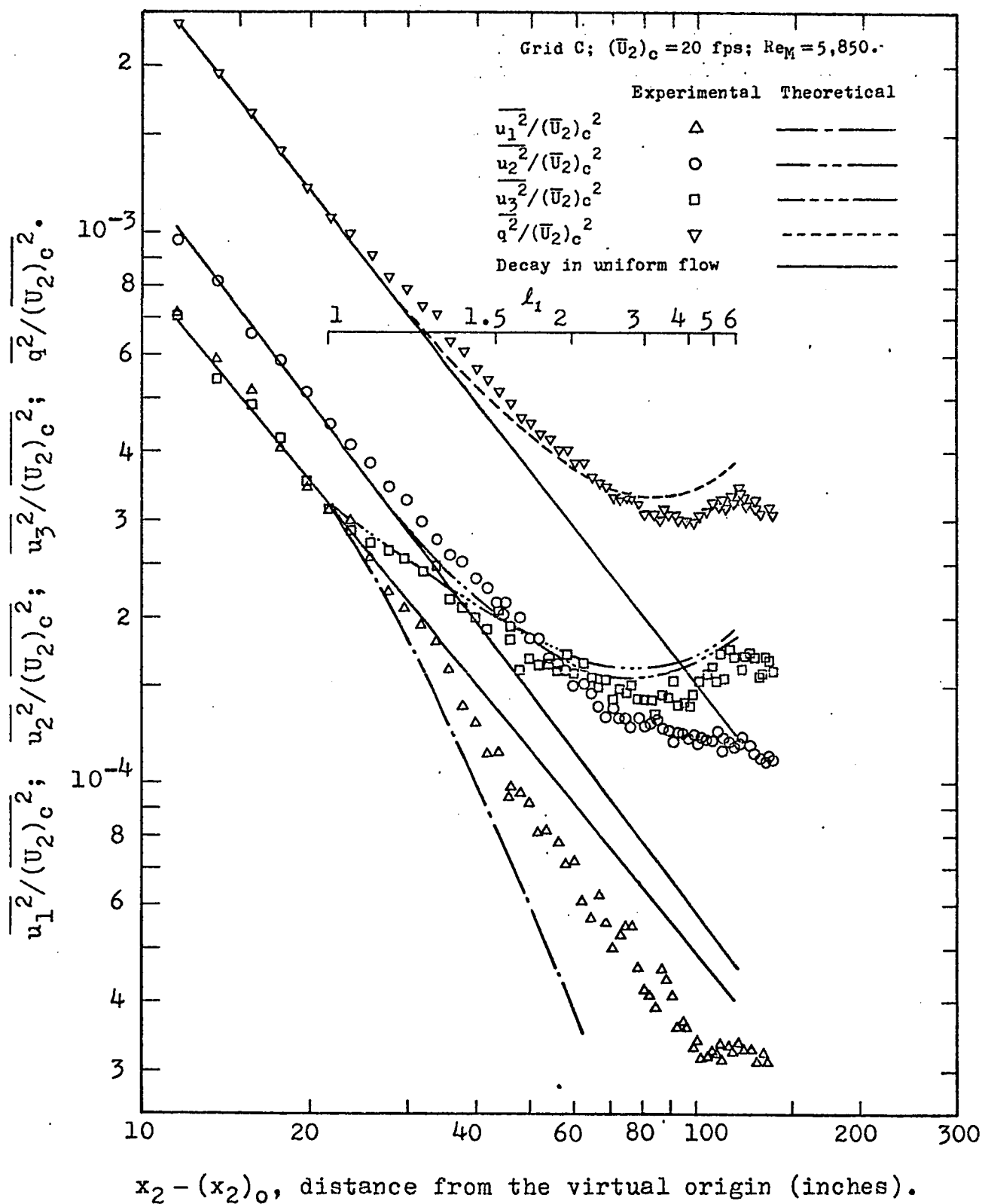
Fig. 29. Variations of turbulent intensities in the distorting
wind-tunnel using grid C and velocity 20 fps.
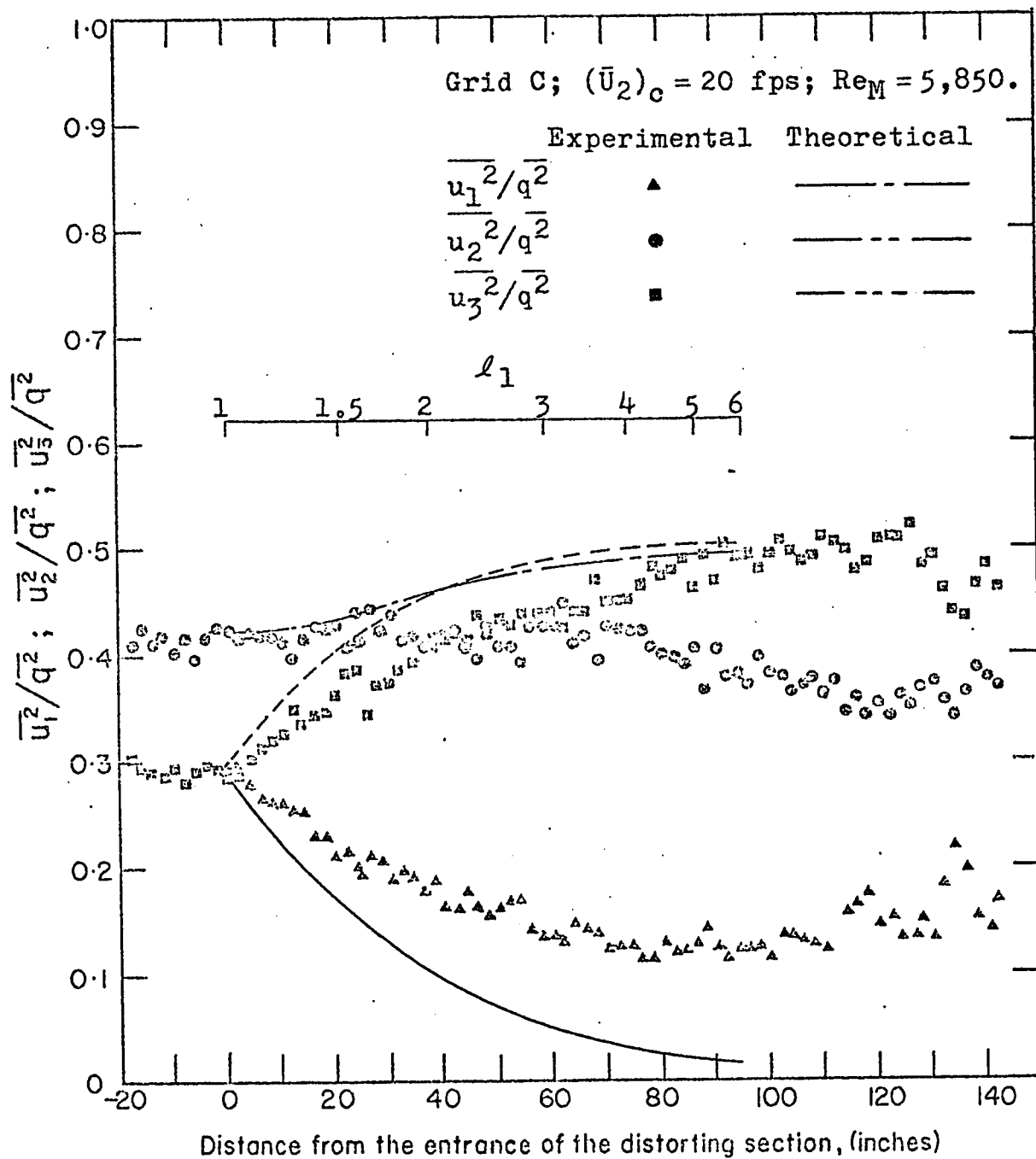
Fig. 30. Variations of the local turbulent intensity ratios in the distorting wind-tunnel, using grid C and velocity 20 fps.

$x_2 - (x_2)_o$, distance from the virtual origin (inches).
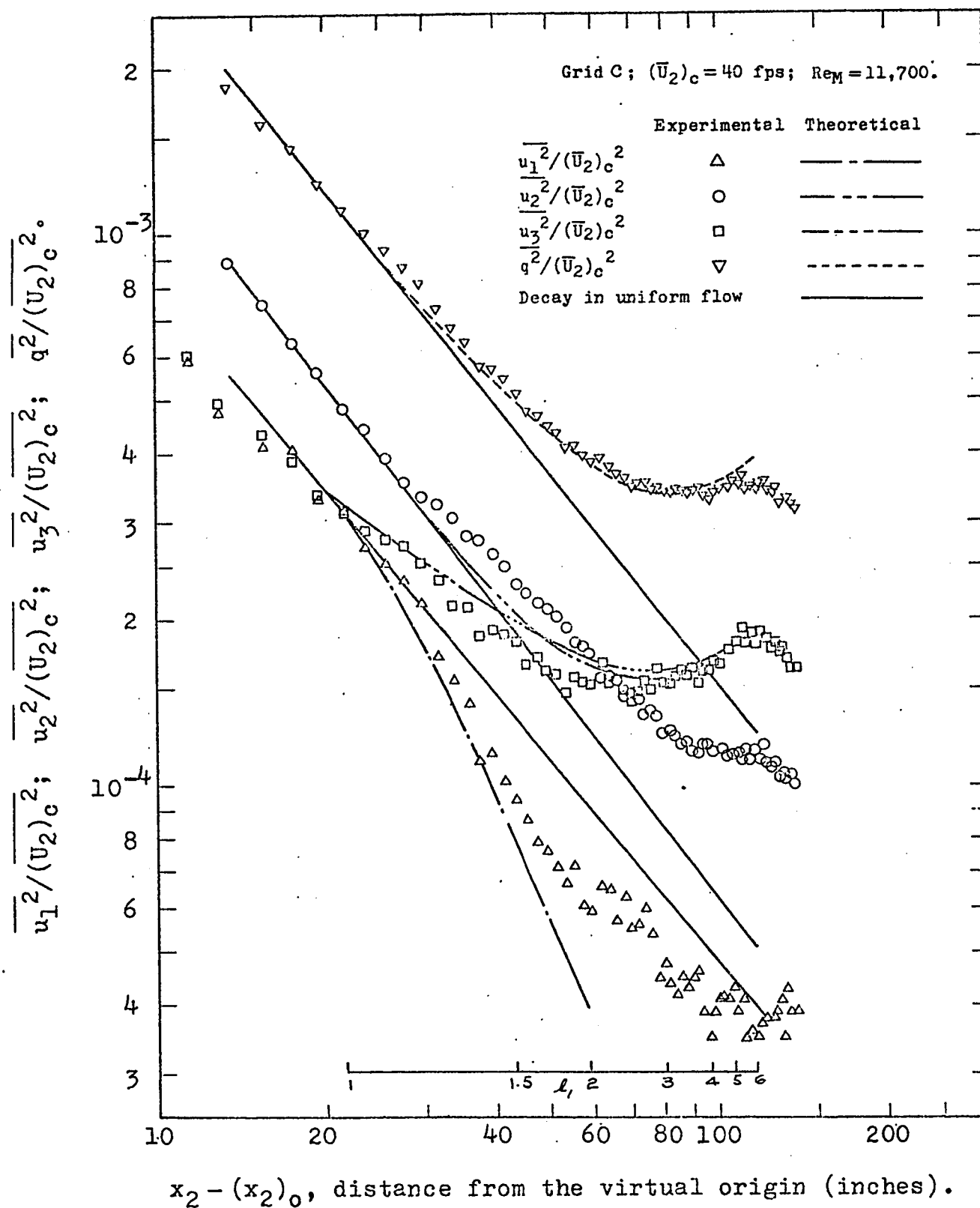
Fig. 31. Variations of the turbulent intensities in the
distorting wind-tunnel using grid C and velocity
40 fps.
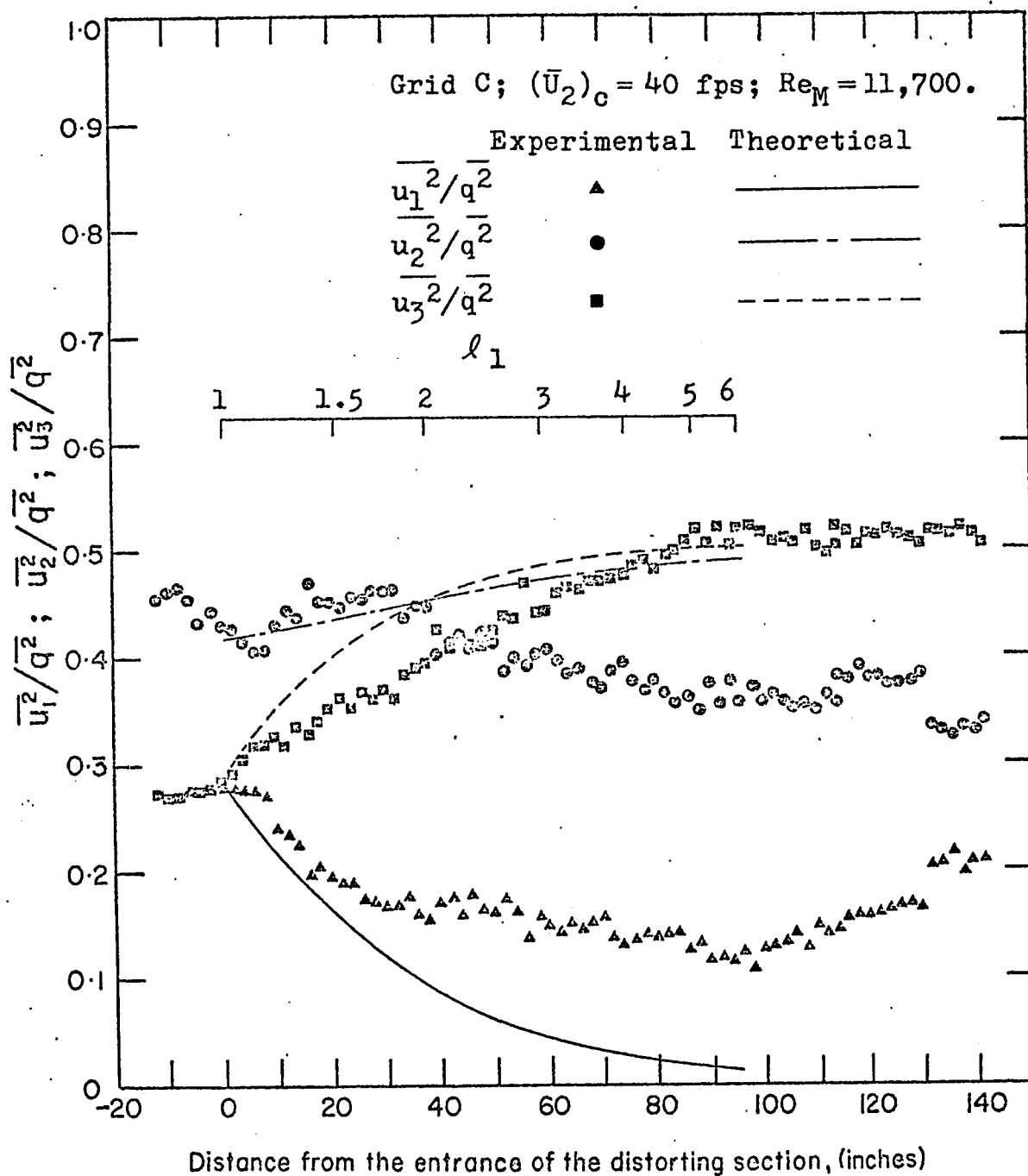
Fig. 32. Variations of the local turbulent intensity ratios in the distorting wind-tunnel using grid C and velocity 40 fps.
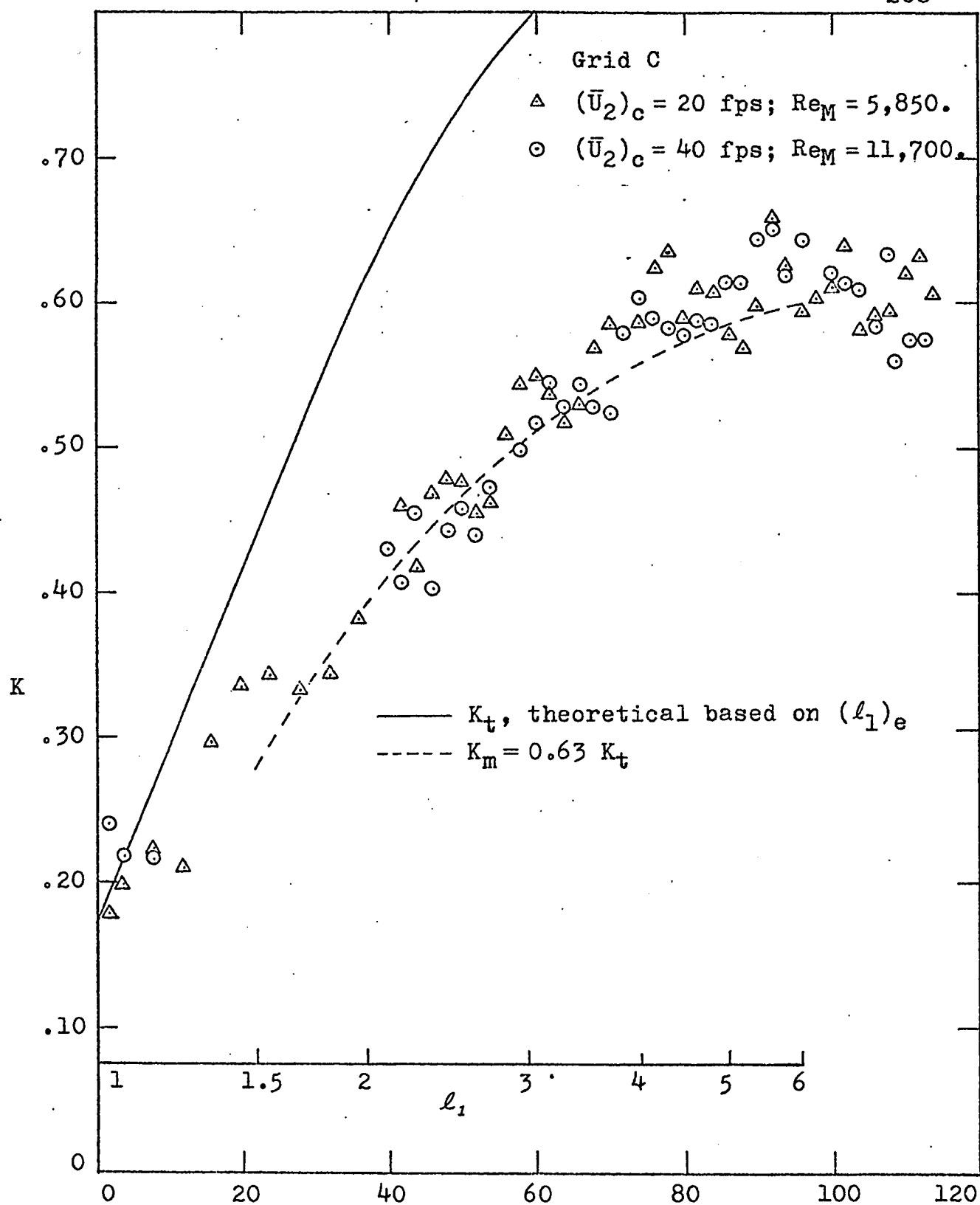
Fig. 33. Variation of the structural measure K in the distorting wind-tunnel using grid C.

GENERAL ARRANGEMENT OF THE BLOWER WIND—TUNNEL

24×22 Mesh Screen

14 × 15 Mesh Screen

17" × 30" Working Section

Honeycomb, 1½" Deep, ¼" Cell

6:1 Two—Dimensional Contraction

14 × 15 Mesh Screen

Centrifugal Fan

107"

54"

104"

54"

151"

33'—4"
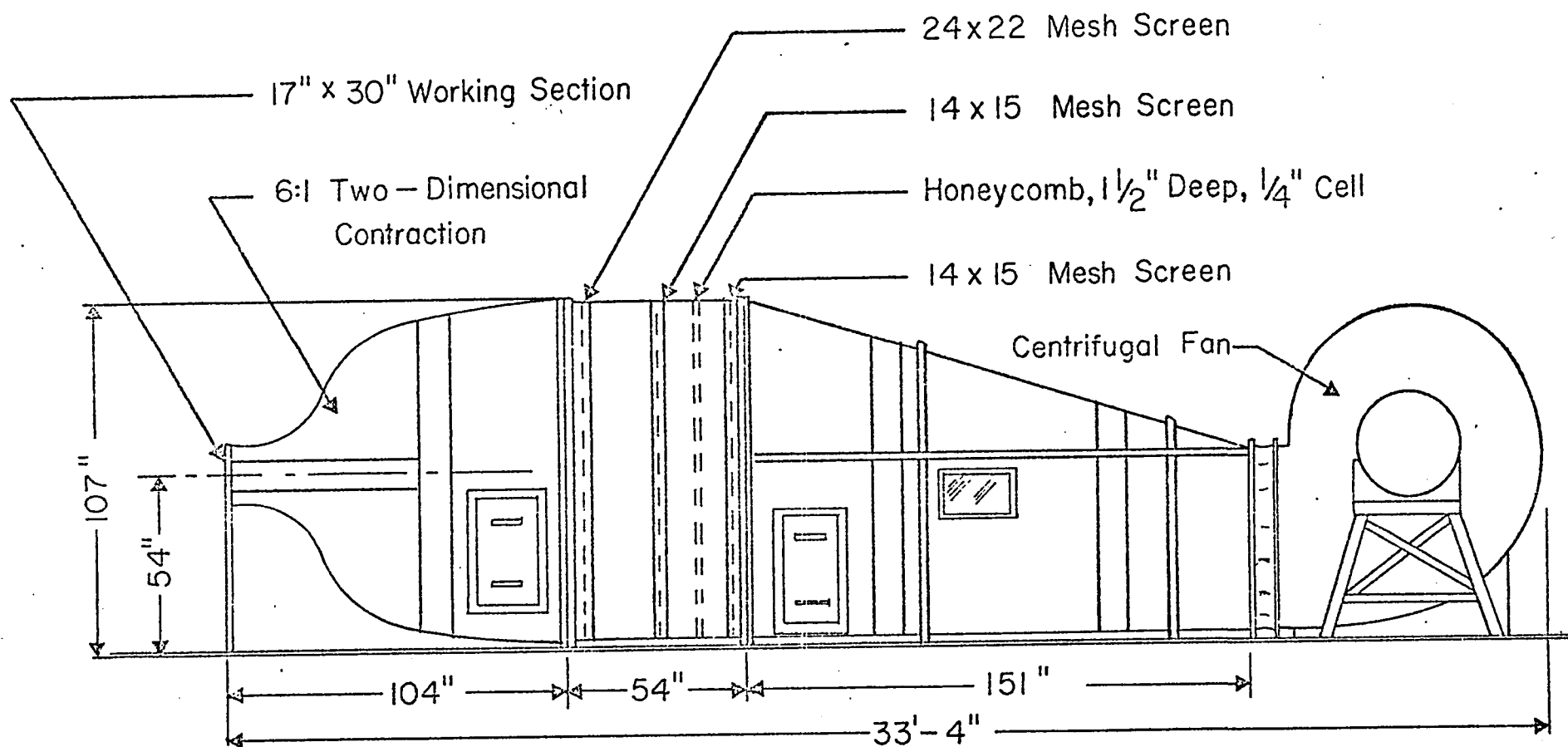
Fig. 34. General arrangement of the blower wind-tunnel
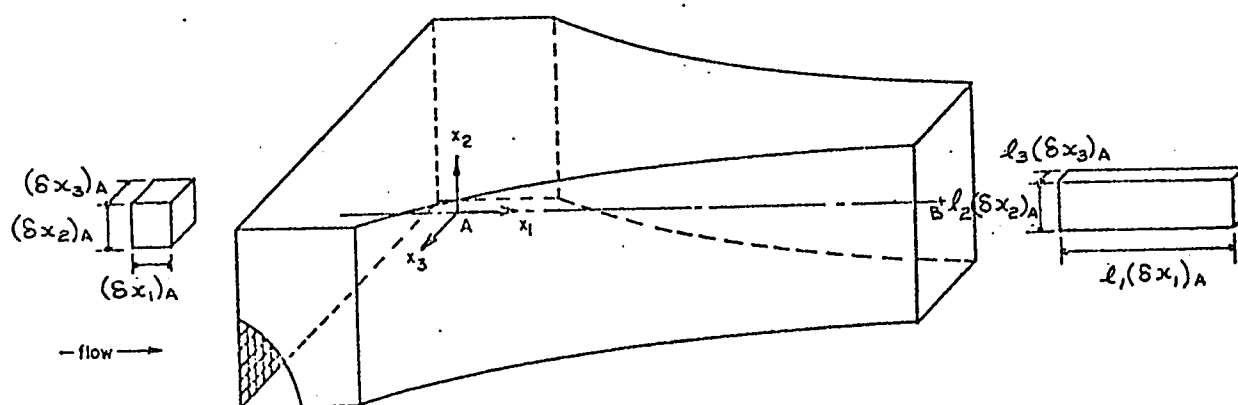
Fig. 35. Schematic representation of fluid distortion caused by a symmetrical two-dimensional contraction
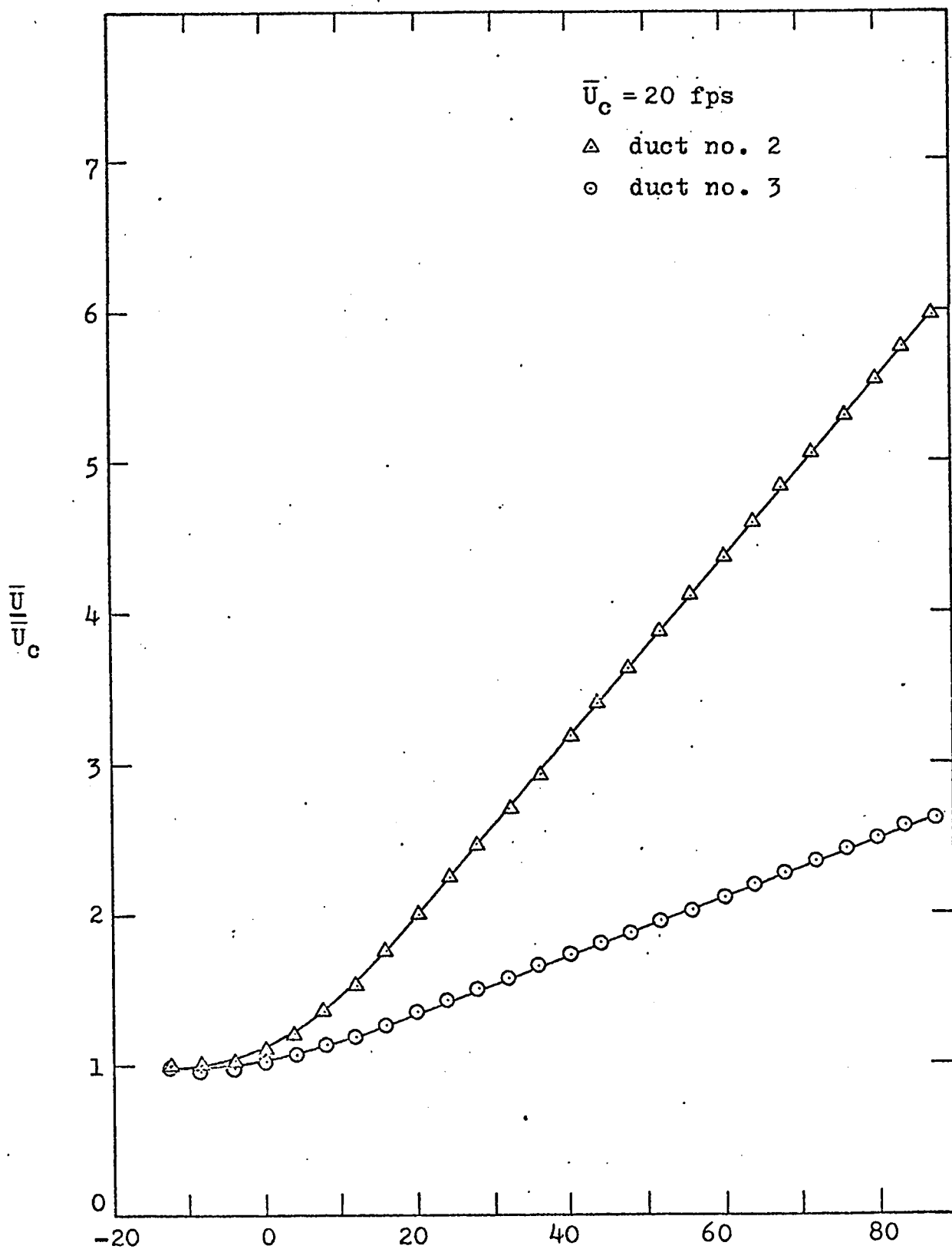
Fig. 36.   Mean velocities along the center-lines of the two-dimensional contractions.
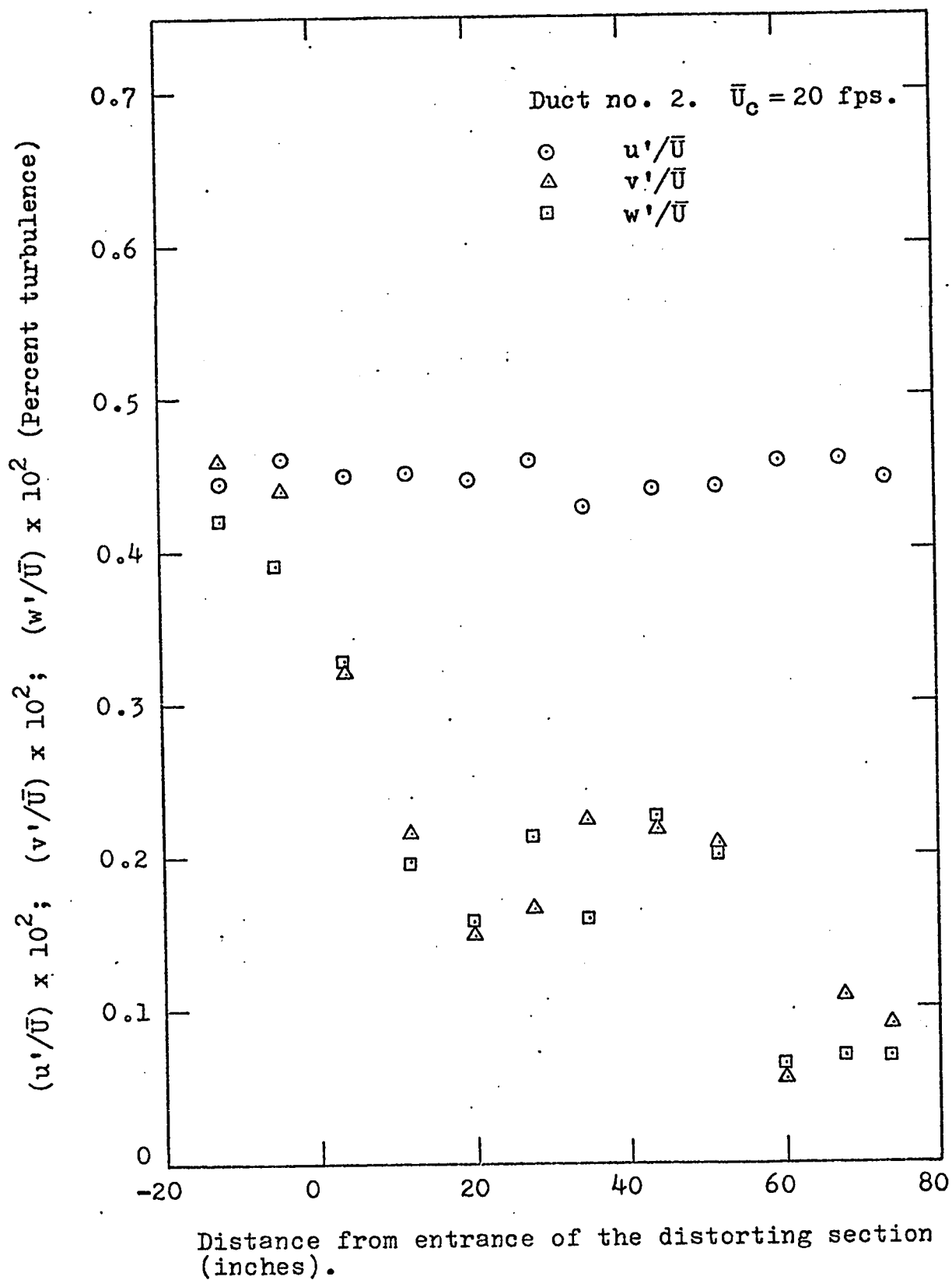
Fig. 37.   Background turbulence along the center-line of the
two-dimensional contraction.
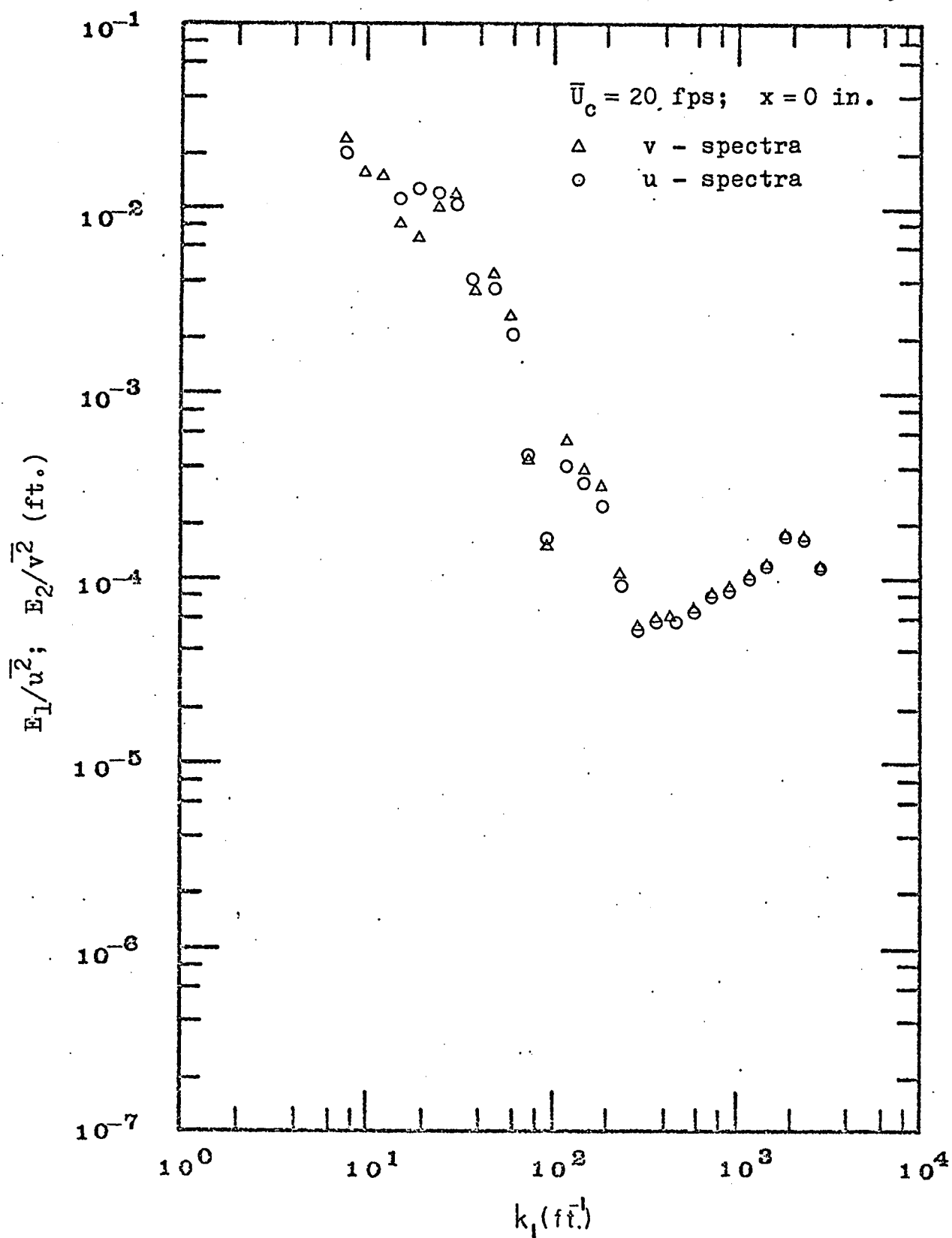
Fig. 38. Spectra of the background turbulence in the blower wind-tunnel
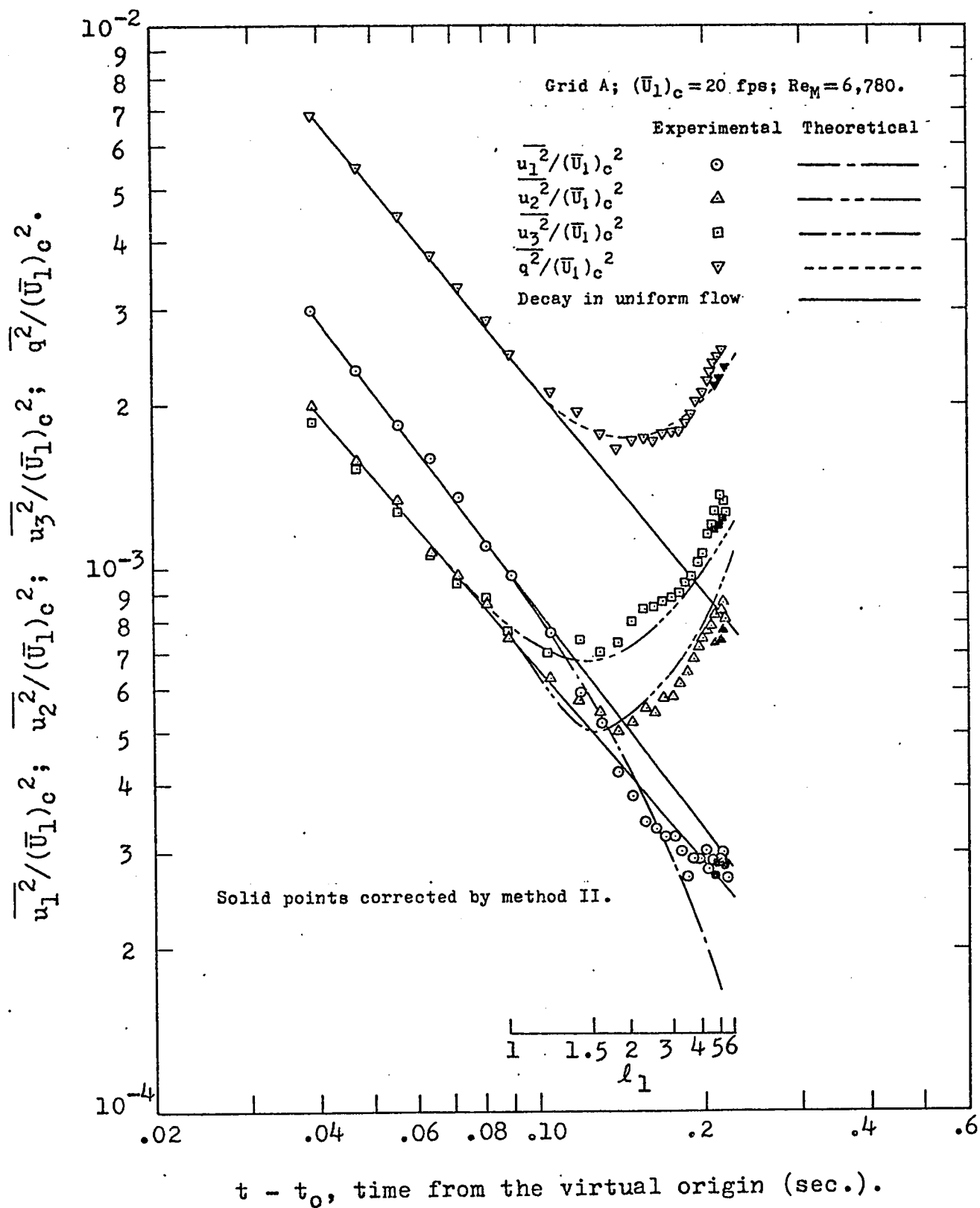
Fig. 39. Variations of turbulent intensities in the two-
dimensional contraction, duct no. 2.
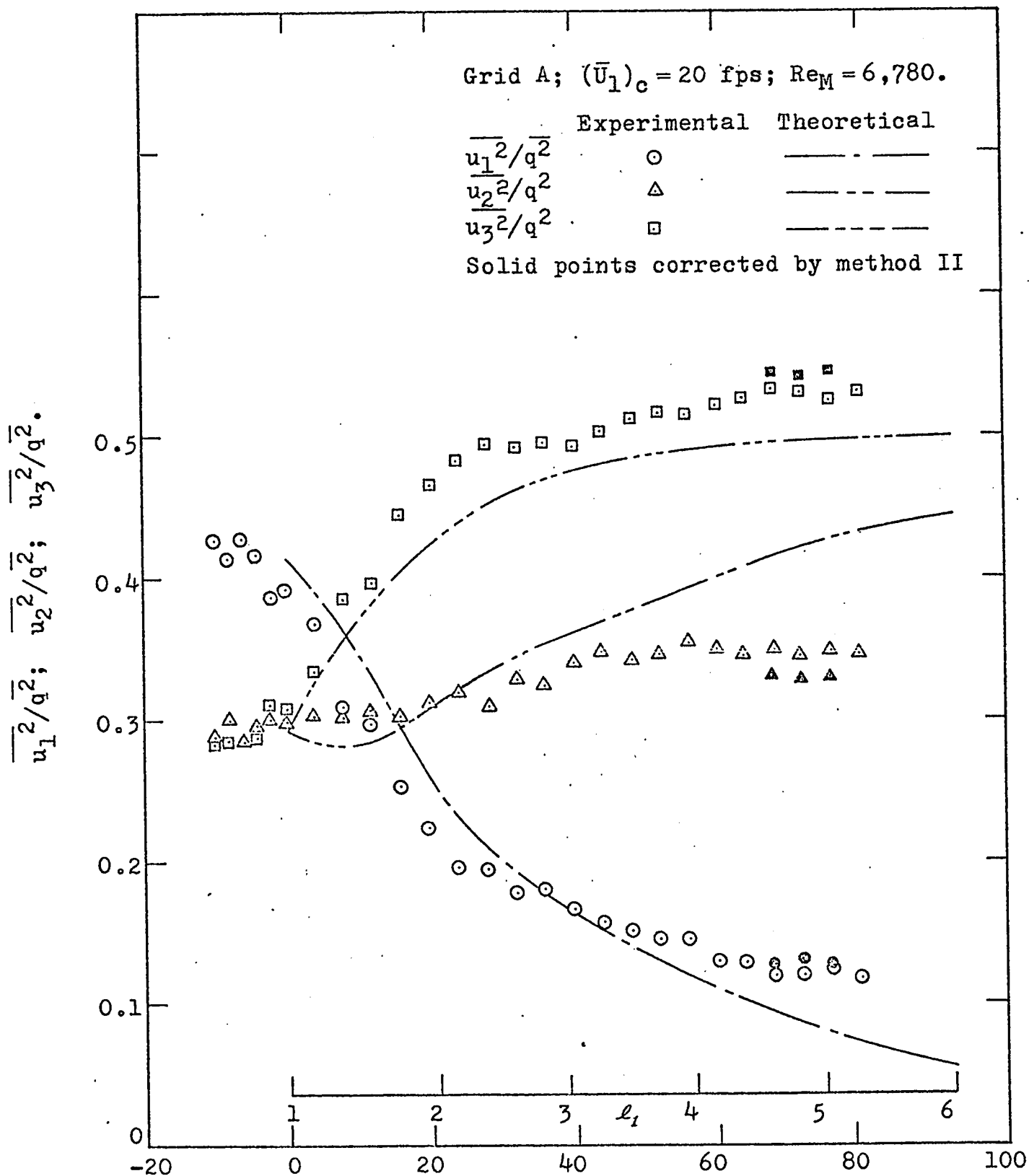
Fig. 40. Variations of the local intensity ratios in the two-
dimensional contraction, duct no. 2.
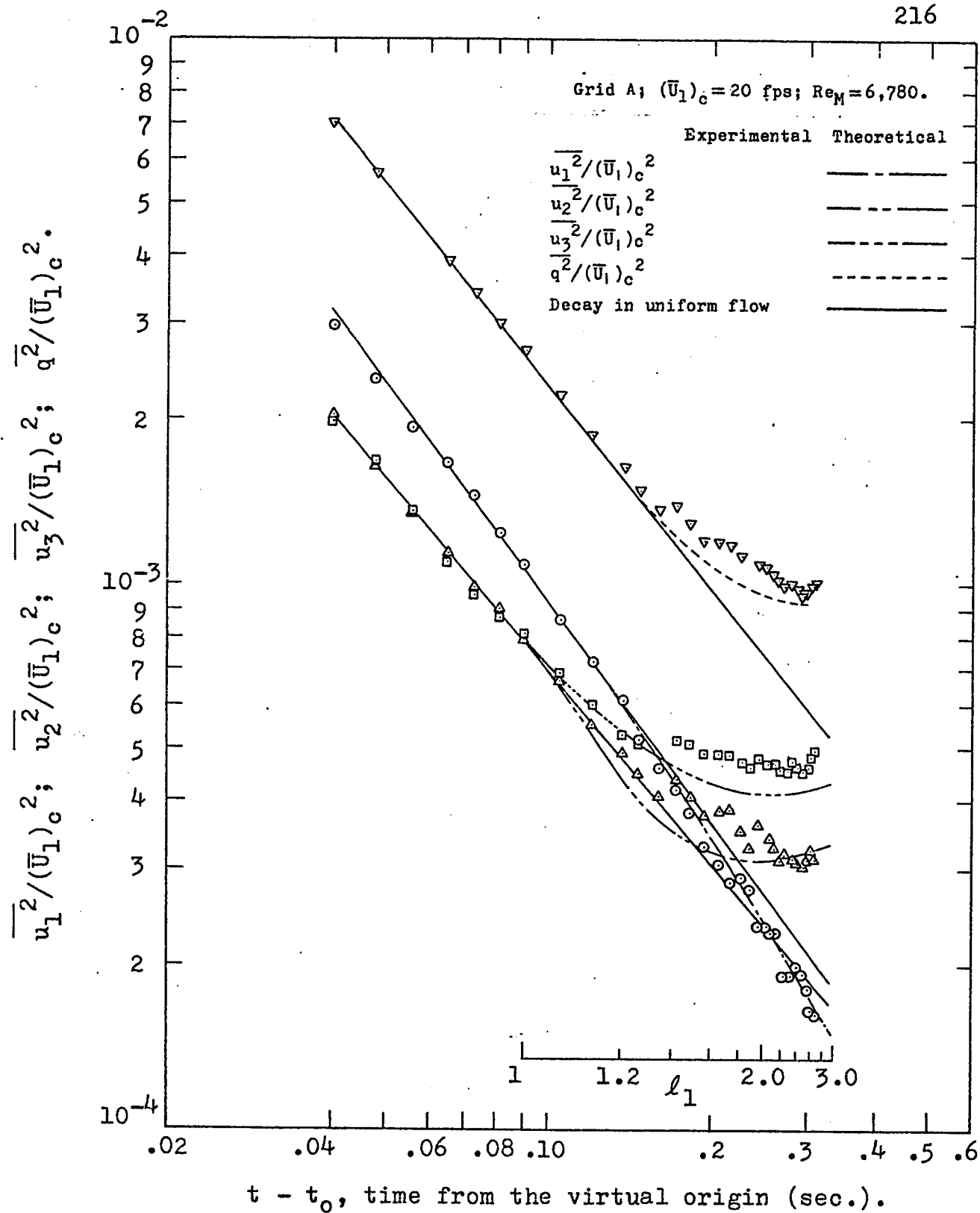
Fig. 41.   Variations of turbulent intensities in the two-dimensional contraction, duct no. 3.
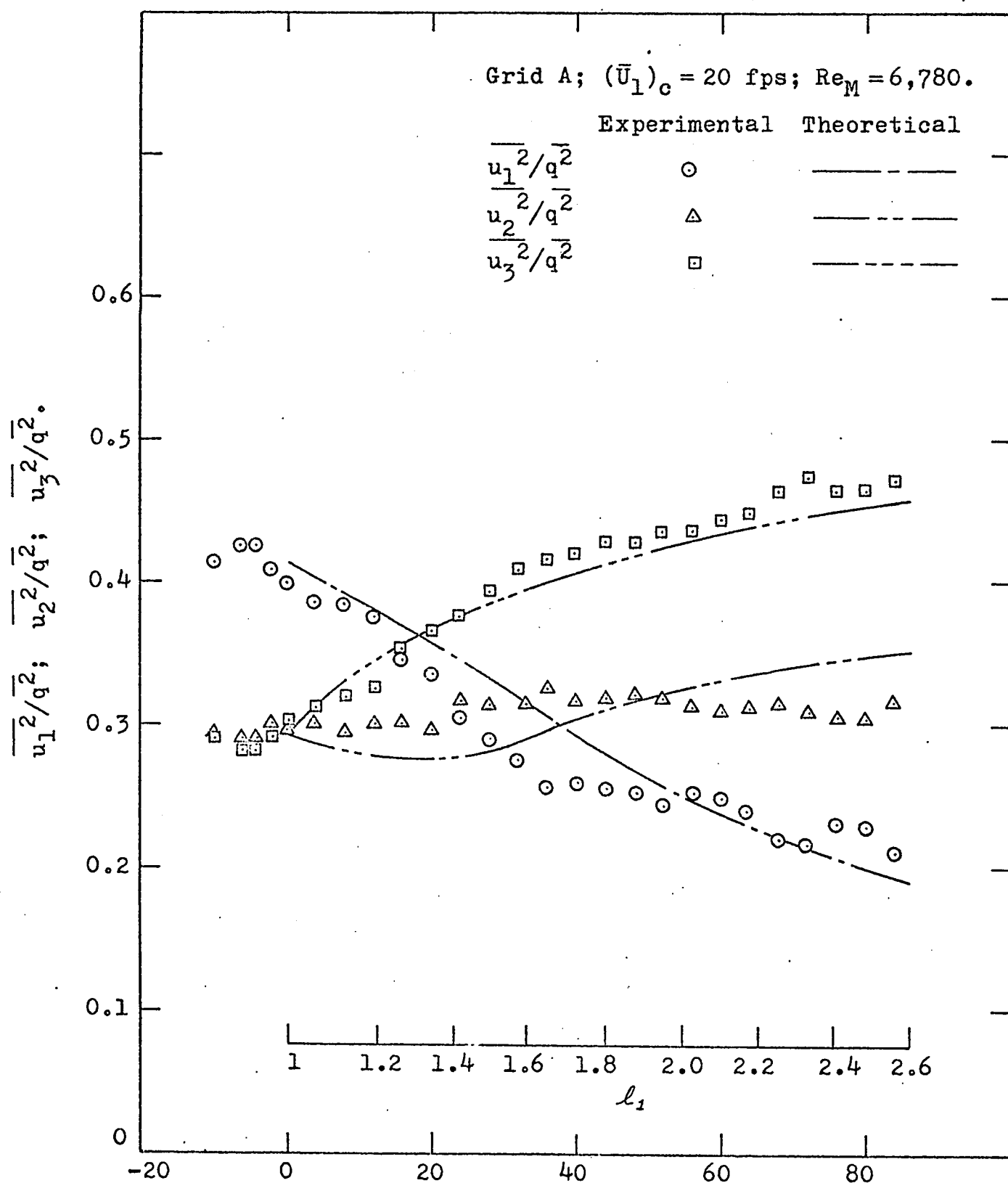
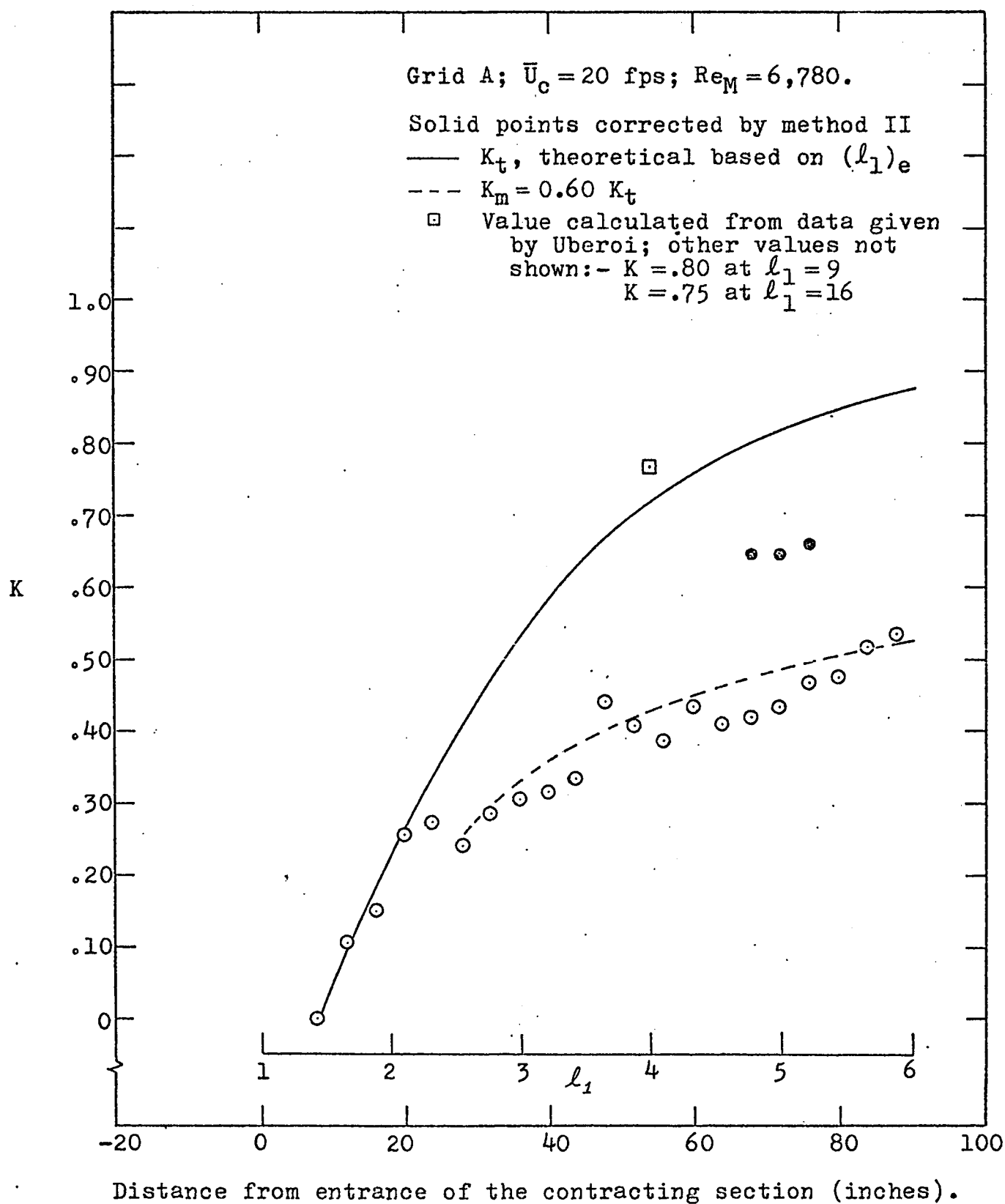Fig. 42. Variations of the local turbulent intensity ratios in the two-dimensional contraction, duct no. 3.
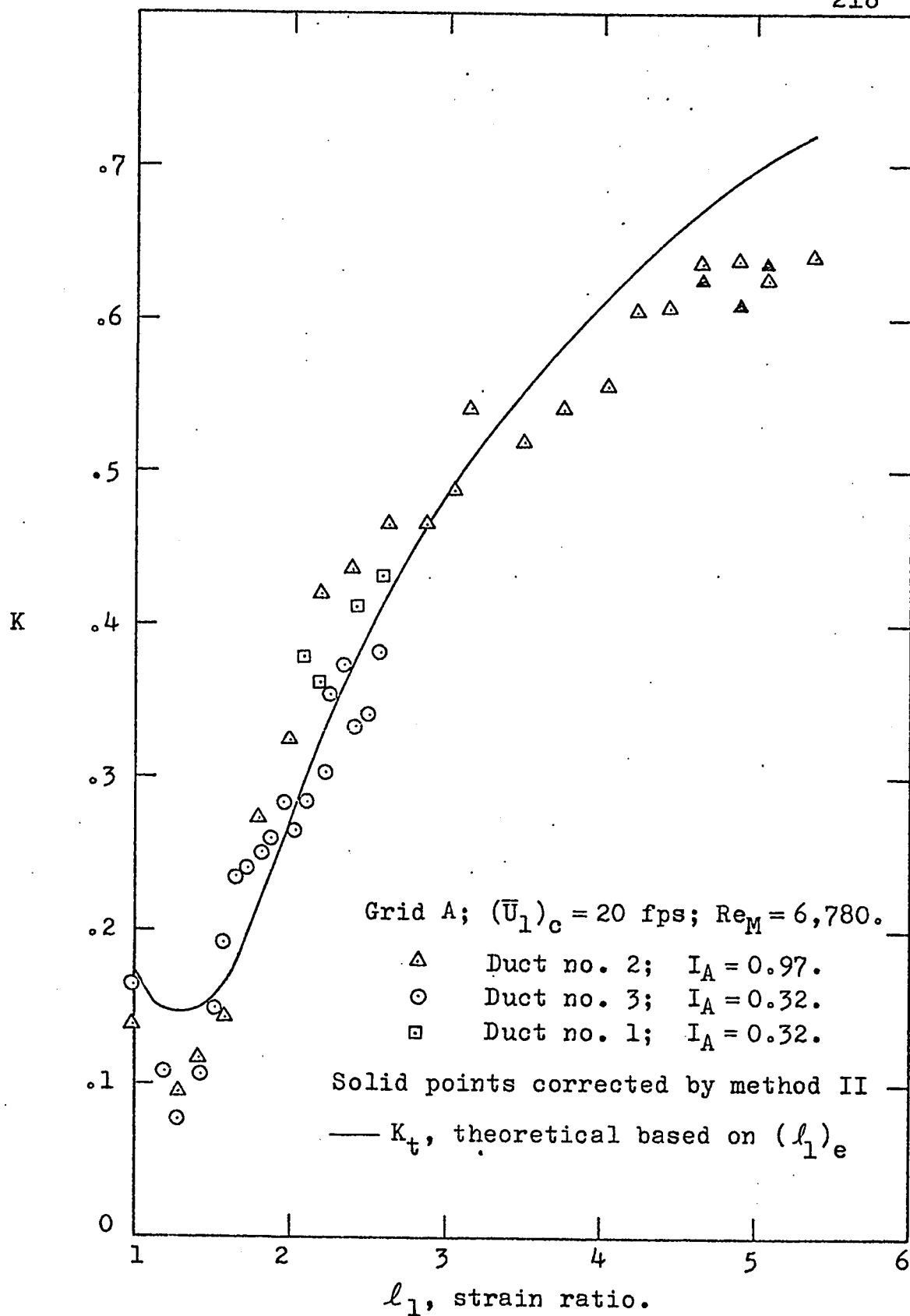
Fig. 43.   Comparison of the structural measure K in the two-
dimensional contractions.
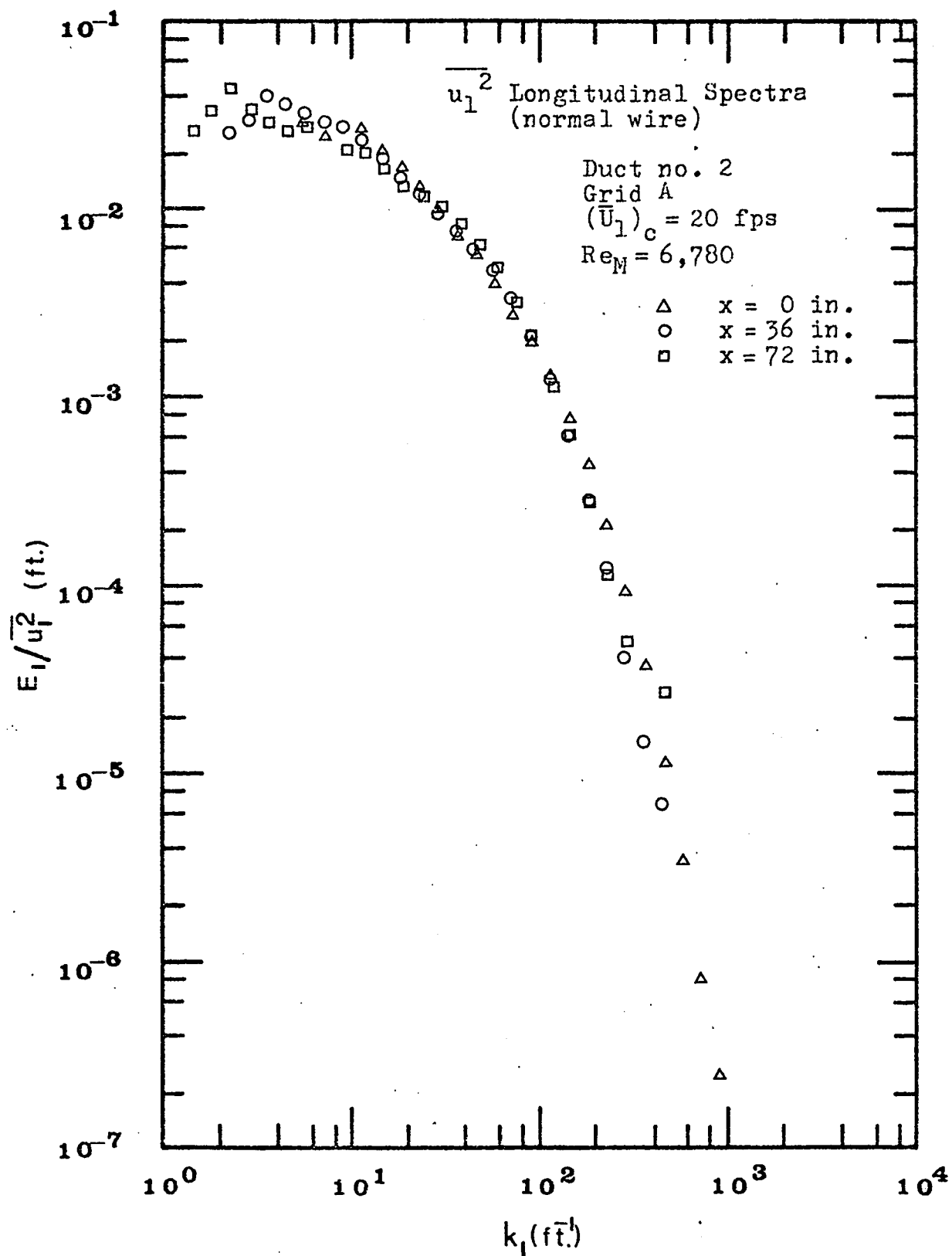
Fig. 44. Changes in the one-dimensional $\overline{u_1^2}$ spectrum in the two-dimensional contraction.
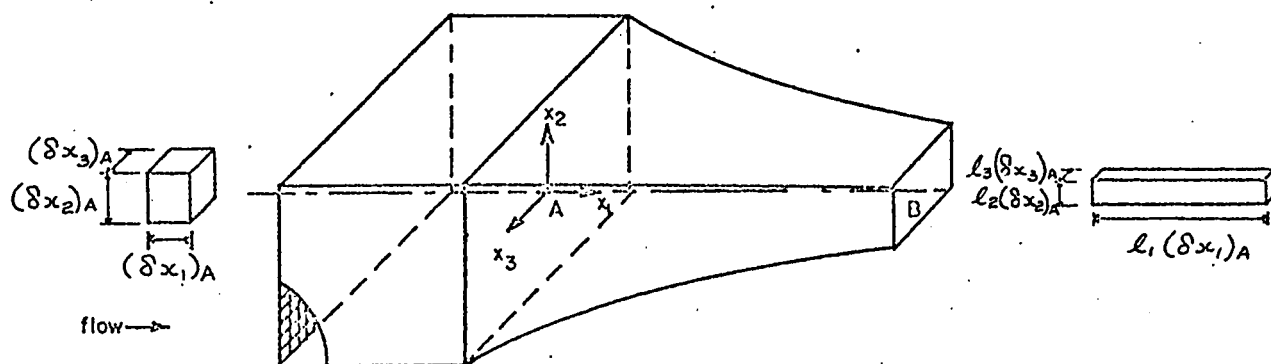
Fig. 45.   Schematic representation of the equivalent
symmetrical contraction.
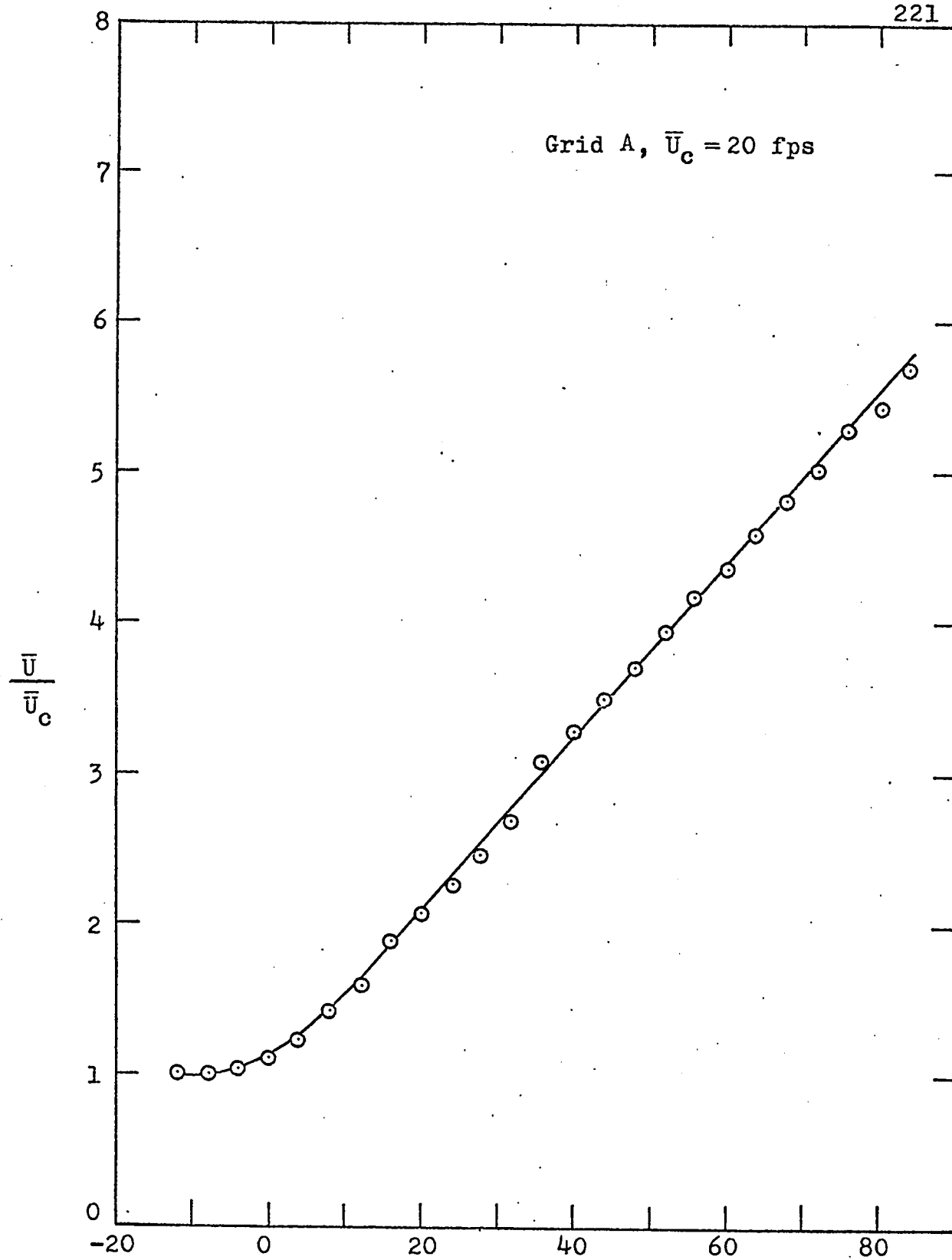
Fig. 46. Mean velocity along the center-line of the
equivalent symmetrical contraction.
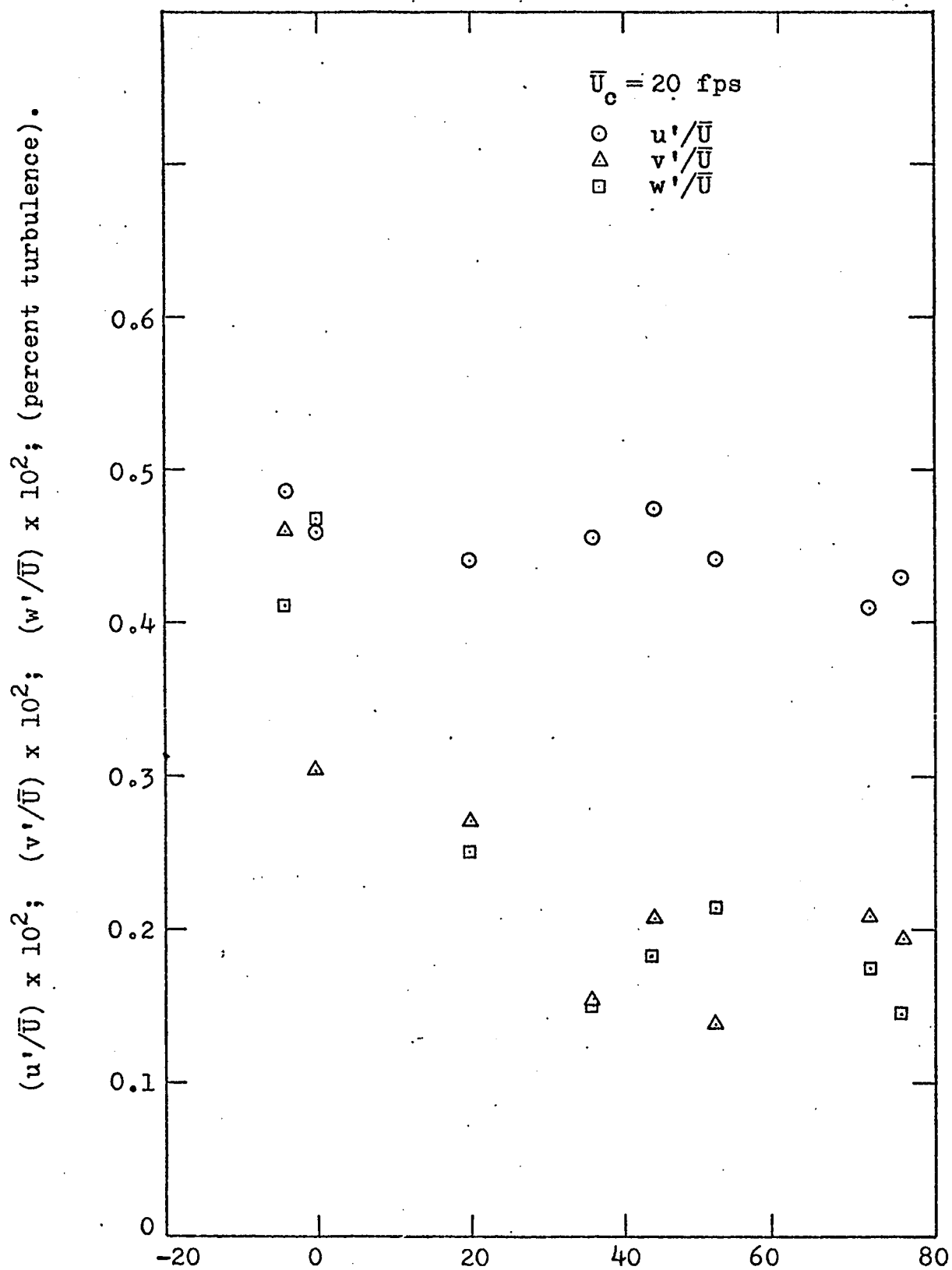
Fig. 47. Background turbulence along the center-line of the equivalent symmetrical contraction.

Fig. 48. Variations of turbulent intensities in the
equivalent symmetrical contraction.
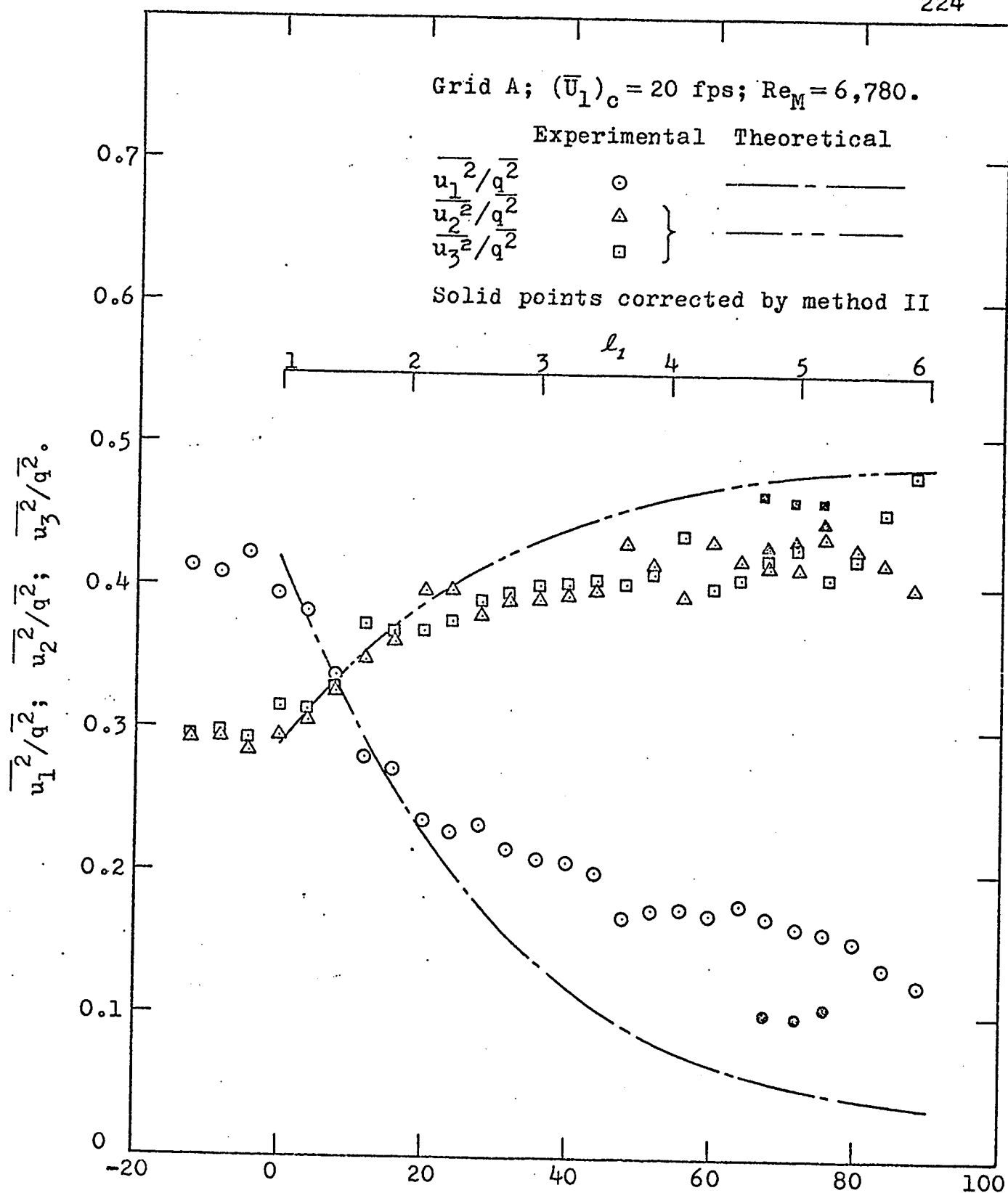
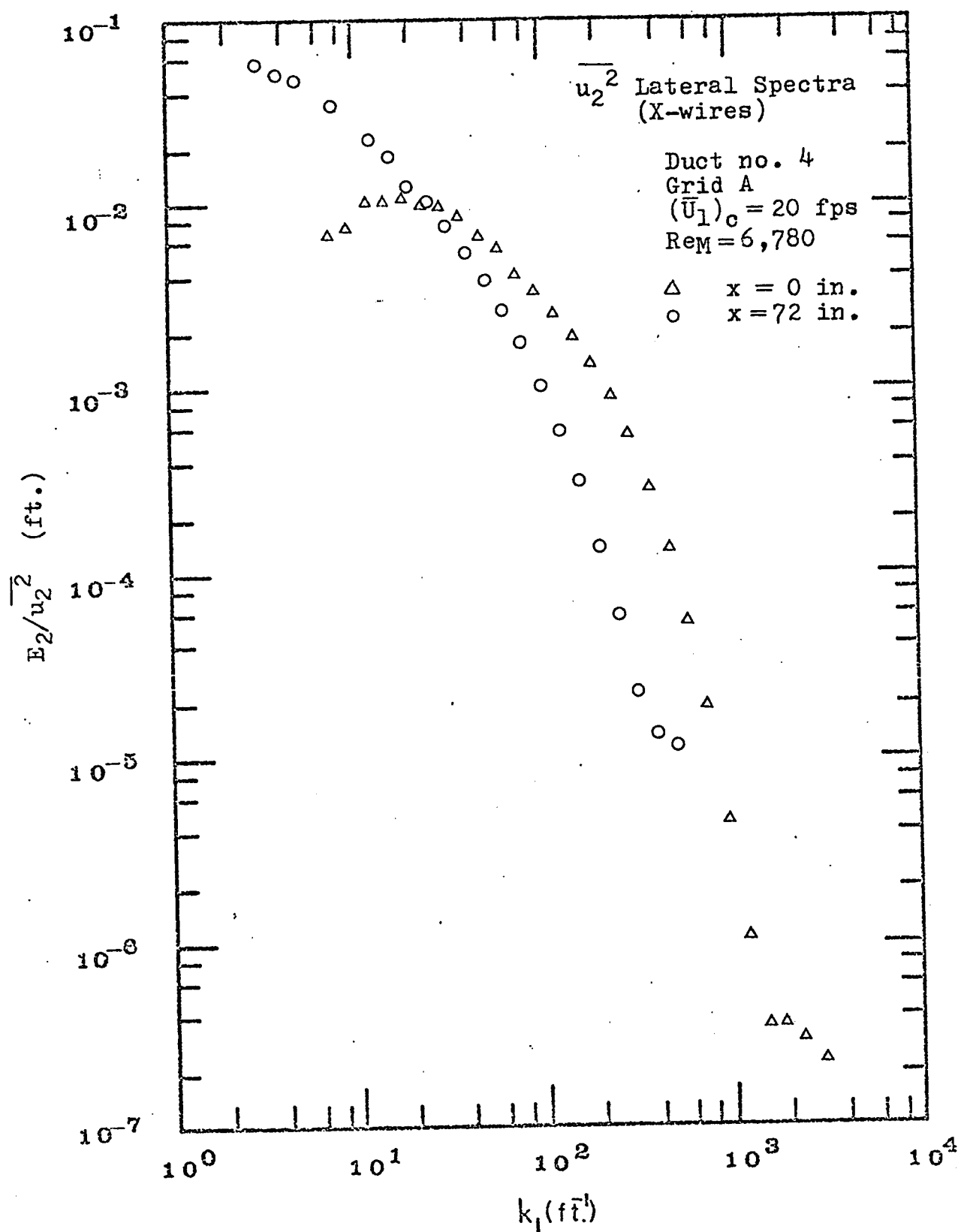Fig. 49. Variations of the local turbulent intensity ratios in the equivalent symmetrical contraction.

Grid A; $\bar{U}_c = 20$ fps; $Re_M = 6,780$.

Solid points corrected by method II

—— K_t, theoretical based on $(\ell_1)_e$

--- $K_m = 0.60\ K_t$

◻ Value calculated from data given
by Uberoi; other values not
shown:- $K = .80$ at $\ell_1 = 9$
$K = .75$ at $\ell_1 = 16$

Distance from entrance of the contracting section (inches).

Fig. 50. Variations of the structural measure K in the
equivalent symmetrical contraction.
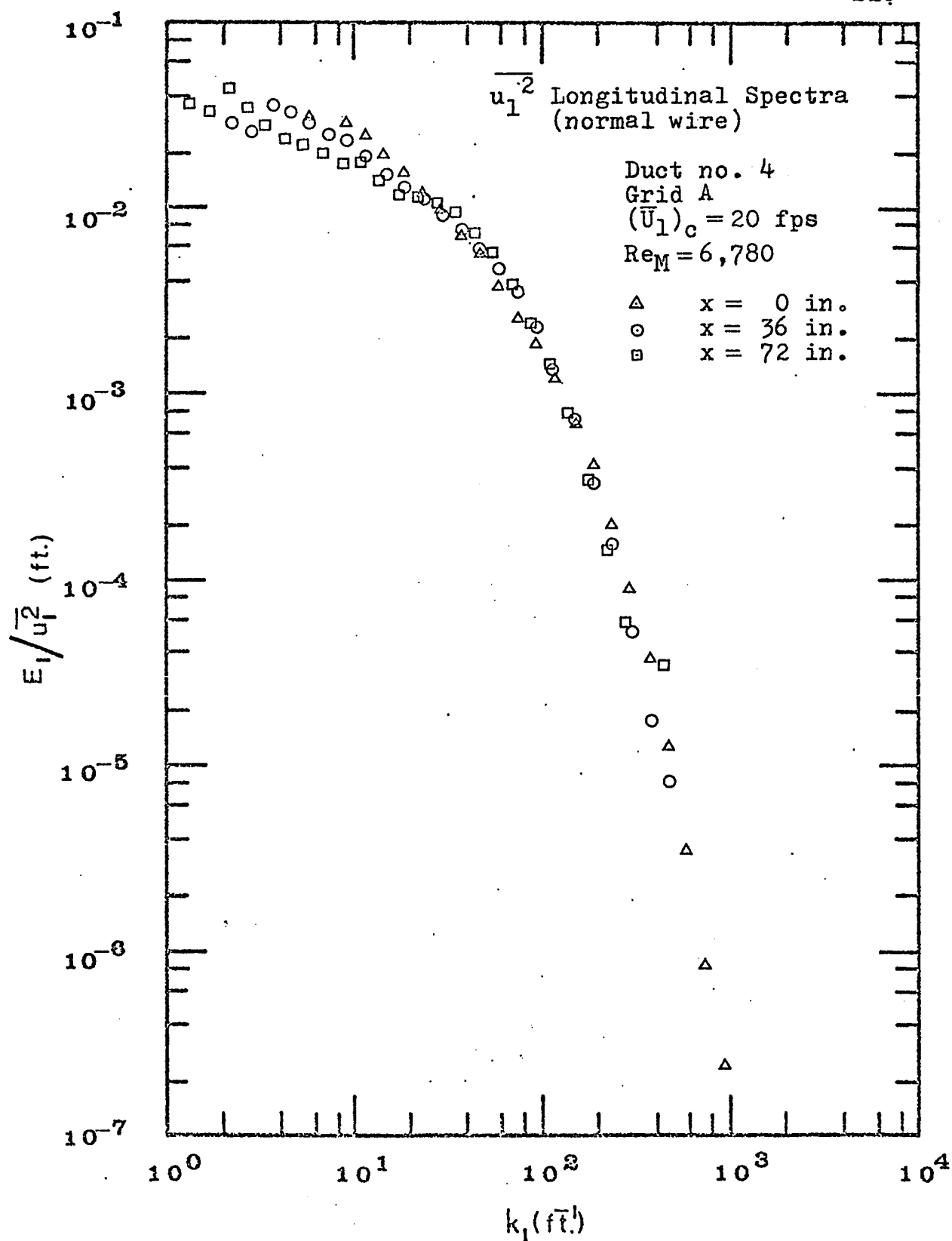
Fig. 51. Changes in the one-dimensional $\overline{u_1^2}$ spectrum in the equivalent symmetrical contraction.

Fig. 52. Changes in the one-dimensional $\overline{u_2^2}$ spectrum in the equivalent symmetrical contraction.
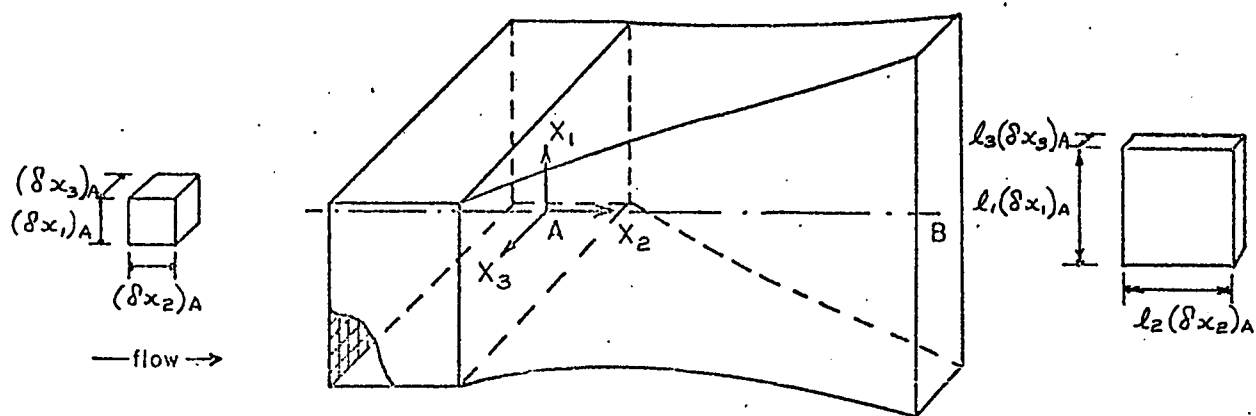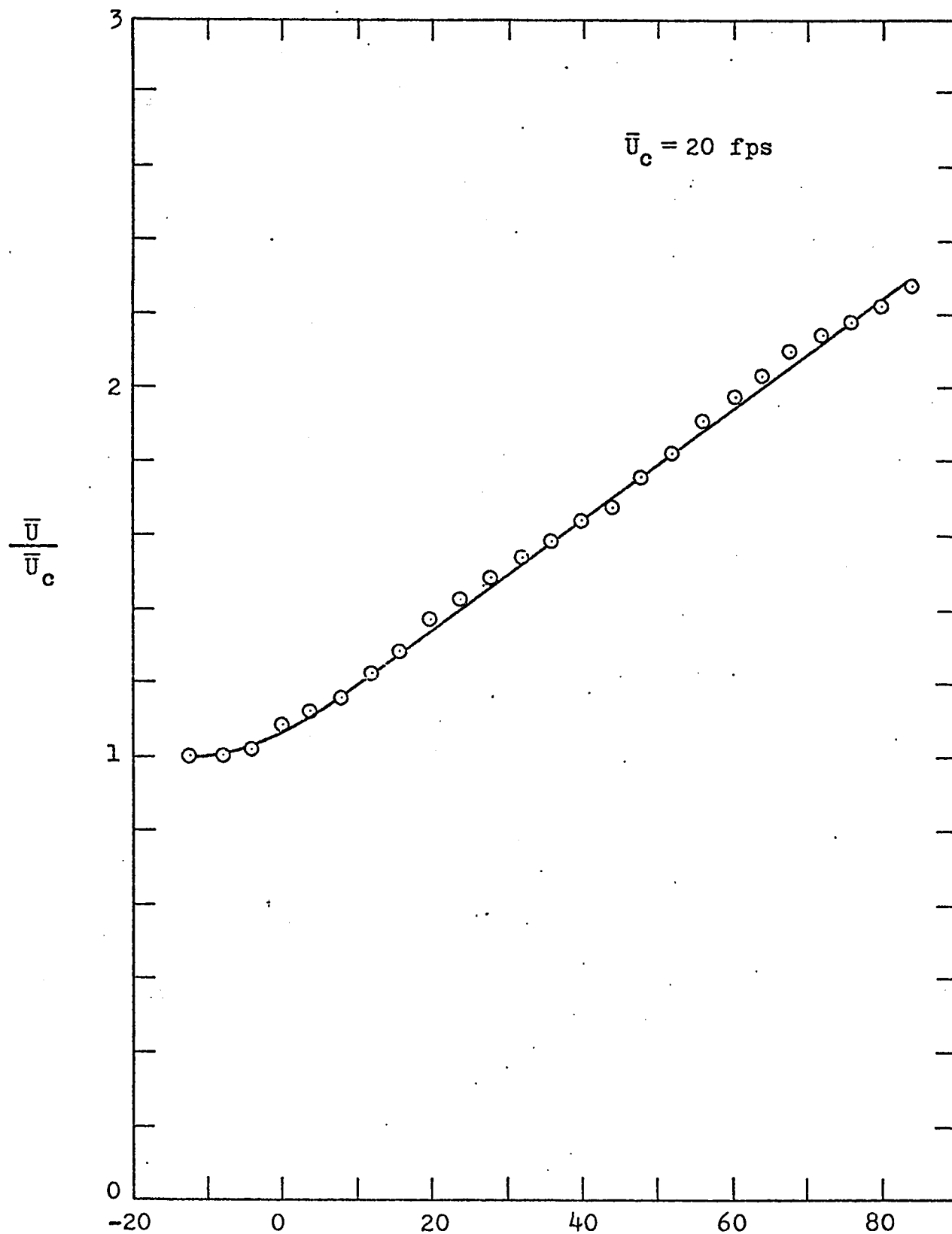
Fig. 53. Schematic representation of the equivalent
symmetrical diffuser.

Distance from entrance of the contracting section (inches).

Fig. 54.   Mean velocities along the center-line of the
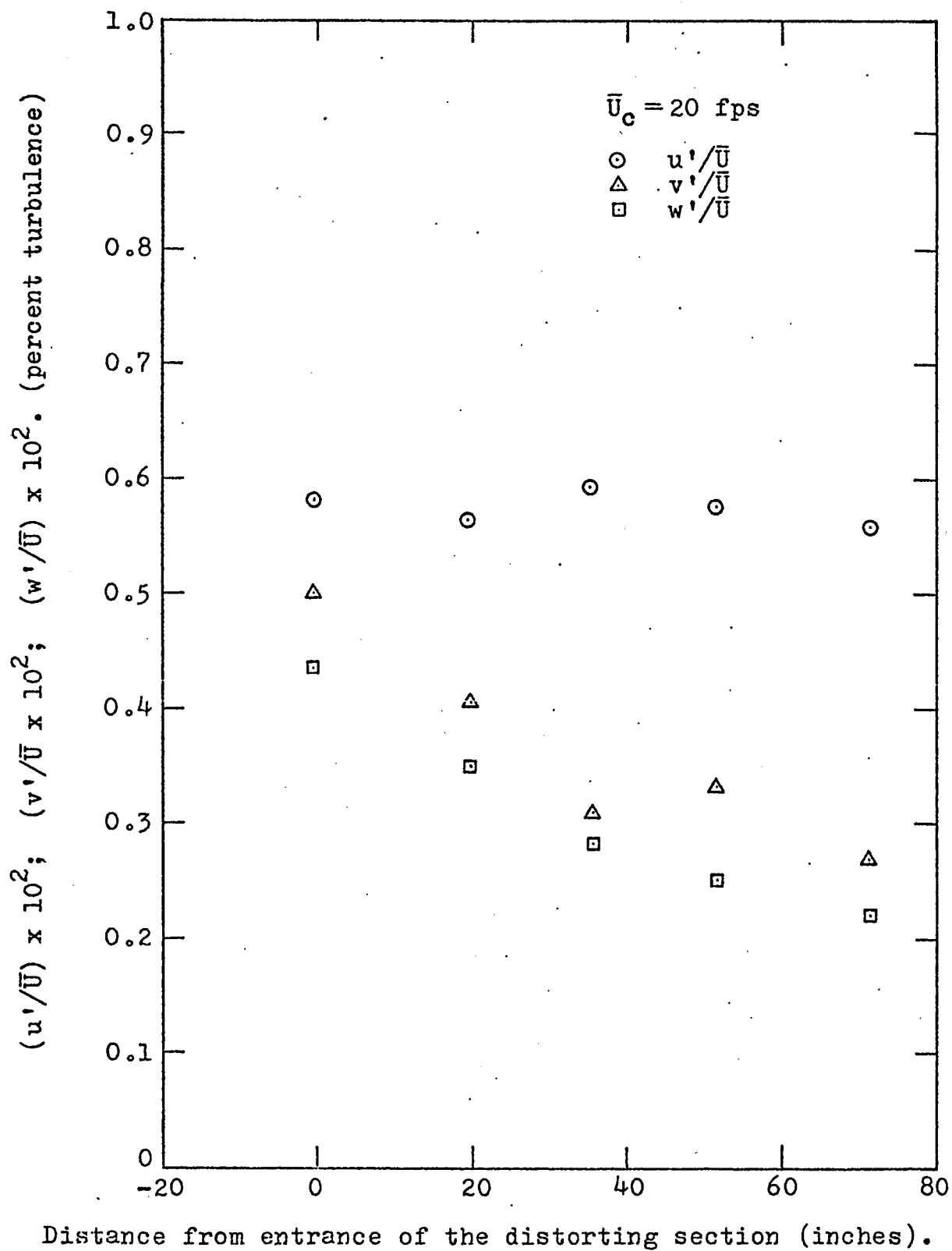equivalent symmetrical diffuser.

Fig. 55. Background turbulence along the center-line of the equivalent symmetrical diffuser.
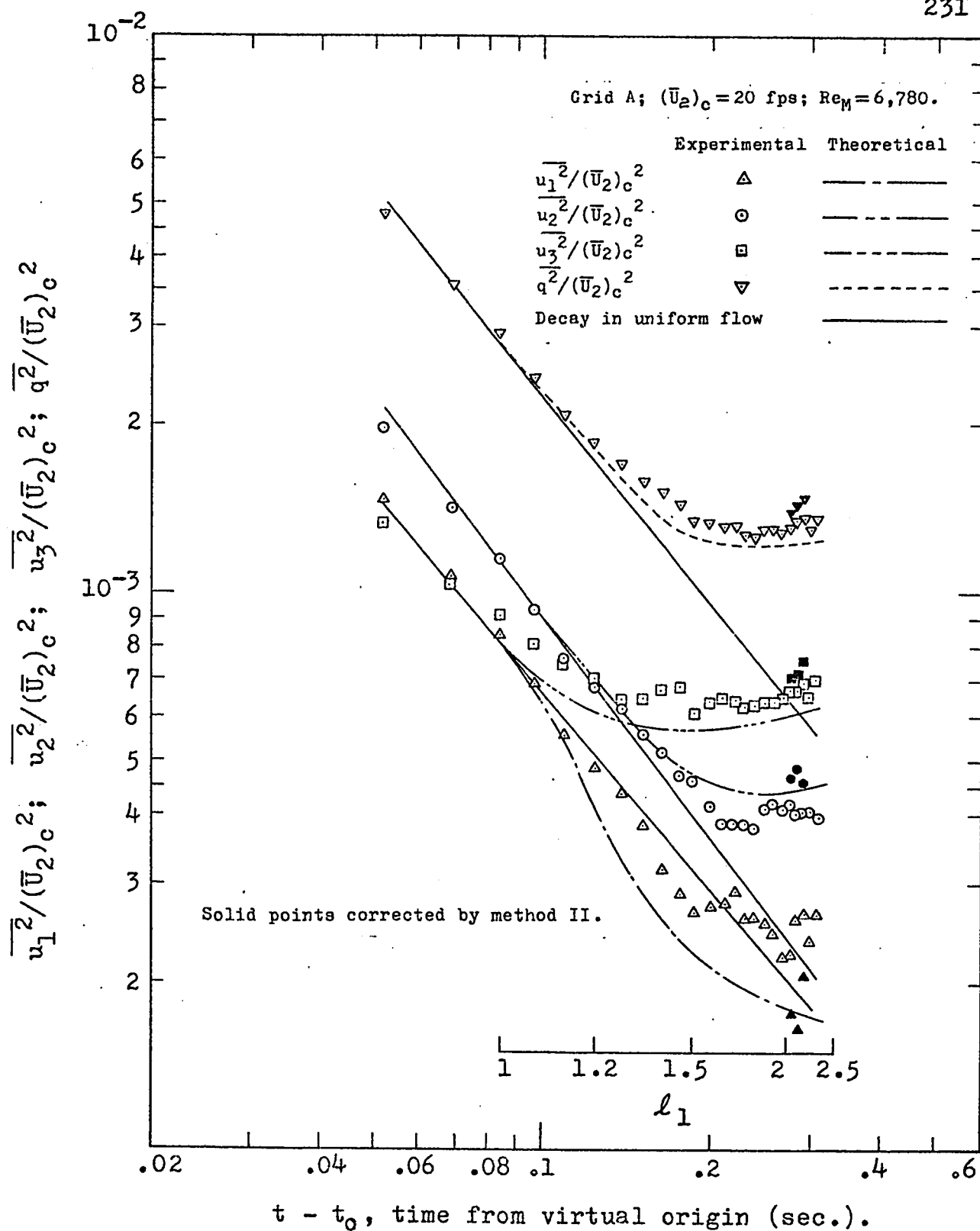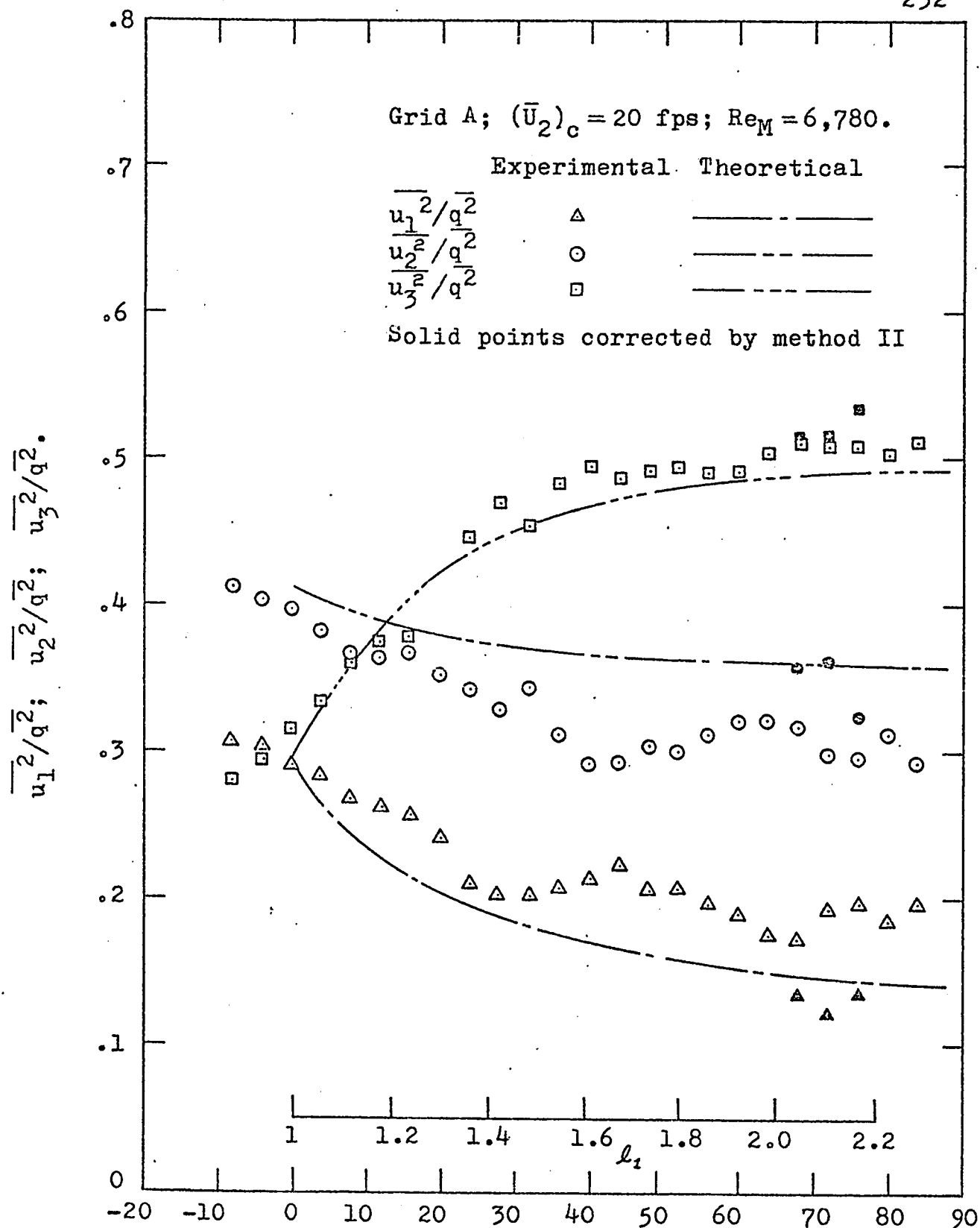
Fig. 56. Variations of turbulent intensities in the
equivalent symmetrical diffuser.

Fig. 57. Variations of the local turbulent intensity ratios
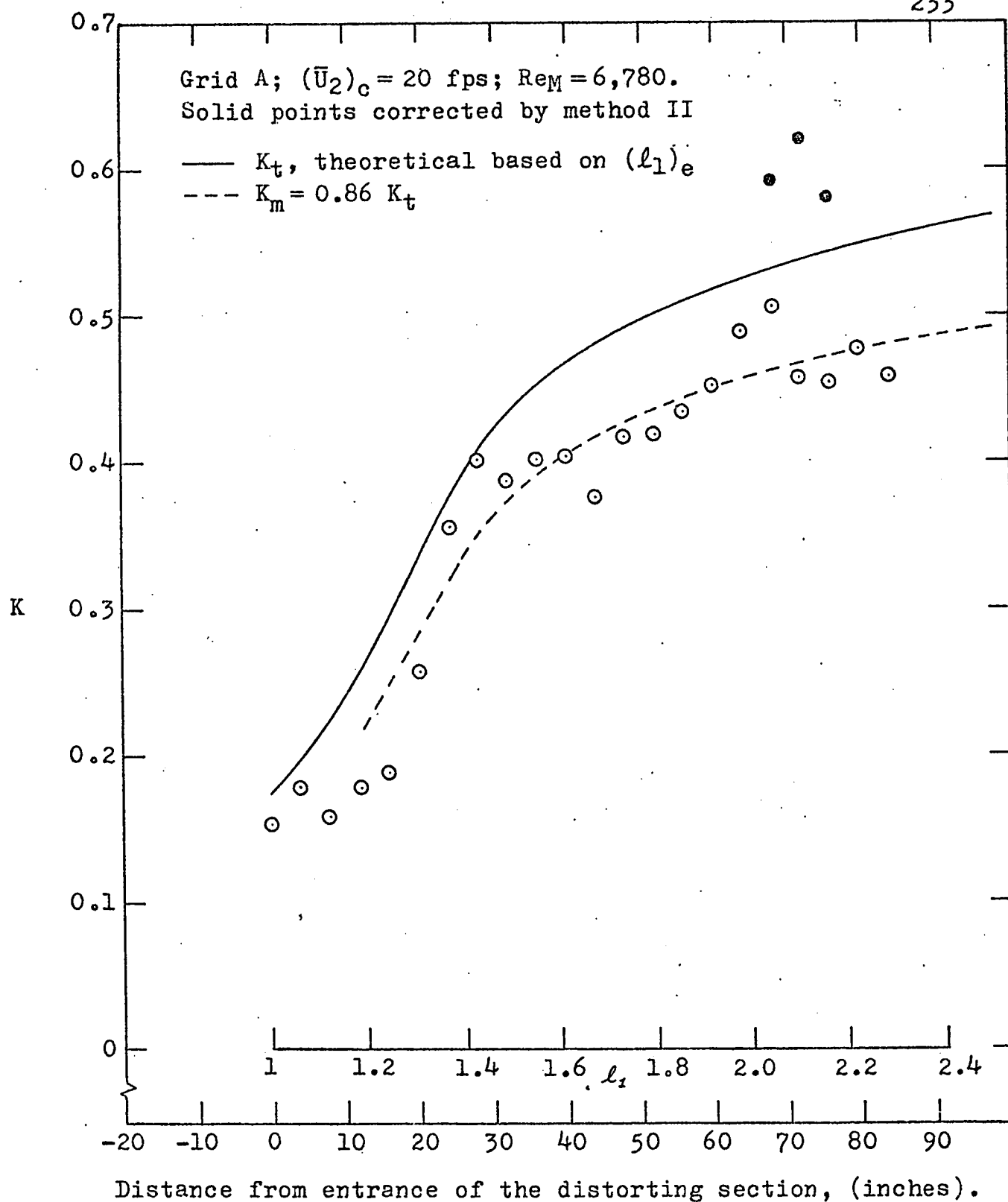in the equivalent symmetrical diffuser.

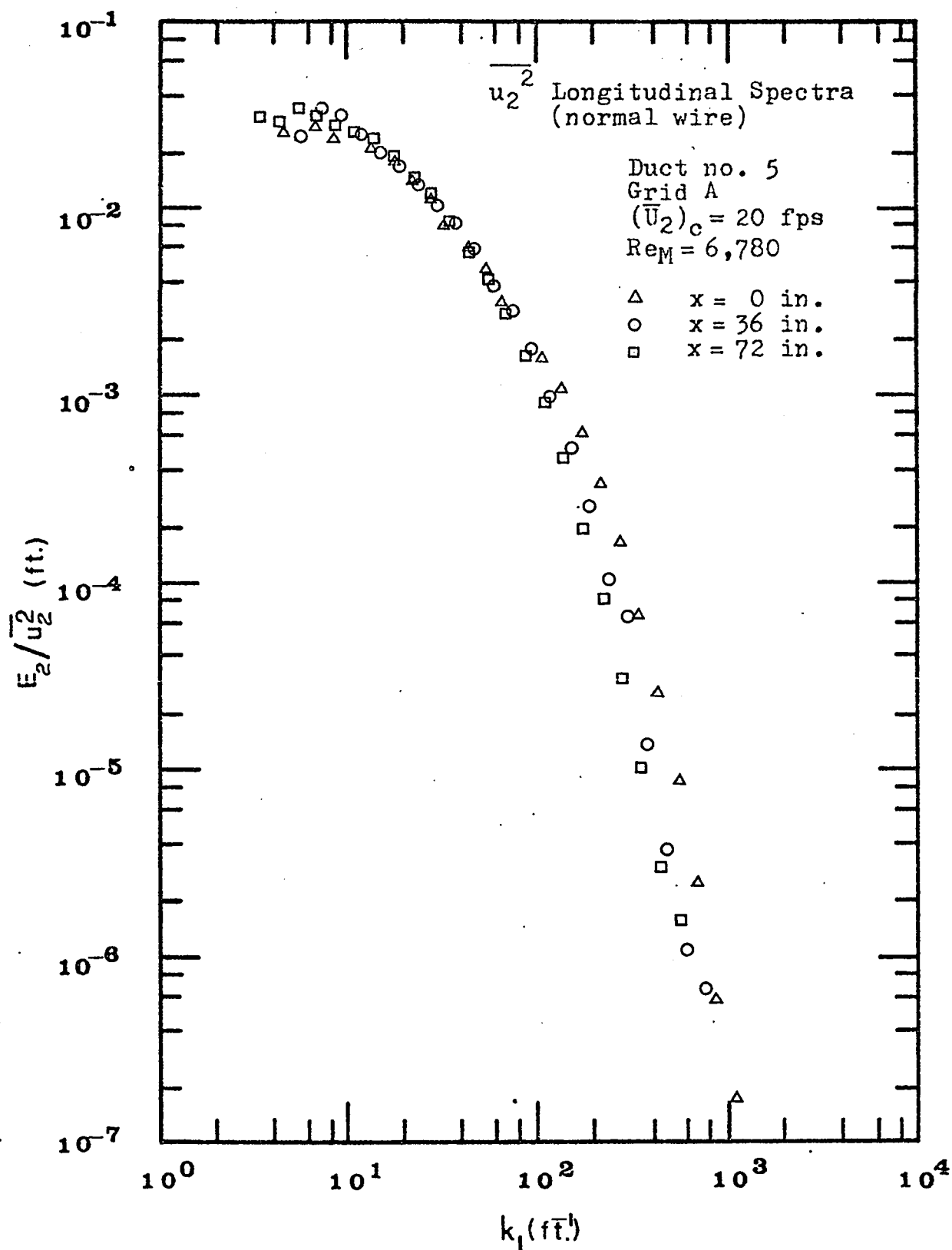Fig. 58. Variations of the structural measure K in the equivalent symmetrical diffuser.

Fig. 59. Changes in the one-dimensional $\overline{u_2^2}$ spectrum in the equivalent symmetrical diffuser.
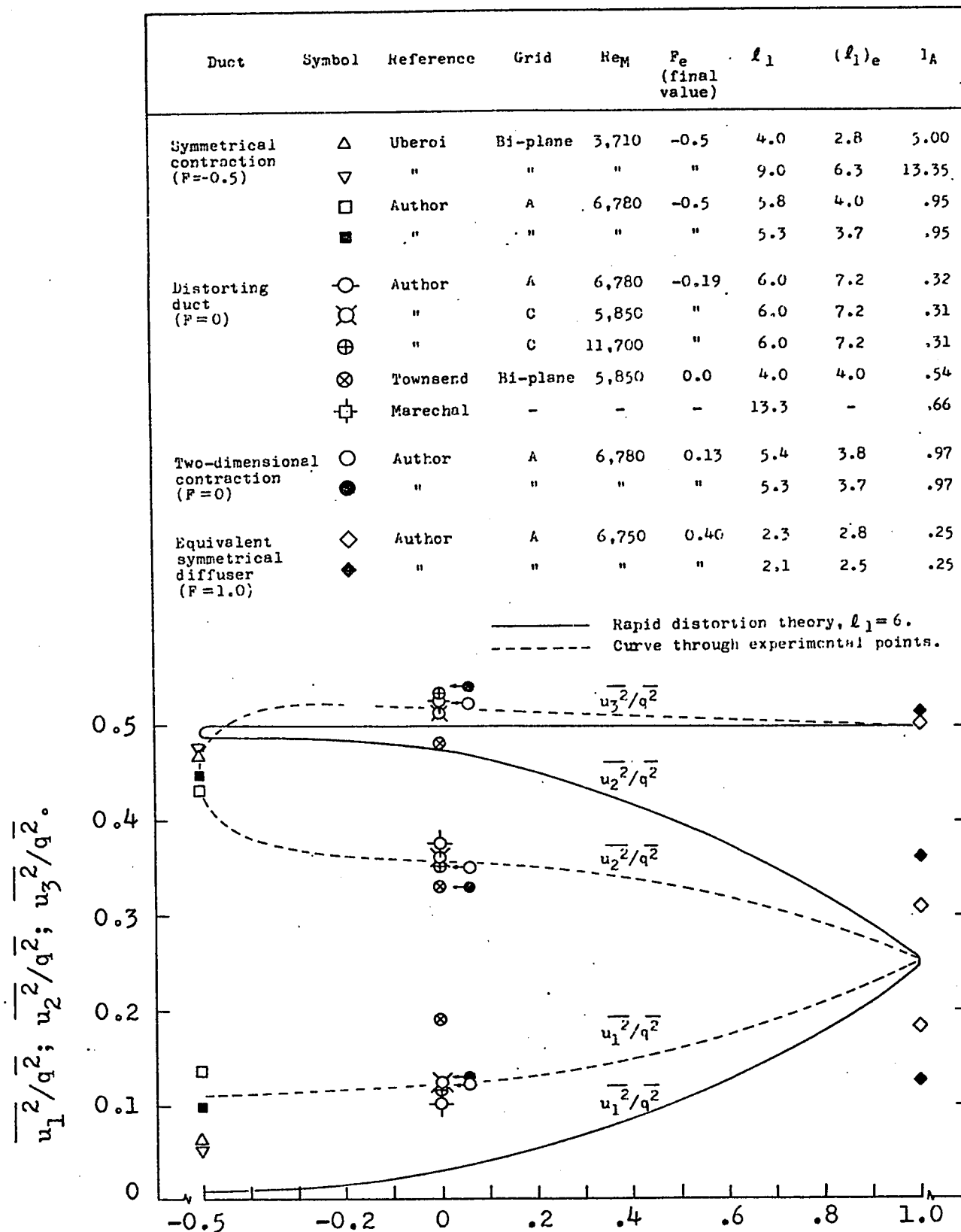
Duct	Symbol	Reference	Grid	Re_M	F_e (final value)	ℓ_1	$(\ell_1)_e$	1_A
Symmetrical contraction (F=-0.5)	△	Uberoi	Bi-plane	3,710	-0.5	4.0	2.8	5.00
	▽	"	"	"	"	9.0	6.3	13.35
	□	Author	A	6,780	-0.5	5.8	4.0	.95
	■	"	"	"	"	5.3	3.7	.95
Distorting duct (F=0)	-O-	Author	A	6,780	-0.19	6.0	7.2	.32
	⋈	"	C	5,850	"	6.0	7.2	.31
	⊕	"	C	11,700	"	6.0	7.2	.31
	⊗	Townsend	Bi-plane	5,850	0.0	4.0	4.0	.54
	⊞	Marechal	–	–	–	13.3	–	.66
Two-dimensional contraction (F=0)	O	Author	A	6,780	0.13	5.4	3.8	.97
	●	"	"	"	"	5.3	3.7	.97
Equivalent symmetrical diffuser (F=1.0)	◇	Author	A	6,750	0.40	2.3	2.8	.25
	◆	"	"	"	"	2.1	2.5	.25

———— Rapid distortion theory, $\ell_1 = 6$.
- - - - - Curve through experimental points.

Fig. 60. Distribution of turbulent energy for different types of strain F.
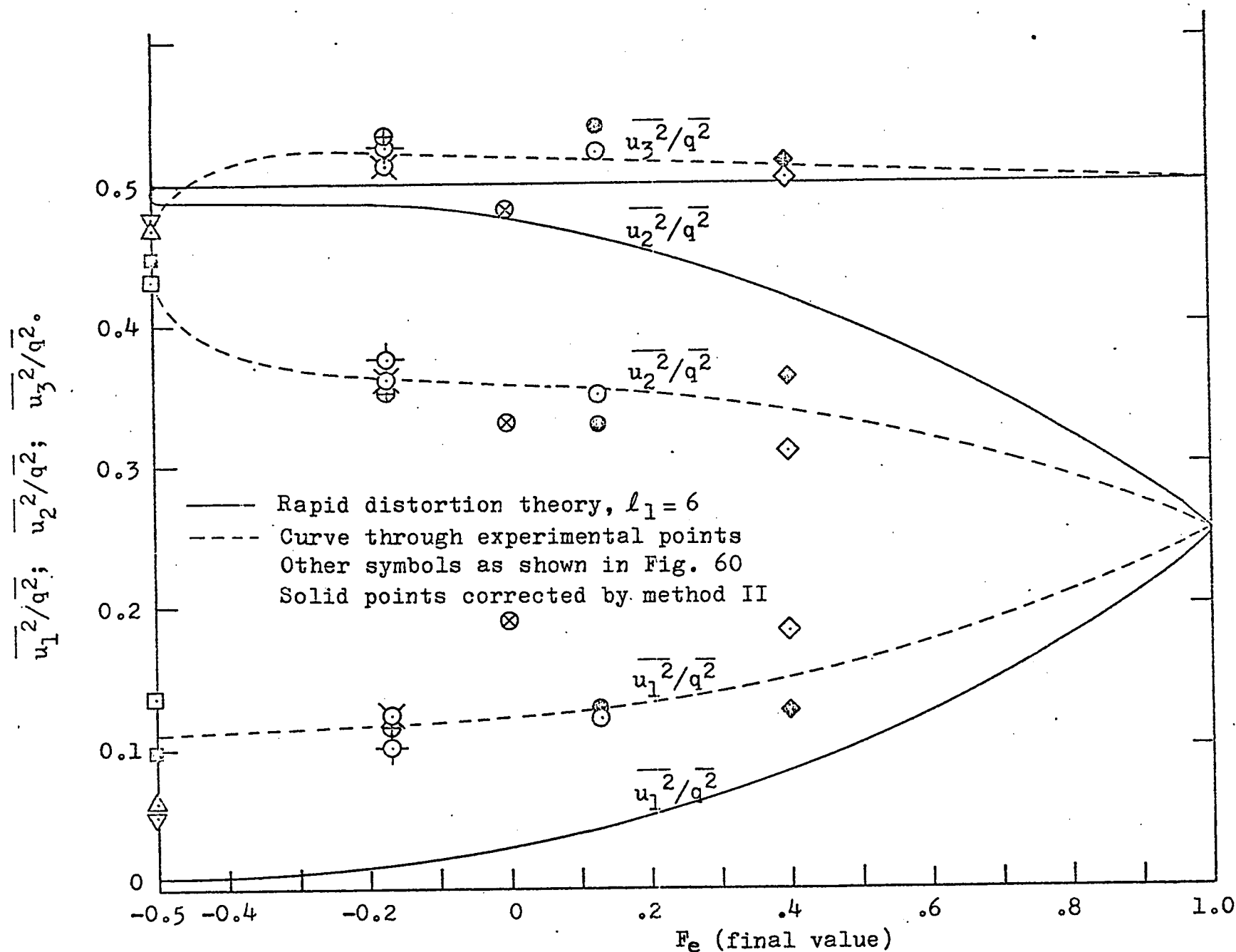
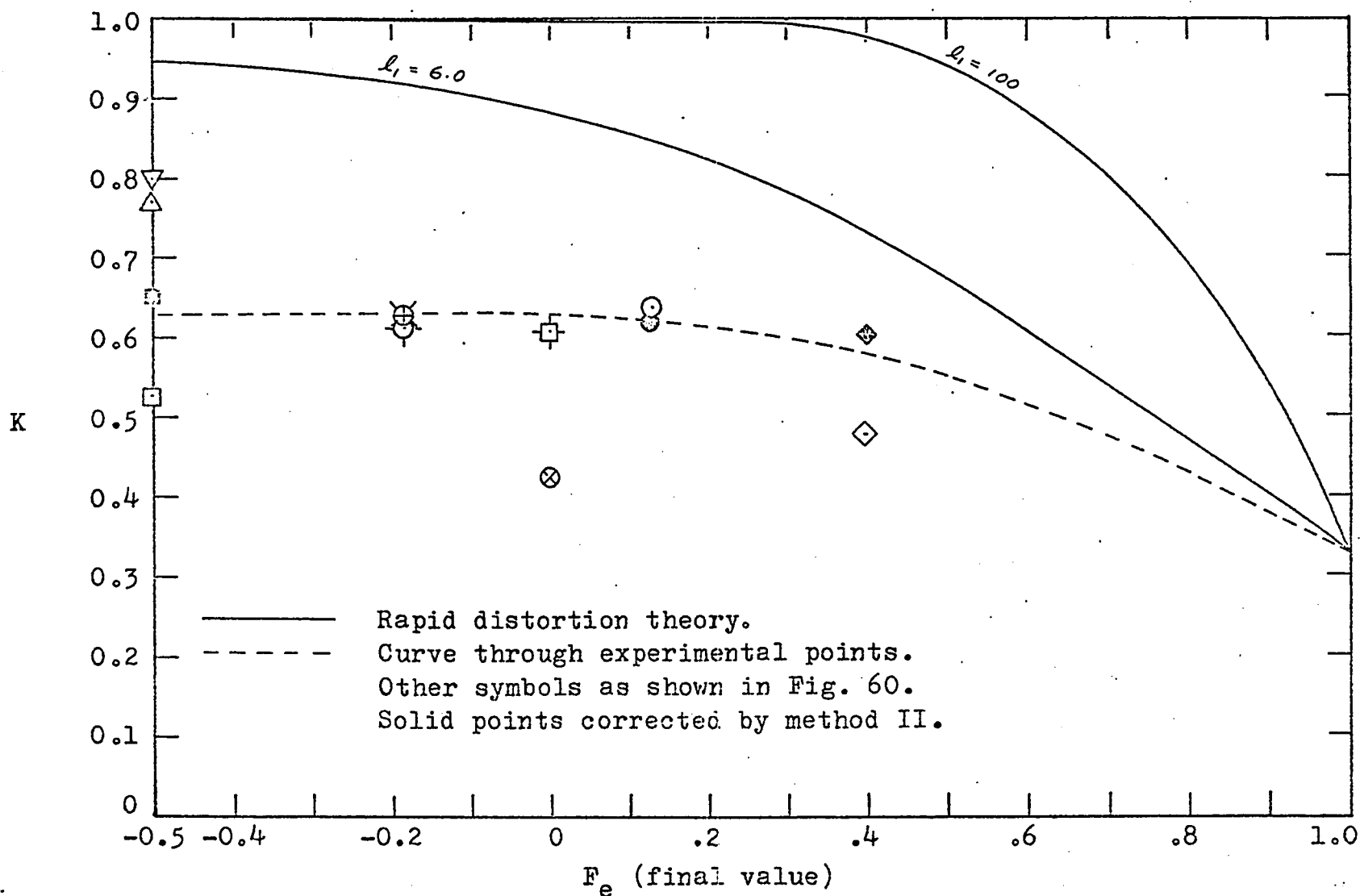Fig. 61. Distribution of turbulent energy for different types of strain F_e.

Fig. 62. Values of the structural parameter K for different types of strain F_e.